Physics of Atomic Nuclei, Vol. 64, No. 11, 2001, pp. 1901–1908. Translated from Yadernaya Fizika, Vol. 64, No. 11, 2001, pp. 1987–1994.

NUCLEI
Experiment

Excitation of Isomeric $1h_{11/2}$ States in Nuclear Reactions Induced by γ Rays and Neutrons and in Beta Decay

A. G. Belov, Yu. P. Gangrsky, L. M. Melnikova, V. Yu. Ponomarev, N. Tsoneva[1], Ch. Stoyanov[1], A. Tonchev[2], and N. Balabanov[3]

Joint Institute for Nuclear Research, Dubna, Moscow oblast, 141980 Russia

Received July 5, 2000; in final form, October 11, 2000

Abstract—Isomeric ratios were measured for $N = 81$ isotones (^{135}Xe, ^{137}Ba, ^{139}Ce, ^{141}Nd, ^{143}Sm). In the experiment reported here, $J^\pi = 11/2^-$ isomers were excited in (n, γ) and (γ, n) reactions and in the β^+ decay of ^{139}Pr and ^{141}Pm. In order to determine the reaction yields, use was made of the activation method involving measurement of the gamma-ray spectra of reaction products. It is found that, in the same reactions, isomeric ratios are different for isotones characterized by different atomic numbers Z. Isomeric ratios were calculated with the spectra of low-lying levels and radiative-transition probabilities established on the basis of the quasiparticle–phonon model. Good agreement between the experimental and calculated values of isomeric ratios is obtained for all isotopes invesigated here. The dependence of isomeric ratios on the atomic number Z of a nucleus is explained by the difference of reaction energies, which leads to different probabilities of excitation of activation levels through which the isomers being considered are populated.

INTRODUCTION

Investigation of nuclear reactions leading to the production of isomeric states is an efficient method for obtaining data on the features of nuclei at low excitation energies. The system of levels through which an isomeric state is populated is one of such features. As a rule, such levels have not yet received adequate study, since they are weakly manifested in the majority of nuclear reactions.

Measurement of isomeric ratios—i.e., ratios of the cross sections for reactions (yields from reactions) leading to the production of a nucleus in an isomeric and in the ground state—that is followed by a comparison of the results of such a measurement with the results of a relevant calculation is the most popular method for studying reactions that involve isomer production. In such calculations, use is made of specific ideas of the properties of nuclear levels, and the degree of agreement between the experimental and calculated values of isomeric ratios is a measure of correctness of these ideas. Usually, the calculations in question rely on the statistical model of the nucleus [1–3] and comply well with experimental data (see, for example, [4–6]) for a number of reactions. It is important that this agreement can be achieved with the level-density parameter a and the spin-cutoff parameter σ (which specify, respectively, the energy and the angular-momentum dependence of the level density) set to values adopted in the model or deduced from independent experimental data.

It is well known that the statistical model faithfully reproduces the spectrum of nuclear levels that occur above the neutron binding energy. At the same time, isomeric ratios are substantially, and even sometimes crucially, affected by lower levels through which gamma-ray cascades populate an isomeric state. However, data on the properties of such levels (specifically, on their spectrum, nucleonic configurations, and wave function) are by far insufficient, so that a correct calculation of this stage of the isomer-production process is often impossible. Obviously, this is one of the reasons behind a noticeable discrepancy between experimental and calculated data. Such a discrepancy is exemplified by the isomeric ratio in the reaction ^{180}Ta(γ, γ'), where the spin difference between the ground-state and the isomeric level is as large as $\Delta J = 8$ and where the measured isomeric ratio is 0.3 [7] (according to statistical-model calculations, it should not exceed 0.001).

It seems natural to calculate isomeric ratios on the basis of a model that would describe well the proper-

[1] Institute for Nuclear Research and Nuclear Energy, Blvd. Tsarigradsko chausse 72, BG-1784 Sofia, Bulgaria.

[2] State University of Idaho, USA.

[3] Hilendarski University, Plovdiv, Bulgaria.

Table 1. Spectroscopic features of nuclei under study

Nucleus	Ground state				Isomeric state			
	$T_{1/2}$	E_γ, keV	I_γ, %	α	$T_{1/2}$	E_γ, keV	I_γ, %	α
^{135}Xe	9.1 h	249.8	93	0.076	15.3 min	526.6	81	0.24
^{137}Ba	Stable				2.55 min	661.6	90	0.11
^{139}Ce	138 d	165.8	80	0.25	56.8 c	754.2	93	0.08
^{141}Nd	2.5 h	1127	0.75	0.002	62.0 d	756.7	92	0.09
^{143}Sm	8.8 min	1056	2.0	0.003	66.0 d	754.0	90	0.11

ties of levels in the excitation-energy range between the isomeric state and the neutron binding energy. For one, this is the quasiparticle–phonon model that was developed by V.G. Soloviev and his colleagues [8–12] and which was successfully used to describe the spectroscopic properties of a wide range of nuclei and nuclear reactions, including those that lead to the excitation of isomeric states [13, 14].

The objective of the present study is to measure isomeric ratios in nuclei having similar properties but in strongly different reactions and to calculate isomeric ratios on the basis of the quasiparticle–phonon model. Our investigation was performed for nuclei that have one hole in the filled neutron shell $N = 82$ (^{135}Xe, ^{137}Ba, ^{139}Ce, ^{141}Nd, ^{143}Sm) and which are produced in the relevant reactions of radiative thermal-neutron capture, (n, γ); photonuclear reactions involving the emission of one neutron, (γ, n), in the giant-dipole-resonance region; and in β^+ decay.

Available experimental data on the isomeric ratios for these nuclei show sizable scatter in the (γ, n) reactions, although these reactions have similar properties. Specifically, the isomeric ratios are much less for ^{141}Nd and especially for ^{143}Sm than for ^{137}Ba and ^{139}Ce [15, 16]. These distinctions are at odds with the results of the calculations according to the statistical model with the values adopted there for the parameters a and σ. In order to achieve agreement, one has to use strongly different values of these parameters for each group of nuclei, but this cannot be reasonably explained.

A totally different type of variation in isomeric ratios is observed for the (n, γ) reactions as one goes over from one nucleus to another: the lightest nucleus ^{135}Xe has the smallest isomeric ratio, and the isomeric ratio grows with increasing atomic number Z [17].

In order to study more comprehensively the behavior of isomeric ratios in the aforementioned region of nuclei, the accuracy of previous measurements was considerably improved: the uncertainties were reduced to 10% for all absolute values of the isomeric ratios and to 5% the for relative ones. This was achieved by using samples enriched in the isotope under study, by more thoroughly calibrating the efficiency of the gamma-radiation detector, and by performing all measurements under identical conditions with a reduced background level.

In addition to measuring isomeric ratios in (n, γ) and (γ, n) reactions, we have also determined the probabilities of isomeric-state excitation in β^+ decay. In the heavy nuclei ^{139}Ce, ^{141}Nd, and ^{143}Sm, there are no direct beta transitions to isomeric states. At the same time, a high beta-decay energy leads to the population of a wide set of nuclei that is comparable with its analog in the (γ, n) reactions. It is the cascade of gamma transitions from these levels that leads to the population of the isomeric state.

SPECTROSCOPIC FEATURES OF THE NUCLEI UNDER INVESTIGATION

The nuclei under investigation have a comparatively simple and nearly identical spectrum of low-lying excitations. All single-particle states following from the shell model ($2d_{3/2}$, $3s_{1/2}$, $2h_{11/2}$, $2d_{5/2}$, $1g_{7/2}$) [8, 18] lie in the energy region extending up to 1.4 MeV. The spin–parity of these nuclei in the ground state is $3/2^+$, while the spin–parity in the first excited state is $1/2^+$. As to $J^\pi = 5/2^+$ and $7/2^+$ single-particle states, they lie much higher (in the energy range 1.1–1.3 MeV). Radiative transitions from all these levels (of the $M1$ or the $E2$ type) lead only to the ground state—they do not populate the isomeric level. It is populated from higher states of spin–parity $J^\pi = 7/2^-$, $9/2^-$, or $9/2^+$.

There are $J^\pi = 11/2^-$ isomeric states in a large number (more than 50) of nuclei from Zr ($Z = 40$) to Yb ($Z = 70$). All these states have close values of the magnetic moment (about half the value computed on the basis of the Schmidt model [19]) and of the reduced probabilities of $M4$ radiative transitions from the isomeric level to the $3/2^+$ ground state (1 to 2 Weisskopf single-particle units). All this suggests the presence of small admixtures of other configurations, although the nuclei involving isomers are

substantially different (ranging from nuclei having a closed proton shell and a nearly closed neutron shell to nuclei from the transition region between spherical nuclei and deformed ones). In the nuclei under investigation, isomeric levels lie comparatively high—from 527 keV in ^{135}Xe to 757 keV in ^{141}Nd. The energies of the isomeric states in question correspond to the energies of gamma rays emitted in their deexcitation (see Table 1).

Table 1 displays the features of the radiative decays of the nuclei under investigation in the ground and isomeric states: the half-lives $T_{1/2}$, the energies $E\gamma$ and the intensities $I\gamma$ of the gamma lines, and the total internal-conversion coefficients α [18]. These data were used to identify product nuclei and to determine their yields.

Data on the statistical properties of the excited states of the nuclei being discussed are much more scanty. By analogy with neighboring nuclei for which the mean spacings between neutron resonances were measured, we can assume that the level-density parameter a and the spin-cutoff parameter σ are about 15 to 20 and 4 to 5, respectively.

EXPERIMENTAL PROCEDURE

Measurements of isomeric ratios in (n, γ) and (γ, n) reactions were performed at the MT-25 microtron installed at the Flerov Laboratory of Nuclear Reactions (Joint Institute for Nuclear Research, Dubna). The description of the microtron and its basic parameters can be found in [20, 21]. An accelerated electron beam served as a source of both bremsstrahlung photons and neutrons.

For a braking target, we used a tungsten disk 2 mm thick followed by a 30-mm-thick aluminum absorber of electrons. A typical electron current during the experiment was 20 μA, the corresponding intensity of bremsstrahlung that had an energy above the (γ, n) threshold and which was incident on a target being about 10^{13} s^{-1}. The maximum energy of the accelerated electrons was 25 MeV; it could be reduced by implementing a transition to a different orbit or by changing a magnetic field. The bremsstrahlung spectrum had a typical shape; its calculation for the conditions of the present experiment (tungsten-disk thickness, solid angle covered by the irradiated sample) is described in [22].

In order to obtain neutrons, an electron beam was directed onto a cylindrical converter made from uranium and surrounded by beryllium. This converter was arranged within a graphite cube of side length 120 cm that served as a moderator for neutrons. The (γ, n) and (γ, f) reactions on uranium and the (γ, n) and $(n, 2n)$ reactions on beryllium were used to produce neutrons. At an electron energy of 25 MeV and an electron current of 20 μA, the thermal-neutron flux at the cube center was 4×10^8 s^{-1} cm^{-2}, the cadmium ratio being 1.8.

The samples subjected to irradiation consisted of the oxides of the elements being investigated (BaO, Ce_2O_3, Nd_2O_3, Sm_2O_3). They had a weight of 200 mg and an area of 1.5×1.5 cm and were packed in thin envelopes of Dacron (20 μm thick). Use was made of both samples of natural isotopic composition and samples enriched in the isotopes being studied (^{136}Ba enriched to 95%, ^{138}Ce enriched to 60%, and ^{144}Sm enriched to 90%). When irradiated, noble gases enriched in the isotopes ^{134}Xe (to 90%) and ^{136}Xe (to 95%) were in quartz-glass ampules of volume about 1 cm^3 at a pressure of 1 atm.

The time of sample irradiation was determined by the half-lives of reaction products. It was about three half-lives for $T_{1/2} < 1$ h and 3 to 4 h for $T_{1/2} > 1$ h. After irradiation, the samples were transported to a room shielded from the radiation of the accelerator, where their gamma-ray spectra were measured. For these measurements, we used a Ge(Li) detector having a volume of 60 cm^3 and a resolution of 2.8 keV for the 1332-keV γ line of ^{60}Co. The measured spectra were processed with the aid of the ACTIV code [23], which makes it possible to separate, in a complex spectrum, γ lines close in energy. The reaction products were identified on the basis of the energies of the γ lines and the time dependence of their intensities (these features of radioactive decay are quoted in Table 1). The absolute intensities of these γ lines (more precisely, their absolute values corrected for the efficiency ε of gamma-radiation detection, the internal-conversion coefficient α, the fraction k of a given γ line in the spectrum, accumulation over the irradiation time t_1, and decay over the time interval t_2 prior to measurements) make it possible to determine the reaction yield

$$Y = \frac{S\lambda(1+\alpha)(1-e^{-\lambda t_1})e^{-\lambda t_2}}{t_3 \varepsilon k}, \qquad (1)$$

where S is the area of the γ line after the background subtraction, λ is the radioactive-decay constant ($\lambda = 0.69/T_{1/2}$), and t_3 is the measurement time. This yield is related to the reaction cross section Σ by the equation

$$Y = A\Sigma I, \qquad (2)$$

where A is the number of atoms of the isotope under investigation in the irradiated sample and I is the flux of bombarding particles (neutrons or photons) that is integrated over the irradiation time. An isomeric ratio (IR) measured experimentally, which is defined as the ratio of the cross sections for the production of

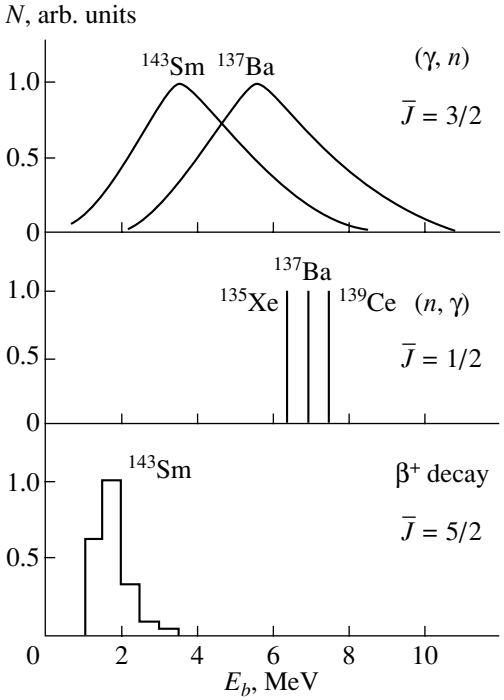

Fig. 1. Excitation-energy distributions of nuclei prior to the gamma-ray cascade in (γ, n) and (n, γ) reactions and in β^+ decay.

a nucleus in the isomeric and in the ground state, can be replaced by the ratio of the corresponding yields, since the measurements were performed for same target and within the same irradiation run; that is,

$$\mathrm{IR} = \frac{\Sigma_i}{\Sigma_g} = \frac{Y_i}{Y_g}, \qquad (3)$$

where the subscripts i and g label quantities referring to the isomeric and the ground state, respectively.

EXPERIMENTAL RESULTS

On the basis of the measurement and data-processing procedures outlined above, we determined isomeric ratios in reactions of three types.

(i) In the reactions of radiative thermal-neutron capture by ^{134}Xe, ^{136}Ba, and ^{138}Ce isotopes, compound nuclei had an excitation energy equal to the corresponding neutron binding energy (see Table 2) and the spin–parity of $J_c^\pi = 1/2^+$. The isomeric states were populated by a gamma-ray cascade, while the isomeric ratios are given by expression (3). The ground-state nucleus produced in the reaction ^{136}Ba$(n, \gamma)^{137}$Ba is stable. In order to obtain the relevant isomeric ratio, we therefore used the value of Σ_g known from [17] and determined Σ_i from a comparison with the well-known cross section for the reaction ^{65}Cu$(n, \gamma)^{66}$Cu [17].

(ii) For photonuclear reactions involving the emission of one neutron at the electron energy (endpoint energy of the bremsstrahlung spectrum) of 25 MeV, we have measured the isomeric ratios for all five nuclei quoted in Table 1. In these reactions, compound nuclei are produced with the spin–parity of $J_c^\pi = 1^-$ and the energy equal to the absorbed-photon energy. Since the bremsstrahlung spectrum and the spectrum of emitted neutrons are both continuous, the product nuclei are characterized by a rather wide excitation-energy distribution, which is given by

$$Y(E_b) = \int_0^{E_0} \int_0^{E_0 - B_n} \sigma(E_\gamma) N(E_\gamma) W(E_n) dE_\gamma dE_n, \quad (4)$$

where E_b is the excitation energy of the final nucleus, B_n is the neutron binding energy in the compound nucleus, $\sigma(E_\gamma)$ is the cross section for the absorption of a photon of energy E_γ, $N(E_\gamma)$ is the number of photons of energy E_γ in the bremsstrahlung spectrum with endpoint energy E_0, and $W(E_n)$ is the probability of the emission of a neutron of kinetic energy E_n from the compound nucleus. In order to calculate these distributions, we used the energy dependences of the cross sections for monochromatic-photon absorption from [24], the kinetic-energy spectra of neutrons from [25], and the bremsstrahlung spectrum computed in [22] for the conditions of the present experiment. Some examples of these distributions are presented in Fig. 1, while the mean excitation energies of the final nuclei for all reactions considered here are quoted in Table 2.

Since, for the relevant (γ, n) reactions, it is not the cross section but the yield integrated over the bremsstrahlung spectrum that is measured experimentally, the isomeric ratio is determined as the yield ratio

$$\mathrm{IR} = \frac{\int_{E_1}^{E_0} \sigma_i(E_\gamma) N(E_\gamma) dE_\gamma}{\int_{E_1}^{E_0} \sigma_g(E_\gamma) N(E_\gamma) dE_\gamma}, \qquad (5)$$

where E_1 is the threshold for the reaction leading to the production of a nucleus in the ground or in the isomeric state. We have $E_1 = B_n$ for the ground state and $E_1 = B_n + E_i$ for the isomeric state.

Just as in the case of (n, γ), a direct measurement of the yield of the stable final nucleus ^{137}Ba was impossible. For this reason, the relevant isomeric ratio was determined from a comparison of the yields of the ^{137}Ba and ^{139}Ce isomers and the known ^{138}Ba(γ, n) and ^{140}Ce(γ, n) cross sections integrated over the bremsstrahlung spectrum [24].

Table 2. Experimental and calculated values of the isomeric ratios for (γ, n) and (n, γ) reactions and for beta decay

Reaction	$\bar{E}_b$, MeV	$\bar{J}$, $\hbar$	Isomeric ratios	
			experiment	calculation
^{134}Xe$(n, \gamma)^{135}$Xe	6.45	1/2	0.013(2)	0.023*
^{136}Xe$(\gamma, n)^{135}$Xe	6.1	3/2	0.110(9)	0.11**
^{136}Ba$(n, \gamma)^{137}$Ba	6.90	1/2	0.022(3)	0.024*
^{138}Ba$(\gamma, n)^{137}$Ba	5.4	3/2	0.120(8)	0.10**
^{138}Ce$(n, \gamma)^{139}$Ce	7.47	1/2	0.025(3)	0.027*
^{140}Ce$(\gamma, n)^{139}$Ce	4.8	3/2	0.130(8)	0.11**
$^{139}\mathrm{Pr} \xrightarrow{\beta^+} {}^{139}\mathrm{Ce}$	1.6	5/2	0.008(2)	0.007**
^{142}Nd$(\gamma, n)^{141}$Nd	4.2	3/2	0.060(6)	0.05**
$^{141}\mathrm{Pm} \xrightarrow{\beta^+} {}^{141}\mathrm{Nd}$	2.1	5/2	0.009(2)	0.010**
^{144}Sm$(\gamma, n)^{143}$Sm	3.5	3/2	0.046(5)	0.05**
$^{143}\mathrm{Eu} \xrightarrow{\beta^+} {}^{143}\mathrm{Sm}$	2.2	5/2	0.007(2)	0.007**

* Calculations according to the statistical model.
** Calculations according to the quasiparticle–phonon model.

(iii) In determining the isomeric ratios for the β^+ decay of and for electron capture by ^{139}Pr ($T_{1/2} = 4.4$ h, $Q_\beta = 2.80$ MeV, $J^\pi = 5/2^+$) and ^{141}Pm ($T_{1/2} = 20.9$ min, $Q_\beta = 4.56$ MeV, $J^\pi = 5/2^+$) nuclei, we obtained them in the reactions ^{141}Pr$(\gamma, 2n)^{139}$Pr ($E_{\gamma 0} = 25$ MeV) and ^{141}Pr$(\alpha, 4n)^{141}$Pm ($E_\alpha = 38$ MeV), respectively, at the MT-25 microtron and the U-200 isochronous cyclotron of the Flerov Laboratory of Nuclear Reactions (JINR, Dubna). By using the experimental facility described above, we have measured the spectra of gamma radiation emitted in the beta decay of ^{139}Pr and ^{141}Pm nuclei. The by-products of the photon- and alpha-particle-induced reactions (^{140}Pr, ^{142}Pm, ^{143}Pm) had significantly different half-lives, and their gamma radiation could easily be discriminated.

An analysis of the spectra of gamma radiation from ^{139}Pr and ^{141}Pm enabled us to determine the probabilities of the population of isomers in the daughter nuclei ^{139}Ce and ^{141}Nd. In this analysis, we also used data on the β^+ decay of these isotopes [18] and of ^{143}Eu, the isomer in the ^{143}Sm nucleus being excited in the last case [26]. By analogy with the (n, γ) and (γ, n) reactions considered above, we also evaluated isomeric ratios in beta decay, determining them as the ratios of the numbers of nuclei produced in the isomeric state to the number of beta transitions to all levels above the isomer:

$$\mathrm{IR} = \frac{N_i}{\sum N_\beta(E_b > E_i)}. \qquad (6)$$

By way of example, one excitation-energy distribution of nuclei originating from β^+ decay (for ^{143}Sm) is displayed in Fig. 1. Because of a finite and comparatively small number of beta transitions, a histogram is presented here instead of a continuous distribution. For the remaining nuclei (^{139}Ce, ^{141}Nd), the analogous distributions have a similar shape. In relation to the corresponding distributions for the relevant (γ, n) reactions, the distributions being discussed are narrower and are shifted toward lower energies.

The isomeric-ratio values measured in this way for all reactions studied here are presented in Table 2, along with the features of final nuclei (mean excitation energies $\bar{E}_b$ and mean angular momenta $\bar{J}$) before the gamma-ray cascade leading to the isomeric or the ground state. Within the combined errors, these isomeric-ratio values agree with the known data from [15–17], but, as was noted above, the former are characterized by a higher accuracy; as a result, we can now draw more reliable conclusions about the distinctions between the isomeric ratios for different nuclei and different reactions for their production.

DISCUSSION OF THE RESULTS

From Table 2 and from Fig. 1, we can see that the conditions of isomer excitation are different in different processes. In beta-decay processes, the cascade of gamma rays begins from a comparatively narrow range of low-lying levels (1.5–3.0 MeV), whose mean angular momentum (5/2) is higher than in other processes. The situation is totally different in the relevant (n, γ) reactions—the excitation energy is the highest

(6.5–7.5 MeV), while the angular momentum is the lowest (1/2). In this respect, the (γ, n) reactions in question occupy an intermediate position—they are characterized by the greatest scatter of excitation energies and angular momenta. This variety of nuclear features leads to considerable distinctions between isomeric ratios and makes it possible to obtain comprehensive information about the spectrum of levels through which the isomers are populated.

An analysis of the spectrum of gamma radiation emitted in the beta decay of ^{139}Pr, ^{141}Pm, and ^{143}Eu revealed that, in all cases, the isomers are populated by radiative $E2$ transitions through $J^\pi = 7/2^-$ levels that are excited immediately after the relevant beta transitions. In the ^{139}Ce (^{141}Nd) nucleus, the isomer is populated through the single $7/2^-$ level at 1.578 (1.420) MeV, while, in the ^{143}Sm nucleus, this occurs through three levels at 1.310, 2.886, and 3.325 MeV. In these three nuclei, the isomeric ratios have close values and are determined primarily by the probabilities of the beta transitions to the $7/2^-$ levels involved.

In the (n, γ) reactions, a sufficiently long cascade of gamma transitions (not less than three) is required for populating the isomer because the spin difference between the compound nucleus and the isomer is large ($\Delta J = 5$). A wide energy gap between the initial level and the isomer (more than 6 MeV) favors the development of such a cascade and makes it possible to calculate the isomeric ratios on the basis of the statistical model. The calculations for this case were performed with the aid of the EMPIRE code [27]. At the parameter values of $a = 18$ and $\sigma = 4.5$, the isomeric ratios calculated in this way are presented in Table 2. Good agreement is seen to be obtained for ^{137}Ba and ^{139}Ce, whence we conclude that, in the (n, γ) reactions, the statistical model is applicable to these nuclei. However, an analysis of gamma radiation emitted in thermal-neutron capture by a ^{136}Ba nucleus [28] has revealed that about half of the contribution to the relevant isomeric ratio comes from a single gamma-ray cascade through ^{137}Ba levels:

$$6.605\ \text{MeV}(1/2^+) \xrightarrow{E1} 2.182\ \text{MeV}(3/2^-)$$
$$\xrightarrow{E2} 1.798\ \text{MeV}(7/2^-) \xrightarrow{E2} 0.661\ \text{MeV}(11/2^-).$$

This gamma-ray cascade indicates that specific states through which the isomer is populated may play an important role in the (n, γ) reactions, as they do in beta decay.

In the (γ, n) reactions, spin-1/2 to spin-9/2 levels that lie in a broad range of excitation energies (Fig. 1) are populated following neutron evaporation. It is the properties of these levels that determine the probability of isomer excitation. They have a complicated structure—their single-particle and collective components are fragmented over a wide energy interval and undergo strong fluctuations. To describe them, it is therefore desirable to use some effective approach. We will invoke an approach based on the aforementioned quasiparticle–phonon model [8–12], which was successfully used to describe a number of nuclear phenomena.

CALCULATION OF ISOMERIC RATIOS WITHIN THE QUASIPARTICLE–PHONON MODEL

For many nuclei, the spectra of excited states in a broad range of excitation energies and their reduced the widths with respect to the radiative transitions from them to the isomeric and the ground state in each nucleus being considered have been calculated within this model; in addition, so-called activation states—that is, states from which isomeric levels are populated as the result of gamma decay—have been singled out on the same basis. In these calculations, both the ground state and excited states characterized by an angular momentum J and its projection M were described in terms of the wave function

$$\Psi^\nu_{JM} = C^\nu_J\{\alpha^+_{JM} + \sum_{\lambda JM} D^{\lambda i}_j(J\nu)[\alpha^+_{jm}Q^+_{\lambda\mu i}]_{JM}\Psi_0\}, \quad (7)$$

where α^+_{jm} is the creation operator for a quasiparticle having the shell quantum numbers j and m; $Q^+_{\lambda\mu i}$ is the creation operator for a phonon having an angular momentum λ, its projection μ, and a number i; Ψ_0 is the wave function for the neighboring even nucleus; and ν is the ordinal number of an excited state in the sequence of states characterized by given J^π. The coefficients C^λ_J and $D^{\lambda i}_j$ are the quasiparticle and the quasiparticle–phonon amplitudes for ν states. The calculations performed with the wave functions (7) are described in detail elsewhere [12, 29].

In the calculations described below, the Woods–Saxon potential with the parameters set to the values from [30, 31] was used for that part of the Hamiltonian which describes the mean field. The strength of the residual interaction was chosen in such a way as to reproduce, in the one-phonon approximation, the experimental values of the energies and reduced probabilities of low-lying collective states in the neighboring even–even nuclei [32]. The wave functions used in our calculations took into account the $\lambda^\pi = 1^\pm$, 2^+, 3^-, 4^+, and 5^- phonons. We employed the effective charges $e_p = (N/A)e$ and $e_n = -(Z/A)e$ for $E1$ transitions and the effective charges $e_p = e$ and $e_n = 0$ for $E2$ transitions. The contribution of electromagnetic transitions of other multipole orders to the processes being considered is negligible.

We have calculated the spectrum of $J^\pi = 1/2^\pm$, $3/2^\pm$, $5/2^\pm$, $7/2^\pm$, $9/2^\pm$, and $11/2^\pm$ excited states up to the excitation energy of 6.5 MeV and their structure. The $1h_{11/2}$ isomeric state is faithfully reproduced in these calculations for all isotones being considered: the deviations from the experimental energy values did not exceed 40 keV. The wave functions are dominated by the single-quasiparticle component (its weight is above 80%).

In calculating the isomeric ratios, we assumed that the isomers are populated by radiative transitions from the $J_i^\pi = 7/2^-$ ($E2$ transitions), $9/2^+$ ($E1$ transitions), and $9/2^-$ ($M1$ transitions) levels. The spectrum of activated levels, together with the calculated reduced widths, is presented in Fig. 2 for the ^{139}Ce nucleus. For the other $N = 81$ isotones being considered, the corresponding spectra are very similar. The ground state is predominantly populated by transitions proceeding from $J_i \leq 5/2$ levels.

Since, following beta decay, the nuclear excitation energy does not exceed 3.0 MeV (Table 2), the population of the isomer in this reaction is due exclusively to the $J_i^\pi = 7/2^-$ excited state at an excitation energy of about 1.5 MeV (Fig. 2). Here, the absolute value of the isomeric ratio is determined, to a considerable extent, by the probability of the population of levels in the daughter nucleus formed upon beta decay. These probabilities were computed by using the initial- and final-state wave functions. Since, in the nuclei being considered, beta decay populates predominantly $J_i^\pi \leq 5/2^+$ levels, which then decay into the ground state, the absolute value of the isomeric ratio is quite modest (see Table 2). Small variations in its magnitude in the ^{139}Ce, ^{141}Nd, and ^{143}Sm nuclei are associated with the details of the nuclear-structure calculations.

The number of activation states involved in the population of the isomer in the (γ, n) reaction, where the daughter nucleus formed upon the decay of the giant dipole resonance has an excitation energy of up to about 6 MeV, is much greater (Fig. 2). The mechanism of ground-state and isomer population in this reaction was considered in detail elsewhere [33]. The isomeric ratio is given by

$$\mathrm{IR} = \frac{\sum\limits_{J_i^\pi}(2J_i+1)T_{l_j}(\varepsilon)\sum\limits_{\nu}(C^\nu_{J_i^\pi})\Gamma^\nu_{J_i^\pi\to\mathrm{is}}}{\sum\limits_{J_i^\pi}(2J_i+1)T_{l_j}(\varepsilon)\sum\limits_{\nu}(C^\nu_{J_i^\pi})\Gamma^\nu_{J_i^\pi\to\mathrm{gs}}}, \qquad (8)$$

where T_{l_j} is the transmission coefficient for a neutron of orbital angular momentum l_j; J is the total angular momentum of the nucleus following neutron emission; $C^\nu_{J^\pi}$ are the spectroscopic factors for the states of spin–parity J^π; and $\Gamma_{J^\pi\to\mathrm{is}}$ and $\Gamma_{J^\pi\to\mathrm{gs}}$ are the partial widths of intermediate-energy states with respect to gamma decay into, respectively, the isomeric and the ground state. In the calculations, it was assumed that an emitted neutron of medium energy can carry away angular momenta of 0, 1, 2, and 3 (this determines the set of final-nucleus spins). The isomeric ratios calculated in this way are displayed in Table 2. The agreement with experimental data is seen to be good. A drop in the isomeric ratio when we go over to ^{143}Sm and ^{141}Nd is explained by the fact that, because of a higher neutron binding energy in the initial nucleus in heavier isotones, a smaller number of $7/2^-$, $9/2^+$, and $9/2^-$ activation levels are populated in the final nucleus.

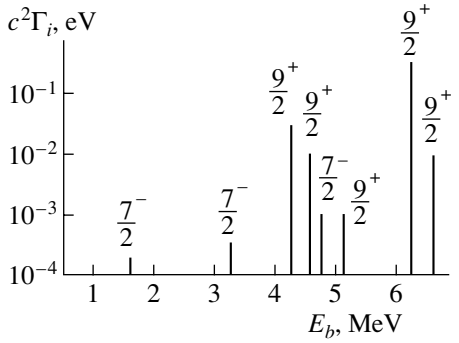

Fig. 2. Calculated reduced widths of ^{139}Ce nuclear levels from which radiative transitions lead to the isomeric state.

The above calculations were performed under the assumption that the direct decay of intermediate-energy states into the ground and the isomeric state dominates over cascade transitions. This assumption is justified at modest excitation energies of the nucleus, in which case the density of excited levels is low and the phase space for possible cascades is severely constrained. That the calculated isomeric ratios are in good agreement with experimental data obtained in the (γ, n) reactions proves the applicability of this assumption up to excitation energies of about 6 MeV. However, the population of isomers in the $N = 81$ isotones in the (n, γ) reactions cannot be explained without taking into account cascade transitions. In these reactions, the spin of the daughter nucleus formed upon thermal-neutron capture is 1/2, and isomer generation requires an angular-momentum transfer of 5—that is, a cascade of not less than three to four gamma transitions. This is the reason why, in particular, the isomeric ratios obtained in the (n, γ) reactions for the set of nuclei under investigation are much less than in the (γ, n) reactions, where the averaged angular momentum of states populated in dipole-resonance decay is 3/2 and where the $7/2^-$, $9/2^+$, and $9/2^-$ levels can be populated upon neutron emission as well.

If one aims at considering cascade transitions within a microscopic approach, the requirements for

the accuracy in describing the details of the structure of excited states at intermediate excitation energies are much more stringent than those for direct transitions to the ground and to the isomeric state. In this case, the description of excited states up to the neutron-separation energy in terms of the wave function (7) is by far insufficient—it must additionally include at least *quasiparticle plus two phonons* and *quasiparticle plus three phonons* terms, and the calculations must be performed without a radical truncation of the basis. Fulfillment of these requirements leads to a configuration space where a diagonalization of the model Hamiltonian presents, at the moment, serious technical difficulties. For the sake of comparison, the isomeric ratios computed for the (n, γ) reactions within the statistical approach at the above values of the parameters a and σ are therefore quoted in Table 2. The calculated isomeric ratio for the ^{135}Xe nucleus below the experimental value admits a natural explanation, because the neutron binding energy is lower in this nucleus. As can be seen from the calculations based on the quasiparticle–phonon model, a smaller number of activation states is therefore involved in the population of the isomeric state.

ACKNOWLEDGMENTS

This work was supported by the Russian Foundation for Basic Research (project no. 00-02-16674) and by the Bulgarian Foundation for Scientific Research (contract no. F801).

REFERENCES

1. H. Bethe, Phys. Rev. **50**, 332 (1936).
2. A. V. Ignatyuk, *Statistical Properties of Excited Nuclei* (Énergoizdat, Moscow, 1983).
3. Yu. V. Sokolov, *Level Density in Atomic Nuclei* (Énergoatomizdat, Moscow, 1990).
4. R. Vandenbosch and J. R. Huizenga, Phys. Rev. **120**, 1305 (1960).
5. L. Ya. Arifov, B. S. Mazitov, and V. G. Ulanov, Yad. Fiz. **34**, 1028 (1981) [Sov. J. Nucl. Phys. **34**, 572 (1981)].
6. Yu. P. Gangrskiĭ, A. P. Tonchev, and N. P. Balabanov, Fiz. Élem. Chastits At. Yadra **27**, 1043 (1996) [Phys. Part. Nucl. **27**, 428 (1996)].
7. A. G. Belov, Yu. P. Gangrsky, A. P. Tonchev, and P. Zuzaan, Hyperfine Interact. **107**, 167 (1997).
8. V. G. Soloviev, *Theory of the Nucleus: Nuclear Models* (Énergoizdat, Moscow, 1981).
9. V. G. Soloviev, *Theory of Atomic Nuclei* (Inst. of Physics Publ., Bristol,1992).
10. A. I. Vdovin and V. G. Soloviev, Fiz. Élem. Chastits At. Yadra **14**, 237 (1983) [Sov. J. Part. Nucl. **14**, 99 (1983)].
11. V. V. Voronov and V. G. Soloviev, Fiz. Élem. Chastits At. Yadra **14**, 1380 (1983) [Sov. J. Part. Nucl. **14**, 583 (1983)].
12. A. I. Vdovin, V. V. Voronov, V. G. Soloviev, and Ch. Stoyanov, Fiz. Élem. Chastits At. Yadra **16**, 245 (1985) [Sov. J. Part. Nucl. **16**, 105 (1985)].
13. V. Yu. Ponomarev, A. P. Dubensky, V. P. Dubensky, and E. A. Boykova, J. Phys. G **16**, 1727 (1990).
14. P. von Neumann-Cosel, V. Yu. Ponomarev, A. Richter, and C. Spieler, Z. Phys. A **350**, 303 (1995).
15. V. M. Mazur, V. A. Zheltonozhskiĭ, and Z. M. Bigan, Yad. Fiz. **58**, 970 (1995) [Phys. At. Nucl. **58**, 898 (1995)].
16. A. G. Belov, Yu. P. Gangrskiĭ, A. P. Tonchev, and N. P. Balabanov, Yad. Fiz. **59**, 585 (1996) [Phys. At. Nucl. **59**, 553 (1996)].
17. S. F. Mughabghab, M. Divadeeman, and W. E. Hobden, *Neutron Cross Sections* (Academic, New York, 1981).
18. E. Broune and R. B. Firestone, *Table of Radioactive Isotopes,* Ed. by V. S. Shirley (Wiley, New York, 1986).
19. P. Raghavan, At. Data Nucl. Data Tables **42**, 189 (1989).
20. S. P. Kapitsa and V. N. Melekhin, *Microtron* (Nauka, Moscow, 1969).
21. A. G. Belov, in *Proceedings of the Workshop on Use of Microtrons in Nuclear Physics, Plovdiv, 1992* (OIYaI, Dubna, 1993), D15-93-80, p. 12.
22. Ph. G. Kondev, A. P. Tonchev, Kh. G. Khristov, and V. E. Zhuchko, Nucl. Instrum. Methods Phys. Res. B **71**, 126 (1992).
23. V. I. Zlokasov, Comput. Phys. Commun. **28**, 27 (1982).
24. S. S. Dietrich and B. L. Berman, At. Data Nucl. Data Tables **38**, 199 (1988).
25. A. M. Goryachev and G. N. Zalesnyĭ, Izv. Akad. Nauk SSSR, Ser. Fiz. **54**, 2240 (1990).
26. G. Kennedy, S. C. Gujrathi, and P. F. Hinrichsen, Can. J. Phys. **52**, 847 (1974).
27. M. Herman, A. Marcinkowski, and K. Stankievicz, Comput. Phys. Commun. **33**, 373 (1984).
28. V. A. Bondarenko, I. L. Kuvaga, P. T. Prokofjev, *et al.,* Nucl. Phys. A **582**, 1 (1995).
29. S. Gales, Ch. Stoyanov, and A. I. Vdovin, Phys. Rep. **166**, 125 (1988).
30. V. A. Chepurnov, Yad. Fiz. **6**, 955 (1966) [Sov. J. Nucl. Phys. **6**, 696 (1967)].
31. K. Takeuchi and P. A. Moldauer, Phys. Lett. B **28B**, 384 (1969).
32. S. Raman, W. C. Nestor, S. Kahane, and K. M. Bhatt, At. Data Nucl. Data Tables **42**, 1 (1989).
33. N. Tsoneva, Ch. Stoyanov, Yu. P. Gangrsky, *et al.,* Phys. Rev. C **61**, 044303 (2000).

Translated by A. Isaakyan

Physics of Atomic Nuclei, Vol. 64, No. 11, 2001, pp. 1909–1916. Translated from Yadernaya Fizika, Vol. 64, No. 11, 2001, pp. 1995–2002.

NUCLEI
Theory

Correlation Features of the Reaction ^{9}Be$(d, p\gamma)^{10}$Be at E_d = 15.3 MeV and Structure of the ^{10}Be Nucleus

N. S. Zelenskaya, A. V. Ignatenko, V. M. Lebedev, N. V. Orlova, and A. V. Spassky

Institute of Nuclear Physics, Moscow State University, Vorob'evy gory, Moscow, 119899 Russia

Received July 3, 2000; in final form, October 17, 2000

Abstract—Double-differential cross sections for the reaction ^{9}Be$(d, p\gamma)^{10}$Be at $E_d = 15.3$ MeV are measured for proton emission into the forward hemisphere. All even spin-tensor components of the density matrix for the 2^+ 3.37-MeV state of the residual nucleus are reconstructed in a model-independent way. The angular distributions of the populations of the magnetic substates and of the tensors of the angular-momentum orientation for the state in question are also obtained. The experimental results are compared with the results of the calculations performed by the coupled-channel method under the assumption of the neutron-stripping mechanism. The calculated correlation features are found to be highly sensitive to the wave functions for the participant nuclei, especially the ^{10}Be nucleus. The importance of taking into account multistep processes in the reaction being considered is demonstrated. © *2001 MAIK "Nauka/Interperiodica".*

1. INTRODUCTION

In [1, 2], the even spin-tensor components $A_{k\kappa}(\theta_p)$ of the density matrix for the 2^+ 3.37-MeV state of the ^{10}Be nucleus produced in the reaction ^{9}Be$(d, p\gamma)^{10}$Be at $E_d = 12.5$ MeV were for the first time found in a model-independent way. It was shown there that, while the number of the components $A_{k\kappa}(\theta_p)$ for the usually assumed mechanism of neutron stripping to the $1p$ state in this reaction is expected to be equal to four ($k \leq 2$, $\kappa \leq k$), experimental data show clear evidence for nonzero values of the $k = 4$ components. The inclusion of the contribution from the f configuration in the wave function for the residual nucleus did not result in satisfactory agreement with experimental data. In order to improve the description of data from [1], the multistep neutron-transfer mechanism associated with the collective excitation of ^{9}Be and ^{10}Be nuclei [3] was taken into account in [2]. Although the selection rules for the stripping mechanism at the orbital-angular-momentum transfer of $l = 1$ allow two values of the total-angular-momentum transfer, $j = 1/2$ and $3/2$, the $j = 1/2$ component was disregarded in [2]. This means that the $(1p)^4_{3/2}(1p)^2_{1/2}$ cluster configuration, which corresponds to the bineutron component in the wave function for the ^{10}Be nucleus, was predominantly considered in the 2^+ state of this nucleus. These assumptions made it possible to improve considerably agreement between the calculated values of $A_{k\kappa}(\theta_p)$ and experimental data. However, the conclusions drawn in [2] could not be considered to be unambiguous because of the small number of relevant experimental points. On the other hand, the observed manifestation of the bineutron component and the evaluation of its effect on the correlation features of the ^{10}Be(2^+) nucleus require more detailed experimental and theoretical investigations. For this purpose, the correlation features of the reaction in question are studied here experimentally at the higher energy of $E_d = 15.3$ MeV, because the manifestations of the cluster structure of nuclei become more spectacular with increasing energy. With the aim of revealing more clearly the bineutron component in the ^{10}Be nucleus, we also analyze the effect of various components of the wave functions for the ^{9}Be and ^{10}Be nuclei on the correlation features of the reaction.

2. EXPERIMENTAL PROCEDURE

The experiment was performed with deuterons accelerated to 15.3 MeV by the 120-cm cyclotron installed at the Institute of Nuclear Physics (Moscow State University). The variation of the projectile energy and a subsequent formation of the beam spot at the target were implemented with the aid of moderating aluminum foils and short-focus magnetic quadrupole lenses (see [14] and references therein). The energy spread of the beam was 160 and 350 keV at $E_d = 15.3$ and 12 MeV, respectively.

The detection of the reaction products and their energy and time analysis were performed by using

a measurement–computational complex with a distributed architecture including a few levels of information processing [5].

In order to measure double-differential cross sections, we detected charged reaction products using four semiconductor silicon detectors of thickness about 1000 μm and angular resolution $\pm 2.5°$. The detectors were placed within the scattering chamber on a special table that could be inclined with respect to the horizontal plane within an angle of $\pi/2$. We measured the angular and energy dependence of the differential cross section by the same detector with an angular resolution of $\pm 1°$. The detector was placed on a horizontal table outside the scattering chamber.

The photons emitted in the reaction being studied were detected by four scintillation detectors containing NaI(Tl) crystals and having an angular resolution of $\pm 12°$. The photon detectors were placed outside the scattering chamber on a horizontal rotating platform with an angular step of 32.5°. Photon–proton coincidences were analyzed in the photon-energy range 2–3.5 MeV, which covers a significant part of the spectrum corresponding to a transition of the excited state of the residual nucleus ^{10}Be(2^+; 3.37 MeV) to the ground state.

The target was made from self-sustaining ^{9}Be plates of thickness 1 to 5 mg/cm^2. The absolute value of the reaction cross section was measured to a precision of about 10%.

The model-independent method that we use here to reconstruct the spin-tensor components $A_{k\kappa}(\theta_p)$ of the density matrix on the basis of the experimental double-differential cross sections $W(\theta_\gamma, \varphi_\gamma; \theta_p)$ for the reaction is described in detail elsewhere [6]. It consists in solving, by the method of least squares, an overdetermined set of linear equations for nine spin-tensor components $A_{k\kappa}(\theta_p)$ of the density matrix that are defined by the relation

$$d^2\sigma/d\Omega_p d\Omega_\gamma \equiv W(\theta_\gamma, \varphi_\gamma; \theta_p)$$
$$= \frac{1}{4\pi}\sum_{k,\kappa} A_{k\kappa}(\theta_p)\bar{P}_k^\kappa(\cos\theta_\gamma)\sqrt{\frac{2}{2k+1}}\cos\kappa\varphi_\gamma,$$

where the angles θ_p, θ_γ, and φ_γ specify the directions of proton and photon emission in the system of spherical coordinates with the z axis and the xz plane coinciding with deuteron-beam direction and the reaction plane, respectively, and where $\bar{P}_k^\kappa$ are associated Legendre polynomials. The normalization is chosen in such a way that $A_{00}(\theta_p) \equiv d\sigma/d\Omega(\theta_p)$. The values of k are determined by the relations $\mathbf{k} = \mathbf{J}_f + \mathbf{J}_f$ and $\mathbf{k} = \mathbf{L} + \mathbf{L}$ (J_f is the spin of the excited state, and L is the multipolarity of the γ transition), and κ can be any integer in the interval from $-k$ to k.

The double-differential cross sections measured in three planes with respect to the reaction plane make it possible to reconstruct all nine even spin-tensor components $A_{k\kappa}(\theta_p)$ for the 2^+ 3.37-MeV state of the ^{10}Be nucleus and to obtain the angular dependences of the population of the magnetic substates, $P_{\pm M}(\theta_p)$, and the components of the orientation tensor of the angular momentum, $t_{k\kappa}(\theta_p)$, for this level of ^{10}Be [6]. In reconstructing $A_{k\kappa}(\theta_p)$, we took into account the finite dimensions of the scintillation detectors [6]. The reliability of the $A_{k\kappa}(\theta_p)$ values reconstructed on the basis of the experimental double-differential cross sections can be estimated by a high confidence level that was not poorer than 0.1 in the majority of cases.

3. EXPERIMENTAL RESULTS

We measured the angular dependences of the differential cross section for the reaction ^{9}Be$(d,p)^{10}$Be leading to the production of a residual nucleus in the ground state or the first excited (2_1^+) state in the interval of θ_p from 20° to 160° (in the laboratory frame). The results are displayed in Fig. 1*a*. It is clear from the figure that the shape of the dependences is typical of direct processes.

The energy dependences of the differential cross section for the reaction were measured for the proton-emission angles of 50° and 90° in the deuteron-energy interval between 12 and 15.3 MeV (see Fig. 1*b*).

The excitation functions corresponding to the transition to the 2_1^+ state are rather smooth, which is typical of direct processes. Small deviations from monotonicity are present only in the energy dependence of the cross section for the transition to the ground state at $\theta_p = 50°$.

The double-differential cross sections for the reaction ^{9}Be$(d,p\gamma)^{10}$Be were measured for 12 values of the proton emission angle in the interval from 20° to 90° (in the laboratory frame); five to nine values of the polar angle θ_γ; and three azimuthal-angle values of $\varphi_\gamma = 180°$, 225°, and 270°. Figures 2 and 3 display the angular dependences of the reconstructed components $A_{k\kappa}(\theta_p)$ for $k = 2$ and 4. These dependences have a rather complex oscillating shape. The absolute values of the components $A_{2\kappa}(\theta_p)$ at small proton-emission angles exceed 0.5, while the amplitude of oscillations of $A_{4\kappa}(\theta_p)$ does not exceed 0.2 over the entire angular region. By using the reconstructed values of $A_{k\kappa}(\theta_p)$, we determined the population of the magnetic substates of the 2_1^+ state of the residual nucleus. The angular dependences are shown in Fig. 4. Figure 5 displays the angular dependences of

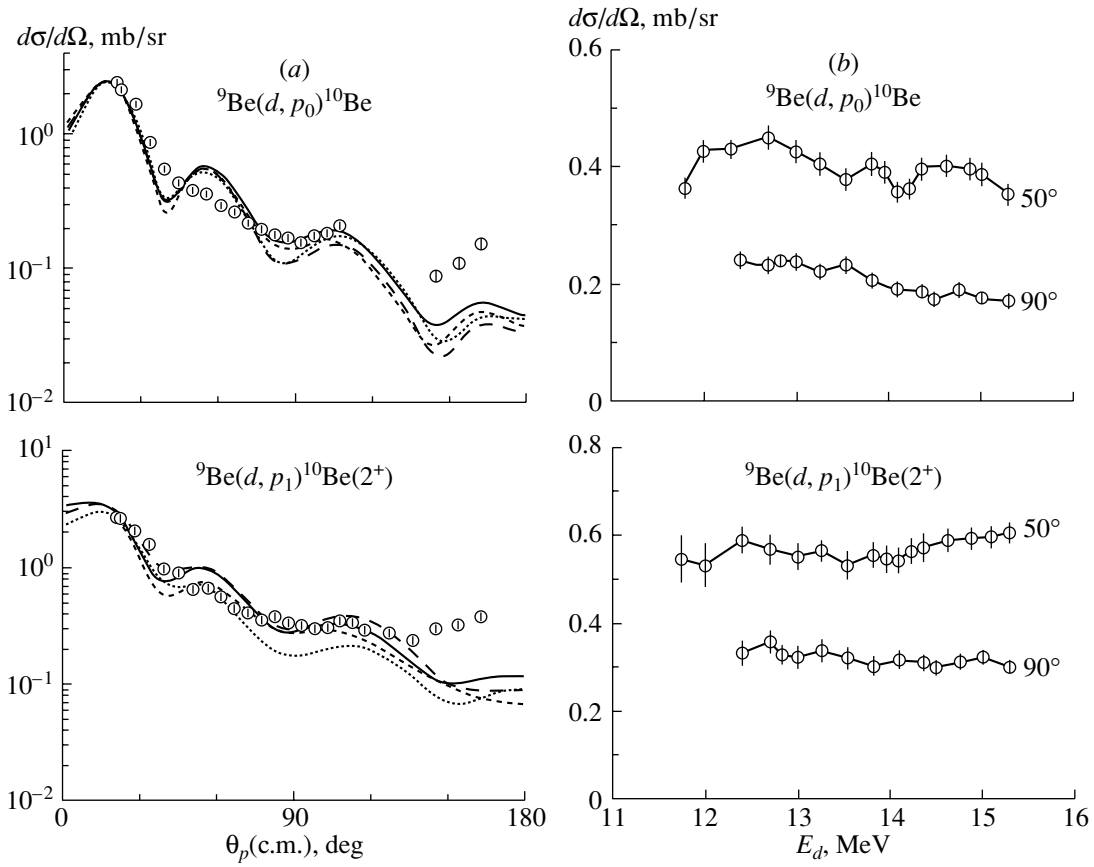

Fig. 1. (*a*) Angular dependences of the differential cross section for the reaction ^{9}Be$(d,p)^{10}$Be occurring at $E_d = 15.3$ MeV and leading to the production of the residual nucleus in the ground (0^+) or the 2_1^+ excited state (proton groups p_0 or p_1, respectively). Here and in the following figures, open circles represent experimental values with statistical errors. Curves show the results of the calculation based on the coupled-channel Born approximation for various values of the deformation parameter β_2 for the ^{9}Be and ^{10}Be nuclei: $+0.5, +0.5$ (solid curve); $-0.5, +0.5$ (short dashes); $+0.5, -0.5$ (long dashes); and $-0.5, -0.5$ (dotted curve). (*b*) Differential cross section for the reaction at two values of the angle θ_p (in the laboratory frame) as a function of energy. The curves represent eyeball fits to the experimental points.

some components of the dimensionless tensor of the angular-momentum orientation for this state [these results were also obtained from the reconstructed values of $A_{k\kappa}(\theta_p)$].

4. CALCULATIONS WITHIN COUPLED-CHANNEL BORN APPROXIMATION AND DISCUSSION OF THE RESULTS

Our present calculations were based largely on the assumption of the cluster-stripping mechanism and were performed by using the CHUCK code [3], which takes into account channel coupling in the initial and in the final state (coupled-channel Born approximation further abbreviated as CCBA) and some auxiliary codes for calculating correlation features.

The optical potentials used were chosen in the Woods–Saxon form, whose parameters are quoted in the table. We did not seek optimum values of these parameters; instead, we employed those from [7]. For the bound-state potentials, we took the usual values of $r_V = 1.25$ fm and $a_V = 0.65$ fm and the Thomas spin–orbit parameter of $\lambda = 25$. We determined the depth of the real part of the potential through the standard procedure of fitting the calculated value of the binding energy of the transferred particle and the nuclear core to a known value. We varied the deformation parameter β_2 in the interval from 0 to ± 1 both in the input and in the output reaction channels. Other details of the calculation are described in [2]. Only the most typical curves are presented in Figs. 1–5 in order to avoid encumbering graphical illustrations.

Our analysis of the calculated and experimental data revealed the following special features of the structure of the nuclei involved (these results proved to be close to those obtained in [2]):

(i) Comparing the theoretical and the experimental correlation features, we were able to determine quite

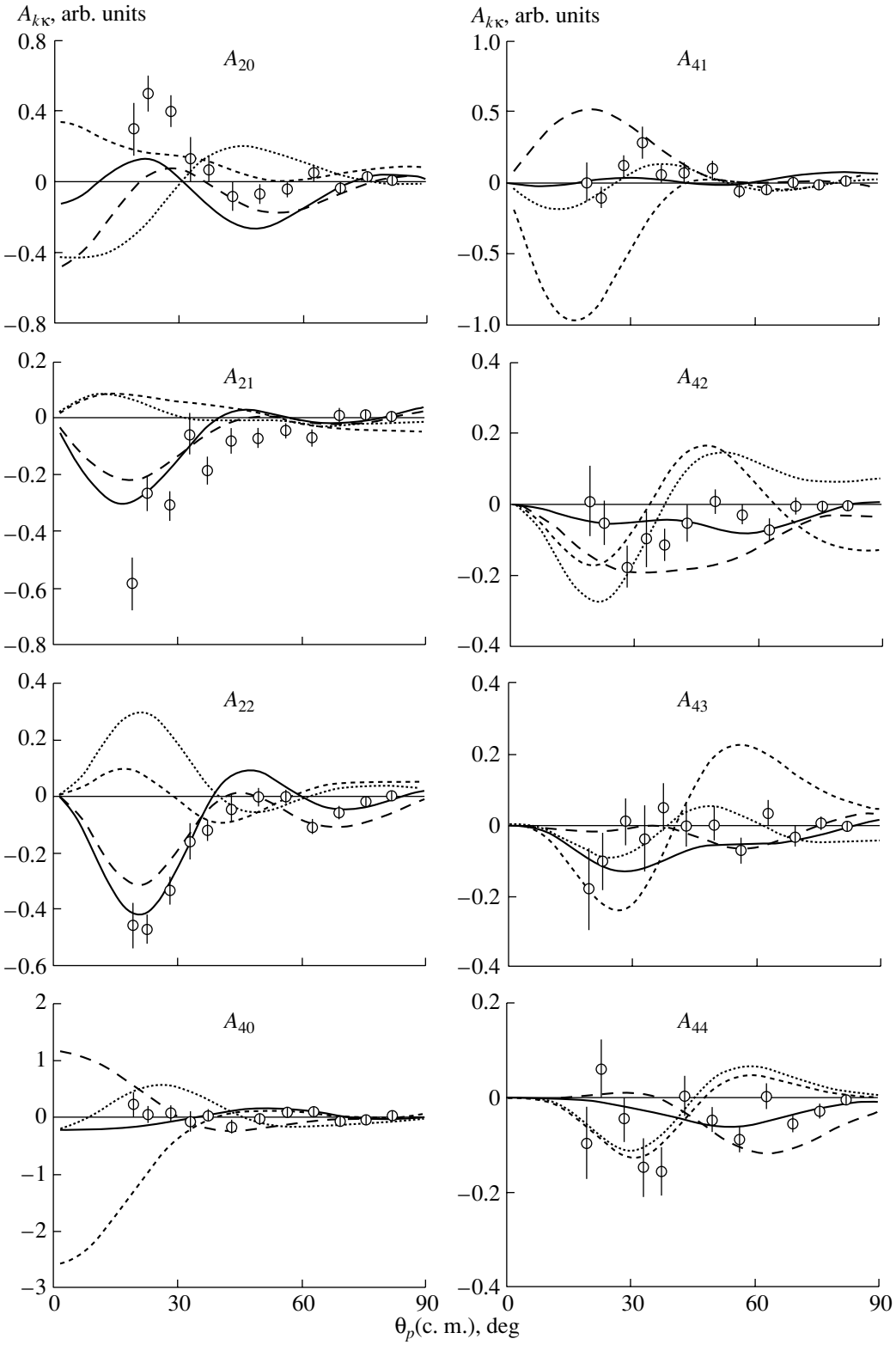

Fig. 2. Angular dependences of the spin-tensor components $A_{k\kappa}$ of the density matrix for the 2^+ 3.37-MeV state of the ^{10}Be nucleus produced in the reaction $^9\mathrm{Be}(d, p\gamma)^{10}\mathrm{Be}$ at $E_d = 15.3$ MeV. The units of measurements along the ordinate are chosen in such a way that $A_{00} \equiv d\sigma/d\Omega$ has dimensions of mb/sr. The notation for the curves is identical to that in Fig. 1*a*.

reliably the magnitude and the sign of the quadrupole deformation of the Be nuclei. In our calculations, we used the deformation parameter β_2, which relates, within the rotational model, the ground to the lowest

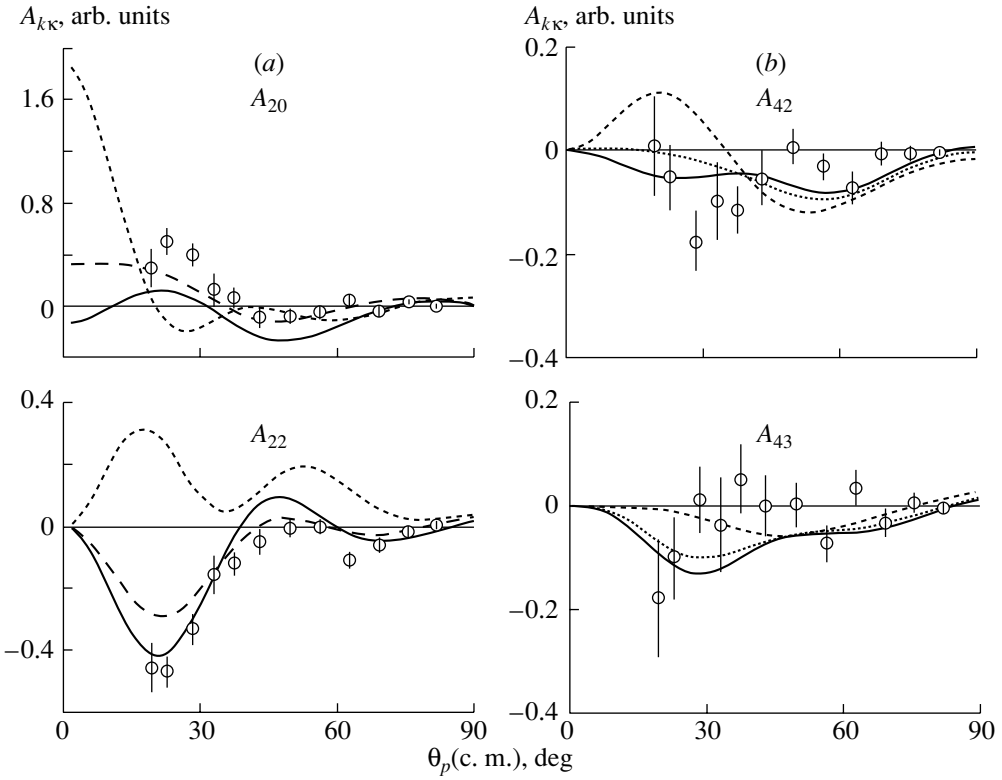

Fig. 3. As in Fig. 2 for a few components $A_{k\kappa}$. The curves in Fig. 3*a* represent the results of the CCBA calculations for various values of the contribution of the $j = 1/2$ spin channel: (solid curve) 0%, (short dashes) 100%, and (long dashes) without the $f = [42]^{31}D_1, ^{31}D_2$ components of the ^{10}Be wave function. The curves in Fig. 3*b* correspond to various calculated contributions of the orbital-angular-momentum transfer of $l = 3$: (solid curve) 20%, (dotted curve) 10%, and (dashed curve) 0%.

excited state [$3/2^-$(g.s.) and $5/2^-$, respectively] of the ^{9}Be nucleus and the 0^+(g.s.) to the 2^+ state of the ^{10}Be nucleus. For both Be nuclei, we chose the eventual value of $\beta_2 = 0.5$. This parameter determines, to a great extent, the amplitude of oscillations for the majority of the components $A_{k\kappa}(\theta_p)$. The above value seems optimal according to the analysis of the entire set of $A_{k\kappa}(\theta_p)$ with $k \neq 0$ and populations $P_{\pm M}(\theta_p)$. The dependence of the results of calculations on the absolute value of β_2 in the output channel proved to be weaker than on that in the input channel. Therefore, the value of $\beta_2(^{10}\text{Be}) = 0.5$ is more ambiguous. Variation in these parameters changes insignificantly the theoretical differential cross section $A_{00} \equiv d\sigma/d\Omega(\theta_p)$ for angles $\theta_p < 40^\circ$ both in shape and in magnitude.

The calculations with zero values of the deformation parameters in both channels on the basis of the OLYMP-3 code [8] (there, the remaining parameters have values close to those used in CCBA) yield populations $P_{\pm M}(\theta_p)$ that are only slightly dependent on the angle, in a glaring contradiction with the experimental results (see Fig. 4).

The calculations revealed that the majority of the angular dependences $A_{k\kappa}(\theta_p)$ are better described with positive values of both β_2 (see Fig. 2). By way of example, we indicate that, at $\beta_2 = -0.5$ in the input channel [$\beta_2(^{10}\text{Be}) = 0.5$], the calculation leads to $A_{21}(\theta_p)$, $A_{22}(\theta_p)$, $A_{40}(\theta_p)$, and $A_{41}(\theta_p)$ that are in antiphase with their experimental counterparts.

The form of the calculated angular distributions of the differential cross section for the reaction ^{9}Be$(d, p_1)^{10}$Be(2^+) undergoes no qualitative changes upon reversal of the signs of β_2, at least at small angles (see Fig. 1*a*). For the transition to the ground state of the final nucleus, the shape and the magnitude of the cross section $d\sigma/d\Omega(\theta_p)$ at the first two maxima are rather stable.

(ii) The theoretical analysis of the quantities $A_{k\kappa}(\theta_p)$ makes it possible to obtain data on the bineutron cluster structure of the ^{10}Be(2^+) nucleus. As was mentioned in the Introduction, the selection rules for the mechanism of neutron stripping to the $1p$ shell allow the orbital-angular-momentum transfer of $l = 1$ and the total-angular-momentum transfers of $j = 1/2$ and $3/2$ in the $3/2^- \to 2^+$ (3.37 MeV)

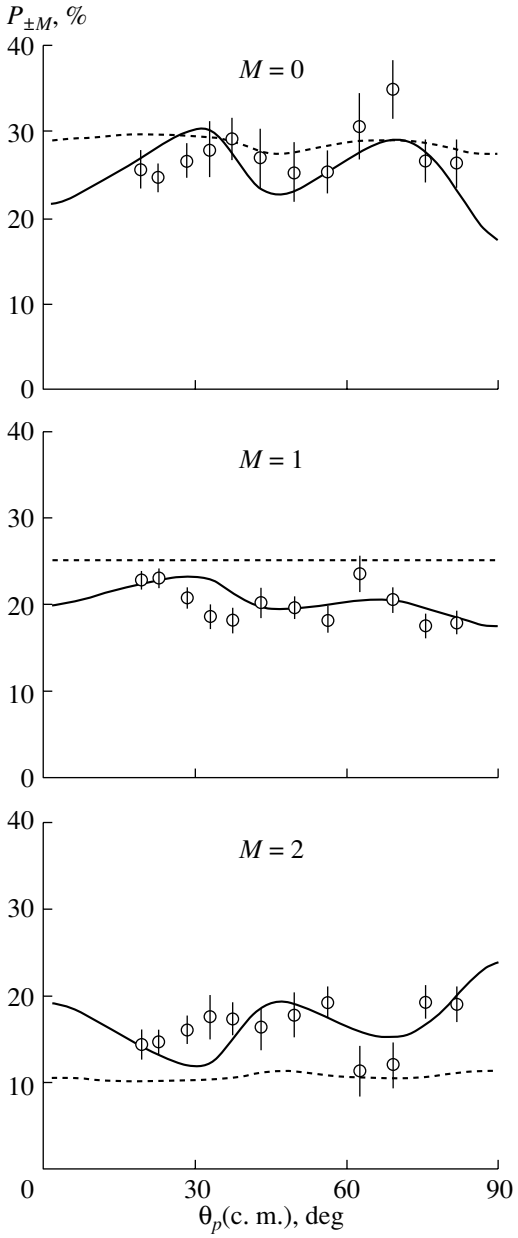

Fig. 4. Angular dependences of the populations of the magnetic substates of the 2_1^+ ^{10}Be state produced in the reaction ^{9}Be$(d, p\gamma)^{10}$Be. The curves represent the results of the calculations performed (solid curve) with and (dashed curve) without allowance for the deformation of ^{9}Be and ^{10}Be nuclei.

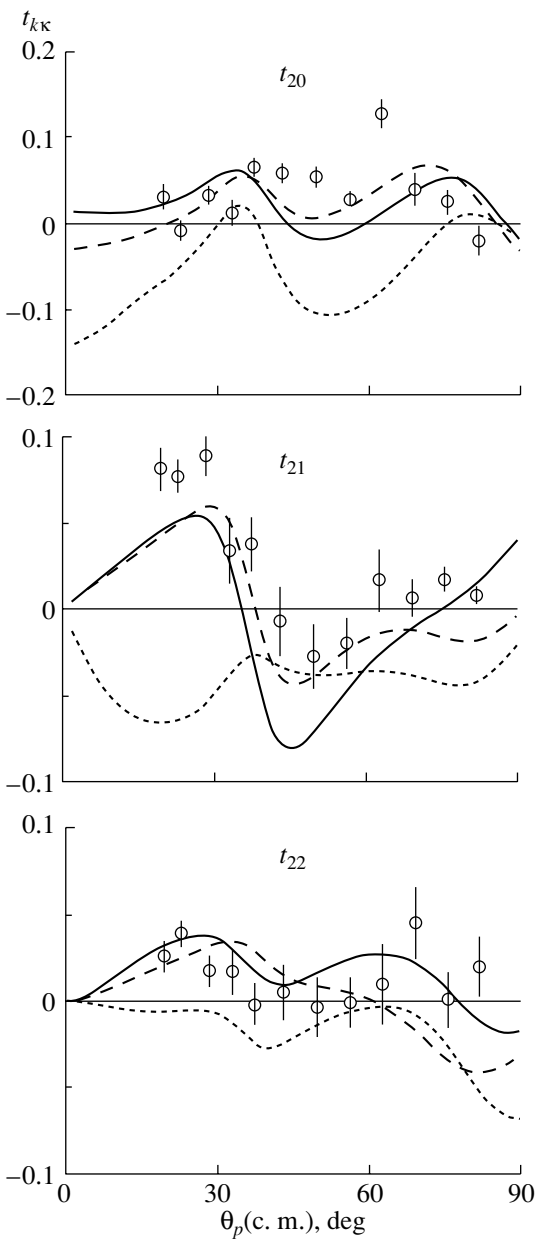

Fig. 5. Angular dependences of some components $t_{k\kappa}$ of the dimensionless tensor of angular-momentum orientation in the 2_1^+ state of the ^{10}Be nucleus. The notation for the curves is identical to that in Fig. 3*a*.

transition. The calculated spectroscopic factor S for $j = 1/2$ is approximately one-half as great as that for $j = 3/2$. The angular dependences of the differential cross section are virtually independent of the values of j that are taken into account in the calculation. Nevertheless, the admixture of $j = 1/2$ abruptly changes the shape of the components $A_{20}(\theta_p)$, $A_{22}(\theta_p)$, and $t_{21}(\theta_p)$ (see Fig. 3*a* and Fig. 5) at small angles in such a way that they appear to be in antiphase with their experimental counterparts. All these components are directly related to the tensor polarization of the nucleus—that is, to its cluster structure.

Let us consider the problem in more detail. It is well known that the nuclei belonging to the middle of the $1p$ shell have a complex structure. This is suggested not only by a significant deformation of these nuclei (in particular, of the beryllium nuclei),

Parameters of the optical potentials

Channel	V, MeV	r_V, fm	a_V, fm	W, MeV	r_W, fm	a_W, fm	V_{so}, MeV	r_{so}, fm	a_{so}, fm	r_C, fm
^{9}Be + d	73.0	1.04	0.87	24.0	2.05	0.41				1.3
^{10}Be + p	55.66	1.17	0.75	11.2*	1.32	0.65	6.2	1.01	0.75	1.25

*The surface potential was taken in the form of the derivative of the Woods–Saxon expression.

but also by the fact that, in the calculations of the wave functions for the $A = 10$ nuclei on the basis of the intermediate-coupling shell model, the quantum numbers of the model are insufficient for unambiguously classifying basis configurations (there are two physically different $f = [42]^{31}D$ configurations [9]). The analysis of the beryllium wave functions within the jj-coupling model shows that the ground state of the ^{9}Be nucleus contains approximately equal fractions of the $(1p)^4_{3/2}(1p)_{1/2}$ and the $(1p)^3_{3/2}(1p)^2_{1/2}$ configuration. The 2^+ state of the ^{10}Be nucleus features predominantly two configurations [9], $(1p)^6_{3/2}$ and $(1p)^4_{3/2}(1p)^2_{1/2}$. It is clear that only the transfer of a $j = 3/2$ nucleon can result in such a rearrangement of the nuclei involved. Most likely, it is for this reason that the total-angular-momentum value of $j = 2$ must be rejected in order to achieve agreement between the results of the calculations and experimental data.

A more profound analysis of the problem reveals that the weight of the $(1p)^6_{3/2}$ configuration in the wave function for the 2^+_1 state of the ^{10}Be nucleus is overestimated, because this symmetric configuration cannot lead to such a significant deformation of the nucleus. At the same time, it can be shown that this overestimation is due to a significant contribution of the $f = [42]^{31}D_1$, $^{31}D_2$ components in the shell-model wave function for this nucleus. According to the calculations, these are the components that strongly affect the amplitude of the $3/2^- \to 2^+(j = 1/2)$ transition. If the weights of these components are set to zero, the spectroscopic factor for the transition being considered decreases by a factor of about 180, while the spectroscopic factor for the $j = 3/2$ transition decreases only by a factor of 2. The angular dependences $A_{k\kappa}(\theta_p)$ calculated without the $f = [42]^{31}D$ components are, as might have been expected, close to those for which the $j = 1/2$ transition is disregarded (see Figs. 3*a* and 5). In other words, the correlation features of the ^{10}Be nucleus—in particular, its tensor polarization—directly indicate that the wave function for the nucleus is dominated by the $(1p)^4_{3/2}(1p)^2_{1/2}$ bineutron cluster configuration. It is also worth noting that this change in the ^{10}Be wave function increases the amplitude of the $5/2^-(2.43$ MeV, ^{9}Be$) \to 2^+(j = 1/2)$ transition by a factor of about 4, but, in this case, the calculations confirm the weak effect of the amplitudes of this transition on the shape of the angular dependences $A_{k\kappa}(\theta_p)$.

Changing the weights of various components of the wave function for the ^{9}Be nucleus did not result in any significant reduction of the relative value of the $j = 1/2$ amplitude in the transition $3/2^- \to 2^+$.

(iii) From our calculations, it follows that, by taking into account the possible admixture of $l = 3$ in the transitions to the 2^+ 3.37-MeV state of the ^{10}Be nucleus within the approach used, we can significantly improve the description of some $k = 4$ components $A_{k\kappa}(\theta_p)$. The estimated weight of the f configuration in different studies varied from 6 to 10% [1, 10]. In order to evaluate the contribution of $l = 3$ (with respect to S for $l = 1$), we used the values 0, 10, and 20% (see Fig. 3*b*). Comparing the experimental and the calculated values of $A_{k\kappa}(\theta_p)$, we arrive at the conclusion that the optimal agreement is attained for a contribution of $l = 3$ not less than 10%.

Thus, allowance for the deformation of the ^{9,10}Be nuclei and an adequate choice of their wave functions (the inclusion of the contribution of $l = 3$ and the disregard of the contribution of $j = 1/2$) result in satisfactory agreement for the entire set of the calculated and experimental components $A_{k\kappa}(\theta_p)$, the populations $P_{\pm M}(\theta_p)$, and the components $t_{k\kappa}(\theta_p)$ of the tensor of the angular-momentum orientation.

5. CONCLUSION

Our calculations for the neutron-stripping mechanism of the reaction ^{9}Be$(d, p\gamma)^{10}$Be by the coupled-channel method have revealed that correlation features are a good tool for studying the details of the reaction mechanism and the structure of the participant nuclei. A comparison of the experimental values of $A_{k\kappa}(\theta_p)$ and other related features with the results of these calculations have made it possible to choose the majority of the model parameters (the magnitude and the sign of β_2, transition amplitudes, etc.). At the same time, the angular distributions of the differential

cross section have shown a relatively weak sensitivity to variations in these parameters.

It also follows from the above analysis that the probability of the multistep mechanism in this reaction is high. The multistep mechanism is associated with the preexcitation of the target nucleus at a sufficiently strong $3/2^- \leftrightarrow 5/2^-$ coupling corresponding to $\beta_2 \sim 0.5$.

Finally, direct evidence for the existence of the bineutron cluster configuration in the ^{10}Be wave function is the most important result obtained from the analysis of the tensor polarization. It should be emphasized that our results furnish an independent corroboration of the inability of the shell model to describe the $A = 10$ nuclei.

The conclusions drawn for the reaction being considered seem to remain valid in the rather wide region of deuteron energies E_d, because they proved to be rather similar to those obtained in [2] at $E_d = 12.5$ MeV.

ACKNOWLEDGMENTS

The work was supported by the Scientific Program "Basic Research at Higher Institutions in Natural and Human Sciences: Universities of Russia" (grant no. 990604) and by the Russian Foundation for Basic Research (project no. 01-02-16196).

REFERENCES

1. O. I. Vasil'eva *et al.*, Yad. Fiz. **45**, 312 (1987) [Sov. J. Nucl. Phys. **45**, 195 (1987)].
2. V. M. Lebedev *et al.*, Yad. Fiz. **61**, 1604 (1998) [Phys. At. Nucl. **61**, 1493 (1998)].
3. P. D. Kunz and J. Cejpek, *The Niels Bohr Institute, Computer Program Library, Computer Code CHUCK,* modified by R.N. Boyd, H. Clement, and E. Sugarbarker for the calculation of angular correlations (1977).
4. L. Z. Ismail *et al.*, Prikl. Yad. Spektrosk. **10**, 239 (1981).
5. A. V. Ignatenko *et al.*, in *Proceedings of the 49th Conference on Nuclear Spectroscopy and Nuclear Structure, St. Petersburg, 1999,* p. 156.
6. N. S. Zelenskaya and I. B. Teplov, Fiz. Élem. Chastits At. Yadra **18**, 1283 (1987) [Sov. J. Part. Nucl. **18**, 546 (1987)]; *Features of Excited Nuclear States and Angular Correlations in Nuclear Reactions* (Énergoatomizdat, Moscow, 1995).
7. S. M. Perey and F. G. Perey, At. Data Nucl. Data Tables **17**, 1 (1976).
8. O. Yu. Balashova *et al.*, *Concise Descriptions of Software Support of Institute of Nuclear Physics of Moscow State University* (Mosk. Gos. Univ., Moscow, 1978), p. 97; I. B. Teplov *et al.*, *State Reserves of Algorithms and Programs* (1985), No. 50850000733.
9. A. N. Boyarkina, *Structure of 1p-Shell Nuclei* (Mosk. Gos. Univ., Moscow, 1973).
10. P. D. Kunz, Ann. Phys. (N.Y.) **11**, 275 (1960).

Physics of Atomic Nuclei, Vol. 64, No. 11, 2001, pp. 1917–1930. Translated from Yadernaya Fizika, Vol. 64, No. 11, 2001, pp. 2003–2015.

NUCLEI
Theory

Analysis of Elastic and Inelastic Hadron Scattering on ^{6,7}Li Nuclei within Diffraction Theory

M. A. Zhusupov and E. T. Ibraeva*

Institute for Experimental and Theoretical Physics,
Al-Faraby Kazakh State National University, Tole-bi 96A, Almaty, 480012 Republic of Kazakhstan
Received June 23, 2000; in final form, December 15, 2000

Abstract—Within Glauber–Sitenko multiple-scattering theory, the differential cross sections for elastic and inelastic proton, positive-pion, and positive-kaon scattering on ^{6,7}Li nuclei are calculated at incident-hadron energies ranging between 0.143 and 1.0 GeV. The ^{6}Li and ^{7}Li wave functions are taken in, respectively, the $\alpha 2N$ and the αt cluster model. The resulting cross sections are investigated as functions of the scattered-particle energy, parameters of the model wave functions, and various scattering multiplicities. It is concluded that a partial filling of the diffraction minimum in the cross section is due to the D-wave contribution to the wave function for the ^{6}Li target nucleus. © *2001 MAIK "Nauka/Interperiodica".*

1. INTRODUCTION

Investigation of elastic and inelastic hadron–nucleus scattering at energies of a few hundred MeV is an important source of information both about the structure of nuclei and about interaction mechanisms. A comparison of processes where different particles—protons, charged pions, and positive kaons—are scattered on the same target nuclei is of particular interest since different particle species interact differently with intranuclear nucleons. For example, positive kaons are weakly absorbed and have a large range in a nuclear medium (5–7 fm), whence it follows that they can be used as a probe for studying the structure of nuclei [1, 2]. At the same time, the interaction of charged pions is of a manifest peripheral character since they can hardly penetrate into the interior of nuclei because of strong absorption [3]. The main objective of the present study is to find out how the aforementioned features may reveal themselves in characteristics of elastic and inelastic hadron scattering on ^{6}Li and ^{7}Li nuclei.

Experimental data on proton scattering by ^{6}Li nuclei were obtained in Uppsala (Sweden) at $E_p = 0.185$ GeV [4] and in Saclay (France) at 0.6 and 1.04 GeV [5]. At the cyclotron laboratory of the Indiana University (IUCF), polarized-proton beams of energy 0.2 GeV were used to study scattering on ^{6}Li [6] and ^{7}Li [7] nuclei. Charged-pion scattering was investigated at the meson factory in the Los Alamos National Laboratory (LAMPF) at an energy of 0.143 GeV for ^{7}Li targets [8] and in the energy range between 0.1 and 0.26 GeV for ^{6}Li targets [9] and at the Paul Scherrer Institute (PSI, Switzerland), where systematic data on differential cross sections were obtained at 0.1, 0.18, and 0.24 GeV for ^{6}Li [10] and at 0.164 GeV for ^{7}Li [11]. Later, the production of targets having a vector polarization made it possible to measure, for $\pi^{\pm}$ ^{6,7}Li interactions, not only the differential cross sections but also polarization properties (iT_{11})—specifically, these results were obtained at energies between 0.1 and 0.219 GeV for ^{6}Li [12] and at 0.134, 0.164, and 0.194 GeV for ^{7}Li [13]. The latest experimental data on positive-kaon scattering by ^{6}Li nuclei come from experiments at the Brookhaven National Laboratory (BNL AGS) [1] for energies of $E_{K^+} = 0.375$ GeV.

All measured features were computed on the basis of dispersion methods [14], the coupled-channel method [12, 13, 15], the optical model [distorted-wave impulse approximation (DWIA)] [2, 4–9, 16–18], and Glauber–Sitenko diffraction-scattering theory [19–27]; for the scattering of protons on ^{12}C and ^{16}O [24, 25], charged pions on ^{12}C [26], and positive kaons on a deuteron [27], a comparison of the last two approaches revealed that the distinctions between the results that they yield for these cases is small—in the differential cross sections, they are manifested only in the region of the diffraction minimum and at large scattering angles. In our calculations, we rely on diffraction theory, where, given the wave functions for the target nucleus and elementary hadron–nucleon amplitudes, one can calculate the scattering-matrix elements that are related to observables (differential cross sections and polarization features) by simple

*e-mail: ibraeva@physics.kz

Table 1. Compilation of the parameters of the proton–nucleon amplitudes

E_p, GeV		σ_{pN}, fm^2	ε_{pN}	β_{pN}, fm^2	References
0.2	pp	2.36	1.15	0.65	[26]
	pn	4.20	0.71	0.68	
0.6	pp	3.96	0.24	0.11	[34]
	pn	3.66	−0.295	0.175	
0.8	pp	4.73	−0.06	0.38	[35]
	pn	3.79	0.2	0.4	
1.0	pp	4.75	−0.1	0.23	[20]
	pn	4.00	−0.4	0.16	

Table 2. Compilation of the parameters of the π^+N amplitudes according to data from [26]

E_π, GeV	$\sigma_{\pi N}$, fm^2	$\varepsilon_{\pi N}$	$\beta_{\pi N}$, fm^2
0.15	10.93	0.522	1.25
0.18	12.76	0.114	0.994
0.23	9.24	−0.43	0.55

Table 3. Compilation of the parameters of the K^+N amplitudes according to data from [23]

E_K, GeV		σ_{KN}, fm^2	ε_{KN}	β_{KN}, fm^2
0.201	K^+p	1.29	−2.190	0.0134
	K^+n	1.31	−0.667	0.0013
0.23	K^+p	1.30	−1.964	0.0197
	K^+n	1.41	−0.575	0.0012
0.375	K^+p	1.32	−1.467	0.0114
	K^+n	1.67	−0.373	0.0015
0.468	K^+p	1.32	−1.258	0.0095
	K^+n	1.71	−0.305	0.0013
0.534	K^+p	1.39	−0.9074	0.0065
	K^+n	1.75	−0.105	0.0011

equations. Listed immediately below are advantages of this theory:

(i) The Glauber multiple-scattering operator Ω is constructed in such a way that it enables one to consider the scattering process microscopically—that is, to trace individual collisions of incident particles with the nucleons (or clusters) of the target nucleus and to take into account all scattering and rescattering multiplicities.

(ii) The parameters of the elementary amplitudes [see Eq. (1) below] have a simple physical meaning (σ is the total cross section, ε is the ratio of the real part of the amplitude to its imaginary part, and β is the slope of the amplitude cone) and admit a convenient comparison with observables: the filling of the minimum in the differential cross sections and the cross-section value at the first maximum are generally associated with the parameter ε and the parameter σ, respectively.

(iii) Diffraction theory, together with the wave function within the dynamical multicluster model, involves no free parameters (in contrast to the optical model) and can be used to describe the scattering of intermediate- and high-energy hadrons.

For a target, we chose ^{6,7}Li nuclei, considering that these are strongly clustered nuclei (the binding energies are equal to 1.47 and 2.47 MeV in the αd and the αt channel, respectively). For these nuclei, there are adequate three- and two-particle wave functions that were calculated for realistic interaction potentials [28–30] and which faithfully reproduce static features, the probabilities of the electromagnetic transitions, and elastic and inelastic Coulomb form factors over a wide range of momentum transfers.

In the present study, we develop a spectroscopic approach [31] (description of a vast body of experimental data within a unified theory featuring realistic wave functions for target nuclei) by extending previous inquiries into reactions induced by protons [32] and charged pions [33] to the case of K^+-meson scattering.

We have calculated the differential cross sections for elastic and inelastic scattering and shown that they are correctly reproduced within diffraction theory. The investigation of these observables versus the model wave functions for the target nucleus, the admixture of small components in these wave functions, and the contribution of various scattering multiplicities to the multiple-scattering operator at various scattered-particle energies makes it possible to draw conclusions both on the structure of the nuclei involved and on special features of interactions of different particle species.

2. ELEMENTARY HADRON–NUCLEON INTERACTIONS

An elementary amplitude that describes phenomenologically the interaction of the scattered particle with intranuclear nucleons is one of the input parameters of diffraction theory. Usually, it is parametrized in the form

$$f_\nu(q) = \frac{k\sigma_\nu}{4\pi}(i+\varepsilon_\nu)\exp\left(-\beta_\nu q^2/2\right), \qquad (1)$$

where k is the incident-hadron momentum; the remaining parameters were discussed in the Introduction, while their values for the various incident-particle species are quoted in Tables 1–3.

From a comparison of the values presented in Tables 1-3 for the parameters of the elementary amplitudes, we can see the following. The total cross sections for the scattering of protons and positive pions are much larger than those for the scattering of positive kaons. According to the optical theorem, $\sigma_{\rm tot}$ is related to the elastic-scattering amplitude at zero angle as

$$\sigma_{\rm tot} = \frac{4\pi}{k}{\rm Im}M_{ii}(0); \qquad (2)$$

that is, the imaginary part of the amplitude (it is dominant in scattering) depends on the total cross section $\sigma_{\rm tot}$, which is much smaller for K^+N scattering than for pN and π^+N scattering. The quantity β is also one to two orders of magnitude less for K^+N scattering than for pN and π^+N scattering, whence we conclude that the S-wave contribution [23] to scattering is dominant; at the same time, the absolute value of ε (ratio of the real part of the amplitude to its imaginary part) is significantly larger (it is even larger than unity), which suggests that positive kaons are absorbed only slightly, so that the interaction proceeds primarily through the elastic channel.

We now compare the elementary interactions of protons, charged pions, and charged kaons with nucleons at the quark level. Most clearly, these interactions can be represented in terms of the diagrams in Fig. 1. The analogous diagrams for $\pi^\pm N$ and $K^\pm N$ are displayed in [16].

At intermediate energies ($p \sim 0.8$ GeV/c, which corresponds to $E_p = 0.295$ GeV), the pN interaction has a nonresonance character (diagrams in Figs. 1a, 1b), but its amplitude is quite large (~35 mb/sr) and involves sizable spin-dependent terms.

Since antiquarks ($\bar d$ in π^+ and $\bar u$ in π^-) enter into the composition of the charged pions, their interaction with nucleons is sufficiently strong and has a pronounced resonance character (diagrams in Figs. 1c–1f). This is the most spectacular in π^+p interaction, where the Δ_{33} resonance occurs at energies above 0.1 GeV. This resonance is rather broad, its magnitude at the maximum (at $E_\pi = 0.169$ GeV) being about 200 mb/sr. In the π^+N system, there are no open channels below the positive-pion-production threshold other than the charge-exchange channel. The ratio of the total cross sections is $\sigma(\pi^+p)/\sigma(\pi^-p) = 3/1$.

The kaon–nucleon interaction differs drastically from the interactions described above because of the presence of a strange quark, which generates nonzero strangeness ($S \neq 0$). Since the strangeness is $S = 1$ for positive kaons and $S = -1$ for negative kaons, the K^+N and the K^-N interaction differ strongly (diagrams in Figs. 1g–1j). Because of $u\bar u$ annihilation, the K^-N interaction generates narrow resonance states (Λ, Σ) and features open channels below the K^-N threshold. This interaction is strong, its amplitude being 42 mb/sr at $p = 0.8$ GeV/c, which corresponds to $E_{K^-} = 0.446$ GeV. On the contrary, the five-quark structure in the K^+N system does not form resonances [the hypothetical Z^* resonance ($duu\bar su$) has not yet been observed]; predominantly, the interaction proceeds through the elastic channel; it is much weaker than that in the K^-N system, its amplitude being 13 mb/sr. That the K^+N interaction is the weakest of all strong interactions is also suggested by a large mean range of the positive kaon in nuclei.

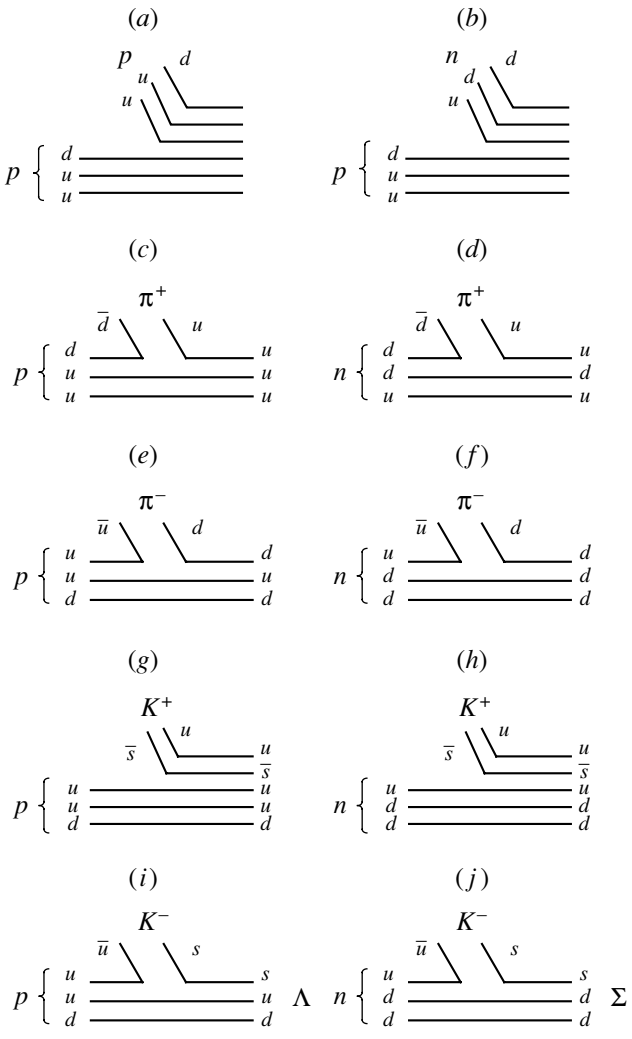

Fig. 1. Quark diagrams for elementary xN interactions ($x \equiv p, \pi^\pm, K^\pm$).

3. ^{6}Li AND ^{7}Li WAVE FUNCTIONS IN CLUSTER MODELS

Presently, ^{6}Li wave functions within three-particle models have been obtained by a few groups of authors [36–38]. Among the first systematic calculations of the wave functions in the αnp model, we would like to mention those that were performed by Kukulin's group from Moscow State University [28] and which yielded accurate results for static features and observables of quasielastic reactions involving electrons [28], protons [21, 32], and charged pions [10, 15, 22, 33]. The most comprehensive description of all properties of ^{6}Li–^{6}He nuclei within the dynamical multicluster model involving a Pauli projection and a full antisymmetrization was presented by Eramzhyan *et al.* [39], who considered, among other things, the neutron halo in ^{6}He, electromagnetic form factors, and the observables of the photodisintegration process ^{6}Li$(\gamma, \pi^+)^6$He and of elastic charged-pion scattering at 0.134 GeV. Previously, it was shown in [40] and [41] that the αnp model makes it possible to reproduce faithfully the observables of two-particle photodisintegration through the ^{3}He*t* and the αd cluster channel, respectively. The model also describes well the experimental spectra and the momentum distributions of protons for transitions to the ground state and excited states of the ^{5}He nucleus [42].

The wave functions that we use were calculated in [28] on the basis of two models. In model 1, the relevant interactions were simulated by the Sack–Biedenharn–Breit (SBB) potential for the αN interaction and the Reid soft-core (RSC) potential for the NN interaction in the ground state and by the SBB potential for the αN interaction and a square-well potential for the NN interaction in the 3^+ excited state. In model 2, the αN and the NN interaction were taken, for either state, in a form leading to an even–odd splitting of the phase shifts and in the form of the RSC potential, respectively. In all models, eigenfunctions are sought in the form of an expansion in multidimensional Gaussian functions. This makes it possible to calculate all matrix elements analytically and to determine wave functions in a large basis involving a great number of the small components. The configuration of a wave function is specified by the set of quantum numbers λ, l, L, and S, where l is the orbital angular momentum of the relative motion of the α particle and the center of mass of two nucleons; λ is the orbital angular momentum of the relative motion of two nucleons; and L and S are, respectively, the total orbital momentum and the total spin of the nucleus being considered.

For the ground-state wave function, we take into account two configurations: $\lambda = l = L = 0,\ S = 1$ (S wave) and $\lambda = 2,\ l = 0,\ L = 2,\ S = 1$ (D wave). The S wave is dominant (its weight is greater than 90%), while the D wave contributes 3% to 7% in the calculations with the various interaction potentials. It is, however, interesting to clarify the dependence of the cross section on the D-wave contribution and to perform a comparison with the results presented in [2, 18], where the contribution of the quadrupole correction to the cross section is estimated within the DWIA. The total weight of the remaining components does not exceed a few percent—for example, the weight of the $\lambda = 0,\ l = 2,\ L = 2,\ S = 1$ configuration in model 2 is 0.0008. Thus, the wave function of the ^{6}Li ground state can be represented as

$$\Psi_i = \sum_{\lambda l} \Psi_L^{(\lambda l)} = \Psi_S^{(00)} + \Psi_D^{(20)}, \tag{3}$$

where

$$\Psi_S^{(00)} = \frac{1}{4\pi} \sum_{i,j} C_{ij}^{(00)} \exp\left(-\alpha_i r^2 - \beta_j R_{\alpha d}^2\right) \times \Phi_\alpha\left(\mathbf{r}_{\mu=1-4}\right) \chi_{1M}, \tag{4}$$

$$\Psi_D^{(20)} = \sum_{M_L M_S} \langle 2M_L 1M_S \mid 1M_J\rangle \times Y_{2M_L}\left(\hat{\mathbf{r}}\right) Y_{00}\left(\hat{\mathbf{R}}_{\alpha d}\right) \Phi_\alpha\left(\mathbf{r}_{\mu=1-4}\right) \chi_{1M_S} \times r^2 \sum_{i'j'} C_{i'j'}^{(20)} \exp\left(-\alpha_{i'} r^2 - \beta_{j'} R_{\alpha d}^2\right) \tag{5}$$

with

$$\Phi_\alpha\left(\mathbf{r}_\mu\right) = \frac{1}{2\sqrt{2}} \left(\frac{t}{\pi}\right)^{9/4} \times \exp\left(-\frac{t}{2} \sum_{\mu=1}^{4} \left(\mathbf{r}_\mu - \mathbf{R}_\alpha\right)^2\right). \tag{6}$$

Here, $t = 0.5828$ fm^{-2} [43]; χ_{1M} is the two-nucleon spin function; $\mathbf{r}_\mu$, $\mathbf{R}_\alpha$, and $\mathbf{R}_d$ are the radius vectors of, respectively, the nucleons forming the alpha particle, the center of mass of the alpha particle, and the center of mass of the deuteron; $\mathbf{R}_{\alpha d} = \mathbf{R}_\alpha - \mathbf{R}_d$ and $\mathbf{r} = \mathbf{r}_5 - \mathbf{r}_6$ are the radius vectors of, respectively, the relative motion of the alpha particle and the deuteron and the relative motion of the nucleons forming the deuteron. The expressions for the expansion coefficients C_{ij}, α_i, and β_j are quoted in [28].

For the $J^\pi = 3^+$ excited state of the ^{6}Li nucleus, we take into account the $\lambda = 0,\ l = 2,\ L = 2$ (D_1 component) and the $\lambda = 2, l = 0, L = 2$ (D_λ component) configuration, their weights being, respectively, 73 to 74% and 22 to 25%. The wave function then has the form

$$\Psi_f = \sum_{\lambda l} \Phi_{M_J}^{(\lambda l)} = \Phi_{M_J}^{(02)} + \Phi_{M_J}^{(20)}, \tag{7}$$

where

$$\Phi^{(02)}_{M_J} = \sum_{M_L M_S} \langle 2M_L 1M_S \,|3M_J\rangle \qquad (8)$$
$$\times Y_{2M_L}(\hat{\mathbf{r}})\, Y_{00}\left(\hat{\mathbf{R}}_{\alpha d}\right) \Phi_\alpha\left(\mathbf{r}_{\mu=1,4}\right) \chi_{1M_S}$$
$$\times R^2_{\alpha d} \sum_{pq} C^{(02)}_{pq} \exp\left(-\alpha_p r^2 - \beta_q R^2_{\alpha d}\right),$$

$$\Phi^{(20)}_{M_J} = \sum_{M_L, M_S} \langle 2M_L 1M_S \,|\, 3M_J\rangle \qquad (9)$$
$$\times Y_{00}\left(\hat{\mathbf{R}}_{\alpha d}\right) Y_{2M_L}(\hat{\mathbf{r}})\, \Phi_\alpha\left(\mathbf{r}_{\mu=1,4}\right) \chi_{1M_S}$$
$$\times r^2 \sum_{p'q'} C^{(20)}_{p'q'} \exp\left(-\alpha_{p'} r^2 - \beta_{q'} R^2_{\alpha d}\right).$$

A large quadrupole moment ($Q \sim 40$ mb) and strong αt clustering in the ground state are features peculiar to the ^{7}Li nucleus. Among the first ^{7}Li wave functions in the αt cluster model that are known to the present authors, there are those computed in [29] on the basis of the Woods–Saxon potential with the parameters proposed in [44]. Not only do these wave functions faithfully reproduce static features and electromagnetic form factors at low momentum transfers, but it also appears that their application to describing the differential cross sections for the two-particle photodisintegration ^{7}Li(γ, t)α, including so subtle a feature of the process as asymmetry in the distribution of tritons for the case of polarized photons [40], is highly successful. The analogous wave functions for the Buck potential were computed in [30]. In either case, use was made of deep attractive αt potentials involving states forbidden by the Pauli exclusion principle [44]. We have performed our calculations with two cluster wave functions for ^{7}Li using the parameter values borrowed from [29] and [30] for models 1 and 2, respectively.

In the ground and in the first excited state, the ^{7}Li nucleus has the quantum numbers $J^\pi, T = 3/2^-$, $1/2$; $L = 1$ and J^π, $T = 1/2^-$, $1/2$; $L = 1$, respectively. The wave function for the ^{7}Li nucleus in the αt model can be represented in the form

$$\Psi_{i,f} = \sum_{M_L M_S} \langle LM_L SM_S \,|JM_J\rangle \qquad (10)$$
$$\times \Phi_\alpha\left(\mathbf{r}_{\mu=1,4}\right) \Phi_t\left(\mathbf{r}_l\right) \Phi_{\alpha t}\left(\mathbf{R}\right) \chi_{\frac{1}{2}M_S},$$

where $\chi_{\frac{1}{2}M_S}$ is the spin function and $\Phi_\alpha(\mathbf{r}_{\mu=1,4})$, $\Phi_t(\mathbf{r}_l)$, and $\Phi_{\alpha t}(\mathbf{R})$ are the wave functions that describe, respectively, the alpha particle, the triton, and their relative motion and which are taken in the form of expansions in a Gaussian basis. Specifically, we set

$$\Phi_t\left(\mathbf{r}_l\right) = N_t \qquad (11)$$
$$\times \sum_k C_k \exp\left(-\frac{1}{2}\alpha_k \sum_{l=1}^{3} \left(\mathbf{r}_l - \mathbf{R}_t\right)^2\right),$$

$$\Phi_{\alpha t}(\mathbf{R}) = \mathbf{R}^L Y_{LM}(\hat{\mathbf{R}}) N_{\alpha t} \qquad (12)$$
$$\times \sum_i C_i \exp(-\alpha_i R^2),$$

where N_t and $N_{\alpha t}$ are the normalization factors for the corresponding wave functions; C_i, C_k, α_i, and α_k are the expansion coefficients taken from [45] for t and from [29, 30] for αt; $\mathbf{R}_t$ is the center-of-mass triton coordinate; and $\mathbf{R} = \mathbf{R}_\alpha - \mathbf{R}_t$ is the coordinate of the relative motion of the alpha particle and the triton in the ^{7}Li nucleus. The wave function Φ_α is identical to that in (6).

4. FORMALISM OF DIFFRACTION THEORY

In diffraction theory, the matrix element (amplitude) for hadron scattering by a nucleus can be represented in the form [43]

$$M_{if}\left(\mathbf{q}\right) \equiv \langle \Psi_f |\, \Omega \,|\Psi_i\rangle = \frac{ik}{2\pi} \qquad (13)$$
$$\times \int d^2\boldsymbol{\rho} \exp\left(i\mathbf{q}\cdot\boldsymbol{\rho}\right) \langle \Psi_f \,|\Omega\left(\boldsymbol{\rho}_1, \ldots, \boldsymbol{\rho}_7\right) \delta\left(\mathbf{R}_A\right)|\, \Psi_i\rangle.$$

Here, Ψ_f and Ψ_i are, respectively, the initial- and the final-state wave functions for the target nucleus [see Eqs. (3), (7), and (10)], which obviously coincide in the case of elastic scattering; $\mathbf{R}_A = \dfrac{1}{A}\sum_{n=1}^{A} \mathbf{r}_n$ is the coordinate of the center of mass of the nucleus; $\boldsymbol{\rho}_i$ are the two-dimensional intranuclear-nucleon coordinates in the impact-parameter ($\boldsymbol{\rho}$) plane, which is orthogonal to the incident hadron beam; $\mathbf{k}$ and $\mathbf{k}'$ are the momenta of, respectively, the incident and the scattered hadron in the c.m. frame; and $\mathbf{q} = \mathbf{k} - \mathbf{k}'$,

$$q = 2k \sin\frac{\theta}{2}, \quad k = \sqrt{\varepsilon^2 - m^2}, \qquad (14)$$

where θ is the scattering angle ($\hbar = c = 1$), is the 3-momentum transfer in the reaction.

The multiple-scattering operator can be written in the form [32]

$$\Omega = \Omega_\alpha + \Omega_b - \frac{1}{2}\left(\Omega_\alpha \Omega_b + \Omega_b \Omega_\alpha\right), \qquad (15)$$

where b stands for the d cluster in ^{6}Li or the t cluster in ^{7}Li,

$$\Omega_\alpha = 1 - \prod_{\nu=1}^{4} \left(1 - \omega_\nu\left(\boldsymbol{\rho} - \boldsymbol{\rho}_\nu\right)\right) = \sum_{\nu=1}^{4} \omega_\nu \qquad (16)$$
$$- \sum_{\nu<\mu} \omega_\nu \omega_\mu + \sum_{\nu<\mu<\eta} \omega_\nu \omega_\mu \omega_\eta - \omega_1 \omega_2 \omega_3 \omega_4,$$

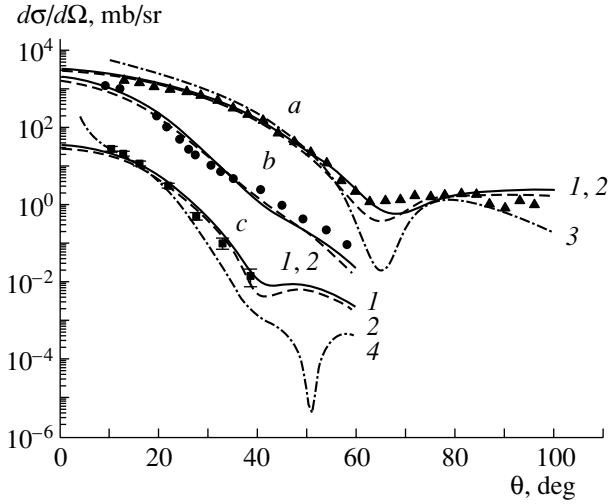

Fig. 2. Differential cross sections for the elastic scattering of (*a*) 0.18-GeV positive pions, (*b*) 0.2-GeV protons, and (*c*) 0.375-GeV positive kaons on ^{6}Li nuclei for various model wave functions: (*1*, solid curve) results of the calculations with the ^{6}Li wave function in model 1, (*2*, dashed curve) results of the calculations with the ^{6}Li wave function in model 2, (curves *3*) results of the DWIA calculations from [15], and (*4*) results of the DWIA calculations from [2]. The points represent the experimental data for (▲) positive pions from [10], (●) protons from [6], and (■) positive kaons from [2]. In order to avoid the overlap of the results, the experimental and the calculated data in Figs. 2*a* and 2*b* are multiplied by a factor of 10.

$$\Omega_b = 1 - \prod_{\nu=5}^{A} \left(1 - \omega_\nu \left(\boldsymbol{\rho} - \boldsymbol{\rho}_\nu\right)\right) \tag{17}$$
$$= 1 - \left[1 - \sum_{\nu=5}^{A} \omega_\nu + \sum_{\nu<\mu} \omega_\nu \omega_\mu - \ldots\right].$$

Here, ω_ν is the profile function, which is expressed in terms of the xN-scattering amplitude ($x \equiv p$, π^+, K^+) as

$$\omega_\nu \left(\boldsymbol{\rho} - \boldsymbol{\rho}_\nu\right) = \frac{1}{2\pi i k} \tag{18}$$
$$\times \int d^2\mathbf{q} \exp\left(-i\mathbf{q} \cdot \left(\boldsymbol{\rho} - \boldsymbol{\rho}_\nu\right)\right) f_\nu \left(\mathbf{q}\right).$$

We choose the xN-scattering amplitude in the form (1). By substituting formula (1) into the profile function (18) and by performing relevant integration, we obtain

$$\omega_\nu \left(\boldsymbol{\rho} - \boldsymbol{\rho}_\nu\right) = \sum_{\varphi,\psi=1}^{2} C_{\varphi\psi} \exp\left[-\left(\boldsymbol{\rho} - \boldsymbol{\rho}_\nu\right)^2 \eta_{\varphi\psi}\right], \tag{19}$$

where

$$C_{\varphi 1} = \frac{\sigma_\nu}{4\pi\beta_\nu^2}, \quad C_{\varphi 2} = -i\frac{\sigma_\nu \varepsilon_\nu}{4\pi\beta_\nu'^2}, \tag{20}$$
$$\eta_{\varphi 1} = \eta_{\varphi 2} = \frac{1}{2\beta_\nu^2},$$

and the subscript $\varphi = 1, 2$ numbers the particle (n, p) with which the incident hadron collides.

We do not describe the ensuing calculations, since they are similar to those for proton scattering from [32]. We only present the expression for the differential cross sections in terms of the amplitude in (13):

$$\frac{d\sigma}{d\Omega} = \frac{1}{2J+1} \sum_{M_L M_L'} |\langle \Psi_f | \, \Omega \, | \Psi_i \rangle|^2. \tag{21}$$

The final expression for scattering on ^{6}Li is obtained by summing the cross section over the angular-momentum projections. The $M_L = \pm 2$ amplitudes are equal; therefore, they are multiplied by a factor of 2 in the cross section. As to the $M_L = \pm 1$ amplitudes, they are equal to zero. For elastic scattering, the differential cross section has the form

$$\frac{d\sigma}{d\Omega} = \frac{1}{3}\left\{\left|\left\langle \Psi^{(00)}_{S,M_L=2} \, |\Omega| \, \Psi^{(00)}_{S,M_L=2} \right\rangle\right|^2 \right. \tag{22}$$
$$+ \frac{6}{5}\left[\left|\left\langle \Psi^{(20)}_{D,M_L=0} \, |\Omega| \, \Psi^{(00)}_{S,M_L=0} \right\rangle\right|^2 \right.$$
$$\left. + 2\left|\left\langle \Psi^{(20)}_{D,M_L=2} \, |\Omega| \, \Psi^{(00)}_{S,M_L=0} \right\rangle\right|^2\right]$$
$$\left. + \left|\left\langle \Psi^{(20)}_{D,M_L=2} \, |\Omega| \, \Psi^{20}_{D,M_L=2} \right\rangle\right|^2\right\}.$$

For inelastic scattering, we have

$$\frac{d\sigma}{d\Omega} = \frac{7}{15}\left\{\left|\left\langle \Phi^{(02)}_{M_L=0} \, |\Omega| \, \Psi^{(00)}_{S} \right\rangle\right|^2 \right. \tag{23}$$
$$+ 2\left|\left\langle \Phi^{(02)}_{M_L=2} \, |\Omega| \, \Psi^{(00)}_{S} \right\rangle\right|^2$$
$$+ \left|\left\langle \Phi^{(20)}_{M_L=0} \, |\Omega| \, \Psi^{(00)}_{S} \right\rangle\right|^2$$
$$\left. + 2\left|\left\langle \Phi^{(20)}_{M_L=2} \, |\Omega| \, \Psi^{(20)}_{D} \right\rangle\right|^2\right\}.$$

Formulas (22) and (23) clearly demonstrate the contributions to the cross section from the various wave-function components and from various values of the angular-momentum projection M_L. In calculating the differential cross sections, each matrix element was treated individually. In the next section, we discuss their contributions to the total cross section.

5. DISCUSSION OF THE RESULTS

We have calculated the differential cross sections for the elastic and inelastic scattering of protons, positive pions, and positive kaons by ^{6,7}Li nuclei at energies ranging between 0.143 and 1.0 GeV and have compared our results with experimental data from [1, 2, 4–13] and with the results obtained by other authors [2, 15].

Let us begin our discussion by considering Fig. 2, which displays the calculated differential cross sections for elastic hadron scattering on ^{6}Li nuclei. Curves *1* and *2* were computed with the three-body $\alpha 2N$ wave functions for the different αN interaction potentials (see Section 3), so that the D-wave admixture to the main S-wave component takes different values for them: 3% in model 1 and 7% in model 2 [28]. A comparison of curves *1* and *2* in Fig. 2 shows that, in the region of small scattering angles, the cross sections computed with the different wave functions do not differ from each other. Small variations arise only in the region of the diffraction minimum and at large scattering angles. For the case of protons (Fig. 2*b*), the distinctions between the differential cross sections for the different wave functions are minimal in the energy range being considered. This is associated with the absolute value of the 3-momentum transfer **q** in the reaction. If the momentum transfer is low (for protons at $E = 0.2$ GeV, it varies between 0.047 GeV/c at $\theta = 5°$ and 0.538 GeV/c at $\theta = 60°$), the projectile particles penetrate to a lesser extent into the interior of the target nucleus (where fine particle-correlation effects, which, strictly speaking, distinguish one version of model from another, must be more noticeable), so that scattering occurs at the periphery of the nucleus. At higher beam energies ($E = 1.04$ GeV), the curves deviate from each other more strongly (see [32]), since, in case of protons, the momentum transfer varies from 0.112 GeV at $\theta = 5°$ to 0.777 GeV/c at $\theta = 35°$; that is, the projectile particles penetrate into the nucleus more deeply, with the result that the effect of particle correlations on the scattering process becomes more pronounced. However, curve *2*, which corresponds to a larger D-wave admixture, lies higher in all cases.

The results of calculations performed by other authors are also illustrated in Fig. 2 for the sake of comparison: curves *3* and *4* represent the results of the DWIA calculations from [15] and [2], respectively. The experimental data for positive pions (Fig. 2*a*) at small scattering angles and in the region of the diffraction minimum are better described by Glauber–Sitenko theory (curve *2*) than by the DWIA (curve *3*); at large scattering angles ($\theta > 70°$), diffraction theory is inapplicable because of intrinsic limitations and provides poorer results. As to large deviations from the experimental data for curve *3* (in calculating this curve, use was also made of the wave function from [28] within model 1, but the D-wave contribution was ignored), the authors of [15] explain this by the absence of absorption channels from the optical potential and by the disregard of the second-order optical potential.

As was mentioned in the Introduction, positive-kaon scattering on ^{6}Li nuclei was first measured in [1], but transitions to the ground state of ^{6}Li and its first excited state at $E^* = 2.18$ MeV were not separated there. The separation procedure was implemented in [2], where a slight deviation from the original data quoted in [1] was found in the angular region $\theta > 25°$. For this reason, the rescaled experimental data from [2] (for the transition only to the ground state of the ^{6}Li nucleus) are presented in Fig. 2*c*, along with the results of the DWIA calculations performed on their basis (curve *4*). From a comparison of curves *1*, *2*, and *4*, we can see that, at the angles in the range $20° < \theta < 40°$, the scattering of positive kaons is also better described by diffraction theory, although the quadrupole noncentral interaction was taken into account in [2] along with the central interaction; however, the contribution of the quadrupole interaction appeared to be overly small to affect the cross-section value. At large scattering angles, the discrepancy between curves *1* and *4* is especially large (a few orders of magnitude), but we cannot definitively conclude which theory is more appropriate because there are presently no experimental data in this region. The calculation within DWIA for K^+-meson scattering was also performed in [18], where the contribution of the quadrupole scattering appeared to be negligibly small.

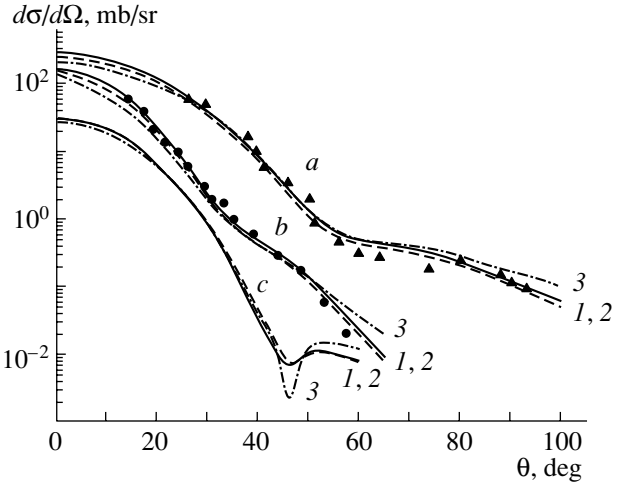

Fig. 3. Differential cross sections for the elastic scattering of (*a*) 0.164-GeV positive pions, (*b*) $E_p = 0.2$-GeV protons, and (*c*) 0.2-GeV positive kaons on ^{7}Li nuclei for various model wave functions: (*1*, solid curve) results of the calculations with the ^{7}Li wave function in model 1, (*2*, dashed curve) results of the calculations with the ^{7}Li wave function in model 2, and (*3*, dash-dotted curve) results of the calculations with the oscillator wave function. Points represent experimental data for (▲) positive pions from [11, 13] and (●) protons from [7].

Let us proceed to consider Fig. 3. Here, we present the differential cross sections calculated for elastic hadron scattering on ^{7}Li nuclei with the αt

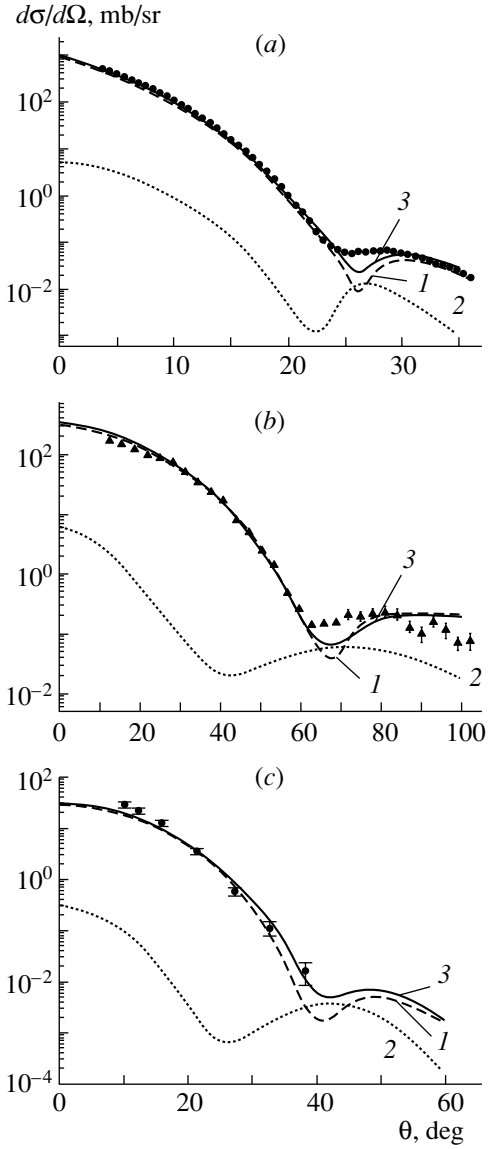

Fig. 4. Structure of the differential cross sections for the elastic scattering of (*a*) 0.6-GeV protons, (*b*) 0.18-GeV positive pions, and (*c*) 0.375-GeV positive kaons on ^{6}Li nuclei: (curve *1*) S-wave contribution, (curve *2*) D-wave contribution, and (curve *3*) their total contribution. The experimental data were borrowed from [5] for protons, [10] for positive pions, and [2] for positive kaons.

cluster wave functions for (curve *1*, model 1) the Woods–Saxon potential and (curve *2*, model 2) the Buck potential and (curve *3*) with the oscillator wave function.

We are now going to indicate features that are common to the wave functions used and features that distinguish them. All of them are single-node ones, and the node occurs at $r = 1.7$ fm in all the cases. The cluster wave functions are similar, but the oscillator wave function differ from them mainly by the behavior at large distances from the center of the nucleus. It decreases extremely fast—in just the same way as all oscillator functions, it has a descending asymptotic behavior, which does not reflect the actual behavior of wave functions—and its value at the first maximum exceeds those of the cluster wave functions by about 40%. As was mentioned in the Introduction, the charged kaon interacts most weakly among all strongly interacting particles; therefore, it can penetrate into the interior of the nucleus more deeply than protons and charged pions of the same fixed energy. Curves *1* and *2* are close in Figs. 3*a*–3*c*, as are the wave functions. This means that the form of the interaction potential used to calculate the wave functions does not strongly affect either static or dynamical observables. We will now find the region where curve *3* shows the greatest distinctions from the first two. In Fig. 3*a* and 3*b*, this is so at small ($\theta < 20^\circ$) and at large ($\theta > 60^\circ$) scattering angles. At small scattering angles, the distinction is due to the fact that the interaction of protons and positive pions with nucleons occurs predominantly at the nuclear periphery, where the cluster wave functions differ strongly from the oscillator wave function (large distances for the wave functions correspond to low momentum transfers—that is, to small scattering angles). At large angles (corresponding to short distances for the wave functions), the distinction arises both from fine effects in the nuclear structure that are disregarded in the oscillator model and from the fact that diffraction theory is applicable only at small scattering angles. The distinction between curves *1* and *2*, on one hand, and curve *3*, on the other hand, is especially pronounced at large scattering angles for positive kaons (Fig. 3*c*); this is because they are scattered in the interior of the nucleus and are therefore more sensitive to the behavior of the wave functions at short distances than in the asymptotic region.

It has already been mentioned in Section 2 that, at zero scattering angle, the amplitude is related to the total cross section [see formula (2)]. The total cross section is considerably larger for π^+N and pN scattering than for K^+N scattering (Tables 1–3); therefore, the experimental data and the calculated curves lie higher for $\pi^{+\,6,7}$Li and $p^{6,7}$Li than for $K^{+\,6,7}$Li.

Let us now consider in more detail the structure of the differential cross sections for elastic-scattering processes on ^{6}Li nuclei that is associated with the S- and the D-wave components. Their partial contributions are shown in Fig. 4 for (*a*) protons, (*b*) positive pions, and (*c*) positive kaons. Curves *1*, *2*, and *3* represent the differential cross sections calculated with allowance for only the S wave [the first term in (22)], only the D wave [the second and the third term in (22)], and their total contribution [all terms in (22)], respectively.

It can clearly be seen that the differential cross section for the partial D wave at $\theta = 0°$ is two orders of magnitude smaller than the differential cross section for the S wave. At $\theta = 0°$, we have $\Omega = 1$ and the overlap integrals of the wave functions for the S wave are two orders of magnitude greater than those for the D wave. However, the minimum in the differential cross section represented by curve *2* is shifted, in relation to curve *1*, toward the region of smaller scattering angles by 10°–30°, while the second maximum in curve *2* coincides with the minimum of curve *1* and partly fills the minimum in curve *3*, which represents the total contribution. In the previous analyses reported in [32] and devoted to proton scattering on ^{6}Li, a similar result was obtained for both wave functions—it was found that the degree of filling of the minimum is in direct proportion to the weight of the D wave in the relevant wave function.

Let us consider the contributions to the cross section from various scattering multiplicities in the operator Ω [see Eqs. (15)–(17)] by using the example of scattering on ^{7}Li nuclei. The results of these calculations are presented in Fig. 5 for the scattering of (*a*) protons, (*b*) positive pions, and (*c*) positive kaons. Curves *1*, *2*, *3*, and *4* in Figs. 5*a* and 5*b* represent, respectively, the results for scattering on the alpha-particle cluster [which are obtained by substituting the first term in (15) into (21)], the results for scattering on the triton cluster [which are obtained by substituting the second term in (15) into (21)], and the results for rescattering on the two clusters [this corresponds to substituting the third and the fourth term in (15) into (21)], and their algebraic sum [formula (21) with the total operator Ω (15)].

The scattering of positive kaons was considered here in the double-scattering approximation, where, in the multiple-scattering operator, one retains only terms associated with single and double collisions:

$$\Omega = 1 - \left[1 - \sum_{\nu=1}^{7} \omega_\nu + \sum_{\nu<\mu} \omega_\nu \omega_\mu\right]. \qquad (24)$$

The validity of this approximation in the case being considered is justified by the fact that, because of the weakness of K^+N interaction, whence it follows that the mean range of positive kaons is large, the multiple-scattering series for K^+A must converge fast, with the result that single scattering will be dominant. Abgrall and Labarsouque [27] calculated directly the contribution of various scattering multiplicities and showed that, in K^{+12}C scattering at a momentum of 715 MeV/c, the sum of single and double collisions correctly describes the differential cross sections in the angular region extending up to 50°. In Fig. 5*c*, curves *1* and *2* correspond, are respectively, to single scattering [substitution of the third term in (24) into the cross section (21)] and to double scattering [substitution of the fourth term in (24) into the cross section (21)], while curve *3* represents their sum. Let us first compare the contributions of different scattering are multiplicities for the various projectile-particle species at similar beam energies. From Figs. 5*a* and 5*b*, it can be seen that, at small an-

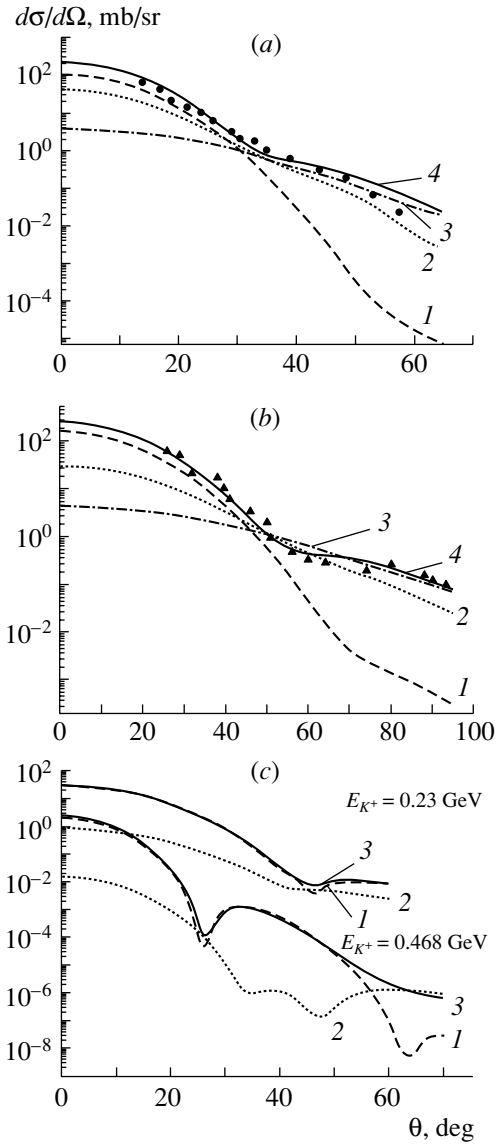

Fig. 5. Contributions of various scattering multiplicities to the differential cross section for the scattering of (*a*) 0.2-GeV protons (the experimental data were borrowed from [7]), (*b*) 0.164-GeV positive pions (the experimental data were borrowed from [11, 13]), and (*c*) positive kaons on ^{7}Li nuclei: curves *1*, *2*, *3*, and *4* in Figs. 5*a* and 5*b* correspond to scattering on the alpha-particle cluster, scattering on the triton cluster, rescattering on the clusters, and the algebraic sum of these contributions, while curves *1*, *2*, and *3* in Fig. 5*c* correspond to single scattering, double scattering, and their sum.

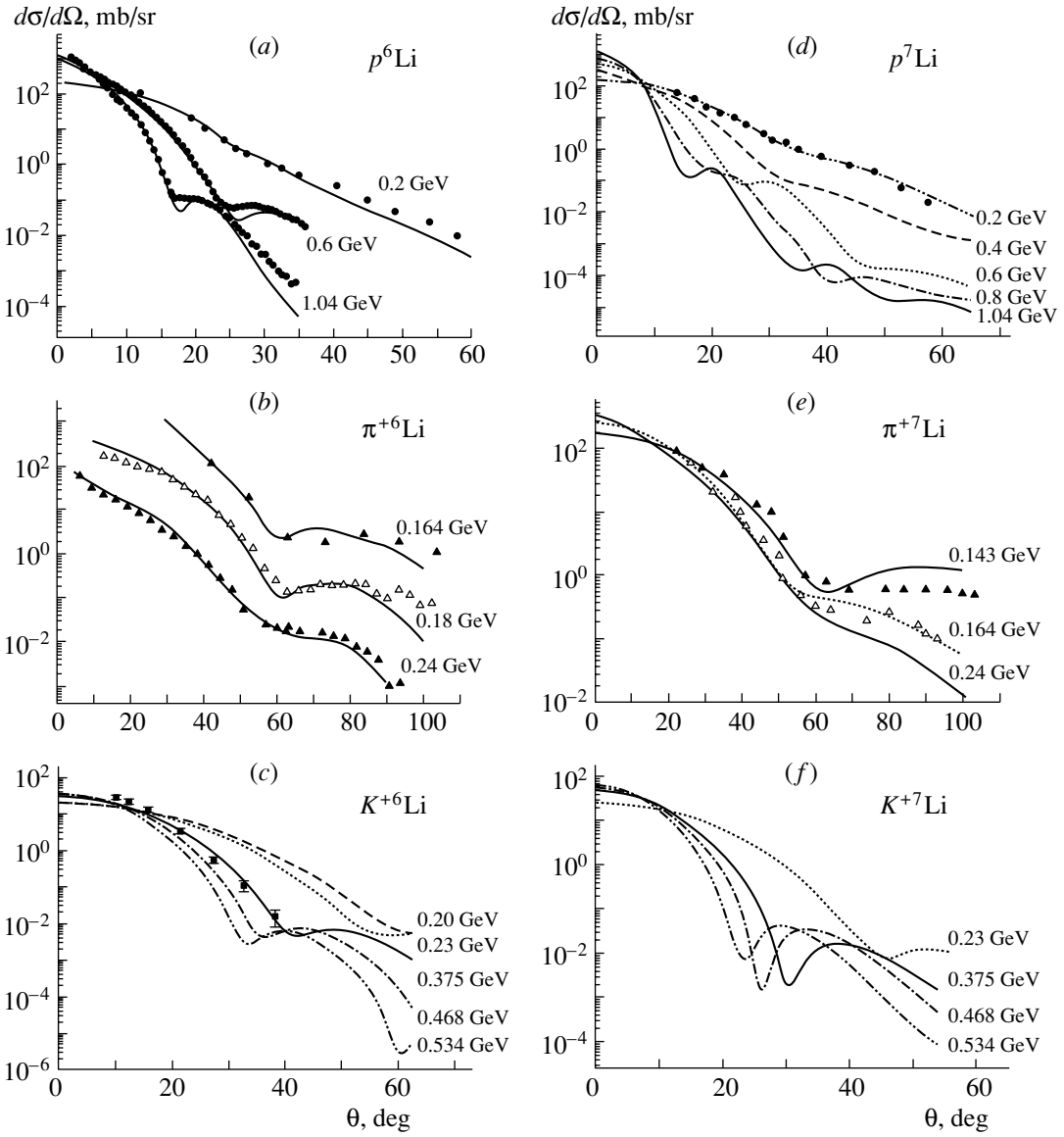

Fig. 6. Differential cross sections calculated for scattering on (*a*–*c*) ^{6}Li and (*d*–*f*) ^{7}Li nuclei at various energies of incident (*a*, *d*) protons, (*b*, *e*) positive pions, and (*c*, *f*) positive kaons. Points represent experimental data (*a*) at 0.2 GeV from [6] and at 0.6 and 1.04 GeV from [5], (*b*) at 0.164 GeV from [12] and at 0.18 and 0.24 GeV from [10], (*c*) from [2], (*d*) from [7], and (*e*) at 0.143 GeV from [8] and at 0.164 GeV from [11, 13].

gles, the main contribution comes from scattering on the clusters—the contribution of rescattering is two orders of magnitude less, but it decreases much more slowly and, at $\theta \sim 30°$ (for protons) and $\theta \sim 50°$ (for positive pions), approaches the first two, becoming dominant in scattering at larger angles. A different pattern is observed in positive-kaon scattering (upper curves in Fig. 5*c*; $E_{K^+} = 0.23$ GeV). Here, the main contribution comes from single scattering over the entire region of angles—the contribution of double scattering is two orders of magnitude less, and only in the region of the diffraction minimum does it become visible in the total cross section. A similar conclusion was drawn by the authors of [23 ,27], who calculated the contributions of various multiplicities in positive-kaon scattering on ^{12}C nuclei.

Let us now try to trace the variation of the double-scattering contribution in response to an increase in the energy of scattered positive kaons. A comparison of curves *2* in Fig. 5*c* at 0.23 and 0.468 GeV reveals that, with increasing energy, the double-scattering contribution increases in the region $\theta > 55°$. The reason for this is that, with increasing energy, incident particles penetrate more deeply into the interior of the nucleus, where collisions occur more frequently and with a greater number of particles, so that higher

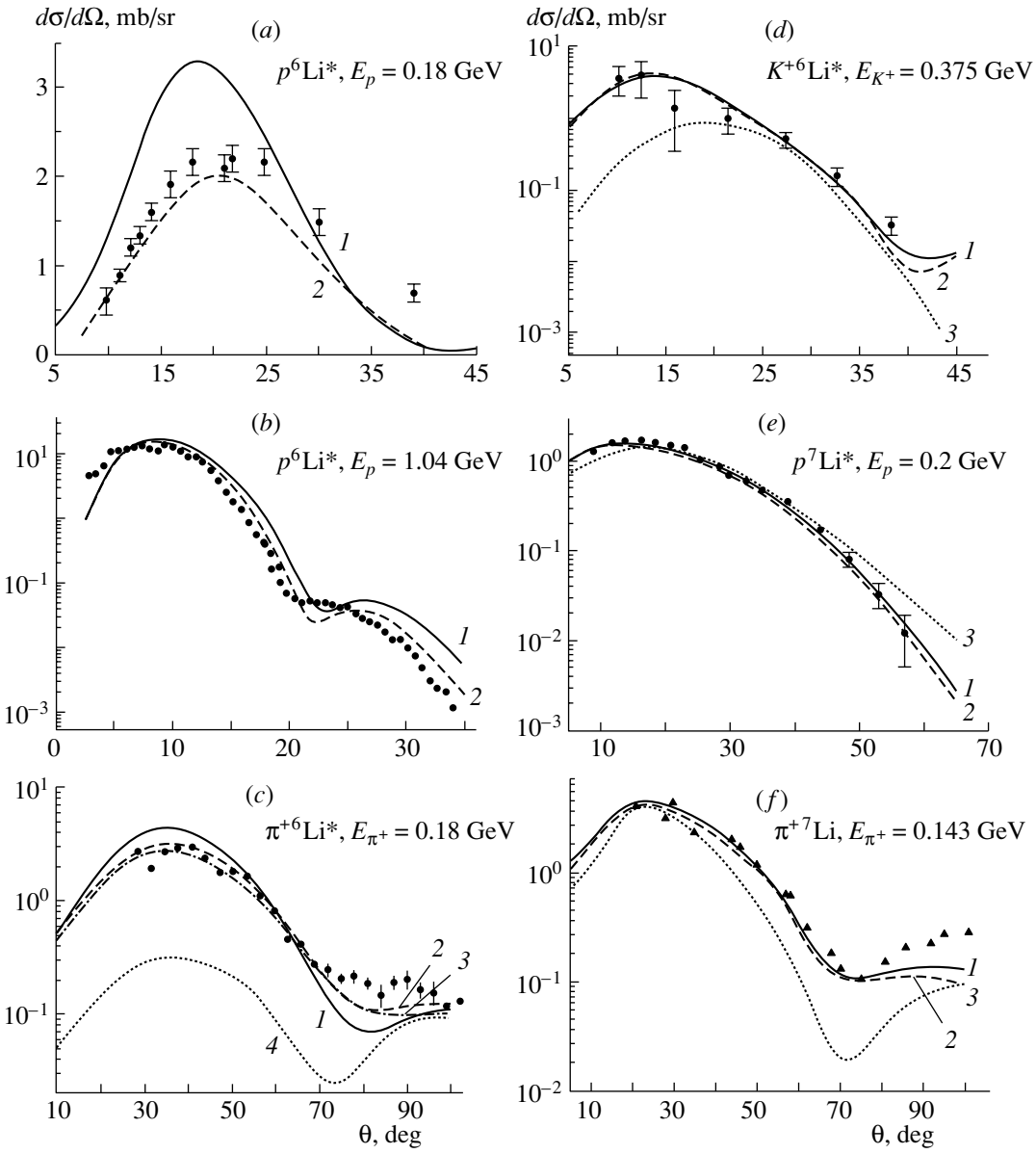

Fig. 7. Differential cross sections for the inelastic scattering of (*a*, *b*, *e*) protons, (*c*, *f*) positive pions, and (*d*) positive kaons to (*a*–*d*) the $J^\pi = 3^+$ level of the ^{6}Li nucleus at $E^* = 2.18$ MeV and (*e*, *f*) the $J^\pi = 1/2^-$ level of the ^{7}Li nucleus at $E^* = 0.48$ MeV. In all panels, curves *1* and *2* display the results of the calculations with the wave functions for models 1 and 2, respectively. The experimental data presented here were borrowed from (*a*) [4], (*b*) [5], (*c*) [10], (*d*) [1, 2], (*e*) [7], and (*f*) [17]. Curves *3* and *4* in Fig. 7*c* represent the contributions of the wave-function components $\Phi^{(02)}$ and $\Phi^{(20)}$, respectively. Curve *3* in Fig. 7*d* shows the results of the DWIA calculations from [2]. Curves *3* in Figs. 7*e* and 7*f* represent the results of the calculations with the oscillator wave function.

multiplicities make greater contributions. The same regularity is observed in the scattering of protons and charged pions as well [32, 33].

In Fig. 6, the differential cross sections calculated for scattering on (*a*–*c*) ^{6}Li and (*d*–*f*) ^{7}Li nuclei are presented for various energies of incident (*a*, *d*) protons, (*b*, *e*) positive pions, and (*c*, *f*) positive kaons. The patterns obtained for the different types of particles are substantially different. The following regularities can be seen for protons and positive kaons: at an energy of about 0.2 GeV, there is no diffraction minimum in the differential cross sections—it appears from about 0.4–0.5 GeV for protons and from somewhat lower energy values for positive kaons. With increasing energy, the minimum is shifted toward the region of smaller scattering angles, and the absolute value of the cross section at $\theta = 0°$ increases somewhat. This minimum is shifted because, the

position of the minimum in K^+A and pA scattering as a function of the momentum transfer **q** is nearly constant; therefore, an increase in the energy leads to a shift of the minimum toward smaller scattering angles [a decrease in θ compensates for an increase in k, as can be seen from (14)]. A modest increase in the absolute value of the cross section at zero angle is explained by the fact that the total cross section increases somewhat with increasing energy (see Tables 1–3)—according to the optical theorem, the total cross section determines the amplitude for zero-angle scattering [see Eq. (2)].

In positive-pion scattering, the minimum in the cross section is not shifted—it is localized at $\theta \approx 60°$. This is due to the existence of a rather broad (of width about 100 MeV) resonance Δ_{33} channel in this region (this channel dominatates the scattering process) and to the absence of open channels below the threshold for positive-pion production. Similar calculations were performed in [46] for π^- ^{3}He scattering and in [47] for $\pi^\pm$ ^{4}He scattering. It was also shown in those studies that, as the energy changes from 0.09 to 0.24 GeV, the minimum in the cross section is not shifted (it occurs in the region between about 85° and 90°). The fact that the diffraction minimum is manifested more clearly at low energies [0.164 and 0.18 GeV for ^{6}Li (Fig. 6*b*) and 0.143 GeV for ^{7}Li (Fig. 6*e*)] than at the higher energy of 0.24 GeV, in which cases we can observe only an inflection point, is somewhat surprising.

Let us now proceed to consider inelastic scattering. Figure 7 displays the differential cross sections for the inelastic scattering of (*a*, *b*, *e*) protons, (*c*, *f*) positive pions, and (*d*) positive kaons to (*a*–*d*) the $J_\pi = 3^+$ level of the ^{6}Li nucleus at $E^* = 2.18$ MeV and (*e*, *f*) the $J_\pi = 1/2^-$ level of the ^{7}Li nucleus at $E^* = 0.48$ MeV. In all the panels of this figure, curves *1* and *2* represent the results of our calculations with the wave functions in models 1 and 2 (see Section 3), respectively. For the ^{6}Li nucleus, a better description of the experimental data is obtained with the wave function in model 2, where use is made of the potential leading to an even–odd splitting of phase shifts for the αN interaction and of the RSC potential for the NN interaction. Most clearly, this can be seen in Fig. 7*a*, where the scale along the ordinate is linear and not logarithmic as in the remaining panels of the figure. For the ^{7}Li nucleus, the calculations with the cluster wave functions yield nearly identical results; for the sake of comparison, the results of the calculation with the oscillator wave function are also shown in Figs. 7*e* and 7*f* (curves *3*). On the basis of a comparison of curves *1*, *2*, and *3*, we can draw a conclusion that is similar to that for the case of elastic scattering (see Figs. 2 and 3 above). Curves *1* and *2* differ from curve *3* at small and large scattering angles—that is, in the region where the oscillator wave function differs most strongly from the cluster wave functions. Specifically, this is so in the interior of the nucleus (the corresponding scattering angles in the differential cross section are large), because short-range nuclear correlations are disregarded in the oscillator potential, and in the asymptotic region, where the momentum transfers are low (the corresponding scattering angles in the differential cross section are small), because the oscillator wave function decreases overly fast.

In Fig. 7*c*, curves *3* and *4* represent the contributions to the cross section from the two wave-function components $\Phi^{(02)}$ [first and second terms in (23)] and $\Phi^{(20)}$ [third and fourth terms in (23)], respectively, while curve *2* corresponds to their sum. That the weight of the first component is nearly three times greater than the weight of the second component determines their partial contributions to the cross section, where the first two terms on the right-hand side of (23) are dominant (curve *3*), while the remaining two terms (curve *4*) generate a small correction that contributes to the cross section only at large scattering angles.

In Fig. 7*d*, curve *3*, calculated in [2] on the basis of the DWIA, is shown for the sake of comparison. We can see that the DWIA description of the behavior of the cross section is not quite satisfactory at small scattering angles ($\theta < 15°$).

6. CONCLUSIONS

(i) For various projectile species, Glauber–Sitenko diffraction theory provides an adequate description of the differential cross sections for scattering on the ^{6,7}Li nuclei over the broad projectile-energy range between 0.1 to 1.0 GeV.

(ii) By using wave functions calculated in two- and three-particle cluster models with realistic interaction potentials, it is possible to calculate analytically the relevant matrix element. Owing to this, the accuracy in describing the differential cross sections within diffraction theory is not inferior to and is even sometimes higher than the corresponding accuracy in the DWIA.

(iii) The important role of the small components in the ^{6}Li wave function has been revealed: making virtually no contribution to the cross section over almost the entire angular range (because of the smallness of the absolute value), they nevertheless increase somewhat the differential cross section in the region where the contribution of the leading component attains a minimum.

(iv) We have considered the contribution to the cross section from various scattering and rescattering multiplicities. It has been established that, for protons and positive pions, it is necessary to take into account all scattering multiplicities, but that, for positive kaons, it is sufficient to retain only single and double scattering. It has been shown that the role of multiple scattering becomes more pronounced with increasing energy of scattered particles.

(v) An analysis of the elementary xN interaction ($x \equiv p$, $\pi^{\pm}$, $K^{\pm}$) from the point of view of the quark structure of particles furnishes deeper insights into the special features of the nuclear interaction, while the distinctions between the parameters of the phenomenological xN amplitudes make it possible to draw a conclusion on how these features manifest themselves at the nuclear level.

(vi) The differential cross sections have been investigated at various energies of scattered particles. It has been shown that, with increasing energy, the diffraction pattern becomes more pronounced (we can observe a larger number of the maxima and minima, their deepening, and a shift of the diffraction minimum toward the region of smaller scattering angles) for protons and positive kaons. At energies between 0.1 and 0.24 GeV, the pattern for positive pions is drastically different, which is due to the Δ_{33} resonance occurring in this region and completely determining the differential cross section.

REFERENCES

1. R. A. Michael *et al.*, Phys. Lett. B **382**, 29 (1996).
2. R. E. Chrien, R. Sawafta, R. J. Peterson, *et al.*, Nucl. Phys. A **625**, 251 (1997); R. J. Peterson, A. A. Ebrahim, and H. C. Bhang, Nucl. Phys. A **625**, 261 (1997).
3. V. S. Buttsev, A. S. Il'inov, and S. E. Chigrinov, Fiz. Élem. Chastits At. Yadra **11**, 900 (1980) [Sov. J. Part. Nucl. **11**, 358 (1980)].
4. R. M. Hutcheon, O. Sundburg, and G. Tibell, Nucl. Phys. A **154**, 261 (1970).
5. G. Bruge, J. Phys. (Paris) **40**, 635 (1979); E. Aslanides, T. Bauer, R. Bertini, *et al.*, Prog. Rep. Nucl. Phys. Dep. CEN, CEA-N-198 (Saclay, 1974/75).
6. C. W. Glower, C. C. Foster, P. Schwandt, *et al.*, Phys. Rev. C **41**, 2487 (1990).
7. C. W. Glower, C. C. Foster, P. Schwandt, *et al.*, Phys. Rev. C **43**, 1664 (1991).
8. E. F. Gibson, J. J. Kraushaar, T. J. Masterson, *et al.*, Nucl. Phys. A **377**, 389 (1982).
9. R. R. Kiziah, M. D. Brown, C. J. Harvey, *et al.*, Phys. Rev. C **30**, 1643 (1984).
10. L. E. Antonuk, D. Bovet, E. Bovet, *et al.*, Nucl. Phys. A **451**, 741 (1986).
11. J. A. Zichy, Thesis No. 6612, ETH (Zurich, 1980).
12. S. Ritt, E. T. Boschitz, R. Meier, *et al.*, Phys. Rev. C **43**, 745 (1991); S. Ritt, E. T. Boschitz, B. Brinkmoller, *et al.*, Phys. Rev. C **49**, 3117 (1994).
13. R. Meier, E. T. Boschitz, B. Brinkmoller, *et al.*, Phys. Rev. C **49**, 320 (1994).
14. L. D. Blokhintsev, I. Borbely, and E. I. Dolinsky, Fiz. Élem. Chastits At. Yadra **8**, 1189 (1977) [Sov. J. Part. Nucl. **8**, 485 (1977)]; L. D. Blokhintsev and A. N. Safronov, Czech. J. Phys. B **32**, 340 (1982).
15. R. A. Eramzhyan, M. Gmitro, T. D. Kaipov, *et al.*, J. Phys. G **14**, 1511 (1988).
16. D. Marlow, P. D. Barnes, N. J. Corella, *et al.*, Phys. Rev. C **25**, 2619 (1982).
17. N. Nose, K. Kume, and S. Yamaguchi, Phys. Rev. C **50**, 321 (1994).
18. E. Romotsky and P. B. Sieger, Phys. Rev. C **57**, 1536 (1998).
19. I. S. Dotsenko and A. D. Fursa, Yad. Fiz. **17**, 770 (1973) [Sov. J. Nucl. Phys. **17**, 402 (1973)].
20. G. D. Alkhasov, Phys. Lett. B **85B**, 43 (1979); G. D. Alkhazov and O. A. Demchenkov, Preprint No. 575, LIYaF (Inst. of Nuclear Physics, Leningrad, 1980).
21. V. V. Goryachiĭ and V. V. Peresypkin, Izv. Akad. Nauk SSSR, Ser. Fiz. **47**, 1013 (1983); V. I. Kukulin and V. V. Peresypkin, Yad. Fiz. **39**, 412 (1984) [Sov. J. Nucl. Phys. **39**, 259 (1984)].
22. J. F. Germond, J. Phys. G **12**, 609 (1986).
23. K. Yamaguchi and Y. Sakamoto, Nuovo Cimento A **108**, 893 (1995).
24. G. Faldt and A. Ingemarsson, J. Phys. G **9**, 261 (1983).
25. M. Arima, K. Masutani, and R. Seki, Phys. Rev. C **44**, 415 (1991).
26. I. M. A. Tag Eldin, E. H. Esmael, M. Y. M. Hassan, *et al.*, J. Phys. G **17**, 271 (1991); **16**, 1051 (1990).
27. Y. Abgrall and J. Labarsouque, Nucl. Phys. A **426**, 431 (1984).
28. V. T. Voronchev, V. M. Krasnopol'sky, and V. I. Kukulin, J. Phys. G **8**, 649 (1982); V. T. Voronchev, T. D. Kaipov, V. M. Krasnopol'sky, *et al.*, Preprint No. PV-0472, IYaI AN SSSR (Inst. for Nuclear Research, USSR Academy of Science, Moscow, 1986); V. I. Kukulin, V. N. Pomerantsev, Kh. D. Razikov, *et al.*, Nucl. Phys. A **586**, 151 (1995).
29. S. B. Dubovichenko and M. A. Zhusupov, Yad. Fiz. **39**, 1378 (1984) [Sov. J. Nucl. Phys. **39**, 870 (1984)]; Izv. Akad. Nauk SSSR, Ser. Fiz. **48**, 935 (1984); Izv. Akad. Nauk Kaz. SSR, Ser. Fiz.-Mat., No. 4, 44 (1984).
30. S. B. Dubovichenko and A. V. Dzhazairov-Kakhramanov, Yad. Fiz. **57**, 784 (1994) [Phys. At. Nucl. **57**, 733 (1994)].
31. M. A. Zhusupov, Izv. Akad. Nauk SSSR, Ser. Fiz. **54**, 2230 (1990).
32. M. A. Zhusupov, E. T. Ibraeva, V. I. Kukulin, and V. V. Peresypkin, Yad. Fiz. **57**, 2013 (1994) [Phys. At. Nucl. **57**, 1937 (1994)]; Izv. Akad. Nauk, Ser. Fiz. **58** (5), 71 (1994); M. A. Zhusupov, E. T. Ibraeva, and B. A. Prmantaeva, Available from KazGosINTI, No. 8482-Ka 98, 29 (1998).

33. M. A. Zhusupov and E. T. Ibraeva, in *Proceedings of the 2nd International Conference on Nuclear and Radiation Physics, Almaty, 1999,* Vol. 1, p. 82; M. A. Zhusupov, E. T. Ibraeva, and B. A. Prmantaeva, in *Proceedings of the Third International Conference on Modern Problems in Nuclear Physics, Bukhara, 1999,* p. 67.
34. G. J. Igo *et al.*, Rev. Mod. Phys. **50**, 523 (1978).
35. L. Ray, Phys. Rev. C **19**, 1855 (1979); **20**, 1857 (1979).
36. D. R. Lehman and M. Rajan, Phys. Rev. C **25**, 2743 (1982); D. R. Lehman and W. C. Parke, Phys. Rev. C **28**, 364 (1983); **29**, 2319 (1984); Few-Body Syst. **1**, 193 (1986).
37. B. V. Danilin, M. V. Zhukov, A. A. Korsheninnikov, *et al.*, Yad. Fiz. **46**, 427 (1987) [Sov. J. Nucl. Phys. **46**, 225 (1987)]; Yad. Fiz. **49**, 360 (1989) [Sov. J. Nucl. Phys. **49**, 223 (1989)]; Yad. Fiz. **53**, 71 (1991) [Sov. J. Nucl. Phys. **53**, 45 (1991)]; M. V. Zhukov *et al.*, Nucl. Phys. A **533**, 428 (1991).
38. Y. Suzuki and Wang Jing Ju, Phys. Rev. C **41**, 736 (1990).
39. R. A. Eramzhyan, G. G. Ryzhikh, and Yu. M. Tchuvil'sky, Yad. Fiz. **62**, 42 (1999) [Phys. At. Nucl. **62**, 37 (1999)].
40. N. A. Burkova and M. A. Zhusupov, Izv. Akad. Nauk SSSR, Ser. Fiz. **51**, 182 (1987); N. A. Burkova, V. V. Denyak, R. A. Eramzhyan, *et al.*, Nucl. Phys. A **586**, 293 (1995).
41. N. A. Burkova, R. A. Eramzhyan, and M. A. Zhusupov, Phys. Lett. B **248**, 15 (1990).
42. M. A. Zhusupov, K. A. Zhusupova, and E. T. Ibraeva, Yad. Fiz. **63**, 223 (2000) [Phys. At. Nucl. **63**, 170 (2000)].
43. R. A. Eramzhyan *et al.*, Phys. Lett. B **228**, 1 (1989).
44. V. G. Neudatchin and Yu. F. Smirnov, in *Modern Problems in Optics and Nuclear Physics* (Naukova Dumka, Kiev, 1974), p. 225.
45. S. B. Dubovichenko and M. A. Zhusupov, Izv. Akad. Nauk Kaz. SSR, Ser. Fiz.-Mat., No. 4, 64 (1987).
46. M. J. Paez and R. H. Landau, Phys. Rev. C **24**, 1120 (1981).
47. B. Brinkmoller, C. L. Blilie, D. Dehnhard, *et al.*, Phys. Rev. C **44**, 2031 (1991).

Translated by A. Isaakyan

Physics of Atomic Nuclei, Vol. 64, No. 11, 2001, pp. 1931–1947. From Yadernaya Fizika, Vol. 64, No. 11, 2001, pp. 2016–2032.

NUCLEI
Theory

Antikaon Production and Medium Effects in Proton–Nucleus Reactions at Subthreshold Beam Energies*

E. Ya. Paryev

Institute for Nuclear Research, Russian Academy of Sciences, pr. Shestidesyatiletiya Oktyabrya 7a, Moscow, 117312 Russia

Received June 1, 2000; in final form, November 13, 2000

Abstract—Inclusive K^--meson production in proton–nucleus collisions in the subthreshold-energy regime is analyzed within an appropriate folding model for incoherent primary proton–nucleon and secondary pion–nucleon production processes, which takes properly into account the struck-target-nucleon momentum and removal-energy distribution (nucleon spectral function), novel elementary cross sections for proton–nucleon reaction channels close to threshold, as well as nuclear mean-field potential effects on the one-step and two-step antikaon-creation processes. A detailed comparison of the model calculations of the K^- differential cross sections for the reactions $p + {}^9\mathrm{Be}$ and $p + {}^{63}\mathrm{Cu}$ at subthreshold energies with the first experimental data obtained at the ITEP proton synchrotron is given. It displays both the relative role of the primary and secondary production channels at incident energies considered and the contributions to K^- production that come from the use of the single-particle part and high-momentum–energy part of the nucleon spectral function. It is found that the pion–nucleon production channel does not dominate in the subthreshold "hard" antikaon production in $p{}^9\mathrm{Be}$ and $p{}^{63}\mathrm{Cu}$ collisions and that the main contributions to the antikaon yields here come from the direct K^--production mechanism. The influence of the nucleon, kaon, and antikaon mean-field potentials on the K^- yield is explored. It is shown that the effect of the nucleon mean field is of importance in explaining the considered experimental data on "hard" antikaon production, whereas the K^+ and K^- optical potentials play a minor role. The sensitivity of subthreshold "soft" antikaon production in $p{}^9\mathrm{Be}$ reactions to the nucleon, kaon, and antikaon mean fields is studied. It is demonstrated that, contrary to the case of "hard" antikaon production, the K^- potential has a very strong effect on the K^- yield, which is comparable with that from the nucleon effective potential.

1. INTRODUCTION

Kaon and antikaon properties in dense matter are the subject of considerable current interest in the nuclear physics community [1]. Knowledge of these properties is important for understanding both chiral-symmetry restoration in a dense nuclear medium and neutron-star properties. Since the pioneering study of Kaplan and Nelson [2] on the possibility of kaon condensation in nuclear matter, there have been many theoretical investigations into the in-medium properties of kaons and antikaons, based on various approaches, such as the effective chiral Lagrangian [3–8], the boson-exchange model [8–10], the Nambu–Jona-Lasinio model [11, 12], the quark–meson coupling model [13], and the coupled-channel [14, 15] and effective KN-scattering length [16] approaches. Although these models give quantitatively different predictions for the kaon and antikaon potentials in a nuclear medium, they agree qualitatively in establishing that, in nuclear matter, K^+ feels a weak repulsive potential of about 20–30 MeV at normal nuclear-matter density ρ_0 ($\rho_0 = 0.17$ fm^{-3}), whereas K^- feels a strong attractive potential that ranges between -140 and -75 MeV at ρ_0. The K^- atomic data also indicate [10, 17, 18] that the real part of the antikaon optical potential can be on the order of (-200 ± 20) MeV at normal nuclear-matter density, while being slightly repulsive at very low densities in accordance with the K^-p scattering length. As a result, deeply bound kaonic nuclei should exist [19]. Moreover, the condensation of antikaons in neutron stars at critical density of about $3\rho_0$ becomes possible, which would then lead to the lowering of the maximum neutron-star mass to the value that is in good agreement with the observed one, as well as to the existence of a large number of low-mass black holes in a galaxy [20]. On the other hand, in the recent chiral approach of Oset and Ramos [21], it was shown that, as nuclear density ρ_N increases, the attraction felt by K^- becomes significantly more moderate than that obtained within other theories

*This article was submitted by the author in English.

and that the effective K^- mass $m^*_{K^-}$ gains, at high densities, the level around the value already achieved at $\rho_N = \rho_0$, namely, $m^*_{K^-}(\rho_N > \rho_0) \approx m^*_{K^-}(\rho_N = \rho_0) = 445$ MeV, which makes the appearance of the phenomenon of K^- condensation in neutron-star matter very unlikely. The in-medium K^- mass of 445 MeV corresponds to a weaker attractive K^- optical potential of about -50 MeV at normal nuclear-matter density. Furthermore, coupled-channel calculations for antikaons in matter performed very recently in [22] demonstrated that the K^- optical potential becomes repulsive at finite momenta or finite temperature. The momentum dependence of the K^+ and K^- potentials at a finite nuclear density was investigated in [23, 24] within the dispersion approach. It was found that, in contrast to [22], the antikaon potential remains attractive even at high momenta. The K^- potential of about -28 MeV at density ρ_0 and an antikaon momentum of 800 MeV/c was extracted in [25] from the data on elastic K^-A scattering within Glauber theory. Therefore, it is very important to have such experimental data that allow one to test the predictions of the above models.

Subthreshold kaon and antikaon production in heavy-ion collisions, where high densities are accessible, is obviously best suited for studying their properties in dense matter. The transport-model calculations [1, 26–33] showed that the in-reaction-plane and out-of-reaction-plane kaon flow is a sensitive probe of K^+ potential in a medium. The dropping K^--mass scenario will lead to a substantial enhancement of the K^- yield in heavy-ion collisions at subthreshold incident energies due to the in-medium shifts of the elementary production thresholds to lower energies. Antikaon enhancement in nucleus–nucleus interactions was observed by the KaoS and FRS collaborations at SIS/GSI [34–38]. This phenomenon was attributed to the in-medium K^--mass reduction [16, 20, 39–42]. Thus, the analysis of the KaoS data [34, 35] within the relativistic transport model [20, 39–41] showed that these data are consistent with the predictions of chiral perturbation theory that K^+ feels a weak repulsive potential and K^- feels a strong attractive potential in a nuclear medium (respectively, of about 20 and -110 MeV at normal nuclear-matter density). This is similar to the findings of Cassing *et al.* [42].

Of special question is the validity of extrapolation of "empirical" kaon and antikaon dispersion relations extracted in [20, 39–42] from densities of $(2–3)\rho_0$ to the density of ordinary nuclei. This can be clarified from the study of subthreshold K^+ and K^- production in proton-induced reactions. The advantage of these reactions is that possible kaon and antikaon mass changes (up to 5% and 20% for K^+ and K^-, respectively), although smaller than those in heavy-ion collisions, can be better controlled owing to their simpler dynamics compared to the case of nucleus–nucleus interactions. Therefore, information obtained from proton-induced reactions will supplement that deduced from heavy-ion collision studies and provide an independent test of theoretical predictions that precursor phenomena of chiral-symmetry restoration should be observable even at normal nuclear-matter density.

Another, very important piece of information that can be extracted from the study of K^+- and K^--meson production in pA collisions at subthreshold incident energies concerns such intrinsic properties of target nuclei as Fermi motion and high-momentum components of the nuclear wave function.

Inclusive K^+ production in proton–nucleus reactions at bombarding energies less than threshold energies in a collision of free nucleons has been extensively studied both experimentally and theoretically in recent years [43–55]. This phenomenon is under study presently at the accelerators COSY–Jülich [56] and CELSIUS [57], as well as at the ITEP proton synchrotron [58, 59]. Up to now, there have been, however, no data on subthreshold K^- production in proton–nucleus collisions. Recently, such experimental data have been obtained at the ITEP proton synchrotron [60]. The main goal of the present work is to analyze these data within the spectral-function approach. Here, we present the analysis of the first experiment [60] on subthreshold K^- production on Be and Cu target nuclei by protons. Some preliminary results of this analysis were reported in [60]. It should be noted that the investigation of inclusive and exclusive subthreshold K^- production in pA interactions is planned in the near future at the accelerator COSY–Jülich [56].

In Section 2, we give a review of the spectral-function approach employed, as well as the parametrizations for the elementary antikaon-production cross sections. In Section 3, we present a detailed comparison of our calculations with the data [60], as well as our predictions for the invariant cross sections for "soft" K^- production on ^{9}Be target nucleus, which might be measured at, for example, the Cooler Synchrotron COSY–Jülich. Finally, the results of this study are summarized in Section 4.

2. THE MODEL AND INPUTS

2.1. Direct K^--Production Mechanism

Apart from participating in elastic scattering, an incident proton can produce K^- directly in the first inelastic pN collision due to nucleon Fermi motion.

Since we are interested in the few-GeV region (up to 3 GeV), we have taken into account [61] the following elementary process having the lowest free production threshold (2.99 GeV for kinematical conditions of the experiment [60] in which the rather "hard" K^- mesons with a momentum of 1.28 GeV/c at the laboratory angle of 10.5° have been detected):

$$p + N \to N + N + K + K^-, \tag{1}$$

where K stands for K^+ or K^0 for the specific isospin channel. In the following calculations, we will include the medium modification of the final hadrons (nucleons, kaon, and antikaon) participating in the production process (1) by using their in-medium masses m_h^* determined below. The kaon and antikaon masses in the medium, $m_{K^\pm}^*$, can be obtained from the mean-field approximation to the effective chiral Lagrangian [27, 62, 63]; i.e.,

$$m_{K^\pm}^*(\rho_N) \approx m_K \left(1 - \frac{\Sigma_{KN}}{2f^2 m_K^2}\rho_S \pm \frac{3}{8f^2 m_K}\rho_N\right), \tag{2}$$

where m_K is the rest mass of a kaon in free space, $f = 93$ MeV is the pion decay constant, and Σ_{KN} is the KN sigma term depending on the strangeness content of a nucleon and reflecting the explicit chiral symmetry breaking due to the nonzero strange-quark mass. It determines the strength of the attractive scalar potential for kaon and antikaon. The scalar and nuclear densities are denoted by ρ_S and ρ_N, respectively. Since the exact value of Σ_{KN} and the size of higher order corrections leading to different scalar attractions for kaon and antikaon are not very well known, the quantity Σ_{KN} was treated in [20, 39] as a free parameter that was adjusted separately for K^+ and K^- to achieve, within the relativistic transport model, good fits to the experimental K^+ and K^- spectra [34, 35] in heavy-ion collisions. Using the values of the "empirical kaon and antikaon sigma terms" obtained in [20, 39] and considering that $\rho_S \approx 0.9\rho_N$ at $\rho_N \le \rho_0$ [27], we can readily rewrite (2) in the form

$$m_{K^\pm}^*(\rho_N) = m_K + U_{K^\pm}(\rho_N), \tag{3}$$

where the $K^\pm$ optical potentials $U_{K^\pm}(\rho_N)$ are proportional to the nuclear density ρ_N,

$$U_{K^\pm}(\rho_N) = U_{K^\pm}^0 \frac{\rho_N}{\rho_0} \tag{4}$$

with

$$U_{K^+}^0 = 22\ \text{MeV},\ \ U_{K^-}^0 = -126\ \text{MeV}. \tag{5}$$

To explore the sensitivity of the K^- spectra from the primary channel (1) in proton–nucleus reactions to the $K^\pm$ potentials in nuclear matter, we will ignore both these potentials in our calculations and also adopt, instead of the antikaon potential (4), (5), the K^- potential extracted [17] from the analysis of kaon atomic data, viz.,

$$U_{K^-}(\rho_N) \tag{6}$$
$$= -129\left[-0.15 + 1.7\left(\frac{\rho_N}{\rho_0}\right)^{0.25}\right]\frac{\rho_N}{\rho_0}\ \text{MeV}.$$

It is easily seen that the potential (6) amounts to −200 MeV in the nuclear interior. According to the predictions of the quark–meson coupling model by Tsushima *et al.* [13], one has $m_{K^0}^* = m_{K^+}^*$ in symmetric nuclear matter. The effective mass m_N^* of secondary nucleons produced in reaction (1) can be expressed via the scalar mean-field potential $U_N(\rho_N)$ as [53]

$$m_N^*(\rho_N) = m_N + U_N(\rho_N), \tag{7}$$

where m_N is the bare nucleon mass. The potential $U_N(\rho_N)$ was assumed to be proportional to the nuclear density [21],

$$U_N(\rho_N) = U_N^0 \frac{\rho_N}{\rho_0}, \tag{8}$$

with the depth at nuclear saturation density ρ_0 relevant [53] to the momentum range of outgoing nucleons for the most part of kinematical conditions of the experiment [60] on subthreshold antikaon production being

$$U_N^0 = -34\ \text{MeV}. \tag{9}$$

To see the sensitivity of antikaon-production cross sections from the one-step process (1) to the effective nucleon potential, we will both neglect this potential in the following calculations and employ, in them, the potential of the type (8) with the depth [21, 52]

$$U_N^0 = -50\ \text{MeV}. \tag{10}$$

The total energies E_h' of secondary hadrons inside the nuclear medium can be expressed in terms of their effective masses m_h^* defined above and in-medium momenta $\mathbf{p}_h'$ as in the free-particle case, namely,

$$E_h' = \sqrt{\mathbf{p}_h'^2 + m_h^{*2}}. \tag{11}$$

It should be pointed out that the use of the quasiparticle dispersion relation (11) with the momentum-independent scalar potentials (4)–(6) entering into the in-medium masses of final $K^\pm$ mesons is very well justified for the K^+ meson [23], whereas, in the case of the K^- meson, it is valid only for small momenta. However, for reasons of simplicity, as well as in view of substantial uncertainties in the model K^- optical potential (see above), we will neglect the explicit momentum dependence of the antikaon mean-field potential in the present study.

Let us now specify the energies and momenta of the incoming proton inside the target nucleus, as well

as of the struck target nucleon participating in the first-chance pN collision (1). The total energy $E_0^{'}$ and momentum $\mathbf{p}_0^{'}$ of the incident proton inside the target nucleus are related to E_0 and $\mathbf{p}_0$ outside the nucleus by the equations [53]

$$E_0^{'} = E_0 - \frac{\Delta\mathbf{p}^2}{2M_A}, \tag{12}$$

$$\mathbf{p}_0^{'} = \mathbf{p}_0 - \Delta\mathbf{p}, \tag{13}$$

where

$$\Delta\mathbf{p} = \frac{E_0 V_0}{p_0}\frac{\mathbf{p}_0}{|\mathbf{p}_0|}. \tag{14}$$

Here, M_A is the mass of the initial target nucleus, and V_0 is the nuclear optical potential that a proton impinging on a nucleus at the kinetic energy ϵ_0 of about a few GeV feels in the interior of the nucleus ($V_0 \approx 40$ MeV). Further, let E_t and $\mathbf{p}_t$ be the total energy and momentum of the struck target nucleon N just before the collision process (1). Taking into account the respective recoil and excitation energies of the residual $(A-1)$ system, one has [52, 53]

$$E_t = M_A - \sqrt{(-\mathbf{p}_t)^2 + (M_A - m_N + E)^2}, \tag{15}$$

where E is the removal energy of the struck target nucleon. After specifying the energies and momenta of all particles involved in the K^--production process (1), we can write the corresponding energy- and momentum-conservation laws

$$E_0^{'} + E_t = E_{N_1}^{'} + E_{N_2}^{'} + E_K^{'} + E_{K^-}^{'}, \tag{16}$$

$$\mathbf{p}_0^{'} + \mathbf{p}_t = \mathbf{p}_{N_1}^{'} + \mathbf{p}_{N_2}^{'} + \mathbf{p}_K^{'} + \mathbf{p}_{K^-}^{'}. \tag{17}$$

From (16) and (17), we obtain the squared invariant energy available in the first-chance pN collision:

$$s = (E_0^{'} + E_t)^2 - (\mathbf{p}_0^{'} + \mathbf{p}_t)^2. \tag{18}$$

On the other hand, according to (16) and (17), one gets

$$s = (E_{N_1}^{'} + E_{N_2}^{'} + E_K^{'} + E_{K^-}^{'})^2 - (\mathbf{p}_{N_1}^{'} + \mathbf{p}_{N_2}^{'} + \mathbf{p}_K^{'} + \mathbf{p}_{K^-}^{'})^2. \tag{19}$$

With use of (11), this leads to the following expression for the in-medium reaction threshold:

$$\sqrt{s_{\rm thr}^*} = 2m_N^* + m_{K^+}^* + m_{K^-}^* = \sqrt{s_{\rm thr}} + 2U_N + U_{K^+} + U_{K^-}, \tag{20}$$

where $\sqrt{s_{\rm thr}} = 2(m_N + m_K)$ is the threshold energy in free space and the effective potentials are given by (4)–(6) and (8)–(10). It is clear from (20) that the threshold for antikaon production in the reaction $pN \to NNKK^-$ is lowered when the in-medium masses are used. For example, the reduction of the K^- threshold in the nuclear interior will be 172 and 204 MeV, respectively, for the potentials (5), (9) and (5), (10). This will strongly enhance the possibility of K^- production in first-chance pN collisions at subthreshold beam energies.

Finally, neglecting K^- production via resonances in pN collisions[1)] [16] and taking into consideration antikaon final-state absorption, we can represent the invariant inclusive cross section for the production on nuclei of K^- mesons with the total energy E_{K^-} and momentum $\mathbf{p}_{K^-}$ from the primary proton-induced reaction channel (1) as (see also [52, 53])

$$E_{K^-}\frac{d\sigma_{pA\to K^-X}^{(\rm prim)}(\mathbf{p}_0)}{d\mathbf{p}_{K^-}} = A\int \rho(\mathbf{r})d\mathbf{r} \times \exp\left[-\mu(p_0)\int_{-\infty}^{0}\rho(\mathbf{r}+x\mathbf{\Omega}_0)dx - \mu(p_{K^-}) \times \int_0^{+\infty}\rho(\mathbf{r}+x\mathbf{\Omega}_{K^-})dx\right] \times \left\langle E_{K^-}^{'}\frac{d\sigma_{pN\to NNKK^-}[\mathbf{p}_0^{'}, \mathbf{p}_{K^-}^{'}, \rho(\mathbf{r})]}{d\mathbf{p}_{K^-}^{'}}\right\rangle, \tag{21}$$

where

$$\left\langle E_{K^-}^{'}\frac{d\sigma_{pN\to NNKK^-}[\mathbf{p}_0^{'}, \mathbf{p}_{K^-}^{'}, \rho(\mathbf{r})]}{d\mathbf{p}_{K^-}^{'}}\right\rangle = \int\int P(\mathbf{p}_t, E)d\mathbf{p}_t dE \times \left[E_{K^-}^{'}\frac{d\sigma_{pN\to NNKK^-}[\sqrt{s}, \mathbf{p}_{K^-}^{'}, \rho(\mathbf{r})]}{d\mathbf{p}_{K^-}^{'}}\right]; \tag{22}$$

$$\mu(p_0) = \sigma_{pp}^{\rm in}(p_0)Z + \sigma_{pn}^{\rm in}(p_0)N, \qquad \mu(p_{K^-}) = \sigma_{K^-p}^{\rm tot}(p_{K^-})Z + \sigma_{K^-n}^{\rm tot}(p_{K^-})N. \tag{23}$$

Here, $E_{K^-}^{'}d\sigma_{pN\to NNKK^-}[\sqrt{s}, \mathbf{p}_{K^-}^{'}, \rho(\mathbf{r})]/d\mathbf{p}_{K^-}^{'}$ is the "in-medium" invariant inclusive cross section for K^- production in reaction (1); $\rho(\mathbf{r})$ and $P(\mathbf{p}_t, E)$ are, respectively, the density and nucleon spectral function normalized to unity; $\mathbf{p}_t$ and E are, respectively, the internal momentum and removal energy of the struck

[1)] It should be pointed out that, in the threshold energy region, K^- mesons can be produced in these collisions also by the decay mainly of the ϕ meson as an intermediate state [64, 65]. Thus, the resonant(ϕ meson)-to-nonresonant K^--production cross-section ratio in pp reactions measured recently by the DISTO collaboration at SATURNE [65] at a beam energy of 2.85 GeV is equal to 0.82. However, in view of the complete lack of other data in the literature for ϕ-meson production in pp interactions at energies close to the threshold needed for accurately estimating the resonant contribution to K^- production in pA reactions, it is natural to assume, in calculating the K^- yields in pA collisions from primary channel (1), that the antikaons are produced directly in this channel.

target nucleon just before the collision; $\sigma_{pN}^{\rm in}$ and $\sigma_{K^-N}^{\rm tot}$ are, respectively, the inelastic and total cross sections of free pN and K^-N interactions; Z and N are, respectively, the numbers of protons and neutrons in the target nucleus ($A = N + Z$); $\mathbf{\Omega}_0 = \mathbf{p}_0/p_0$ ($\mathbf{p}_0$ is the beam momentum) and $\mathbf{\Omega}_{K^-} = \mathbf{p}_{K^-}/p_{K^-}$; and s is the pN center-of-mass energy squared. The expression for s is given above by formula (18). In (21), it is assumed that the K^--meson production cross sections in pp and pn interactions are the same [29, 61, 66] and that any difference between the proton and the neutron spectral functions is disregarded [52, 53]. In addition, it is suggested that the way of the produced antikaon out of the nucleus is not disturbed by the K^- optical potential and K^-N elastic rescatterings, as well as that $\sigma_{K^-N}^{\rm tot}(p'_{K^-}) \approx \sigma_{K^-N}^{\rm tot}(p_{K^-})$. Such approximations are allowed in calculating the K^--production cross sections for kinematics of the experiment reported in [60]. As a result, the in-medium antikaon momentum $\mathbf{p}'_{K^-}$ is assumed to be parallel to the vacuum momentum $\mathbf{p}_{K^-}$ and the relation between them is given by

$$\sqrt{\mathbf{p}'^2_{K^-} + m^{*2}_{K^-}} = \sqrt{\mathbf{p}^2_{K^-} + m^2_{K^-}}. \qquad (24)$$

In our approach, the invariant inclusive cross section for K^- production in the elementary process (1) has been described by the four-body phase-space calculations normalized to the corresponding total cross section [52]:

$$E'_{K^-}\frac{d\sigma_{pN\to NNKK^-}[\sqrt{s}, \mathbf{p}'_{K^-}, \rho(\mathbf{r})]}{d\mathbf{p}'_{K^-}} = \sigma_{pN\to NNKK^-}(\sqrt{s}, \sqrt{s^*_{\rm th}}) f_4(s, \mathbf{p}'_{K^-}), \qquad (25)$$

$$f_4(s, \mathbf{p}'_{K^-}) = I_3(s_{NNK}, m^*_{K^+}, m^*_N, m^*_N) \times [2I_4(s, m^*_{K^+}, m^*_{K^-}, m^*_N, m^*_N)]^{-1}, \qquad (26)$$

$$I_3(s, m^*_{K^+}, m^*_N, m^*_N) = \left(\frac{\pi}{2}\right)^2 \times \int\limits_{4m^{*2}_N}^{(\sqrt{s}-m^*_{K^+})^2} \frac{\lambda(s_{NN}, m^{*2}_N, m^{*2}_N)}{s_{NN}} \times \frac{\lambda(s, s_{NN}, m^{*2}_{K^+})}{s}\, ds_{NN}, \qquad (27)$$

$$I_4(s, m^*_{K^+}, m^*_{K^-}, m^*_N, m^*_N) = \frac{\pi}{2} \int\limits_{4m^{*2}_N}^{(\sqrt{s}-m^*_{K^+}-m^*_{K^-})^2} \frac{\lambda(s_{NN}, m^{*2}_N, m^{*2}_N)}{s_{NN}} \times I_3(s, m^*_{K^-}, \sqrt{s_{NN}}, m^*_{K^+}) ds_{NN}, \qquad (28)$$

$$\lambda(x, y, z) = \sqrt{\left[x - (\sqrt{y} + \sqrt{z})^2\right]\left[x - (\sqrt{y} - \sqrt{z})^2\right]}, \qquad (29)$$

$$s_{NNK} = s + m^{*2}_{K^-} - 2(E'_0 + E_t)E'_{K^-} + 2(\mathbf{p}'_0 + \mathbf{p}_t)\mathbf{p}'_{K^-}. \qquad (30)$$

Here, $\sigma_{pN\to NNKK^-}(\sqrt{s}, \sqrt{s^*_{\rm th}})$ is the "in-medium" total cross section for K^- production in reaction (1). This cross section is equivalent [28, 42, 53] to the vacuum cross section $\sigma_{pN\to NNKK^-}(\sqrt{s}, \sqrt{s_{\rm thr}})$ in which the free threshold $\sqrt{s_{\rm thr}}$ is replaced by the effective threshold $\sqrt{s^*_{\rm thr}}$ as given by Eq. (20). For the free total cross section $\sigma_{pN\to NNKK^-}(\sqrt{s}, \sqrt{s_{\rm thr}})$, we have used the parametrization[2)] suggested in [61, 66] that has been corrected for the new data point (500 pb) for $pp \to ppK^+K^-$ reaction from the COSY-11 collaboration at COSY–Jülich [67] taken at 6.1-MeV excess energy, viz.,

$$\sigma_{pp\to ppK^+K^-}(\sqrt{s}, \sqrt{s_{\rm th}}) = \begin{cases} 0.098\left(1 - \dfrac{s_{\rm thr}}{s}\right)^{2.23}\ [\text{mb}] & \text{for } 0 < \sqrt{s} - \sqrt{s_{\rm thr}} \le 0.1\ \text{GeV} \\ F\left(\dfrac{s}{s_{\rm thr}}\right)\ [\text{mb}] & \text{for } \sqrt{s} - \sqrt{s_{\rm thr}} > 0.1\ \text{GeV}, \end{cases} \qquad (31)$$

where

$$F(x) = \left(1 - \frac{1}{x}\right)^3 [2.8F_1(x) + 7.7F_2(x)] + 3.9F_3(x) \qquad (32)$$

and

$$F_1(x) = (1 + 1/\sqrt{x})\ln x - 4(1 - 1/\sqrt{x}), \qquad (33)$$
$$F_2(x) = 1 - (1/\sqrt{x})(1 + \ln x/2),$$
$$F_3(x) = \left(\frac{x-1}{x^2}\right)^{3.5}.$$

[2)] It should be mentioned that this parametrization was proposed for the inclusive $pp \to K^-X$ cross section, which is assumed to be the same as that for $pp \to ppK^+K^-$ at beam energies of interest [61, 66].

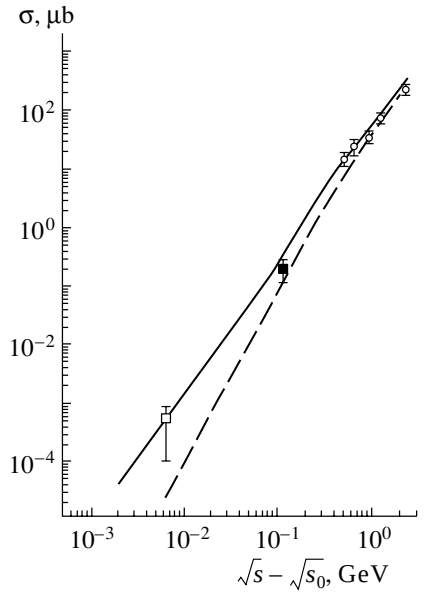

Fig. 1. Total antikaon-production cross section in proton–proton collisions as a function of the available energy above the threshold. The notation is explained in the main body of the text.

A comparison of the results of our calculations by (31) (solid curve) with the experimental data close to the threshold for $pp \to ppK^+K^-$ reaction from the installation COSY-11 [67] (open square), from the DISTO collaboration at SATURNE [65] (full square), and with the K^- inclusive production cross sections at higher energies (open circles) [61, 66] is shown in Fig. 1. In this figure, we also show the predictions from the current parametrization (dashed curve) employed in the recent study [23] of the antikaon production in proton–nucleus collisions. It is seen that our parametrization (31) accounts well for the K^- cross sections measured in the experiments [65, 67] near the production threshold, whereas the one from [23] underestimates the lowest data point by a factor of about 10.

For K^--production calculations in the case of ^{9}Be and ^{63}Cu target nuclei reported here, we have employed, for the nuclear density $\rho(\mathbf{r})$, respectively, the harmonic-oscillator and a two-parameter Fermi density distribution,

$$\rho(\mathbf{r}) = \rho_N(\mathbf{r})/A \tag{34}$$
$$= \frac{(b/\pi)^{3/2}}{A/4}\left\{1 + \left[\frac{A-4}{6}\right] br^2\right\}\exp\left(-br^2\right),$$

$$\rho(\mathbf{r}) = \rho_0\left[1 + \exp\left(\frac{r-R}{a}\right)\right]^{-1}, \tag{35}$$

with $b = 0.329$ fm^{-2} [60], $R = 4.20$ fm, and $a = 0.55$ fm [68].

Another very important ingredient for the calculation of the K^--production cross sections in proton–nucleus reactions in the subthreshold-energy regime—the nucleon spectral function[3] $P(\mathbf{p}_t, E)$ (which represents the probability of finding a nucleon with momentum $\mathbf{p}_t$ and removal energy E in the nucleus)—was taken from [52, 53] for a ^{9}Be target nucleus; for ^{63}Cu, it is assumed to be identical to that for ^{208}Pb [71]. The latter was taken from [72]. The adopted spectral function contains information on both the single-particle motion of intranuclear nucleons (at low p_t and E) and short-range nucleon–nucleon correlations (at high p_t and E). The description of its structure at high values of the nucleon momentum (up to ~ 0.8 GeV/c) and removal energy (up to ~ 0.5 GeV) relevant to the kinematical conditions of the experiment [60] (see below) is based on the convolution model [71]. It should be noted that, in specific cases (see, for example, [73]), the analysis of hadron production on nuclei requires knowledge of the nucleon spectral function at larger values of three-momentum and removal energy. Such an extrapolated spectral function was obtained in [73].

Let us now simplify expression (21) for the invariant differential cross section for K^- production in pA collisions from the one-step process. Since we are interested in the spectra of emitted antikaons at forward laboratory angles, i.e., when $\mathbf{\Omega}_{K^-} \approx \mathbf{\Omega}_0$, we have

$$E_{K^-}\frac{d\sigma^{(\mathrm{prim})}_{pA\to K^-X}(\mathbf{p}_0)}{d\mathbf{p}_{K^-}} \tag{36}$$
$$= 2\pi A\int\limits_0^{+\infty} r_\perp dr_\perp \int\limits_{-\infty}^{+\infty} dz\rho\left(\sqrt{r_\perp^2 + z^2}\right)$$
$$\times \exp\left[-\mu(p_0, p_{K^-}; r_\perp, z)\right]$$
$$\times\left\langle E'_{K^-}\frac{d\sigma_{pN\to NNKK^-}[\mathbf{p}'_0, \mathbf{p}'_{K^-}, \rho(\sqrt{r_\perp^2 + z^2})]}{d\mathbf{p}'_{K^-}}\right\rangle,$$

where

$$\mu(p_0, p_{K^-}; r_\perp, z) = \mu(p_0)t(r_\perp, z) \tag{37}$$
$$+ \mu(p_{K^-})t(r_\perp, -z)$$

and

$$t(r_\perp, z) = \int\limits_{-\infty}^{z}\rho\left(\sqrt{r_\perp^2 + x^2}\right)dx. \tag{38}$$

The quantities $\mu(p_0)$ and $\mu(p_{K^-})$ entering into (37) are defined above by formula (23). In the case of

[3] It should be noticed that the full energy–momentum distribution of the struck target nucleons was not taken previously into account [23, 58, 69, 70] in analyzing the subthreshold and near-threshold antikaon production in proton–nucleus reactions.

the harmonic-oscillator density distribution (34), the integral in (38) has the simple form

$$t(r_\perp, z) = \left(\frac{2b}{\pi A}\right)\left\{1 + \left[\frac{A-4}{6}\right] br_\perp^2 + \left[\frac{A-4}{12}\right] + f(z) - f(-z)\right\}\exp(-br_\perp^2), \quad (39)$$

$$f(z) = \Theta(z)\left\{\left[1 + \left(\frac{A-4}{6}\right) br_\perp^2 + \left(\frac{A-4}{12}\right)\right]\mathrm{erf}(z\sqrt{b}) - \left(\frac{A-4}{6}\right)\frac{z\sqrt{b}}{\sqrt{\pi}}\exp(-bz^2)\right\}, \quad (40)$$

$$\Theta(z) = \frac{z+|z|}{2|z|}, \quad \mathrm{erf}(x) = \frac{2}{\sqrt{\pi}}\int\limits_0^x \exp(-t^2)dt.$$

Considering that, for K^- mesons with a momentum of 1.28 GeV/c, the elementary cross section is $\sigma^{\mathrm{tot}}_{K^-N} \approx 30$ mb [61] and that $\sigma^{\mathrm{in}}_{pN} \approx 30$ mb [52] for the beam energy range of interest, we have

$$\mu(p_0) = \mu(p_{K^-}) = \mu = 30A \text{ mb}. \quad (41)$$

Then, expression (37) is reduced to the simpler form

$$\mu(p_0, p_{K^-}; r_\perp, z) = \mu t(r_\perp), \quad (42)$$

$$t(r_\perp) = t(r_\perp, z) + t(r_\perp, -z) = 2\int\limits_0^{+\infty}\rho(\sqrt{r_\perp^2 + x^2})dx. \quad (43)$$

For the harmonic-oscillator density distribution (34), the quantity $t(r_\perp)$, in view of Eqs. (39) and (40), has the simple form

$$t(r_\perp) = \left(\frac{4b}{\pi A}\right)\left\{1 + \left[\frac{A-4}{6}\right] br_\perp^2 + \left[\frac{A-4}{12}\right]\right\}\exp(-br_\perp^2). \quad (44)$$

Let us now consider the two-step K^--production mechanism.

3. TWO-STEP K^--PRODUCTION MECHANISM

Kinematical considerations show that, in the bombarding energy range of our interest ($\leq$3.0 GeV), not only may the following two-step production process contribute to K^- production in pA interactions, but it is even dominant [23, 69] at subthreshold energies. In the first inelastic collision with an intranuclear nucleon, an incident proton can also produce a pion through the elementary reaction

$$p + N_1 \to N + N + \pi. \quad (45)$$

Then, the intermediate pion, which is assumed to be on-shell, produces an antikaon on a nucleon of the target nucleus via the elementary subprocess with the lowest free production threshold (1.98 GeV for kinematics of the experiment reported in [60]),[4)]

$$\pi + N_2 \to N + K + K^-, \quad (46)$$

provided that this subprocess is energetically possible. To allow for the influence of the nuclear environment on the secondary K^--production process (46), it is natural to use, in calculations of the K^--production cross section from this process, the same in-medium modifications of the masses of final hadrons (kaon, antikaon, and nucleon) as those, (3) and (7), for hadrons from primary pN collisions due to the corresponding mean-field potentials $U_{K^\pm}(\rho_N)$ and $U_N(\rho_N)$. For the sake of numerical simplicity, these potentials are assumed here to be density-independent with depths (5) and (9) taken at the nuclear saturation density. Evidently, this enables us to obtain an upper limit on the respective cross sections. Moreover, in order to reproduce the high-momentum tails of the pion spectra at forward laboratory angles from reaction (45), which are responsible for K^- production through the $\pi N \to NKK^-$ channel, it is necessary to take into account, in calculating these spectra, as was shown in [53], the modification of the mass of each low-energy nucleon produced together with a high-energy pion by the effective potential (9). But, since we will employ (see below), in our calculations of the antikaon production from secondary process (46), the pion spectra from proton–nucleus interactions also measured in the experiment reported in [60] instead of the theoretical ones, this modification will be automatically included. Then, taking into account the antikaon final-state absorption and using the results given in [52, 53], we easily get the following expression for the K^--production cross section for pA reactions from the secondary pion-induced reaction channel (46), which includes the medium effects under consideration on the same footing as that employed in the calculation of the K^--production cross section (21) from primary proton-induced reaction channel (1):

$$E_{K^-}\frac{d\sigma^{(\mathrm{sec})}_{pA\to K^-X}(\mathbf{p}_0)}{d\mathbf{p}_{K^-}} \quad (47)$$

[4)]It is important to note that the elementary processes $\pi N \to N\pi KK^-$ with one pion in final states, as our calculations with the total cross sections of these processes taken from [20] showed, play a minor role in subthreshold antikaon production in pA reactions for kinematics of the experiment reported in [60].

$$= \sum_{\pi=\pi^+,\pi^0,\pi^-} \int_{4\pi} d\mathbf{\Omega}_\pi \int_{p_\pi^{\rm abs}}^{p_\pi^{\rm lim}(\vartheta_\pi)} p_\pi^2 dp_\pi \frac{d\sigma^{\rm (prim)}_{pA\to\pi X}(\mathbf{p}_0)}{d\mathbf{p}_\pi}$$
$$\times \frac{I_V[A, \sigma^{\rm in}_{pN}(p_0), \sigma^{\rm tot}_{\pi N}(p_\pi), \sigma^{\rm tot}_{K^-N}(p_{K^-}), \vartheta_\pi, \vartheta_{K^-}]}{I'_V[A, \sigma^{\rm in}_{pN}(p_0), \sigma^{\rm tot}_{\pi N}(p_\pi), \vartheta_\pi]}$$
$$\times \int\int P(\mathbf{p}'_t, E')d\mathbf{p}'_t dE'$$
$$\times \left[E'_{K^-} \frac{d\sigma_{\pi N\to K^-X}(\sqrt{s_1}, \mathbf{p}'_{K^-})}{d\mathbf{p}'_{K^-}}\right],$$

where

$$I_V[A, \sigma^{\rm in}_{pN}(p_0), \sigma^{\rm tot}_{\pi N}(p_\pi), \sigma^{\rm tot}_{K^-N}(p_{K^-}), \vartheta_\pi, \vartheta_{K^-}] = A^2 \int\int d\mathbf{r} d\mathbf{r}_1 \Theta(x_\parallel)\delta^{(2)}(\mathbf{x}_\perp)\rho(\mathbf{r})\rho(\mathbf{r}_1) \quad (48)$$
$$\times \exp\left[-\mu(p_0)\int_{-\infty}^{0} \rho(\mathbf{r}_1 + x'\mathbf{\Omega}_0)dx' - \mu(p_\pi)\int_0^{x_\parallel} \rho(\mathbf{r}_1 + x'\mathbf{\Omega}_\pi)dx'\right] \exp\left[-\mu(p_{K^-})\int_0^{\infty} \rho(\mathbf{r} + x'\mathbf{\Omega}_{K^-})dx'\right],$$

$$I'_V[A, \sigma^{\rm in}_{pN}(p_0), \sigma^{\rm tot}_{\pi N}(p_\pi), \vartheta_\pi] \quad (49)$$
$$= A\int \rho(\mathbf{r})d\mathbf{r} \exp\left[-\mu(p_0)\int_{-\infty}^{0} \rho(\mathbf{r} + x\mathbf{\Omega}_0)dx - \mu(p_\pi)\int_0^{\infty} \rho(\mathbf{r} + x\mathbf{\Omega}_\pi)dx\right],$$

$$\mathbf{r} - \mathbf{r}_1 = x_\parallel \mathbf{\Omega}_\pi + \mathbf{x}_\perp, \quad (50)$$
$$\mathbf{\Omega}_\pi = \mathbf{p}_\pi/p_\pi,$$
$$\cos\vartheta_\pi = \mathbf{\Omega}_0\mathbf{\Omega}_\pi, \quad \cos\vartheta_{K^-} = \mathbf{\Omega}_0\mathbf{\Omega}_{K^-};$$
$$\mu(p_\pi) = (A/2)[\sigma^{\rm tot}_{\pi p}(p_\pi) + \sigma^{\rm tot}_{\pi n}(p_\pi)],$$
$$\Theta(x_\parallel) = (x_\parallel + |x_\parallel|)/2|x_\parallel|,$$

$$E'_{K^-} \frac{d\sigma_{\pi N\to K^-X}(\sqrt{s_1}, \mathbf{p}'_{K^-})}{d\mathbf{p}'_{K^-}} \quad (51)$$
$$= \frac{Z}{A} E'_{K^-} \frac{d\sigma_{\pi p\to K^-X}(\sqrt{s_1}, \mathbf{p}'_{K^-})}{d\mathbf{p}'_{K^-}}$$
$$+ \frac{N}{A} E'_{K^-} \frac{d\sigma_{\pi n\to K^-X}(\sqrt{s_1}, \mathbf{p}'_{K^-})}{d\mathbf{p}'_{K^-}},$$

$$s_1 = (E_\pi + E'_t)^2 - (\mathbf{p}_\pi + \mathbf{p}'_t)^2, \quad (52)$$

$$E'_t = m_N - E' - C_{\rm rec}, \quad (53)$$

$$p_\pi^{\rm lim}(\vartheta_\pi) = \frac{\beta_A p_0 \cos\vartheta_\pi + (E_0 + M_A)\sqrt{\beta_A^2 - 4m_\pi^2(s_A + p_0^2\sin^2\vartheta_\pi)}}{2(s_A + p_0^2\sin^2\vartheta_\pi)}, \quad (54)$$

$$\beta_A = s_A + m_\pi^2 - M_{A+1}^2, \; s_A = (E_0 + M_A)^2 - p_0^2. \quad (55)$$

Here, $d\sigma^{\rm (prim)}_{pA\to\pi X}(\mathbf{p}_0)/d\mathbf{p}_\pi$ are the inclusive differential cross sections for pion production on nuclei from the primary proton-induced reaction channel (45); $E'_{K^-}d\sigma_{\pi p\to K^-X}/d\mathbf{p}'_{K^-}$ ($E'_{K^-}d\sigma_{\pi n\to K^-X}/d\mathbf{p}'_{K^-}$) is the in-medium inclusive invariant differential cross section for K^- production in πp (πn) collisions via the subprocess in (46); $\sigma^{\rm tot}_{\pi N}(p_\pi)$ is the total cross section of the free πN interaction; $\mathbf{p}_\pi$ and E_π are, respectively, the momentum and total energy of a pion; $p_\pi^{\rm abs}$ is the absolute threshold momentum for antikaon production on the residual nucleus by an intermediate pion ($p_\pi^{\rm abs} \approx 1.88$ GeV/c for the production of K^- mesons with a momentum of 1.28 GeV/c at a laboratory angle of 10.5°); and $p_\pi^{\rm lim}(\vartheta_\pi)$ is the kinematical limit for pion production at the laboratory angle ϑ_π from proton–nucleus collisions. The quantities $\mu(p_0)$ and $\mu(p_{K^-})$ are defined above by (23). Finally, the quantity $C_{\rm rec}$ in (53) takes properly into account the recoil energies of residual nuclei in the two-step production process ($C_{\rm rec} \approx 3$ and 16 MeV for the initial ^{9}Be target nucleus and $C_{\rm rec} \approx 0.4$ and 2 MeV for the ^{63}Cu target nucleus in the case where, in (47), use is made of uncorrelated and correlated

parts of the nucleon spectral function, respectively). The in-medium momentum $\mathbf{p}'_{K^-}$ of the antikaon produced in the secondary $\pi N \to NKK^-$ channel is related to the free momentum $\mathbf{p}_{K^-}$ by Eq. (24), in which, according to the aforesaid, one has to set $m^*_{K^-} = m_K + U^0_{K^-}$ with $U^0_{K^-} = -126$ MeV.

Because we are interested in the high-momentum parts of the pion spectra $d\sigma^{(\mathrm{prim})}_{pA\to\pi X}(\mathbf{p}_0)/d\mathbf{p}_\pi$ at forward laboratory angles, as was noted above, and since the high-momentum tails of the experimental pion spectra $d\sigma^{(\mathrm{expt})}_{pA\to\pi X}(\mathbf{p}_0)/d\mathbf{p}_\pi$ at these angles are populated mainly by the pions from first-chance pN collisions (45) [53], we will employ, in our calculations of the K^- cross sections from the two-step process (45), (46), the experimental pion yields at small angles and for high momenta. In the case of ^{9}Be and ^{63}Cu target nuclei, these yields were measured in the experiment reported in [60] at a laboratory angle of 10.5° for incident proton energies of 1.75 and 2.25 GeV and the results of measurements, with the aid of those from [74, 75], were parametrized as [in GeV mb/(GeV/c)^3][60, 76]

$$E_{\pi^+}\frac{d\sigma^{(\mathrm{expt})}_{p^9\mathrm{Be}\to\pi^+X}(\mathbf{p}_0)}{d\mathbf{p}_{\pi^+}} = 220(1-x_\mathrm{F}^R)^{3+3p_\perp^2}, \quad (56)$$

$$E_{\pi^-}\frac{d\sigma^{(\mathrm{expt})}_{p^9\mathrm{Be}\to\pi^-X}(\mathbf{p}_0)}{d\mathbf{p}_{\pi^-}} = 130(1-x_\mathrm{F}^R)^{3+5p_\perp^2};$$

$$E_{\pi^+}\frac{d\sigma^{(\mathrm{expt})}_{p^{63}\mathrm{Cu}\to\pi^+X}(\mathbf{p}_0)}{d\mathbf{p}_{\pi^+}} \quad (57)$$

$$= 3650(x_\mathrm{F}^R)^4(1-x_\mathrm{F}^R)^{2+2x_\mathrm{F}^R+3p_\perp^2},$$

$$E_{\pi^-}\frac{d\sigma^{(\mathrm{expt})}_{p^{63}\mathrm{Cu}\to\pi^-X}(\mathbf{p}_0)}{d\mathbf{p}_{\pi^-}}$$

$$= 2460(x_\mathrm{F}^R)^4(1-x_\mathrm{F}^R)^{2+2.2x_\mathrm{F}^R+5p_\perp^2},$$

where the radial scaling variable x_F^R is given by

$$x_F^R = \overset{*}{p}/\overset{*}{p}_{\max}, \quad (58)$$

$$\overset{*}{p} = \sqrt{\overset{*2}{p}_L + p_\perp^2}, \quad \overset{*}{p}_{\max} = \frac{1}{2\sqrt{s_A}}\lambda(s_A, m_\pi^2, M_{A+1}^2),$$

and $\overset{*}{p}_L$ and $p_\perp$ are the longitudinal and transverse momenta of the pion in the pA c.m. frame, respectively; and $\overset{*}{p}_{\max}$ is the maximum value of $\overset{*}{p}$ allowed by the kinematics. The quantity s_A is defined above by (55). The π^0 spectrum also needed for our calculations can be approximately expressed in terms of the $\pi^\pm$ spectra as

$$E_{\pi^0}\frac{d\sigma^{(\mathrm{expt})}_{pA\to\pi^0X}(\mathbf{p}_0)}{d\mathbf{p}_{\pi^0}} \quad (59)$$

Parameters in the approximation of the partial cross sections for the production of K^- mesons in πN collisions

Reaction	A, mb	B	i	j
$\pi^+ + n \to p + K^+ + K^-$	0.1757	0.4938	1	2
$\pi^- + p \to n + K^+ + K^-$	0.1800	0.0549	2	3
$\pi^- + p \to p + K^0 + K^-$	0.0576	0.0549	2	3
$\pi^- + n \to n + K^0 + K^-$	0.0647	0.2910	1	2

$$= \frac{1}{2}\left[E_{\pi^+}\frac{d\sigma^{(\mathrm{expt})}_{pA\to\pi^+X}(\mathbf{p}_0)}{d\mathbf{p}_{\pi^+}} + E_{\pi^-}\frac{d\sigma^{(\mathrm{expt})}_{pA\to\pi^-X}(\mathbf{p}_0)}{d\mathbf{p}_{\pi^-}}\right].$$

In our method, the Lorentz-invariant inclusive cross section for K^- production in πN collisions (46) has been described by the three-body phase-space calculations normalized to the respective "in-medium" total cross section $\sigma_{\pi N\to NKK^-}\times\left(\sqrt{s_1}, \sqrt{s^*_{1,\mathrm{thr}}}\right)$. According to [77], one has

$$E'_{K^-}\frac{d\sigma_{\pi N\to NKK^-}(\sqrt{s_1}, \mathbf{p}'_{K^-})}{d\mathbf{p}'_{K^-}} \quad (60)$$

$$= \frac{\pi}{4}\frac{\sigma_{\pi N\to NKK^-}(\sqrt{s_1}, \sqrt{s^*_{1,\mathrm{thr}}})}{I_3(s_1, m^*_{K^+}, m^*_{K^-}, m^*_N)}\frac{\lambda(s_{KN}, m^{*2}_{K^+}, m^{*2}_N)}{s_{KN}},$$

$$s_{KN} = s_1 + m^{*2}_{K^-} - 2(E_\pi + E'_t)E'_{K^-} \quad (61)$$

$$+ 2(\mathbf{p}_\pi + \mathbf{p}'_t)\mathbf{p}'_{K^-},$$

where

$$\sqrt{s^*_{1,\mathrm{thr}}} = \sqrt{s_{1,\mathrm{thr}}} + U^0_N + U^0_{K^+} + U^0_{K^-}, \quad (62)$$

where $\sqrt{s_{1,\mathrm{thr}}} = m_N + 2m_K$ is the vacuum threshold energy and the quantities I_3 and λ are defined by the (27) and (29), respectively. Like above, we assume that the "in-medium" cross section $\sigma_{\pi N\to NKK^-}(\sqrt{s_1}, \sqrt{s^*_{1,\mathrm{thr}}})$ is equivalent to the vacuum cross section $\sigma_{\pi N\to NKK^-}(\sqrt{s_1}, \sqrt{s_{1,\mathrm{thr}}})$ in which the free threshold $\sqrt{s_{1,\mathrm{thr}}}$ is replaced by the effective threshold $\sqrt{s^*_{1,\mathrm{thr}}}$ as given by (62). For the free total cross section $\sigma_{\pi N\to NKK^-}(\sqrt{s_1}, \sqrt{s_{1,\mathrm{thr}}})$, we have used the following parametrization suggested in [77]:

$$\sigma_{\pi N\to NKK^-}(\sqrt{s_1}, \sqrt{s_{1,\mathrm{thr}}}) \quad (63)$$

$$= \frac{A[(\sqrt{s_1} - \sqrt{s_{1,\mathrm{thr}}})/\mathrm{GeV}]^i}{B + [(\sqrt{s_1} - \sqrt{s_{1,\mathrm{thr}}})/\mathrm{GeV}]^j},$$

where the constants A, B, i, and j are given in the table.

In order to obtain the total cross sections for the reactions $\pi^0 p \to pK^+K^-$, $\pi^0 n \to nK^+K^-$, and

$\pi^0 n \to pK^0K^-$, where data are not available, we have employed isospin considerations. They have shown that there exist the following relations[5] between the cross sections $\sigma_{\pi N\to NKK^-}$:

$$2\sigma_{\pi^-p\to nK^+K^-} + \sigma_{\pi^-n\to nK^0K^-} + \sigma_{\pi^-p\to pK^0K^-} \tag{64}$$
$$= 2[2\sigma_{\pi^0p\to pK^+K^-} + \sigma_{\pi^0n\to pK^0K^-}],$$

$$\sigma_{\pi^0p\to pK^+K^-} = \sigma_{\pi^0n\to nK^+K^-}, \tag{65}$$

and

$$\sigma_{\pi^0n\to pK^0K^-} \approx \sigma_{\pi^-p\to nK^+K^-}. \tag{66}$$

Using (64)–(66), one gets

$$\sigma_{\pi^0p\to pK^+K^-} = \sigma_{\pi^0n\to nK^+K^-} \tag{67}$$
$$= \frac{1}{4}\left(\sigma_{\pi^-n\to nK^0K^-} + \sigma_{\pi^-p\to pK^0K^-}\right).$$

Within the representation (60), the inclusive invariant differential cross sections $E'_{K^-}d\sigma_{\pi p\to K^-X}/d\mathbf{p}'_{K^-}$ and $E'_{K^-}d\sigma_{\pi n\to K^-X}/d\mathbf{p}'_{K^-}$ for antikaon production in πp and πn interactions appearing in (51) can be written as

$$E'_{K^-}\frac{d\sigma_{\pi^+p\to K^-X}(\sqrt{s_1},\mathbf{p}'_{K^-})}{d\mathbf{p}'_{K^-}} = 0, \tag{68}$$

$$E'_{K^-}\frac{d\sigma_{\pi^+n\to K^-X}(\sqrt{s_1},\mathbf{p}'_{K^-})}{d\mathbf{p}'_{K^-}}$$
$$= E'_{K^-}\frac{d\sigma_{\pi^+n\to pK^+K^-}(\sqrt{s_1},\mathbf{p}'_{K^-})}{d\mathbf{p}'_{K^-}};$$

$$E'_{K^-}\frac{d\sigma_{\pi^0p\to K^-X}(\sqrt{s_1},\mathbf{p}'_{K^-})}{d\mathbf{p}'_{K^-}} \tag{69}$$
$$= E'_{K^-}\frac{d\sigma_{\pi^0p\to pK^+K^-}(\sqrt{s_1},\mathbf{p}'_{K^-})}{d\mathbf{p}'_{K^-}},$$

$$E'_{K^-}\frac{d\sigma_{\pi^0n\to K^-X}(\sqrt{s_1},\mathbf{p}'_{K^-})}{d\mathbf{p}'_{K^-}}$$
$$= E'_{K^-}\frac{d\sigma_{\pi^0n\to nK^+K^-}(\sqrt{s_1},\mathbf{p}'_{K^-})}{d\mathbf{p}'_{K^-}}$$
$$+ E'_{K^-}\frac{d\sigma_{\pi^0n\to pK^0K^-}(\sqrt{s_1},\mathbf{p}'_{K^-})}{d\mathbf{p}'_{K^-}};$$

$$E'_{K^-}\frac{d\sigma_{\pi^-p\to K^-X}(\sqrt{s_1},\mathbf{p}'_{K^-})}{d\mathbf{p}'_{K^-}} \tag{70}$$
$$= E'_{K^-}\frac{d\sigma_{\pi^-p\to nK^+K^-}(\sqrt{s_1},\mathbf{p}'_{K^-})}{d\mathbf{p}'_{K^-}}$$
$$+ E'_{K^-}\frac{d\sigma_{\pi^-p\to pK^0K^-}(\sqrt{s_1},\mathbf{p}'_{K^-})}{d\mathbf{p}'_{K^-}},$$

$$E'_{K^-}\frac{d\sigma_{\pi^-n\to K^-X}(\sqrt{s_1},\mathbf{p}'_{K^-})}{d\mathbf{p}'_{K^-}}$$
$$= E'_{K^-}\frac{d\sigma_{\pi^-n\to nK^0K^-}(\sqrt{s_1},\mathbf{p}'_{K^-})}{d\mathbf{p}'_{K^-}}.$$

Let us now simplify expression (47) describing the invariant differential cross section for K^- production in pA collisions via the two-step process. Considering that the main contribution to the cross section for antikaon production at forward laboratory angles comes from fast pions moving in the beam direction and that the πN total cross section $\sigma^{\rm tot}_{\pi N}$ in the energy region of interest is approximately constant with a magnitude of $\langle\sigma^{\rm tot}_{\pi N}\rangle \approx 35$ mb [52], we can recast this expression into the form

$$E_{K^-}\frac{d\sigma^{(\rm sec)}_{pA\to K^-X}(\mathbf{p}_0)}{d\mathbf{p}_{K^-}} \tag{71}$$
$$= \frac{I_V[A,\sigma^{\rm in}_{pN}(p_0),\langle\sigma^{\rm tot}_{\pi N}\rangle,\sigma^{\rm tot}_{K^-N}(p_{K^-}),0^\circ,0^\circ]}{I'_V[A,\sigma^{\rm in}_{pN}(p_0),\langle\sigma^{\rm tot}_{\pi N}\rangle,0^\circ]}$$
$$\times\sum_{\pi=\pi^+,\pi^0,\pi^-}\int\limits_{4\pi}d\mathbf{\Omega}_\pi\int\limits_{p^{\rm abs}_\pi}^{p^{\rm lim}_\pi(\vartheta_\pi)}p_\pi^2dp_\pi\frac{d\sigma^{(\rm prim)}_{pA\to\pi X}(\mathbf{p}_0)}{d\mathbf{p}_\pi}$$
$$\times\int\int P(\mathbf{p}'_t,E')d\mathbf{p}'_tdE'$$
$$\times\left[E'_{K^-}\frac{d\sigma_{\pi N\to K^-X}(\sqrt{s_1},\mathbf{p}'_{K^-})}{d\mathbf{p}'_{K^-}}\right],$$

where, according to (52),

$$s_1 = (E_\pi + E'_t)^2 - (p_\pi\mathbf{\Omega}_0 + \mathbf{p}'_t)^2. \tag{72}$$

For a nucleus of radius $R = 1.3A^{1/3}$ fm and with a uniform nucleon density, the expressions for $I_V[A,\sigma^{\rm in}_{pN}(p_0),\langle\sigma^{\rm tot}_{\pi N}\rangle,\sigma^{\rm tot}_{K^-N}(p_{K^-}),0^\circ,0^\circ]$ and $I'_V[A,\sigma^{\rm in}_{pN}(p_0),\langle\sigma^{\rm tot}_{\pi N}\rangle,0^\circ]$ are simplified to become

$$I_V[A,\sigma^{\rm in}_{pN}(p_0),\langle\sigma^{\rm tot}_{\pi N}\rangle,\sigma^{\rm tot}_{K^-N}(p_{K^-}),0^0,0^0] \tag{73}$$
$$= \frac{9A^2}{2\pi R^2(a_2-a_3)}\left[I(a_1,a_3) - I(a_1,a_2)\right],$$

$$I(a_1,a) = \frac{1}{(a_1-a)}\left\{\frac{1}{a^2}\left[1-(1+a)e^{-a}\right]\right. \tag{74}$$
$$\left. - \frac{1}{a_1^2}\left[1-(1+a_1)e^{-a_1}\right]\right\};$$

$$I'_V[A,\sigma^{\rm in}_{pN}(p_0),\langle\sigma^{\rm tot}_{\pi N}\rangle,0^\circ] = \frac{3A}{(a_3-a_2)a_2^2} \tag{75}$$

[5] It should be noted that these relations are in line with those between the cross sections $\sigma_{\pi N\to NKK^-}$ derived in [78] by employing the K^*-resonance exchange model.

$$\times\left\{1-(1+a_2)e^{-a_2}-\left(\frac{a_2}{a_3}\right)^2\left[1-(1+a_3)e^{-a_3}\right]\right\},$$

where $a_1=3\mu(p_{K^-})/2\pi R^2$, $a_2=3\mu(p_0)/2\pi R^2$, and $a_3=3A\langle\sigma_{\pi N}^{\rm tot}\rangle/2\pi R^2$. In the case of $a_1=a_2$ relevant to the kinematical conditions of the experiment reported in [60] [see (41)], the quantity $I(a_1,a_2)$ entering into (73) can be represented, in view of (74), in the simpler form

$$I(a_1,a_2=a_1)=I(a_1) \qquad (76)$$
$$=\frac{2}{a_1^3}\left[1-(1+a_1+\frac{a_1^2}{2})e^{-a_1}\right].$$

Finally, it is interesting to note that, in the case of $a_1=a_2=a_3$, which is realistic enough as well, expression (73) can be reduced to a substantially simpler form, viz.,

$$I_V[A,\sigma_{pN}^{\rm in}(p_0),\langle\sigma_{\pi N}^{\rm tot}\rangle,\sigma_{K^-N}^{\rm tot}(p_{K^-}),0^\circ,0^\circ] \qquad (77)$$
$$=\frac{9A^2}{4\pi a_1R^2}\left[3I(a_1)-e^{-a_1}\right],$$

where the quantity $I(a_1)$ is defined above by (76).

Let us now discuss the results of our calculations for antikaon production in pBe and pCu interactions in the framework of the model outlined above.

4. RESULTS AND DISCUSSION

At first, we will concentrate on the results of our calculations for the direct K^--production mechanism.

Figure 2 shows a comparison of the invariant cross section calculated by (36), (41)–(44) for the production of K^- mesons with a momentum of 1.28 GeV/c at a laboratory angle of 10.5° from the primary $pN\to NNKK^-$ channel with the data from the experiment reported in [60] for $p+{}^9\mathrm{Be}\to K^-+X$ reaction at various bombarding energies. One can see the following:

(i) Our model for the primary antikaon production process based on nucleon spectral function fails completely [especially at "low" beam energies (dash-dotted curve)] to reproduce the experimental data at subthreshold beam energies (at energies ≤ 2.99 GeV for the kinematical conditions of the experiment reported in [60]) without allowance for the influence of the corresponding nuclear mean-field potentials on the one-step production process (1).

(ii) The simultaneous inclusion of potentials for final nucleons, kaon, and antikaon (dashed curve with two dots) leads to an enhancement of the K^- yield by about a factor of 1.6 (3) at "high" ("low") incident energies as well as to a reasonable description of the experimental data, except for the four lowest data points.

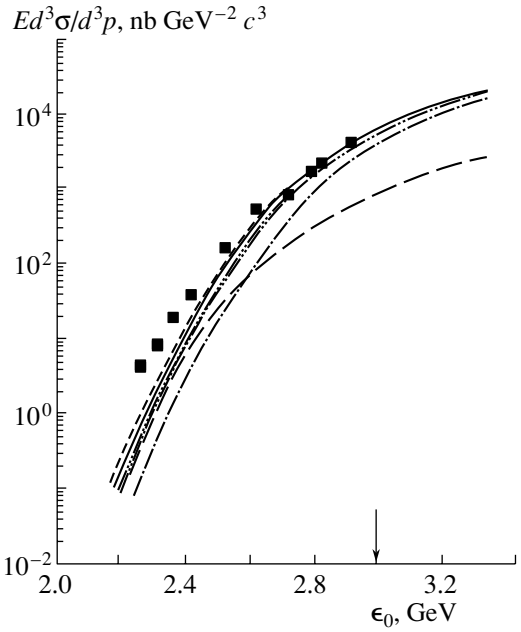

Fig. 2. Lorentz-invariant cross sections for the production of K^- mesons with a momentum of 1.28 GeV/c at the laboratory angle of 10.5° in $p+{}^9$Be reactions as functions of the laboratory kinetic energy ϵ_0 of the proton. The experimental data (full squares) were taken from [60]. The curves are our calculation with the density-dependent potentials. The dashed curves with one, two, and three dots and the solid and short-dashed curves represent the results of the calculations for the primary production process (1) with the total nucleon spectral function at $V_0=40$ MeV, $U_N(\rho_N)=0$, $U_{K^+}(\rho_N)=0$, $U_{K^-}(\rho_N)=0$; $V_0=40$ MeV, $U_N(\rho_N)=-34(\rho_N/\rho_0)$ MeV, $U_{K^+}(\rho_N)=22(\rho_N/\rho_0)$ MeV, $U_{K^-}(\rho_N)=-126(\rho_N/\rho_0)$ MeV; $V_0=40$ MeV, $U_N(\rho_N)=-34(\rho_N/\rho_0)$ MeV, $U_{K^+}(\rho_N)=0$, $U_{K^-}(\rho_N)=0$; $V_0=40$ MeV, $U_N(\rho_N)=-34(\rho_N/\rho_0)$ MeV, $U_{K^+}(\rho_N)=0$, $U_{K^-}(\rho_N)=-126(\rho_N/\rho_0)$ MeV; and $V_0=40$ MeV, $U_N(\rho_N)=-50(\rho_N/\rho_0)$ MeV, $U_{K^+}(\rho_N)=0$, $U_{K^-}(\rho_N)=0$, respectively. The long-dashed curve denotes the same as the dashed curve with two dots, but it is assumed in addition that the total nucleon spectral function is replaced by its correlated part. The arrow indicates the threshold for the reaction $pN\to NNKK^-$ occurring on a free nucleon for the kinematics under consideration.

(iii) The previous scenario is hardly distinguishable from the one employing only the attractive outgoing nucleon effective potential (dashed curve with three dots), which indicates that the simultaneous application of kaon and antikaon potentials has no effect on the K^- yield and is mainly governed by the nucleon mean-field potential.

(iv) Although the K^+ and K^- potentials are substantially different in magnitude, the effect of the K^+ potential alone (compare the solid curve and the

dashed curve with two dots) is comparable to that of the K^- potential alone (compare the solid curve and the dashed curve with three dots) and they act in opposite directions; namely, the inclusion of the K^+ or K^- potential alone results in the reduction or the enhancement of the antikaon yield by a factor of about 1.2 (1.5) at "high" ("low") beam energies, which are insufficient to describe the data in case where the antikaon potential alone is included.

(v) Our calculations including simultaneously both attractive antikaon (4), (5) and nucleon (8), (9) effective potentials (solid curve in Fig. 2) reproduce quite well the experimental data in the energy region[6] $\epsilon_0 \geq 2.4$ GeV, but they underestimate the data at lower bombarding energies, as in the cases considered above with the different scenarios for the in-medium masses of hadrons produced in the primary production process (1).[7]

(vi) The application of the effective nucleon potential (8), (10) alone (short-dashed curve) leads to a result that also gives a rather qood description of the experimental data, except for the three lowest data points, which means, in view of the aforesaid, that the determination of the K^- potential from the excitation function for "hard" antikaons appears to be difficult.

(vii) The antikaon yield from the one-step K^--production mechanism is entirely governed by the correlated part of the nucleon spectral function only in the far subthreshold energy region (at bombarding energies of $\epsilon_0 \leq 2.4$ GeV), which intimates that internal nucleon momenta greater than the Fermi momentum are needed for K^- production in the direct process (1) at the given kinematics and these beam energies.[8]

The results presented in Fig. 2 indicate, as was also noted above, that the one-step production process (1) misses the experimental data in the energy region far below the free threshold (at beam energies $\epsilon_0 \leq 2.4$ GeV) even when the influence of the nuclear density-dependent mean-field potentials (4)–(6) and (8)–(10) has been included. But K^- creation due to first-chance pN collisions (1) in this energy region occurs, as is evident from the foregoing, when incident protons collide with the short-range two-nucleon (or multinucleon) correlations inside the target nucleus, which means that the local baryon density around the spatial creation points of hadrons in these collisions can be high [54]. Therefore, the antikaon production in the far subthreshold energy region should be evaluated more likely for the density-independent potentials with depths (5) and (9) taken at normal nuclear density ρ_0 than for the density-dependent fields (4) and (8) where the local average nuclear density is involved.

The results of such calculations obtained both for the one-step (1) and for the two-step (45), (46) reaction channels, as well as the same experimental data as those presented in Fig. 2, are shown in Fig. 3. One can see the following:

(i) Our calculations for the one-step reaction channel (1) with the parameter values of $V_0 = 40$ MeV, $U_N^0 = 0$, $U_{K^+}^0 = 22$ MeV, and $U_{K^-}^0 = -126$ MeV (dash-dotted curve) underestimate substantially the data in the energy region far below the threshold, whereas the additional inclusion of the nucleon effective potential $U_N^0 = -34$ MeV (dashed curve with two dots) leads to quite a good description of the data in this energy region, which means that the K^- yield is almost totally determined by the nucleon mean-field potential (compare also the dashed curves with two and three dots in Fig. 3).

(ii) The scenario where only an attractive antikaon density-independent potential with depth $U_{K^-}^0 = -126$ MeV is used does not allow us to reproduce the data in the far subthreshold energy region (compare the thin solid curve and the dashed curve with three dots), which is in line with our findings inferred above from the analysis of the same data with the density-dependent potential.

(iii) The results of our calculations of the antikaon yield from the secondary reaction channel (46) including the influence of the different in-medium scenarios on it are significantly lower[9] than the data and calculated cross sections from the primary process (1) (dashed curves with two and three dots, thin solid curve), which implies the dominance of the one-step K^--production mechanism for antikaon production considered at all beam energies of interest.

Let us now consider subthreshold K^- production from $p + {}^{63}$Cu reactions within the above model.

Figure 4 presents invariant cross sections measured and calculated by (36) and (41)–(43) for the

[6] This counts in favor of the scenario where, for positive-charged kaons, virtually no medium modifications are needed to reproduce the data in this energy region.

[7] It should be pointed out that the use in the calculation of the K^- optical potential (6), extracted from the kaonic atomic data, instead of the potential (4), (5), leads to an increase in the "low"-energy ($\epsilon_0 \leq 2.5$ GeV) and "high"-energy ($\epsilon_0 > 2.5$ GeV) parts of the antikaon excitation function only by about 15 and 5%, respectively.

[8] Calculations show that the minimal internal nucleon momenta needed for K^- production in the primary process (1) at incident energies of 2.25, 2.30, 2.35, and 2.40 GeV corresponding to the four lowest data points in Fig. 2, respectively, are 424, 374, 331, and 291 MeV/c.

[9] For example, the two-step (thick solid curve)-to-one-step (thin solid curve) K^--production cross-section ratio is about 1/5 at "low" kinetic energies ($\epsilon_0 \approx 2.2$–2.3 GeV) and about 1/20 at "high" beam energies ($\epsilon_0 \approx 2.7$–2.9 GeV).

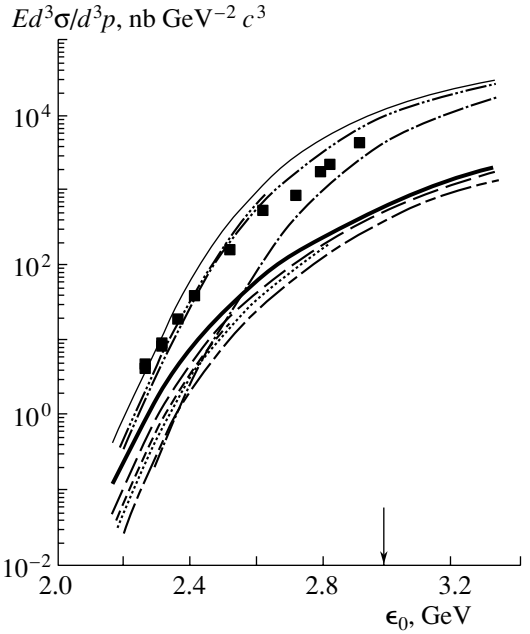

Fig. 3. Lorentz-invariant cross sections for the production of K^- mesons with a momentum of 1.28 GeV/c at a laboratory angle of 10.5° in $p + {}^9$Be reactions as functions of the laboratory kinetic energy of the proton. The experimental data (full squares) were taken from the experiment reported in [60]. The curves represent the results of our calculation with density-independent potentials. The dashed curves with one, two, and three dots and the thin solid curve correspond to the calculations for the primary production process (1) with the total nucleon spectral function at $V_0 = 40$ MeV, $U_N^0 = 0$, $U_{K^+}^0 =$ 22 MeV, and $U_{K^-}^0 = -126$ MeV; $V_0 = 40$ MeV, $U_N^0 = -34$ MeV, $U_{K^+}^0 = 22$ MeV, and $U_{K^-}^0 = -126$ MeV; $V_0 = 40$ MeV, $U_N^0 = -34$ MeV, $U_{K^+}^0 = 0$, and $U_{K^-}^0 =$ 0; and $V_0 = 40$ MeV, $U_N^0 = -34$ MeV, $U_{K^+}^0 = 0$, and $U_{K^-}^0 = -126$ MeV, respectively. The dotted, short-, and long-dashed curves show the results of the calculations by (71)–(76) for the secondary production process (46) at $U_N^0 = 0$, $U_{K^+}^0 = 0$, and $U_{K^-}^0 = 0$; $U_N^0 = 0$, $U_{K^+}^0 = 0$, and $U_{K^-}^0 = -126$ MeV; and $U_N^0 = -34$ MeV, $U_{K^+}^0 = 22$ MeV, and $U_{K^-}^0 = -126$ MeV, respectively. The curve with alternating short and long dashes and the thick solid curve represent the results of our calculations for the secondary production process (46) at $U_N^0 = 0$, $U_{K^+}^0 = 22$ MeV, and $U_{K^-}^0 = -126$ MeV and $U_N^0 = -34$ MeV, $U_{K^+}^0 = 0$, and $U_{K^-}^0 = -126$ MeV, respectively. The arrow indicates the threshold for the reaction $pN \to NNKK^-$ occurring on a free nucleon for the kinematics under consideration.

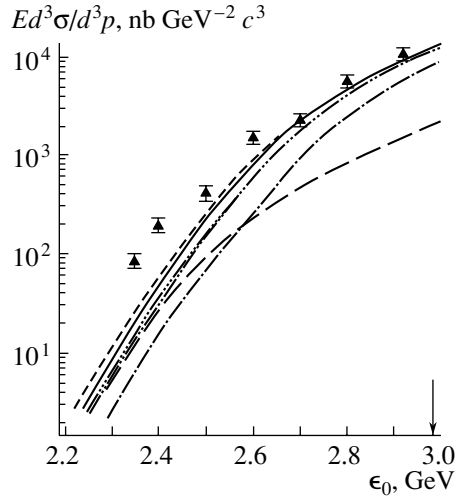

Fig. 4. Lorentz-invariant cross sections for the production of K^- mesons with a momentum of 1.28 GeV/c at a laboratory angle of 10.5° in $p + {}^{63}$Cu reactions as functions of the laboratory kinetic energy of the proton. The experimental data (full triangles) were taken from the experiment [60]. The curves represent our calculation with density-dependent potentials. The notation for the curves is identical to that in Fig. 2. The arrow indicates the threshold for the reaction $pN \to NNKK^-$ occuring on a free nucleon for the kinematics under consideration.

production of K^- mesons with a momentum of 1.28 GeV/c at a laboratory angle of 10.5° from the primary $pN \to NNKK^-$ channel in p^{63}Cu reactions at various bombarding energies. We can clearly see the following:

(i) Only a simultaneous inclusion of the attractive antikaon [(4), (5)] and nucleon [(8), (9)] effective potentials (solid curve in Fig. 4) or the application of the nucleon potential (8), (10) alone (short-dashed curve) allows us to describe rather well the experimental data, except for the two lowest data points, which is consistent with our previous findings of Fig. 2.

(ii) The use of only the attractive outgoing nucleon potential (8), (9) (dashed curve with three dots) leads to an enhancement of the K^- yield by about a factor of 2.5 (1.5) at a beam energy of 2.5 (2.9) GeV, whereas the additional inclusion of the K^- potential (4), (5) (solid curve) results in a further enlargement of the antikaon yield by a factor of about 1.5 (1.1), which indicates that the effect of the nucleon mean field is of importance for explaining experimental data on "hard" antikaon production at the incident energies considered and the influence of the K^- optical potential alone is insufficient for describing the data under consideration.

(iii) A simultaneous application of the kaon and antikaon potentials has virtually no effect on the K^- yield (compare the dashed curves with two and three dots), as in the case of K^- production on a ^{9}Be target nucleus discussed above.

(iv) The main contribution to K^- production in the far subthreshold energy region (at beam energies

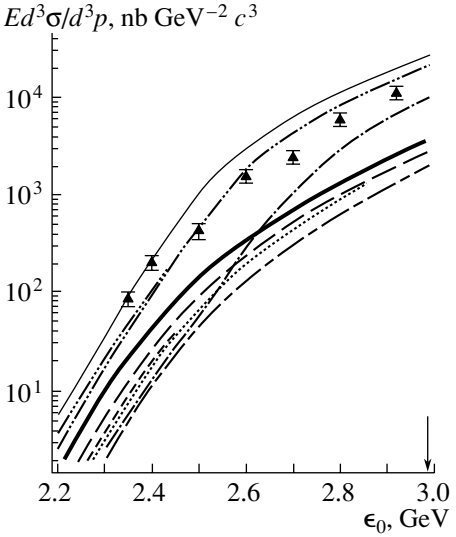

Fig. 5. Lorentz-invariant cross sections for the production of K^- mesons with a momentum of 1.28 GeV/c at a laboratory angle of 10.5° in $p + {}^{63}$Cu reactions as functions of the laboratory kinetic energy of the proton. The experimental data (full triangles) were taken from the experiment reported in [60]. The curves represent our calculation with density-independent potentials. The notation for the curves is identical to that in Fig. 3. The arrow indicates the threshold for the reaction $pN \to NNKK^-$ occuring on a free nucleon for the kinematics under consideration.

$\epsilon_0 \leq 2.4$ GeV) comes from the use in our calculations with the density-dependent mean-field potentials of only the correlated part of the nucleon spectral function (long-dashed curve), which means, in line with the conclusion drawn above from the analysis of the K^- data from p^9Be interactions, that antikaon production in this energy region should be evaluated for density-independent potentials rather than for density-dependent fields.

The results of such calculations performed for the one-step [(1)] and two-step [(45), (46)] reaction channels are given in Fig. 5, along with the same experimental data as those presented in Fig. 4. We can see the following:

(i) Our calculations for the one-step reaction channel (1) with the parameters set to the values of $V_0 = 40$ MeV, $U_N^0 = 0$, $U_{K^+}^0 = 22$ MeV, and $U_{K^-}^0 = -126$ MeV (dash-dotted curve) essentially miss the data in the energy region $\epsilon_0 \leq 2.6$ GeV, whereas the additional inclusion of the nucleon effective potential $U_N^0 = -34$ MeV (dashed curve with two dots) leads to a fairly good description of the data at 2.5- and 2.6-GeV incident, energies as well as to a much better description of the two lowest data points in relation to the previous one and to that obtained by adopting the corresponding density-dependent potentials (cf. Fig. 4).

(ii) The scenario where only attractive nucleon and antikaon density-independent potentials with depths $U_N^0 = -34$ MeV and $U_{K^-}^0 = -126$ MeV are used (thin solid curve) allows us to reproduce quite well these data points, which also counts in favor of the conclusion drawn above that, for positively charged kaons, virtually no medium modifications are needed to explain the data under consideration.

(iii) The application of only the antikaon density-independent potential with depth $U_{K^-}^0 = -126$ MeV does not allow us to describe the data at energies far below the free K^--production threshold (compare the thin solid curve and dashed curve with the three dots), and the K^- yield is mainly determined by the nucleon mean-field potential, which is in line with our findings of Figs. 2–4.

(iv) The two-step-to-one-step antikaon-creation cross-section ratio calculated with allowance for the influence of the same nuclear mean fields on hadrons produced in secondary (46) and primary (1) reaction channels (thick and thin solid curves, long-dashed curve, and dashed curve with two dots in Fig. 5) is about 1/3 and 1/10, respectively, at "low" and "high" bombarding energies, which indicates that, as in the case of a ^{9}Be target nucleus considered above (see Fig. 3), the one-step K^--production mechanism also dominates in the subthreshold "hard" antikaon production in p^{63}Cu collisions [60].

It should be emphasized that the latter is in line with the findings inferred in [53] that concern the role played by the direct K^+-production mechanism in subthreshold kaon creation in p^9Be interactions under the same kinematical conditions [54, 55, 58] as those used in the experiment reported in [60]. Therefore, the reaction $p + A \to K^- + X$ in the subthreshold regime and for "hard" kinematics along with the $p + A \to K^+ + X$ one may be recommended for experimentally studing the high-momentum components within a target nucleus.

Taking into account what was considered above, one may conclude that the determination of the K^- potential in nuclear matter from the measurements of the primary-proton-energy dependence of the double-differential cross sections for the production of "hard" antikaons on light and medium target nuclei in the subthreshold-energy regime appears to be difficult. On the other hand, the recent studies [23, 58] of subthreshold and near-threshold K^- production in pA reactions, carried out within a coupled-transport approach [23] and a simple folding model [58] based on the internal nucleon momentum distribution, indicate that the K^- potential has a strong effect on

the K^- yields at low antikaon momenta. Therefore, it is interesting to explore the sensitivity of the "soft" (low-momentum) K^- production in pA interactions at subthreshold incident energies to the medium effects considered here within the approach outlined above.

Finally, Fig. 6 shows invariant cross sections calculated according to (36)–(40) for the production of K^- mesons with a momentum of 0.4 GeV/c at a laboratory angle of 10.5° from the primary $pN \to NNKK^-$ channel in p^9Be collisions at various beam energies. In the calculations, the nucleon, kaon, and antikaon effective potentials were assumed to be density-independent. The elementary cross sections $\sigma^{\rm tot}_{K^-p}$ and $\sigma^{\rm tot}_{K^-n}$ at $p_{K^-} = 0.4$ GeV/c, needed for our calculations, were borrowed from [20, 61]. It can be seen that, in contrast to the case of "hard" antikaon production discussed above, the K^- potential has a dramatic effect on the antikaon excitation function at all subthreshold energies (compare the solid curve and the dashed curve with three dots in Fig. 6), which is nearly identical to that from the nucleon effective potential (compare the dashed curve with three dots and the long-dashed curve) in the energy range $1.6 \le \epsilon_0 \le 2.0$ GeV and even greater than the latter at $\epsilon_0 > 2.0$ GeV. While the kaon potential has a minor effect on the K^- yield at incident energies of $\epsilon_0 > 2.0$ GeV (compare the solid curve and the dashed curve with two dots), at lower beam energies, it reduces the K^--production cross section by a factor of about 2–2.5. As a result, the sensitivity to the kaon and antikaon potentials (compare the dashed-dotted and the long-dashed curves) is higher than that to the nucleon mean field at kinetic energies in excess of 2 GeV, whereas, at lower bombarding energies, the effect of the nucleon potential is dominant. It is apparent that at least the former case opens the opportunity to determine the K^- potential in nuclear matter experimentally.

Thus, our results demonstrate that measurements of the differential cross sections for subthreshold "soft" K^- production on various target nuclei will allow us to shed light on the antikaon potential in a nuclear medium. Such measurements might be conducted at, for example, the COSY accelerator using a proton beam in the COSY–ANKE detector system.

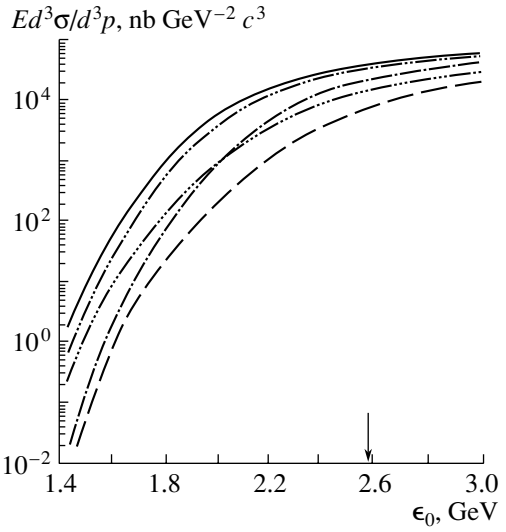

Fig. 6. Lorentz-invariant cross sections for the production of K^- mesons with a momentum of 0.4 GeV/c at a laboratory angle of 10.5° in $p + {}^9$Be reactions as functions of the laboratory kinetic energy of the proton. The long-dashed curve represents the results of the calculation for primary production process (1) with the total nucleon spectral function at $V_0 = 40$ MeV, $U^0_N = 0$, $U^0_{K^+} = 0$, and $U^0_{K^-} = 0$. The rest of the notation is identical to that in Fig. 3.

5. SUMMARY

In this study, we have presented the analysis of the first experimental data [60] on subthreshold K^- production on Be and Cu target nuclei by protons. The measured yields of K^- mesons with a momentum of 1.28 GeV/c at a laboratory angle of 10.5° from $p + {}^9$Be and $p + {}^{63}$Cu reactions in the subthreshold energy region have been compared with the results of the calculations within an appropriate folding model for incoherent primary proton–nucleon and secondary pion–nucleon production processes, which takes properly into account the struck-target nucleon momentum and removal energy distribution and novel elementary cross section for the proton–nucleon reaction channel close to the threshold, as well as nuclear mean-field potential effects on the one-step and two-step antikaon production processes. It has been shown that the effect of the nucleon mean field is of importance for explaining the considered experimental data on "hard" antikaon production, whereas the K^+ and K^- optical potentials play a minor role and the scenario with zeroth K^+ potential is favorable. It has also been found that the pion–nucleon production channel does not dominate in the subthreshold "hard" antikaon production in p^9Be and p^{63}Cu collisions under consideration and that the main contributions to the antikaon yields here come from the direct K^--production mechanism, which offers the possibility of investigating the high-momentum tail of the internal nucleon momentum distribution also via the antikaon production on light and medium target nuclei at subthreshold beam energies.

The sensitivity of subthreshold "soft" antikaon

production in p^9Be reactions to the nucleon, kaon, and antikaon effective potentials has been explored. It has been demonstrated that, in contrast to the case of "hard" antikaon production, the K^- potential has a very strong effect on the K^- yield at all subthreshold energies, which is comparable with that from the nucleon effective potential. This gives the opportunity to determine the antikaon potential experimentally. Therefore, measurements of the differential cross sections (spectra and excitation functions) for K^- production on various target nuclei at low antikaon momenta are extremely needed nowadays for obtaining deeper insight into the properties of K^- in a nuclear medium and into the relative weight of the primary and secondary reaction channels in subthreshold antikaon production, as well as into the role played by nucleon–nucleon correlations in this phenomenon.

ACKNOWLEDGMENTS

I am grateful to Yu.T. Kiselev and V.A. Sheinkman for information about experimental results from the ITEP synchrotron on subthreshold antikaon production in proton–nucleus collisions and for many valuable and inspiring discussions during the course of this work.

REFERENCES

1. W. Cassing and E. L. Bratkovskaya, Phys. Rep. **308**, 65 (1999).
2. D. B. Kaplan and A. E. Nelson, Phys. Lett. B **175**, 57 (1986).
3. G. E. Brown *et al.*, Nucl. Phys. A **567**, 937 (1994).
4. C. H. Lee *et al.*, Nucl. Phys. A **585**, 401 (1995).
5. G. E. Brown and M. Rho, Phys. Rep. **269**, 333 (1996); C. H. Lee, Phys. Rep. **275**, 255 (1996).
6. G. Mao *et al.*, nucl-th/9811021.
7. A. Bhattacharyya *et al.*, Phys. Lett. B **401**, 213 (1997).
8. J. Schaffner-Bielich *et al.*, Nucl. Phys. A **625**, 325 (1997).
9. J. Schaffner and I. N. Mishustin, Phys. Rev. C **53**, 1416 (1996).
10. E. Friedman *et al.*, Phys. Rev. C **60**, 024314 (1999).
11. M. Lutz *et al.*, Nucl. Phys. A **574**, 755 (1994).
12. M. C. Ruivo *et al.*, Nucl. Phys. A **651**, 59 (1999).
13. K. Tsushima *et al.*, Phys. Lett. B **429**, 239 (1998).
14. V. Koch, Phys. Lett. B **337**, 7 (1994).
15. T. Waas *et al.*, Phys. Lett. B **379**, 34 (1996); **365**, 12 (1996).
16. G. Q. Li *et al.*, Phys. Lett. B **329**, 149 (1994).
17. E. Friedman *et al.*, Phys. Lett. B **308**, 6 (1993); Nucl. Phys. A **579**, 518 (1994).
18. E. Friedman, Nucl. Phys. A **639**, 511c (1998).
19. T. Kishimoto, nucl-th/9910014.
20. G. Q. Li *et al.*, Nucl. Phys. A **625**, 372 (1997).
21. E. Oset and A. Ramos, Nucl. Phys. A **635**, 99 (1998); A. Ramos and E. Oset, nucl-th/9906016.
22. J. Schaffner-Bielich *et al.*, nucl-th/9907095.
23. A. Sibirtsev and W. Cassing, Nucl. Phys. A **641**, 476 (1998).
24. A. Sibirtsev and W. Cassing, nucl-th/9909024.
25. A. Sibirtsev and W. Cassing, nucl-th/9909053.
26. G. Q. Li *et al.*, Phys. Rev. Lett. **74**, 235 (1995).
27. G. Q. Li and C. M. Ko, Nucl. Phys. A **594**, 460 (1995).
28. E. L. Bratkovskaya *et al.*, Nucl. Phys. A **622**, 593 (1997).
29. G. Song *et al.*, Nucl. Phys. A **646**, 481 (1999).
30. Bao-An Li and C. M. Ko, Phys. Rev. C **54**, 3283 (1996).
31. Z. S. Wang *et al.*, Nucl. Phys. A **628**, 151 (1998).
32. Z. S. Wang *et al.*, Eur. Phys. J. A **5**, 275 (1999).
33. P. Crochet, Nucl. Phys. A **654**, 765c (1999).
34. R. Barth *et al.*, Phys. Rev. Lett. **78**, 4007 (1997).
35. P. Senger (for KaoS Collab.), Acta Phys. Pol. B **27**, 2993 (1996).
36. E. Grosse, Nucl. Phys. A **654**, 501c (1999).
37. F. Laue *et al.*, Phys. Rev. Lett. **82**, 1640 (1999).
38. A. Schröter *et al.*, Z. Phys. A **350**, 101 (1994).
39. G. Q. Li *et al.*, Phys. Rev. Lett. **79**, 5214 (1997).
40. G. E. Brown *et al.*, Nucl. Phys. A **639**, 455c (1998).
41. G. Q. Li *et al.*, Nucl. Phys. A **654**, 523c (1999).
42. W. Cassing *et al.*, Nucl. Phys. A **614**, 415 (1997).
43. V. P. Koptev *et al.*, Zh. Éksp. Teor. Fiz. **94** (11), 1 (1988) [Sov. Phys. JETP **67**, 2177 (1988)].
44. A. Shor *et al.*, Nucl. Phys. A **514**, 717 (1990).
45. W. Cassing *et al.*, Phys. Lett. B **238**, 25 (1990).
46. A. Sibirtsev and M. Büscher, Z. Phys. A **347**, 191 (1994).
47. W. Cassing *et al.*, Z. Phys. A **349**, 77 (1994).
48. A. Sibirtsev, Phys. Lett. B **359**, 29 (1995).
49. H. Müller and K. Sistemich, Z. Phys. A **344**, 197 (1992).
50. M. Debowski *et al.*, Z. Phys. A **356**, 313 (1996).
51. A. Sibirtsev *et al.*, Z. Phys. A **358**, 357 (1997).
52. S. V. Efremov and E. Ya. Paryev, Eur. Phys. J. A **1**, 99 (1998).
53. E. Ya. Paryev, Eur. Phys. J. A **5**, 307 (1999).
54. A. V. Akindinov *et al.*, Heavy Ion Phys. **4**, 325 (1996).
55. Yu. T. Kiselev *et al.*, Preprint No. 56-96, ITÉF (Inst. of Theoretical and Experimental Physics, Moscow, 1996).
56. D. Grzonka and K. Kilian, Nucl. Phys. A **639**, 569c (1998).
57. A. Badala *et al.*, Phys. Rev. Lett. **80**, 4863 (1998).
58. Yu. T. Kiselev (for FHS Collab.), J. Phys. G **25**, 381 (1999).
59. A. V. Akindinov *et al.*, Preprint No. 37-99, ITÉF (Inst. of Theoretical and Experimental Physics, Moscow, 1999).
60. A.V. Akindinov *et al.*, Preprint No. 41-99, ITÉF (Inst. of Theoretical and Experimental Physics, Moscow, 1999).
61. S. V. Efremov and E. Ya. Paryev, Z. Phys. A **348**, 217 (1994).
62. X. S. Fang *et al.*, Phys. Rev. C **49**, R608 (1994).
63. G. Q. Li and C. M. Ko, Phys. Rev. C **54**, 1897 (1996).

64. E. L. Bratkovskaya *et al.*, Eur. Phys. J. A **4**, 165 (1999).
65. F. Balestra (DISTO Collab.), Phys. Lett. B **468**, 7 (1999).
66. S. V. Efremov and E. Ya. Paryev, Yad. Fiz. **57**, 563 (1994) [Phys. At. Nucl. **57**, 532 (1994)].
67. W. Oelert, Nucl. Phys. A **639**, 13c (1998).
68. C. Gobbi *et al.*, Phys. Rev. C **50**, 1594 (1994).
69. A. Sibirtsev *et al.*, Z. Phys. A **351**, 333 (1995).
70. E. Ya. Paryev, in *Proceedings of the International Conference on Physics with GeV-Particle Beams, Jülich, Germany, 1994,* Ed. by H. Machner and K. Sistemich (World Sci., Singapore, 1995), p. 483.
71. C. Ciofi degli Atti and S. Simula, Phys. Rev. C **53**, 1689 (1996).
72. E. Ya. Paryev, Eur. Phys. J. A **7**, 127 (2000).
73. O. Benhar, S. Fantoni, and G. I. Lykasov, Eur. Phys. J. A **5**, 137 (1999).
74. E. Moeller *et al.*, Phys. Rev. C **28**, 1246 (1983).
75. J. Papp *et al.*, Phys. Rev. Lett. **34**, 601 (1975); **34**, 991 (1975).
76. Yu. T. Kiselev and V. A. Sheinkman, private communication.
77. S. V. Efremov and E. Ya. Paryev, Z. Phys. A **351**, 447 (1995).
78. A. Sibirtsev *et al.*, Z. Phys. A **358**, 101 (1997).

Physics of Atomic Nuclei, Vol. 64, No. 11, 2001, pp. 1948–1954. From Yadernaya Fizika, Vol. 64, No. 11, 2001, pp. 2033–2039.

ELEMENTARY PARTICLES AND FIELDS
Experiment

Status of an Experiment Aimed at Laboratory Searches for the Electron-Antineutrino Magnetic Moment at a Level of $\mu_\nu \leq 3 \times 10^{-12}\mu_B$*

B. S. Neganov[1)], V. N. Trofimov[1)], A. A. Yukhimchuk[2)], L. N. Bogdanova[**], A. G. Beda, and A. S. Starostin

Institute for Theoretical and Experimental Physics, Bol'shaya Cheremushkinskaya ul. 25, Moscow, 117259 Russia

Received November 11, 2000

Abstract—An experiment aimed at directly detecting antineutrino–electron scattering by using a 40-MCi tritium β-active source will make it possible to lower the present-day laboratory limit on the neutrino magnetic moment by two orders of magnitude. The experiment brings together novel unique technologies in studying rare processes of neutrino–electron scattering: (i) an artificial source of antineutrinos from tritium decay of 40-MCi activity with the antineutrino flux density of about 6×10^{14} cm^{-2} s^{-1} and (ii) new types of detectors capable of detecting electrons of energy down to about 10 eV, namely, a silicon cryogenic detector based on the ionization-into-heat conversion effect and a high-pure germanium detector with an internal signal amplification in the electric field. A compact installation located at a specially equipped underground laboratory ($\leq$100 mwe) will provide favorable background conditions for running the experiment. With a background level of about 0.1 event/(kg keV d) and detector assembly masses of 3 and 5 kg for the silicon and germanium ones, respectively, a limit of $\mu_\nu \leq 3 \times 10^{-12}\mu_B$ on the electron-antineutrino magnetic moment will be obtained within 1 to 2 years of data acquisition. The status of the experiment and the state of the art are presented. © *2001 MAIK "Nauka/Interperiodica".*

1. MOTIVATION

The possible existence of a neutrino magnetic moment μ_ν considerably exceeding the value allowed by the minimal extended standard model [1], $\mu_\nu \sim m_\nu \times 10^{-19}\mu_B$ ($\mu_B = e\hbar/2m_e$ being the Bohr magneton and m_ν (eV) being the neutrino mass), is of fundamental importance. The prospects for checking the Standard Model of electroweak interactions and searches for phenomena beyond its initial premises are motivated by at least two observations, viz., the solar-neutrino deficit and the anticorrelation of the measured neutrino flux with solar activity [2]. A large-magnetic-moment hypothesis, $\mu_\nu \sim 10^{-11}\mu_B$ [3], is so far the unique possibility of explaining the anticorrelation (if confirmed) within the standard solar model [4]. A number of extensions of the theory beyond the minimal Standard Model are proposed, where the required magnitude of μ_ν can be achieved independently of a possible neutrino mass [5, 6].

The present direct laboratory limits on the neutrino magnetic moment are derived from the measurement of $\bar{\nu}e$ scattering in reactor experiments with electron antineutrinos and are $\mu_\nu \leq (1.9–2.4) \times 10^{-10}\mu_B$ [7]. More stringent (but model-dependent) limits are found from stellar physics or cosmology, $\mu_\nu \leq (0.01–0.1) \times 10^{-10}\mu_B$ (see, e.g., [8] for an overview). These bounds were derived from astrophysical considerations against excess cooling of evolved stars, cosmological considerations for nucleosynthesis, or from SN1987A. Presently, uncertainties existing in the majority of astrophysical calculations preclude treating them as reliable constraints. This refers, in particular, to the lowest bound, $\mu_\nu \leq 0.01 \times 10^{-10}\mu_B$, derived from SN1987A. On the other hand, stellar-evolution limits have probably gone about as far as they can, with all uncertainties. Figure 1 taken from [8] shows that the globular-cluster limit of $\mu_\nu \leq 0.03 \times 10^{-10}\mu_B$ is the most restrictive one for neutrino masses m_ν below a few eV. A positive discovery of μ_ν at this level would indicate serious problems with the understanding of stellar dynamics.

In view of an ample gap between existing experimental constraints and those deduced from astrophysics, it is relevant to access the direct labora-

*This article was submitted by the authors in English.

[1)]Joint Institute for Nuclear Research, Dubna, Moscow oblast, 141980 Russia.

[2)]Russian Federal Nuclear Center, All-Russia Scientific Research Institute of Experimental Physics, Sarov, Russia.

[**]e-mail: ludmila@neron.itep.ru

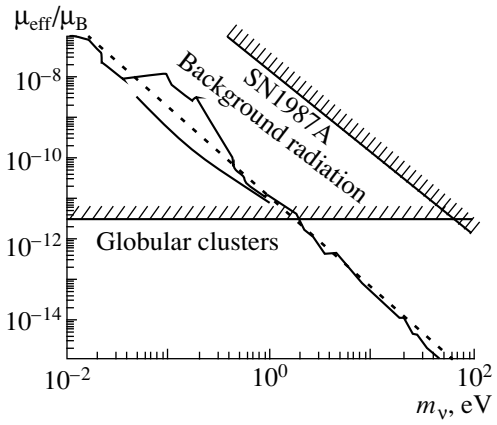

Fig. 1. Astrophysical limits on neutrino transition moments from various searches for neutrino radiative decays. The dashed line approximates their envelope (for a detailed explanation, see [8]). Of various stellar-energy-loss limits on μ_ν, the lowest globular-cluster bound is shown. For neutrino masses below a few eV, it is more restrictive than those from neutrino radiative decays.

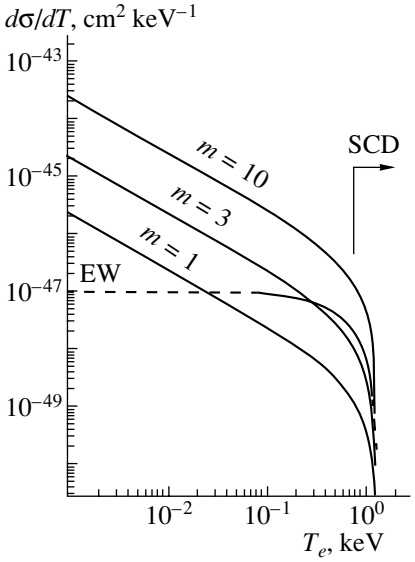

Fig. 2. Differential cross sections for $\tilde{\nu}e$ scattering with respect to the electron recoil energy for a ^{3}H emitter. The contribution from magnetic scattering is shown for $\mu_\nu = m \times 10^{-12}\mu_B$ ($m = 1, 3, 10$). The dashed line represents the standard electroweak cross section. The arrow indicates the energy threshold for existing semiconductor detectors (SCD).

tory limit on μ_ν below $10^{-11}\mu_B$. The lowest limit expected in current [9] and standing by [10] reactor experiments is $\mu_\nu \leq (0.3–0.5) \times 10^{-10}\mu_B$. The existing projects with artificial radioactive sources plan to reach the same level [11]. A forthcoming project has a goal to set a limit on the electron-neutrino magnetic moment at a level of $\mu_\nu \leq 0.03 \times 10^{-10}\mu_B$. The detection of a neutrino magnetic moment at this level would reveal the structure beyond the standard theory and would be influential in the understanding of scenarios with magnetic-field-induced spin precession in the Sun, supernovae, active galactic nuclei, or the early Universe.

2. IDEA OF THE EXPERIMENT

Laboratory measurements of μ_ν are based on the observation of the antineutrino–electron scattering. For $\mu_\nu \neq 0$, the differential cross section with respect to the kinetic energy T of the recoil electron is given by the sum of the standard-electroweak-interaction cross section (EW) and the electromagnetic one (EM). At small recoil energies, $T \ll E_\nu$ (E_ν is the neutrino energy), these two components behave in different ways: the weak part is virtually constant, while the EM one grows in proportion to $1/T$ toward lower energies, being virtually independent of E_ν (Fig. 2). Lowering the threshold for recoil-electron detection, one may choose the energy interval where the EM contribution to the cross section is larger than the EW one. This allows one to improve the sensitivity of the measurements with respect to μ_ν.

The experiment proposed in [12] exploits new unique technologies for studying rare processes of neutrino–electron scattering. These are

(i) new types of semiconductor detectors capable of detecting electrons from neutrino–electron scattering with a recoil energy in the range 10–100 eV, where the electromagnetic scattering dominates over weak scattering (Fig. 2);

(ii) an artificial tritium source (ATS) with an antineutrino flux density of about 6×10^{14}cm^{-2} s^{-1}, which can be achieved in a compact detector array (of volume 1–1.5 l) located inside a thick spherical-shell-shaped source (Fig. 3).

Working with an artificial source, one can choose an optimum ratio of effect-to-background measurement times. With a background level of about 0.1 event/(kg keV d), a limit of $\mu_\nu \leq 3 \times 10^{-12}\mu_B$ on the antineutrino magnetic moment will be obtained within 1 to 2 years of data acquisition.

3. 40-MCi TRITIUM SOURCE

The choice of tritium as a preferable source of antineutrinos for μ_ν measurements is motivated by many physical reasons, of which only a few were mentioned above (see [12, 13]). However, a 40-MCi ATS is necessary (4 kg of tritium) for ensuring the required antineutrino flux density. Presently, a significant amount of tritium has been stored owing to

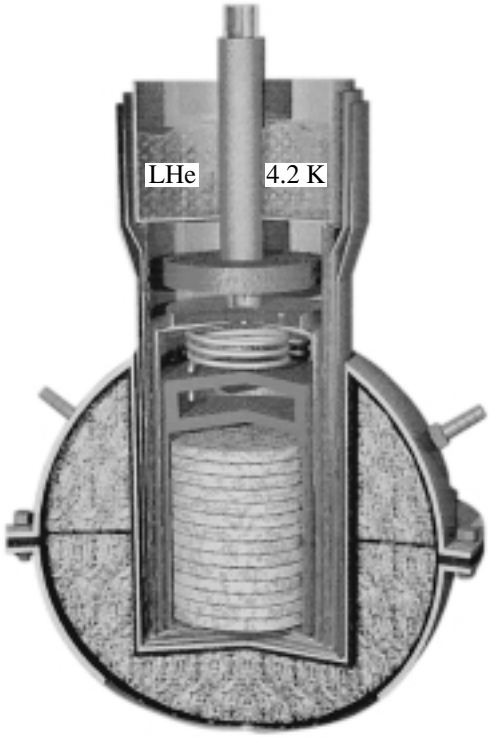

Fig. 3. Schematic arrangement of the experiment according to [12]: a semiconductor detector array of net volume 1–1.5 l is located in a cylinder-shaped cavity inside a spherical tritium source. The source activity is 40 MCi, and the diameter is 35 cm.

the reduction of nuclear weapons. The suggestion to use already available tritium for fundamental science and, specifically, for the proposed experiment [12] was recently approved in Russia. An intense tritium source is presently being developed in the Russian Federal Nuclear Center VNIIEF (formerly Arzamas-16).

The source being of extraordinary activity, its absolute safety should be provided at all stages of its life cycle (ATS saturation with tritium, its transportation, storage and exploitation during the experiment, and further utilization). Some physical, technical, and technological aspects of source designing and construction, as well as safety problems, were considered in [13].

The most important requirements for an ATS are as follows:

(i) Tritium must be chemically bound to titanium with the largest initial degree of saturation, $TiT_{1.9}$.

(ii) The construction must admit insertion of a cylinder-shaped detector array (Fig. 3).

(iii) The construction must ensure the vacuum-tightness of the inner source shell and the strength reliability 0.999999 for 6 years of source exploitation. The compensation of the pressure resulting from titanium tritide heating by tritium decay or from an accidental heating must be foreseen.

(iv) The construction must enable the extraction of radiogenic helium during ATS exploitation.

(v) The ATS must be equipped with a system for permanently monitoring the pressure and temperature and with a calorimeter, these being the sensors of the tritium state in the ATS.

Moreover, the conditions of the low-background experiment put forward specific requirements on the ATS structural materials and on the procedure for its manufacturing and maintaining.

4. ULTRALOW-THRESHOLD SEMICONDUCTOR DETECTORS

To use all the exceptional advantages of the tritium source for the measurement of the neutrino magnetic moment, novel detectors capable of recording recoil electrons at a threshold of about 10 eV are developed.

Detectors using the Neganov–Trofimov–Luke (NTL) effect [14]. Cryogenic detectors have been intensively developed recently by many groups and have reached a thermal threshold as low as 500 eV per 150–250 g of the detector mass. These detectors are used to detect recoil nuclei in the keV range that are produced by weakly interacting massive particles (WIMPs), which are regarded as the most probable dark matter (DM) candidates [15]. While being an outstanding achievement in detector technique, this result is still insufficient for the proposed tritium experiment. A radical threshold improvement for cryodetectors can be obtained through an application of the ionization-into-heat conversion phenomenon (NTL effect) observed in Si and Ge at ultralow temperatures [16]. This method can ensure a threshold for recoil electrons in the range 10–100 eV, while keeping the thermal threshold and, consequently, the calorimeter mass relatively large, say, 100 eV and 100 g, respectively. The NTL effect was successfully used in Dubna for a calorimetric measurement of light-absorption spectrum in silicon at 1 K [17] and was later observed in a large-volume silicon spectrometer [18].

Detectors with amplification. Another approach is to develop a high-purity germanium (HPGe) detector operating at 77 K with a physical amplification of ionization. Presently, germanium detectors are widely used in low-background measurements because of the high purity of germanium crystals: radioactive impurity does not exceed 10^{-14} g/g. Thresholds of 2–10 keV, being mainly determined by leakage currents and electronic and microphone noises, are too high for the experiment

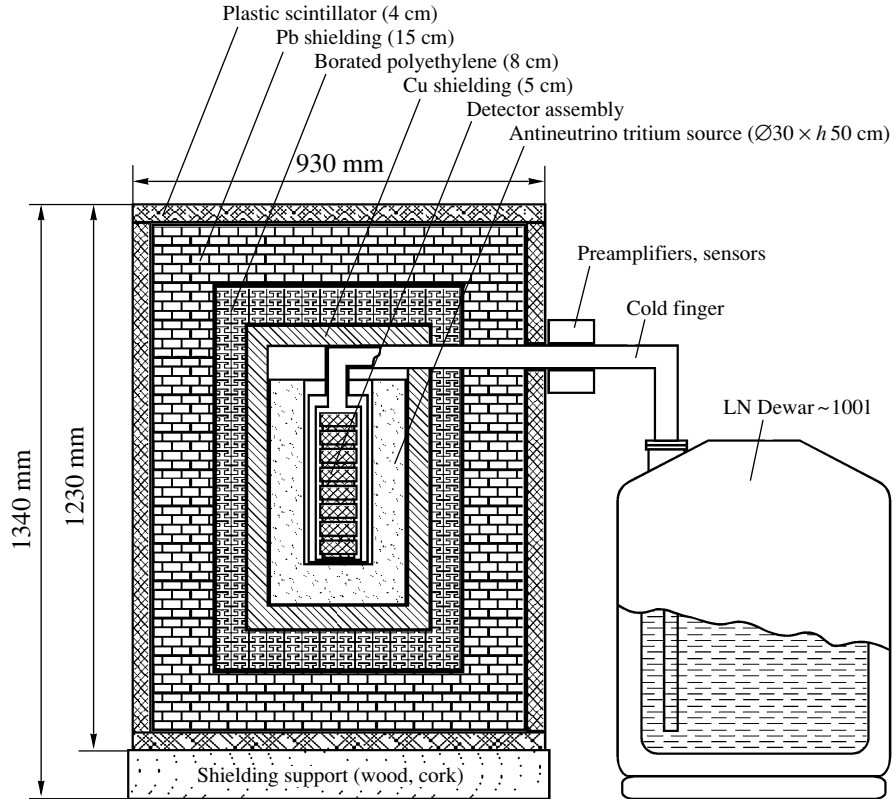

Fig. 4. Layout of the installation for μ_ν measurements with an ATS.

aimed at measuring the neutrino magnetic moment with an ATS (see Fig. 2).

Using an internal proportional amplification of the signal, one can attain an effective reduction of the germanium-detector threshold. This principle has been realized now in silicon avalanche photodiodes (APD), where the gain of about 10^2–10^4 is implemented by an avalanche multiplication of electrons in an electric field of $E_{\rm cr} = (5-6) \times 10^5$ V/cm. Such a value of $E_{\rm cr}$ is accomplished by a high concentration of impurities in a narrow junction. As a result, the sensitive volume of an APD is only a few mm^3.

Avalanche multiplication of electrons or holes in a HPGe detector of a 100-cm^3 sensitive volume can be achieved by the special configuration of the electric field due to the large difference of cathode and anode sizes [19]. Such an avalanche germanium detector (AGD) is designed similarly to a multiwire proportional chamber (MWPC). In contrast to MWPC, the electric field in AGD is determined not only by the applied voltage and electrode dimensions but also by a donor (n-type) or an acceptor (p-type) impurity concentration. The AGD threshold is governed by the magnitude of the bulk leakage current, and a threshold of $E_{\rm th} \simeq 10$ eV is expected for a planar microstrip Ge detector of a volume 100 cm^3 [19].

A prototype avalanche germanium strip detector of volume 20 cm^3 is being manufactured now.

5. EXPERIMENTAL INSTALLATION

When a more detailed consideration of the future installation units began, it was understood that an ATS of the cylinder-shell-layered shape would more adequately meet some technological requirements for its manufacture and maintenance. Calculations showed that the antineutrino flux density inside a cylinder of external diameter $D = 30$ cm is on the same order of magnitude as inside the sphere shown in Fig. 3. This allowed consideration of the future installation design for cylinder-like source geometry. The final optimization of the source dimensions can be performed as soon as the detectors' effective size is determined. Owing to the low endpoint energy of the tritium-decay spectrum ($E_0 = 8.6$ keV), no special passive shielding between the ATS and the detectors is needed: bremsstrahlung is absorbed within the source.

The spectrometer including AGD must have a mass of 4 to 5 kg; it can be manufactured from 5–7 separate modules of volume 150 cm^3, each having a mass of about 0.8 kg. Cryogenic silicon detectors of

volume 100 cm^3, mounted 14–16 on a stack, provide a net mass of about 3 kg.

The scheme of the installation is shown in Fig. 4. For shielding, a classical scheme is proposed: an air-proof 5-cm-thick container of low-background copper surrounding the source is followed by a 8-cm-thick layer of borated polyethylene and a 15-cm-thick layer of lead. An external plastic scintillator of thickness 4 cm vetoes charged cosmic-ray particles. Gaseous nitrogen circulating around the copper container removes airborne radioactivity (Rn). The cryostat cup made from low-background copper houses the detectors. The low temperature of the dilution refrigerator (for cryodetectors) (not shown in Fig. 4) or of the nitrogen Dewar (for an AGD) is transferred to the cryostat cup by a cold finger.

The construction of the shield and of the ATS support (not shown in Fig. 4) must allow access to and extraction of the tritium source.

A compact installation will be located at a specially equipped underground laboratory ($\geq$100 mwe) ensuring favorable background conditions.

Preparation of two types of detectors for recording antineutrino–electron scattering opens the possibility of simultaneously running two independent experiments with the same installation. An identical setup, but with deuterium instead of tritium, will be constructed and located in the same site nearby to measure the background. While one spectrometer measures the effect + background (data acquisition for 50% of total experiment duration proves to be optimal), the other one measures the background with its deuterium-filled twin, and vice versa. This would enable control operation of both spectrometers and would substantially increase statistics assembled throughout ATS effective functioning.

6. BACKGROUND

The main sources of background in the future experiment are environmental radioactivity, intrinsic contamination of the ATS and shielding materials, intrinsic contamination of the detector (including the cosmogenic component, especially for Si cryodetectors), airborne radioactivity (Rn), cosmic radiation, and neutrons from natural fission (α, n) reactions. Traditional and specially developed background-suppression methods will be used:

(i) operation deep underground (about 100 mwe) [the muon flux at this depth is about 2 μ/m^2 s, and the background from secondary cosmic neutrons is on the same order of magnitude as the environmental (α, n) radioactivity];

(ii) passive shielding for reducing external-radiation and neutron backgrounds;

(iii) material selection (the use of radiation-pure materials for detectors, ATS, and passive and active shielding reduces the background of the installation);

(iv) active background discrimination based on the veto and coincidence techniques (a veto with the use of a plastic scintillator discriminates charged particles passing through the detector and neutrons correlated with muon capture in the installation; anticoincidences between separate modules of the detector array suppress the radiation background);

(v) pulse-shape-analysis methods developed for suppressing microphone and electronic noises.

Monte Carlo simulations can be used to understand the structure of the background with the aim of reducing it. The quality of computer-intense modeling depends on a detailed knowledge of experimental geometry, location of characteristic backgrounds, and a complete implementation of all physical processes involved. In the experiment studying neutrino–electron scattering, the background to single-electron events—i.e., recoil electrons with $E \leq 1000$ eV—comes mainly from the photons with energy $E \leq 1000$ eV, Compton electrons with $E_e \leq 1000$ eV, electromagnetic scattering of neutrons on electrons, and nuclear recoils from neutron–nucleus scattering.

The radiation background in semiconductor detectors, which plays a decisive role in the future experiment, has been well studied for the region above 2 keV in dark-matter searches [20]. The lowest measured background was 0.08 event/(kg keV d) for Ge detectors [15]. For Si detectors, the radiation background is somewhat larger.

Since technologies available now allow one to obtain tritium of extremely high degree of purification, the main attention should be paid to titanium chosen as a tritium carrier in the ATS. Monte Carlo calculations of the background due to Ti radioactive contamination by the U–Th chain and ^{40}K were performed. This component should not exceed a value of about 0.1 event/(kg keV d). Then, the allowed level of Ti radioactive contamination proved to be $\leq 10^{-10}$ g/g. Industrial titanium is of purity about 10^{-9}–10^{-8} g/g. Therefore, special efforts are needed to ensure its required radioactive purity.

As to the correlated background, we note that tritium antineutrino coherent scattering off nuclei is insignificant, producing nuclear recoils of a fraction of eV.

7. EXPECTED RESULTS

The expected per day numbers of antineutrino–electron magnetic-scattering events for two values of μ_ν (effect) and of weak-scattering events are shown in the table for two energy intervals of recoil-electron detection. The antineutrino flux density was taken to be about 6×10^{14} cm^{-2} s^{-1}, and the detector mass was 5 kg. In the calculations, the electron binding in the atom was taken into account [21]. For a more detailed consideration, effects of atom binding in the crystal must be included. The numbers of background events were calculated under the assumption that the background level is 0.1 event/(kg keV d).

It can clearly be seen from the table that, at low threshold, the number of expected events changes insignificantly when the effect is observed for 10–200 eV region in relation to the total recoil energy range 10–1260 eV. At the same time, narrowing energy range of recoil-electron detection to 10–200 eV reduces both noncorrelated and correlated background (weak interaction contribution) noticeably. Of course, the assumption about the uniform background below 1 keV should be carefully checked, which is the primary task in such measurements.

The sensitivity of the experiment to the neutrino magnetic moment can be determined by using the data from the table. Under the assumption that the total duration of the measurements is 400 days (200 days with an ATS and 200 days of background measurements), the achievable limits are $\mu_\nu \leq 2.5 \times 10^{-12}\mu_\mathrm{B}$ for the energy interval 10–1260 eV and $\mu_\nu \leq 2.2 \times 10^{-12}\mu_\mathrm{B}$ for 10–200 eV at a 95% C.L.

Number of $\bar{\nu}e$ magnetic- and weak-scattering events (N_M and N_W, respectively) and background (B.g.) expected per day for various energy intervals of detected recoil electrons

Energy interval, eV	N_M		N_W	B.g.
	$\mu_\nu = 1 \times 10^{-11}\mu_\mathrm{B}$	$\mu_\nu = 3 \times 10^{-12}\mu_\mathrm{B}$		
10–200	1.4	0.13	0.04	0.1
10–1260	2.4	0.22	0.15	0.5

8. STATUS AND CONCLUSIONS

The Program "Measurement of the Neutrino Magnetic Moment at a Level of $\mu_\nu \leq (1-3) \times 10^{-12}\mu_\mathrm{B}$" was approved by the Ministry for Atomic Energy of the Russian Federation (Minatom). R&D on the ATS, two types of detectors, and all relevant problems have begun in JINR, ITEP, and RFNC VNIIEF.

An experimental study of neutrino properties and interactions with matter is a challenge for low-energy physics. The discovery of a neutrino magnetic moment at a level of $\mu_\nu \leq 3 \times 10^{-12}\mu_\mathrm{B}$ would indicate physics beyond the Standard Model of electroweak interactions and would radically change the modern astrophysical scenario. In particular, these results would impact our understanding of the observed variations of the solar-neutrino flux. The novel detector technologies developed for this experiment can be further considered for other elementary-particle-physics research (dark-matter search, neutrino coherent scattering on nuclei, solar-neutrino measurements) and for other fields of fundamental and applied physics requiring detection of low-energy particles.

ACKNOWLEDGMENTS

We appreciate enlightening discussions with Prof. V.G. Zinov and especially his suggestion concerning the ATS shape. We are also grateful to E.V. Demidova and M.G. Gavrilov for assistance in the calculations.

This work was performed under the contract 66.04.19.19.00.802 with the Department of Atomic Science and Technology of Minatom.

REFERENCES

1. B. W. Lee and R. Shrock, Phys. Rev. D **16**, 1444 (1977); K. Fujikawa and R. Shrock, Phys. Rev. Lett. **45**, 963 (1980).
2. R. Davis, B. T. Cleveland, and J. K. Rowley, in *Proceedings of 2nd International Symposium "Underground Physics 87"* (Nauka, Moscow, 1988); P. Vogel and J. Engel, Phys. Rev. D **39**, 3378 (1989); D. S. Oakley *et al.*, Astrophys. J. Lett. **437**, L63 (1994).
3. M. B. Voloshin, M. I. Vysotsky, and L. B. Okun', Zh. Éksp. Teor. Fiz. **91**, 754 (1986) [Sov. Phys. JETP **64**, 446 (1986)].
4. J. N. Bahcall and R. Ulrich, Rev. Mod. Phys. **60**, 297 (1988).
5. M. Fukugita and T. Yanagida, Phys. Rev. Lett. **58**, 1807 (1987).
6. M. B. Voloshin, Yad. Fiz. **48**, 804 (1988) [Sov. J. Nucl. Phys. **48**, 512 (1988)].
7. F. Reines, H. S. Gurr, and H. W. Sobel, Phys. Rev. Lett. **37**, 315 (1976); G. S. Vidyakin, V. N. Vyrodov, I. I. Gurevich, *et al.*, Pis'ma Zh. Éksp. Teor. Fiz. **55**, 212 (1992) [JETP Lett. **55**, 206 (1992)]; A. I. Derbin *et al.,* Pis'ma Zh. Éksp. Teor. Fiz. **57**, 755 (1993) [JETP Lett. **57**, 768 (1993)].
8. G. G. Raffelt, Phys. Rep. **320**, 319 (1999).

9. R. Amsler *et al.*, Nucl. Instrum. Methods Phys. Res. A **396**, 115 (1997); M. Moretti, C. Broggini, and G. Fiorentini, Phys. Rev. D **57**, 4160 (1998); C. Broggini, Nucl. Phys. B (Proc. Suppl.) **70**, 188 (1999).
10. A. G. Beda, E. V. Demidova, A. S. Starostin, and M. B. Voloshin, Yad. Fiz. **61**, 72 (1998) [Phys. At. Nucl. **61**, 66 (1998)].
11. A. V. Davydov and Yu. N. Isaev, Yad. Fiz. **59**, 486 (1996) [Phys. At. Nucl. **59**, 459 (1996)]; A. V. Golubchikov, O. A. Zaimidoroga, O. Yu. Smirnov, and A. P. Sotnikov, Yad. Fiz. **59**, 1989 (1996) [Phys. At. Nucl. **59**, 1916 (1996)]; V. N. Kornoukhov, Yad. Fiz. **60**, 639 (1997) [Phys. At. Nucl. **60**, 558 (1997)]; I. R. Barabanov *et al.*, Astropart. Phys. **8**, 67 (1997); B. P. Bergelson, A. V. Davydov, Yu. N. Isaev, and V. N. Kornoukhov, Yad. Fiz. **61**, 1347 (1998) [Phys. At. Nucl. **61**, 1245 (1998)]; O. G. Miranda, V. Semikoz, and J. W. F. Valle, Phys. Rev. D **58**, 013007 (1998).
12. V. N. Trofimov, B. S. Neganov, and A. A. Yukhimchuk, Yad. Fiz. **61**, 1373 (1998) [Phys. At. Nucl. **61**, 1271 (1998)].
13. B. S. Neganov, V. N. Trofimov, A. A. Yukhimchuk, and L. N. Bogdanova, Yad. Fiz. **64**, 308 (2001) [Phys. At. Nucl. **64**, 261 (2001)].
14. B. S. Neganov and V. N. Trofimov, USSR Patent No. 1037771; Otkrytiya Izobret. **146**, 215 (1985); P. N. Luke, J. Appl. Phys. **64**, 6858 (1988).
15. B. Cabrera, Nucl. Instrum. Methods Phys. Res. A **370**, 150 (1996); T. Shutt, D. S. Akerib, *et al.*, Nucl. Phys. B (Proc. Suppl.) **51**, 318 (1996); S. Cooper *et al.,* Proposal to the Gran Sasso Laboratory for a Dark Matter Search Using Cryogenic Detectors, MPI-PhE/93-29, Nov. 1993.
16. B. Neganov, V. Trofimov, and V. Stepankin, J. Low Temp. Phys. **93**, 745 (1993).
17. B. Neganov, V. Trofimov, and V. Stepankin, J. Low Temp. Phys. **93**, 417 (1993).
18. V. N. Trofimov, Nucl. Instrum. Methods Phys. Res. A **370**, 168 (1996).
19. A. S. Starostin and A. G. Beda, Yad. Fiz. **63**, 1370 (2000) [Phys. At. Nucl. **63**, 1297 (2000)]; hep-ex/0002063.
20. D. S. Akerib *et al.*, Nucl. Phys. B (Proc. Suppl.) **70**, 64 (1999).
21. V. I. Kopeikin, L. A. Mikaelyan, V. V. Sinev, and S. A. Fayans, Yad. Fiz. **60**, 2032 (1997) [Phys. At. Nucl. **60**, 1859 (1997)].

Physics of Atomic Nuclei, Vol. 64, No. 11, 2001, pp. 1955–1960. Translated from Yadernaya Fizika, Vol. 64, No. 11, 2001, pp. 2040–2045.

ELEMENTARY PARTICLES AND FIELDS
Experiment

Experimental Value of G_A/G_V from a Measurement of Both P-Odd Correlations in Free-Neutron Decay

Yu. A. Mostovoi[1)], I. A. Kuznetsov[2)], V. A. Solovei[2)], A. P. Serebrov[2)], I. V. Stepanenko[2)], T. K. Baranova[2)], A. V. Vasiliev[2)], Yu. P. Rudnev[2)], B. G. Yerozolimsky[3)], M. S. Dewey[4)], F. Wietfeldt[4)], O. Zimmer[5)], and V. V. Nesvizhevsky[5)]

Received May 23, 2000; in final form, September 7, 2000

Abstract—A new experimental value of the fundamental weak-interaction parameter $\lambda = G_A/G_V$ (-1.2686 ± 0.0046) is obtained for the first time by an original method that consists in measuring both P-odd correlations in free-neutron decay. © *2001 MAIK "Nauka/Interperiodica".*

1. INTRODUCTION

The ratio of the axial-vector and vector constants of weak interaction, $\lambda = G_A/G_V$, is a fundamental parameter of the theory. Usually, it is determined from data on the neutron lifetime or on the coefficient A of correlation between the electron-emission and the neutron-spin direction. Either method requires additional data, the value of G_V from $0^+ \leftrightarrow 0^+$ transitions in the first case and the degree of neutron polarization in the second case.

In order to determine λ, we used the measurement of two P-odd correlations, $A(e, s)$ and $B(\nu, s)$, for the outgoing electron and antineutrino, respectively. The quantities λ, A, and B are related by the simple equation $\lambda = (A - B)/(A + B)$. Its form allows one to replace A and B by the actually measured products of these quantities and the neutron polarization S; that is,

$$\lambda = \frac{A - B}{A + B} \equiv \frac{SA - SB}{SA + SB}. \qquad (1)$$

Owing to this, it is not necessary to measure the beam polarization if it has the same value in both measurements.

The error in determining λ by this method is

$$\Delta\lambda = \frac{2SA \times SB}{(SA + SB)^2} \qquad (2)$$

$$\times \sqrt{\left(\frac{\Delta SA}{SA}\right)^2 + \left(\frac{\Delta SB}{SB}\right)^2}.$$

It follows that the error of $\Delta\lambda \sim \pm 0.0055$ can be achieved if $\Delta SA/SA$ and $\Delta SB/(SB)$ have been determined with the same relative error of about 1.5%. The P-odd nature of the correlations in question makes it possible to attain such an accuracy without precision spectroscopy owing to the relative character of measurement of the experimental asymmetry $X = (N^\uparrow - N^\downarrow)/(N^\uparrow + N^\downarrow)$ by the change in the counting rate for decay events in response to polarization reversal ($N^\uparrow$ versus $N^\downarrow$) under invariable conditions of decay-product detection.

2. EXPERIMENTAL PROCEDURE

This experiment is based on the procedure developed in measuring the correlations A [1–3] and B [4, 5]. Experience gained in combining measurements under conditions of the same experiment is summarized in [6]. This article reports on the latest technical upgrade of the setup and on the eventual result of the measurements of $\lambda = G_A/G_V$ in the PF1 beam from the reactor installed at the Laue–Langevin Institute (Grenoble, France) in 2000.

The layout of the setup is shown in the figure. The coincidence of the emergence of the decay electron and the emergence of the recoil proton was traced in the experiment. The electron energy and the time of proton delay were recorded. For this purpose, we used an electron detector (*2*) based on a plastic scintillator ($\varnothing = 75$ mm) and a proton detector (*3*) based on two microchannel plates ($\varnothing = 70$ mm).

A verification of the linearity of the scale of our electron-energy measurement and a determination of the energy of the reference source were performed

[1)]Russian Research Centre Kurchatov Institute, pl. Kurchatova 1, Moscow, 123182 Russia.
[2)]Petersburg Nuclear Physics Institute, Russian Academy of Sciences, Gatchina, 188350 Russia.
[3)]Harvard University, Cambridge, MA 02138, USA.
[4)]National Institute of Standards and Technology, Gaithersburg, MD 20899, USA.
[5)]Laue–Langevin Institute, 38042 Grenoble, France.

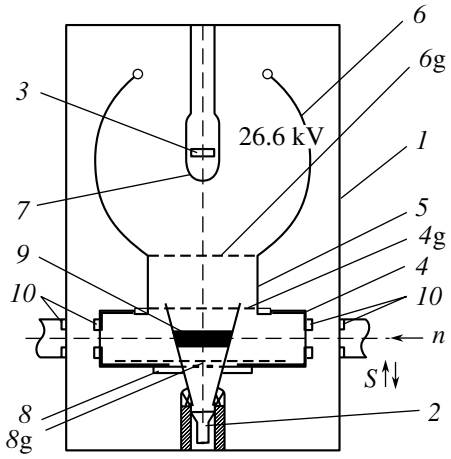

Layout of the setup used: (*1*) vacuum chamber, (*2*) electron detector, (*3*) proton detector, (*4*) electrode of the neutron-beam flight, (*4g*) grid, (*5*) time-of-flight electrode, (*6*) spherical electrode, (*6g*) grid, (*7*) spherical grid, (*8*) electron collimator, (*8g*) grid, (*9*) decay region, and (*10*) lithium collimators.

with the aid of a magnetic spectrometer by relying on the conversion lines of ^{198}Au, the relevant accuracy being about 1%. Thus, the accuracy in calibrating the energy of recorded electrons was determined completely by the electron-detector energy resolution dE/E, which was about 25% at $E = 200$ keV.

The detectors were placed opposite each other on the two sides of the neutron beam. The beam region (*9*) where decay events were recorded was separated by a collimator (*8*) arranged between the beam and the electron detector. Emphasis on decay-electron recording ensured an unaltered determination of the decay region in the measurements of SA and SB, because it was independent of the conditions of proton recording.

Protons that had passed through the time-of-flight electrode (*5*) and the grid labeled with the symbol *6*g in the figure were focused onto the detector by the electric field of a quasispherical capacitor formed by two electrodes (*6*, *7*). The diameter of the focusing-system inlet window, covered with the grid *6*g, was 260 mm. An experimental test showed that, at a voltage of 26.6 kV, all protons that had passed through this window were collected at the detector within a spot of diameter less than 50 mm.

In the requirements on the flight base, which determines the proton delay time, there is a contradiction between the measurements of SA and SB. In order to ensure optimal conditions in both measurements, the setup was designed in such a way that the focusing system, together with the proton detector, could be movable. This made it possible to change the length of the time-of-flight electrode, without breaking a vacuum, from 35 mm in measuring SA to 145 mm in measuring SB.

In measuring SA, the coincidence of the electron and the recoil proton was used only to separate the decay electron. In this case, a loss of protons would lead to a methodological error. The removal of all protons from the decay region (*9*) and their transfer to the detector *3* was ensured by a voltage of 2 kV applied between the grids *4*g and *8*g. That there were no impediments associated with the electrode *5* at the length of 35 mm was checked by consequently shutting off the paths of protons punching through the grids *6*g and *7*g. This showed that, to within fractions of a percent, there were no trajectories passing through 15% of the grid area at the grid periphery.

In measuring SB, it was impossible to determine directly the antineutrino momentum, but it could be calculated for any electron energy E_e on the basis of the recoil-proton momentum and its projection onto the electron momentum. This enabled us to measure the (ν, s) asymmetry by analyzing changes in the shape of the proton-delay spectrum in response to polarization reversal. The observed shape of this spectrum is governed by the position of the electrode *5*, its flight-base length, which was equal to 145 mm, ensuring the required accuracy of the analysis of proton delay time.

The emission of the photon accompanying neutron decay can distort such an analysis, but the degree of distortion in a particular experiment depends on the conditions under which decay events are recorded. The calculation performed in [7] showed that the role of photon emission is negligible in our case.

The vacuum chamber used was surrounded by three pairs of current loops that induced the guiding magnetic field of 4×10^{-4} T and ensured the compensation of the Earth's field to a value not higher than 3×10^{-6} T. The radio-frequency flipper was switched on and off to reverse polarization. The sign of the guiding field was changed periodically to suppress the possible uncertainty associated with the calculation of the contribution of the $a(e, \nu)$ correlation of the outgoing antineutrino and electron and the uncertainty associated with effects that could be caused by an asymmetry in flipper operation.

3. STRUCTURE OF AMPLITUDE–TIME MEASUREMENTS

Information about the recorded coincidences of signals from the electron and proton detectors was accumulated as two-dimensional $[E_i, t_k]$ matrices $[(i = 1{-}64) \times (t = 1{-}256)]$ for the electron energy E and the proton delay time t. In the run of 1998 [6], data accumulation was implemented in the CAMAC

standard. A radically new measuring system with sorting performed directly by a computer was used in the latest measurements. This system employs the VME standard [8]. It has two parallel event-recording channels (the electron and the proton one) synchronized by a unified time scale. Time measurement by counting quartz-generator signals ensured, to a high degree, invariability of the scale-division unit of the time channel and enabled us to fix the proton-delay time with a precision of about 15 ns.

For each event, the system forms a single "word" that carries, in a coded form, information about the time of pulse arrival, the pulse amplitude, and the flipper state and records this word in one of the two buffers of the crate buffer memory, which are used alternately within a 0.4-s cycle. While event accumulation proceeds in one buffer, the data accumulated in the other buffer over the preceding 0.4-s cycle are transferred to the computer, processed, and summarized in its long-time memory in the form of four $[E, t]$ matrices, whereupon this buffer is cleared for a new cycle.

For the usual proton-delay time, the coincidence of events for the two flipper states were sorted in the first pair of matrices. Events accumulated there consisted of true neutron-decay events and random coincidences caused by loads of the electron and the proton channel. The second pair of matrices accumulated only random coincidences. For this, the same channel loads were sorted under the condition of an additional delay organized in the proton channel in order to remove correlated events from the coincidence range. The remaining counts were due only to random coincidences at the unchanged load of the electron and the proton channel.

The difference of the event and the background matrix separates neutron-decay events, while their sum makes it possible to determine the statistical error of the calculation. The sum of the matrices corresponding to the two flipper states yielded the matrix of the unpolarized experimental spectrum.

In measuring SA and SB, this system was adopted without any changes. The measurements of SA and SB were based on 865000 and 375000 decay events, respectively. Sixteen sets of measurements were performed for the SA–SB pair. The energy scale was calibrated by using a reference electron source for each set of measurements of SA and SB.

4. COMPUTER MODEL OF THE EXPERIMENT

In order to calculate the sought correlations, it is necessary to know the mean values of the relative electron velocity and of the cosines of the angles of emission of the neutron-decay products. They were calculated by means of a Monte Carlo code that was developed for a beta-decay simulation and which was successfully used in the experiment reported in [5]. The model took into account all necessary geometric parameters, the decay-electron spectrum in the form of the Fermi function, the response functions of the electron and the proton detector, the properties of the amplitude analyzer and of the time-to-code converter, and the calculated map of the field between the electrodes *6* and *7*. In order to process the results of the measurement of SA, a calculation of proton acceleration in the field between the grids *4*g and *8*g was included in the code.

The results of the simulation were represented in the form of four matrices in terms of the same coordinates i and k as those used in the experimental matrices. One of the matrices contained the calculated two-dimensional spectrum for an unpolarized beam, while the other three matrices contained the accumulated sums of the values of $\cos\theta_\nu$, $v/c \times \cos\theta_e$, and $v/c \times \cos\theta_{e,\nu}$. These data made it possible to obtain the required mean values for any chosen part of the matrix.

A comparison of the experimental and calculated spectra was performed with the aid of a special code that scanned all experimental spectra in order to choose the required intervals of the energy and time channels, calculated the sum of the matrices corresponding to the two flipper states in these channels, selected the same channels in the calculated two-dimensional spectrum for an unpolarized beam, compared the matched spectra in the normalized form, and calculated the SB value for them.

In processing the results of the measurements of SB, the matching of the matrices obtained from the experiment and from the simulation is the most delicate procedure, which is based on the analysis of the time-spectrum shape.

5. CALCULATIONS OF SA AND SB

Coincidences for calculating SA were selected by summing events in the interval extending from the 16th to the 56th energy channel and corresponding to events associated with an electron energy of 200 to 800 keV and in the interval from the 67th to the 88th time channel, where there was a peak of neutron-decay events. The delay of the decay proton ruled out the background of instantaneous coincidences caused by recording cascade photons and rescattered electrons. The resulting values of $(N \pm \Delta N)^{\uparrow}$ and $(N \pm \Delta N)^{\downarrow}$ were used to calculate the relative variation in the counting of decay events and its statistical error $(X \pm \Delta X)$ for each of 16 sets of measurements.

The product SA and the statistical error in it are related to $X \pm \Delta X$ by the equation

$$SA \pm \Delta SA = \frac{X \pm \Delta X}{\langle v/c \times \cos\theta_e \rangle}, \qquad (3)$$

where $\langle v/c \times \cos\theta_e \rangle$ is the mean value of the product of the relative electron velocity and the cosine of its emission angle. This mean value was calculated from the lower energy threshold of electron detection on the basis of the energy-scale calibration by a reference source. The calibration accuracy was about 0.5 of a channel for the maximum of the source peak in the 46th or 47th channel.

At 200 keV, $\langle v/c \times \cos\theta_e \rangle$ was equal to 0.806 ± 0.001. The error was determined from the variation of $\langle v/c \times \cos\theta_e \rangle$ in response to the variation of the energy boundary of the 16th channel within the calibration accuracy. The precision of SA measurement by this procedure was $\pm 0.12\%$. Its sign tended to be random in some sets; therefore, the error is four times less over 16 sets.

Two corrections were introduced in calculating SA. The experimental correction took into account a 0.6% reduction of the (e, s) correlation because of recording decay electrons scattered in the chamber. It was measured to within 10% with aid of the reference source by using the number of counts for the fraction of its electrons hitting the detector as the result of scattering in the chamber. The methodological uncertainty in SA from the introduction of this correction is $\pm 0.06\%$.

The theoretical correction took into account the mimicking of (e, s) asymmetry due to the weak-magnetism effect and the G_A–G_V interference. This correction was calculated on the basis of the formulas for A from [9]; the result is 0.012. To correct SA for it, this correction should be multiplied by the degree S of neutron polarization, but the resulting correction to the correction appears to be negligible (about 0.00007) because of the smallness of the theoretical correction itself.

The weighted mean value over 16 individual measurements of SA was $SA = -0.1097 \pm 0.0016$, the distribution of their results being normal with standard deviation $\sigma = \pm 0.0014$. The total methodological uncertainty associated with the determination of the energy of the 16th channel and with taking into account electron scattering in the chamber is $\delta SA/SA \sim 0.09\%$.

In measuring SB, the relative change X in counting depends simultaneously on three correlations, SA, SB, and a:

$$X = \frac{SB\langle \cos\theta_\nu \rangle + SA\langle v/c \times \cos\theta_e \rangle}{1 \pm a\langle v/c \times \cos\theta_{e\nu} \rangle}. \qquad (4)$$

We used the value of -0.1097 ± 0.0016 for SA and the value of -0.1017 ± 0.0051 for a, which were obtained in the present experiment and in [10], respectively. The error in a allows one to calculate the contribution of the correlation to a precision higher than 0.4%. The symbol $\pm$ indicates the change in the relative sign of the contributions to X from the even correlation a and the odd correlations SA and SB upon the reversal of the direction of the guiding magnetic field.

The sought asymmetry SB and the statistical error in it were found for each $[E_i, t_k]$ cell of the experimental and calculated matrices from relative variations in counting decay events, $(X \pm \Delta X)_{i,k}$:

$$(SB \pm \Delta SB)_{i,k} = \frac{(X \pm \Delta X)_{i,k} \times (1 \pm a\langle v/c \times \cos\theta_{e\nu} \rangle_{i,k}) - SA\langle v/c \times \cos\theta_e \rangle_{i,k}}{\langle \cos\theta_\nu \rangle_{i,k}}. \qquad (5)$$

After that, these values were averaged over the selected intervals of the energy and time channels. The uncertainty in matching the experimental and calculated matrices determines the methodological uncertainty of this procedure. Three individual features of the experimental time-coincidence spectra made it possible to control it.

First, the peak of instantaneous correlated coincidences determined the position of the absolute time zero to a precision of 1.5 channels.

Second, the delay of the arrival of the fastest protons is virtually independent of the electron energy, since it is determined by the sum of the electron and the antineutrino momentum. The value of this delay enabled us to measure directly the length of the flight base, a basic geometric parameter that controls the shape of the time spectrum.

Finally, the width of the time-delay spectrum of decay protons is extremely sensitive to the actual value of the decay-electron energy, because it is determined by the difference of the electron and the antineutrino momentum. For example, a transition from $E = 340$ keV to $E = 511$ keV changes the width by a factor of 2, from 80 to 40 channels. This allowed one to verify the correctness of the energy-scale division chosen on the basis of the identity of matching the calculated and measured time spectra in various regions of the energy spectrum and used in the calculation.

A constant value of the asymmetry SB within

Table

	1	2	3	4	5	6	7	8
λ	−1.2959	−1.2927	−0.2731	−1.2595	−1.2396	−1.2567	−1.2969	−1.2839
$\Delta\lambda$	0.0235	0.0196	0.0189	0.0211	0.0177	0.0188	0.0171	0.0169
	9	10	11	12	13	14	15	16
λ	−1.2800	−1.2659	−0.2813	−1.2451	−1.2484	−1.2567	−1.2870	−1.2658
$\Delta\lambda$	0.0186	0.0187	0.0187	0.0163	0.0200	0.0144	0.0203	0.0181

the statistical errors as obtained by averaging $SB_{i,k}$ events over 15 intervals of $\langle\cos\theta_\nu\rangle$ was the final criterion of the correctness of matching the matrices. This criterion is especially sensitive in the region where the zero of the experimental asymmetry must coincide with the zero of the calculated cosine. The methodological uncertainty caused by the use of this criterion was found from the change in SB associated with small variations in the energy-scale division such that they did not lead to any appreciable changes in $SB_{i,k}$ in this region. The uncertainty determined by using this method did not exceed one-third of the statistical error in an individual set.

The statistical error in the measurement of SB in an individual set was $\Delta SB/SB \sim 1.7\%$. The weighted mean value over 16 individual measurements of SB was $SB = 0.9233 \pm 0.0037$, the distribution of their results being normal with standard deviation $\sigma = \pm 0.0047$. The methodological uncertainty was ± 0.0012. The difference of the statistical error and the standard deviation is in agreement with the above estimate of the methodological uncertainty.

6. CALCULATION OF $\lambda = G_A/G_V$

We used formulas (1) and (2) to calculate $\lambda = G_A/G_V$. Sixteen individual values obtained for G_A/G_V are quoted in the table.

The weighted mean value over 16 measurements is $\lambda = -1.2686 \pm 0.0046$. A statistical analysis shows that the distribution of the 16 individual values is normal with standard deviation $\sigma = \pm 0.0048$, which corresponds to the normalized χ^2 value of 1.08.

The methodological uncertainty in the resulting value of λ was found from the change in its value in response to variations in SA and SB within the methodological uncertainties in them. The result is $\delta\lambda = \pm 0.0007$.

The value of $\langle SB\rangle = 0.9233 \pm 0.0047$ determined in this study and the correlation coefficient $B = -2(\lambda - \lambda^2)/(1 + 3\lambda^2) = 0.9876 \pm 0.0004$ corresponding to the value obtained for λ make it possible to determine precisely the polarization of the neutron beam used ($S = \langle SB\rangle/B = 0.935 \pm 0.005$). A direct measurement of this polarization by the second-reflection method yielded $S = 0.940 \pm 0.010$. Good agreement of these values is an independent piece of evidence for the correctness of the procedure used.

7. CONCLUSION

For the first time, the fundamental quantity λ has been determined by using only experimental data on free-neutron decay induced by weak interaction (without recourse to data from any other measurements).

A key point of our experiment has been the use of two P-odd correlations. This has ensured an effective link between λ and the measured quantities, eliminated the need for polarization measurements, and rendered measurement of the experimental asymmetry relative.

We have obtained a new experimental value,

$$\lambda = -1.2686 \pm 0.0046 \pm 0.0007,$$

that agrees well with the world-average value recommended by the Particle Data Group and deduced from the measurements of correlations:

$$\lambda = -1.2670 \pm 0.0035 \text{ [11]}.$$

Our result for λ has enabled us to calculate the corresponding values of the angular-correlation coefficients a, A, and B and the degree S of polarization of the beam used:

$$a = -0.1045 \pm 0.0014,$$
$$A = -0.1168 \pm 0.0017,$$
$$B = 0.9876 \pm 0.0004,$$
$$S = 0.935 \pm 0.005.$$

The correctness of our procedure has been verified by a direct polarization measurement that was based on the second-reflection method.

A low level of the methodological uncertainty opens the possibility for improving further the accuracy in testing the standard theory of weak interaction.

ACKNOWLEDGMENTS

This work was supported by the International Association for the Promotion of Cooperation with Scientists from the Independent States of the Former Soviet Union (grant no. 96-537) and by the Russian Foundation for Basic Research (project no. 96-02-18672).

REFERENCES

1. B. G. Erozolimskiĭ, A. I. Frank, Yu. A. Mostovoĭ, *et al.*, Yad. Fiz. **30**, 692 (1979) [Sov. J. Nucl. Phys. **30**, 356 (1979)].
2. B. G. Erozolimskiĭ, I. A. Kuznetsov, I. A. Kuĭda, *et al.*, Yad. Fiz. **52**, 1583 (1990) [Sov. J. Nucl. Phys. **52**, 999 (1990)].
3. B. Yerozolimsky, I. Kuznetsov, Yu. Mostovoy, *et al.*, Phys. Lett. B **412**, 240 (1997).
4. I. A. Kuznetsov, A. P. Serebrov, I. V. Stepanenko, *et al.*, Phys. Rev. Lett. **75**, 794 (1995).
5. A. P. Serebrov, I. A. Kuznetsov, I. V. Stepanenko, *et al.*, Zh. Éksp. Teor. Fiz. **113**, 1963 (1998) [JETP **86**, 1074 (1998)].
6. I. Kuznetsov, Yu. Rudnev, *et al.*, Nucl. Instrum. Methods Phys. Res. A **440**, 539 (2000).
7. Yu. A. Mostovoĭ, I. A. Kuznetsov, A. P. Serebrov, and B. G. Yerozolimsky, Yad. Fiz. **64**, 156 (2001) [Phys. At. Nucl. **64**, 151 (2001)].
8. A. N. Bazhenov *et al., Electronic Support of Experimental Assemblies* (S.-Peterburg Inst. Yad. Fiz., Ross. Akad. Nauk, Gatchina, 1998).
9. D. H. Wilkinson, Nucl. Phys. A **377**, 474 (1982).
10. C. Stratova, R. Dobrozemski, *et al.*, Phys. Rev. D **18**, 3978 (1978).
11. Particle Data Group (C. Caso *et al.*), Eur. Phys. J. C **3**, 1 (1998).

Physics of Atomic Nuclei, Vol. 64, No. 11, 2001, pp. 1961–1970. Translated from Yadernaya Fizika, Vol. 64, No. 11, 2001, pp. 2046–2055.

ELEMENTARY PARTICLES AND FIELDS
Experiment

Measurement of the Tensor Analyzing Power A_{yy} in the Inelastic Scattering of 4.5-GeV/c Deuterons on Beryllium at an Angle of 80 mrad

L. S. Azhgirey*, V. V. Arkhipov, S. V. Afanasiev, V. K. Bondarev[1)], V. N. Zhmyrov, L. S. Zolin, V. I. Ivanov, A. Yu. Isupov, A. A. Kartamyshev[2)], V. A. Kashirin, V. I. Kolesnikov, V. A. Kuznetsov, V. P. Ladygin, N. B. Ladygina, A. G. Litvinenko, S. G. Reznikov, P. A. Rukoyatkin, A. Yu. Semenov, I. A. Semenova, G. D. Stoletov, G. Filipov[3)], and A. N. Khrenov

Joint Institute for Nuclear Research, Dubna, Moscow oblast, 141980 Russia

Received August 17, 2000; in final form, November 27, 2000

Abstract—The tensor analyzing power A_{yy} and the vector analyzing power A_y for the inelastic scattering of 4.5-GeV/c deuterons on beryllium nuclei at angle of about 80 mrad are measured in the vicinity of baryon-resonance excitation. These new data, presented as a function of t, comply well with the results of previous 4.5-, 5.5-, and 9-GeV/c measurements at zero angle in overlapping regions of t; all available data are described by a unified dependence on $|t|$ up to about 0.9 $(\text{GeV}/c)^2$. The experimental results are compared with the results of calculations performed within the multiple-scattering model and the model involving omega-meson exchange in the t channel. © *2001 MAIK "Nauka/Interperiodica".*

1. INTRODUCTION

Reactions induced by relativistic deuterons have been intensively studied in recent years. In particular, high-energy, coherent deuteron–nucleus interactions not accompanied by deuteron breakup have been the subject of investigations in various laboratories worldwide [1–11]. It is expected that the intrinsic properties of the nuclear structure of the deuteron, possibly including nonnucleonic degrees of freedom, may manifest themselves in processes involving high momentum transfers. In this respect, inelastic deuteron–nucleus scattering accompanied by high momentum transfers supplements investigations of the short-distance structure of the deuteron that are performed by exploring elastic proton–deuteron and electron–deuteron scattering and deuteron-breakup reactions induced by hadrons, electrons, and photons.

At the same time, inelastic deuteron scattering is an effective tool for studying systems having a specific isospin value because, in $A(d,d')X$ reactions, the isospin of an unobservable system X must coincide with the isospin of the target nucleus A. This circumstance was used, for example, in searches for the $\Delta\Delta$ dibaryon of isospin $T=0$ in $d(d,d')X$ reactions [6]. Inelastic deuteron scattering on hydrogen, $^1\text{H}(d,d')X$, is selective to isospin-1/2 systems; therefore, it can serve as a source of information about the excitation of baryon resonances like $N^*(1440)$, $N^*(1520)$, and $N^*(1680)$.

Differential cross sections for inelastic deuteron scattering were measured in Saclay at 2.95 GeV/c for hydrogen targets [1, 4], in Dubna at deuteron momenta up to 9 GeV/c for various targets [3, 5, 7], and at Fermilab at higher energies for reactions occurring on hydrogen [2]. Calculations within the multiple-scattering formalism revealed [7] that the differential cross sections for $^1\text{H}(d,d')X$ reactions are satisfactorily described by double hadron–hadron scattering. Within this approach, the amplitudes for $NN \to NN^*$ elementary processes were determined for the $N^*(1440)$, $N^*(1520)$, and $N^*(1680)$ resonances [7].

Data on polarization effects in inelastic deuteron scattering are scanty at present. High-energy polarized deuterons were used to study the tensor analyz-

[1)]St. Petersburg State University, St. Petersburg, Russia; Joint Institute for Nuclear Research, Dubna, Moscow oblast, 141980 Russia.

[2)]Russian Research Centre Kurchatov Institute, pl. Kurchatova 1, Moscow, 123182 Russia.

[3)]Institute for Nuclear Research and Nuclear Energy, Blvd. Tsarigradsko chaussee 72, BG-1784 Sofia, Bulgaria; Joint Institute for Nuclear Research, Dubna, Moscow oblast, 141980 Russia.

*e-mail: azhgirey@cv.jinr.ru

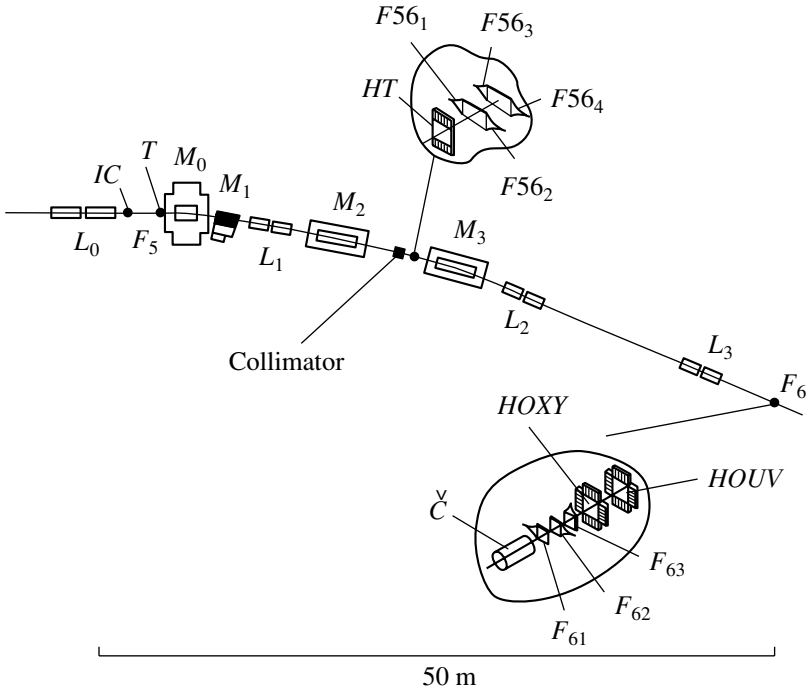

Fig. 1. Layout of the SFERA facility and the $VP1$ ion guide: (F_5, F_6) foci of the ion guide, (M_i) magnets, (L_i) lenses, (IC) ionization chamber, (T) target, (F_{61}, F_{62}, F_{63}) trigger counters, ($F56_{1-4}$) scintillation counters, (HT) scintillation hodoscope for time-of-flight measurements, ($HOXY$, $HOUV$) beam-profile hodoscopes, and ($\check{C}$) Cherenkov counter.

ing power T_{20} in the vicinity of the excitation of the Roper resonance [$P_{11}(1440)$] for hydrogen and carbon targets in Dubna [8] and for hydrogen targets in Saclay [9]. In the scattering of 9-GeV/c deuterons on hydrogen and carbon, the tensor analyzing power T_{20} was measured for excitation masses of up to $M_X \sim 2.2$ GeV/c^2 [10]. It turned out that, at momentum transfers of $t \sim -0.3\,(\mathrm{GeV}/c)^2$, this analyzing power takes negative values of large magnitude. Within the model assuming the mechanism of omega-meson exchange [12], this behavior was interpreted as that which is associated with the longitudinal isoscalar form factor for the excitation of the Roper resonance [13]. Also, large values of the tensor analyzing power A_{yy} around $M_X \sim 2.2$ GeV/c^2, where M_X is the mass of the undetected system, were observed in measuring this quantity and the vector analyzing power A_y at 9 GeV/c and the secondary-deuteron emission angle of 80 mrad [11]; this observation has yet to be explained. In addition, data on the tensor analyzing power T_{20} are known for the reaction $p(d,p)pn$ induced by 3.5- to 6.5-GeV/c deuterons for zero secondary-proton emission angle [14].

The present article reports on a continuation of the series of investigations begun in [11] and devoted to polarization effects in relativistic-deuteron-induced reactions leading to the emission of secondary particles of high transverse momenta. Here, we present new data on the tensor analyzing power A_{yy} and the vector analyzing power A_y in the inelastic scattering of 4.5-GeV/c deuterons on a beryllium target for secondary-deuteron emission at an angle of about 80 mrad.

The ensuing exposition is organized as follows. In Section 2, we describe the details of our experiment. A comparison with existing data and with predictions of various theoretical models is performed in Section 3. The basic conclusions of our study are formulated in Section 4.

2. DESCRIPTION OF THE EXPERIMENT

Our experiment employed the SFERA facility described in [15] and a polarized deuteron beam from the synchrophasotron installed at the Joint Institute for Nuclear Research (JINR, Dubna). The layout of the experiment is shown in Fig. 1. Polarized deuterons were produced by the POLARIS ion source [16]. The sign of the beam polarization was changed regularly from one accelerator pulse to another in the 0, −, + sequence, where 0 means the absence of polarization, while the signs + and − correspond to the sign of p_{zz}, the quantization axis being orthogonal to the plane containing the mean orbit of the beam in the accelerator.

Tensor analyzing power A_{yy} and vector analyzing power A_y for the inelastic scattering of 4.5-GeV/c deuterons on a beryllium target at an angle of about 80 mrad

p, GeV/c	Δp(FWHM), GeV/c	t, (GeV/c)^2	M_X, GeV/c^2	$A_{yy} \pm dA_{yy}$	$A_y \pm dA_y$
2.577	0.111	−0.917	1.752	-0.178 ± 0.240	0.082 ± 0.272
2.822	0.127	−0.683	1.711	0.070 ± 0.159	-0.072 ± 0.179
3.067	0.139	−0.508	1.647	0.084 ± 0.096	0.053 ± 0.108
3.361	0.149	−0.345	1.549	0.211 ± 0.067	0.015 ± 0.075
3.651	0.165	−0.253	1.418	0.364 ± 0.056	0.155 ± 0.063
4.047	0.189	−0.165	1.196	0.293 ± 0.063	0.098 ± 0.071

The tensor polarization of the beam was periodically checked in the course of the experiment by measuring asymmetry in the emission of protons of momentum $p_p \sim (2/3)p_d$ at zero angle in the deuteron breakup $d + A \to p + X$ on a nuclear target [17]. Previously, it was shown that, in the deuteron-breakup reaction occurring under such conditions, the tensor analyzing power is very large, $T_{20} = -0.82 \pm 0.05$, and is independent of the target atomic number (for $A > 4$) or the incident-deuteron momentum in the range between 2.5 and 9.0 GeV/c [18]. The tensor polarization of the beam as averaged over the entire experimental time proved to be $p^+_{zz} = 0.798 \pm 0.002(\text{stat.}) \pm 0.040(\text{syst.})$ and $p^-_{zz} = -0.803 \pm 0.002(\text{stat.}) \pm 0.040(\text{syst.})$ for, respectively, the + and the − spin states of the beam.

The invariability of the vector polarization of the beam was monitored by measuring asymmetry in quasielastic proton–proton scattering on a thin target made from CH_2 and arranged at the focus F_4 (not shown in Fig. 1) of the ion guide VP1 at a distance of about 20 m in front of the facility [19]. The absolute values of the vector polarization were obtained from the asymmetry measured in the scattering of 4.5-GeV/c protons at a angle of 8° by using the polarimeter analyzing power of $A(CH_2) = 0.146 \pm 0.007$ [20]. For the different spin states, the vector polarization of the beam was $p^+_z = 0.231 \pm 0.014(\text{stat.}) \pm 0.012(\text{syst.})$ and $p^-_z = 0.242 \pm 0.014(\text{stat.}) \pm 0.012(\text{syst.})$.

A beam of tensorially polarized deuterons that was characterized by a momentum of 4.5 GeV/c and an intensity of 5×10^8 particles per accelerator spill and which was extended in time over 0.5 s as the result of a slow extraction was incident on a beryllium target 20 cm thick positioned at the focus F_5 of the ion guide *VP*1 (see Fig. 1). The beam intensity was monitored by an ionization chamber arranged in front of the target. The position of the beam and its profiles at specific loci of the ion guide was checked by the control system of the accelerator in each pulse. The dimensions of the beam at the target position were $\sigma_x \sim 0.4$ cm and $\sigma_y \sim 0.9$ cm in the horizontal and the vertical direction, respectively.

Our data were obtained for six values of the momentum of secondary particles in the range between 2.5 and 4.0 GeV/c. Secondaries emitted from the target at an angle of about 80 mrad were transported to the focus F_6 with the aid of three deflecting magnets (the magnet M_0 was switched off) and three doublets of lenses. The acceptance of the facility was determined from a Monte Carlo simulation with allowance for the parameters of the incident deuteron beam; nuclear interactions and multiple scattering in the target, in air, in windows, and in the detectors; energy losses of primary and secondary deutrons; etc. The momentum and polar-angle acceptances were (FWHM) $\Delta p/p \sim \pm 2\%$ and ± 8 mrad, respectively.

For a trigger, we used coincidences of signals from the scintillation counters F_{61}, F_{62}, and F_{63}. Along with inelastically scattered deuterons, our equipment recorded protons from deuteron breakup. The recorded particles were identified in an off-line analysis on the basis of information about the time of flight over the base of length about 34 m from the start counter F_{61} to the stop counters $F56_1$–$F56_2$ and $F56_3$–$F56_4$ and the scintillation hodoscope HT. The resolution in the time of flight was better than 0.2 ns (1σ). The time-of-flight spectra obtained for all six settings of the magnetic elements are shown in Fig. 2. At the highest momentum of recorded particles, only deuterons are seen in the time-of-flight spectrum; however, the relative contribution of protons becomes more pronounced with decreasing momentum. In data processing, we chose only those events for which at least two measured times of flight were correlated. This made it possible to eliminate completely the background of protons.

Measurements without a target were performed for 4.0-GeV/c secondaries. The ratio of the deuteron yields in the experiments without and with the beryllium target of thickness 20 cm was less than 1%.

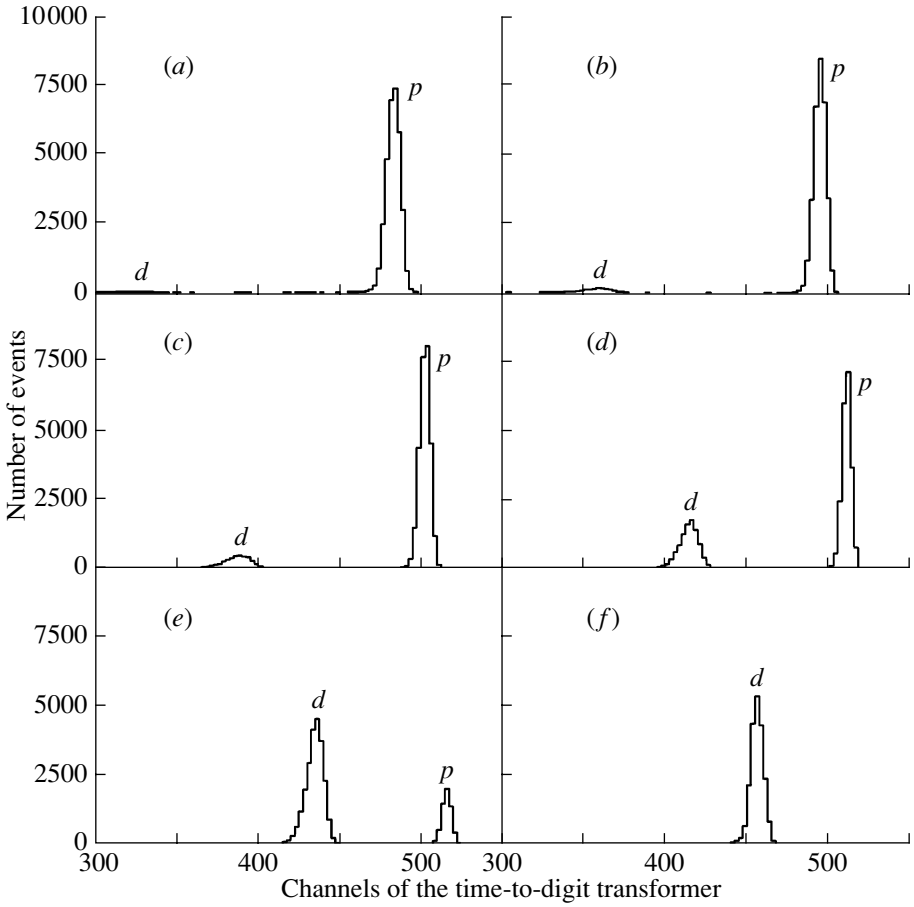

Fig. 2. Time-of-flight spectra obtained at various values of the excitation currents in the magnetic elements. The corresponding momenta of secondary deuterons were (*a*) 2.5, (*b*) 2.75, (*c*) 3.0, (*d*) 3.3, (*e*) 3.6, and (*f*) 4.0 GeV/c.

The tensor analyzing power A_{yy} and the vector analyzing power A_y were calculated on the basis of the numbers n^+, n^-, and n^0 of deuterons recorded for the different polarization states of the beam by using the expressions

$$A_{yy} = 2\frac{p_z^-(n^+/n^0 - 1) - p_z^+(n^-/n^0 - 1)}{p_z^- p_{zz}^+ - p_z^+ p_{zz}^-}, \quad (1)$$

$$A_y = -\frac{2}{3}\frac{p_{zz}^-(n^+/n^0 - 1) - p_{zz}^+(n^-/n^0 - 1)}{p_z^- p_{zz}^+ - p_z^+ p_{zz}^-},$$

where the above numbers of deuterons were reduced to the same intensity of the beam and were corrected for the dead-time effect [21]. These expressions, which take into account different values of the polarizations for the different spin states of the beam, are significantly simplified for $p_z^+ = p_z^-$ and $p_{zz}^+ = p_{zz}^-$.

The tensor analyzing power A_{yy} and the vector analyzing power A_y according to the data on inelastic deuteron scattering from the present experiment are displayed in the table. The quoted errors are purely statistical. The systematic errors were 5 and 8% for A_{yy} and A_y, respectively.

The values presented in the table for the secondary-deuteron momentum p, the momentum acceptance (FWHM) Δp, the 4-momentum t, and the missing mass M_X were obtained from our Monte Carlo simulation, in which the t dependence of the differential cross sections for $(d, d')X$ reactions was taken in the form

$$\frac{d^2\sigma}{dt dM_X^2} \sim e^{-b|t|}, \quad (2)$$

where the slope parameter was set to $b = 18$ (10) $(\mathrm{GeV}/c)^{-2}$ for $M_X \leq 1200$ ($M_X > 1200$) MeV/c^2 [4]. With allowance for the energy loss in the target, the averaged momentum of primary deuterons was 4.465 GeV/c.

Since a comparatively thick target (36 g/cm^2) was used in our experiment, we could not rule out, from the outset, the contribution of deuterons that suffered, after the interaction event, additional elastic scattering on a different target nucleus (macroscopic double scattering). However, the Monte Carlo simulation revealed that, at 4.0 GeV/c, the contribution of such

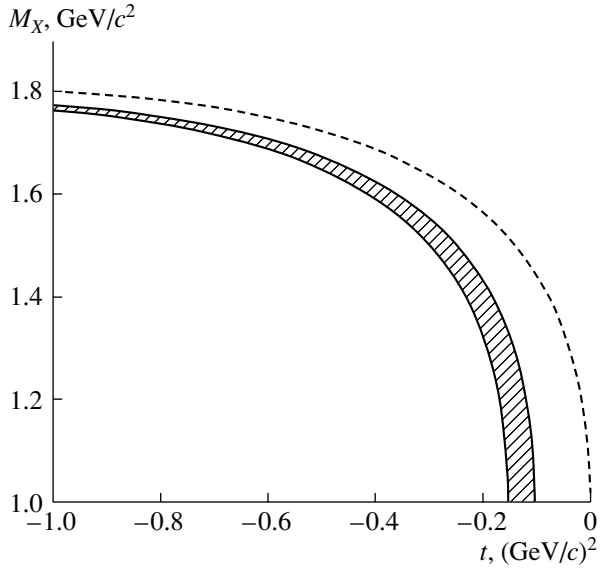

Fig. 3. Kinematical diagram of the dependence of the missing mass M_X on the square t of the 4-momentum transfer for $(d, d')X$ reactions at the primary-deuteron momentum of 4.5 GeV/c. The region of t and M_X values covered by the acceptance of the facility in the present experiment is shaded. The dashed curve corresponds to the conditions of the experiment that was reported in [8] and which was performed for zero emission angle (the midpoint of the acceptance).

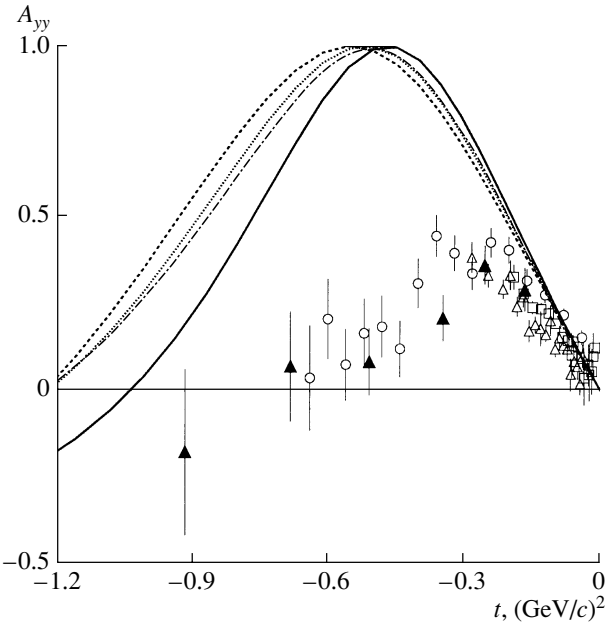

Fig. 4. Tensor analyzing power A_{yy} for inelastic deuteron scattering (closed triangles) on beryllium at 4.5 GeV/c for an emission angle of about 80 mrad and on hydrogen at (open triangles) 4.5 and (open squares) 5.5 GeV/c [8] and (open circles) at 9 GeV/c [10] for zero emission angle versus the square t of the 4-momentum transfer. The solid, the dashed, the dotted, and the dash-dotted curve represent the results of the calculations performed in the plane-wave impulse approximation with the deuteron wave functions for the Paris potential [22], the Bonn potential A, the Bonn potential B, and the Bonn potential C [23], respectively.

deuterons is not greater than 0.5% of the total number of secondaries and that it decreases with decreasing momentum.

The values of the mixing mass M_X that are presented in the table were calculated under the assumption that the reaction in question proceeds on a target having a mass equal to the proton mass. In this case, the square t of the 4-momentum transfer and the missing mass M_X are related by the equation

$$M_X^2 = t + m_p^2 + 2m_p Q, \qquad (3)$$

where m_p is the proton mass and Q is the difference of the energies of the incident and the scattered deuteron. The region of t and M_X values covered by the acceptance of the facility in the present experiment is shaded in the kinematical diagram displayed in Fig. 3. The dashed curve corresponds to the primary deuteron momentum of 4.5 GeV/c and zero emission angle, which were realized in the experiment reported in [8]. It can be seen that the same missing mass M_X corresponds to different values of t under the conditions of that experiment and our present experiment. In view of this, data that we obtained for an emission angle of about 80 mrad provide new information about the t dependence of the tensor analyzing power A_{yy}.

3. RESULTS AND DISCUSSION

Our data on the tensor analyzing power A_{yy} in the inelastic scattering of 4.5-GeV/c on beryllium at an angle of about 80 mrad are displayed in Fig. 4 versus the square of the 4-momentum transfer (closed triangles). We can see that A_{yy} is positive, attains values of about 0.3 in the region $|t| = 0.2$–0.4 (GeV/c)^2, and decreases to zero at high $|t|$. Data on the tensor analyzing power in the case of deuteron emission at zero angle for hydrogen targets at primary energies of 4.5 and 5.5 GeV/c [8] and of 9.0 GeV/c [10] are also shown in Fig. 4 (open symbols). (We recall that $A_{yy} = -T_{20}/\sqrt{2}$ for these data.) In can be seen that the results of our present experiment comply well with previous data from [8, 10] in the region where they overlap. Irrespective of the primary momentum and the deuteron emission angle, all available data on A_{yy} fit approximately in a unified dependence on t. It can also be seen that there is no visible dependence on the atomic number A of the target. This confirms conclusions drawn previously in connection with the experiments performed at 4.5 and 5.5 GeV/c

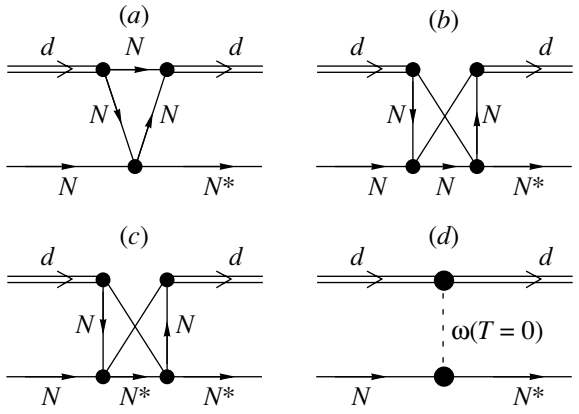

Fig. 5. Diagrams representing baryon-excitation mechanisms in deuteron–nucleon collisions: (*a*) plane-wave impulse approximation, (*b*, *c*) double-collision mechanism, and (*d*) omega-meson-exchange mechanism.

[8] and at 9.0 GeV/c [10] for the case of zero deuteron emission angle. That no dependence of the tensor analyzing power on the target atomic number has been observed suggests that rescattering in the target and medium effects (these factors are of considerable importance in the case of delta-isobar excitation [24]) are insignificant in the case being considered. Hence, nuclear targets are also appropriate for deducing information about baryon excitation in inelastic deuteron scattering.

The curves in Fig. 4 represent the results of the calculations in the plane-wave impulse approximation (PWIA). The relevant mechanism is schematically represented by the diagram in Fig. 5*a*. In this approach, the tensor analyzing power A_{yy} is independent of the $NN \to NN^*$ elementary amplitude—it is determined by the charge form factor G_C and the quadrupole form factor G_Q for the deuteron; that is,

$$A_{yy} = \frac{1}{2}\frac{2\sqrt{2}G_C G_Q + G_Q^2}{G_C^2 + G_Q^2}, \qquad (4)$$

where

$$G_C(q) = \int_0^\infty \left(u^2(r) + w^2(r)\right) j_0(rq/2)dr, \qquad (5)$$

$$G_Q(q) = \int_0^\infty 2w(r)\left(u(r) - \frac{w(r)}{2\sqrt{2}}\right) j_2(rq/2)dr. \qquad (6)$$

Here, $u(r)$ and $w(r)$ are, respectively, the wave functions for the S- and the D-wave state of the deuteron in configuration space; j_0 and j_2 are, respectively, a zero- and a second-order Bessel function; and $q^2 = -t$.

The solid curve in Fig. 4 represents the results of the calculations with the deuteron wave function for the Paris potential [22], while the dashed, the dotted, and the dash-dotted curve correspond to the deuteron wave functions for, respectively, the A, the B, and the C version of the Bonn potential [23]. A strong deviation of the present data from the PWIA predictions, as well as the fact that the tensor analyzing power behaves differently in $(d, d')X$ reactions and in elastic electron–deuteron and proton–deuteron scattering (see [25, 26] and [27], respectively), indicates that the quantity A_{yy} is sensitive to baryon-resonance excitation.

Within the multiple-scattering model, such a deviation could be due to a sizable contribution of double scattering (diagrams in Figs. 5*b*, 5*c*). The diagram in Fig. 5*b* corresponds to resonance formation in the second nucleon–nucleon collision; in the process represented by the diagram in Fig. 5*c*, a resonance is formed in the first nucleon–nucleon interaction, whereupon the resonance is elastically scattered on the second nucleon of the deuteron. The calculations show that the contribution of double scattering is of importance at $|t|$ values greater than approximately 0.4 (GeV/c)^2 [7]. Thus, we see that, in the multiple-scattering model, the behavior of the tensor analyzing power A_{yy} is determined by the spin structure of the deuteron and by the elementary amplitudes for $NN \to NN^*$ and $NN^* \to NN^*$ processes.

The sensitivity of the tensor analyzing power for inelastic deuteron scattering on protons to baryon-resonance excitation was indicated in [12], where the quantity A_{yy} was considered within the model assuming the mechanism of omega-meson exchange in the t channel. The diagram corresponding to this model is shown in Fig 5*d*. The differential cross section and polarization observables can be calculated on the basis of the known electromagnetic properties of the deuteron and of baryon resonances N^* within the vector-dominance model. The details of the model involving omega-meson exchange in the t channel are described elsewhere [12, 13]. Here, we will therefore briefly touch only upon the basic features of the model.

Within the omega-meson-exchange model, the tensor analyzing power for inelastic deuteron scattering is expressed in terms of the ratio of the differential cross sections for the absorption of longitudinally and transversely polarized virtual isoscalar photons by nucleons [12], $r = \sigma_L/\sigma_T$; that is,

$$A_{yy} = \frac{V_1^2 + (2V_0V_2 + V_2^2)r}{4V_1^2 + (3V_0^2 + V_2^2 + 2V_0V_2)r}, \qquad (7)$$

where the structure functions V_0, V_1, and V_2 are related to the standard deuteron electric, magnetic, and quadrupole form factors (G_C, G_M, and G_Q, respectively) [12, 13].

In the case involving the excitation of N^* resonances, the ratio r can be represented in the form

$$r_{N^*} = \frac{|A_l^p + A_l^n|^2}{|A_{1/2}^p + A_{1/2}^n|^2 + |A_{3/2}^p + A_{3/2}^n|^2}, \quad (8)$$

where A_l^N is the longitudinal form factor for the excitation of N^* on a proton ($N = p$) or a neutron ($N = n$) and $A_{1/2}^N$ and $A_{3/2}^N$ are two possible transverse form factors corresponding to the the values of $1/2$ and $3/2$ for the total helicity of the $\gamma^* + N$ system. Within the model based on the mechanism of omega-meson exchange in the t channel [12, 13], the tensor analyzing power can therefore be represented as the product of two terms that are determined by the electromagnetic properties of the deuteron, on one hand, and by the form factors for the $N \to N^*$ transition, on the other hand.

The tensor analyzing power for $d + p \to d + X$ processes as a function of t was analyzed [13] by using, for the transverse and the longitudinal helicity amplitude, the results obtained on the basis of the algebraic collective string model of baryons [28] with allowance for the finite widths of the $P_{11}(1440)$, $S_{11}(1535)$, $D_{13}(1520)$, and $S_{11}(1650)$ resonances. However, only the Roper resonance $P_{11}(1440)$ has a nonzero isoscalar longitudinal form factor—the other three resonances considered here cannot be excited by isoscalar longitudinal virtual photons, since the isoscalar longitudinal amplitudes for the $S_{11}(1535)$ and $D_{13}(1520)$ resonances vanish because of spin–flavor symmetry and since the isoscalar and isovector longitudinal couplings of the $S_{11}(1650)$, $D_{15}(1675)$, and $D_{13}(1700)$ resonances are identically equal to zero. It follows that, within the omega-meson-exchange model, the t dependence of the tensor analyzing power for inelastic deuteron scattering is determined by the contribution of the Roper resonance and by the t dependence of the deuteron form factors [13]. If we disregard the finite values of the resonance widths, the tensor analyzing power in question taken in this approximation is a universal primary-deuteron-momentum-independent function of t.

In Fig. 6, the data at 4.5 GeV/c that were obtained for emission angles of about 80 mrad and zero and which are shown by closed and open triangles, respectively, are contrasted against the results of the calculations performed within the omega-meson-exchange model [13]. The calculations employed the deuteron form factors computed in the relativistic impulse approximation [29] and the standard values of the paramaters of the collective string model [28] (the constituent quark mass of $m = 0.366$ GeV, the magnetic moment of $\mu = 0.127$ GeV^{-1}, and the fixed scale parameter of $a_0 = 0.232$ fm). The solid and the dashed curve represent the results of the calculations performed without and with allowance for finite resonance widths, respectively. It can be seen that the results of the calculations are in reasonably good agreement with data up to $|t| \sim 0.3$ (GeV/c)^2; at higher values of $|t|$, serious discrepancies are observed, which may be due to the contributions of the $F_{15}(1680)$ and $P_{13}(1720)$ resonances, not included in the calculations. Just like the Roper resonance, they have nonzero isoscalar longitudinal form factors. Therefore, the contributions of these resonances can substantially affect the t dependence of the tensor analyzing power at high t. At the same time, the model relying on meson exchange in the t channel alone may be inadequate in this region; possibly, it is necessary to take into account the contributions of harder processes as well—for example, the baryon-resonance excitation in the approximation of one-nucleon exchange [30, 31]. Moreover, exchanges of other mesons (σ, η, etc.) and the double-scattering mechanism [1, 7] can contribute significantly at high t.

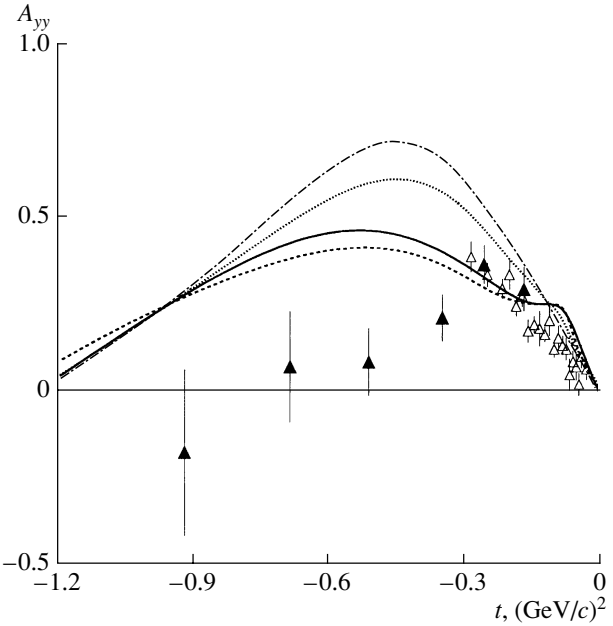

Fig. 6. Tensor analyzing power A_{yy} for inelastic deuteron scattering on (closed triangles) beryllium at 4.5 GeV/c for an emission angle of about 80 mrad according to the data of the present experiment and (open triangles) hydrogen at 4.5 and 5.5 GeV/c [8] for zero emission angle versus the square t of the 4-momentum transfer. The solid and the dashed curve represent the results of the calculations on the basis of the omega-meson-exchange model [13] without and with allowance for the resonance widths, respectively, at $\xi = 0$. The dotted and the dash-dotted curve were computed within the same model at the string-tension values of $\xi = 0.5$ and 1, respectively.

In the QCD string model, it is expected that, with increasing excitation energy, strings will stretch (swelling of hadrons). Within the collective string

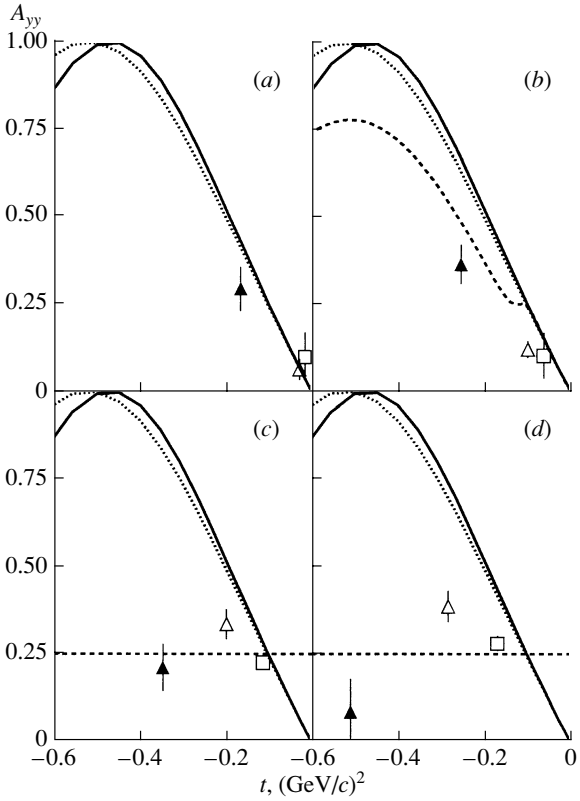

Fig. 7. Data on A_{yy} (closed triangles) from the present experiment and relevant data obtained at (open triangles) 4.5 and (opens squares) 5.5 GeV/c for zero emission angle [8] versus the square t of the 4-momentum transfer at four various values of the missing mass M_X: (a) $M_X \sim$1200 MeV/c^2, (b) $M_X \sim$1440 MeV/c^2, (c) $M_X \sim$1550 MeV/c^2, and (d) $M_X \sim$1650 MeV/c^2. The solid and dotted curves represent the results of the calculations in the plane-wave impulse approximation with the deuteron wave function for, respectively, the Paris potential [22] and the B version of the Bonn potential [23]. The dashed curves were computed on the basis of the omega-meson-exchange model [13].

model [28], this effect is taken into account by introducing the string tension ξ in the expression for the scale parameter a via the relation

$$a = a_0 \left(1 + \xi \frac{W - M}{M}\right), \qquad (9)$$

where $a_0 = 0.232$ fm is a fixed scale parameter of the collective string model, while M and W are the nucleon and the baryon mass, respectively. The string tension ξ varies between 0 and 1. The dashed, the dotted, and the dash-dotted curve in Fig. 6 represent the results of the calculations performed within the omega-meson exchange model [13] with ξ set to 0, 0.5, and 1, respectively. It can be seen that the tensor analyzing power is highly sensitive to ξ. It was indicated in [13] that the introduction of the swelling of hadrons that corresponds to $\xi \sim 0.5$–1 (such values are consistent with the results of an analysis of the spectrum of experimental masses in terms of the Regge trajectories) leads to a better description of experimental data on A_{yy} [8–10] in the range of primary deuteron momenta between 3.7 and 9 GeV/c. However, data of the present study and data obtained at 4.5 GeV/c for deuteron emission at zero angle are better reproduced within the omega-meson-exchange model at the string-tension value of $\xi \sim 0.2$. On the other hand, the mechanism of delta-isobar excitation in the incident particle and the mechanism of Roper resonance excitation in the target nucleus (via sigma-meson exchange) should be taken into account in this region [32]. However, the t dependence of the tensor analyzing power would then be governed by the interference between the mechanisms considered in [32] and the omega-meson-exchange mechanism [13], which is sensitive to the string tension ξ. Therefore, definitive conclusions on the value of ξ on the basis of the present experimental data alone would be premature at present.

The data on A_{yy} from the present experiment (closed triangles), along with the data taken at 4.5 and 5.5 GeV/c for zero emission angle [8] (open triangles and squares, respectively), versus the square t of the 4-momentum transfer are displayed in Figs. 7a, 7b, 7c, and 7d for four values of the missing mass M_X around 1200, 1440, 1550, and 1650 MeV/c^2, respectively. The solid and dotted curves represent the results of the PWIA calculations with the deuteron wave function for the Paris potential [22] and the version B of the Bonn potential [23]. The experimental data in Fig. 7a correspond to the region where the mechanism of delta-isobar excitation in the incident particle [32] is dominant, so that the tensor analyzing power is determined primarily by the behavior of the deuteron form factors. The dashed curves in Figs. 7b, 7c, and 7d represent the predictions of the omega-meson-exchange model [13] for $P_{11}(1440)$, $D_{13}(1520)$ and $S_{11}(1535)$, and $S_{11}(1650)$ resonances, respectively. As was indicated above, the t dependence of the tensor analyzing power is determined exclusively by the longitudinal form factor for the Roper resonance $P_{11}(1440)$, because the longitudinal form factors for the $D_{13}(1520)$, $S_{11}(1535)$, and $S_{11}(1650)$ resonances vanish [13]. In the last case, the tensor analyzing power A_{yy} is independent of t and amounts to +0.25. It can be seen that, in the vicinity of the Roper resonance (Fig. 7b) and at $M_X \sim$ 1550 MeV/c^2 (Fig. 7c), the behavior of A_{yy} is consistent with the predictions of the omega-meson-exchange model [13], but that, at $M_X \sim$ 1650 MeV/c^2 (Fig. 7d), a deviation from the constant value of +0.25 is observed. It was indicated above, however, that, at these missing-mass values, it may prove to be necessary to take additionally into account

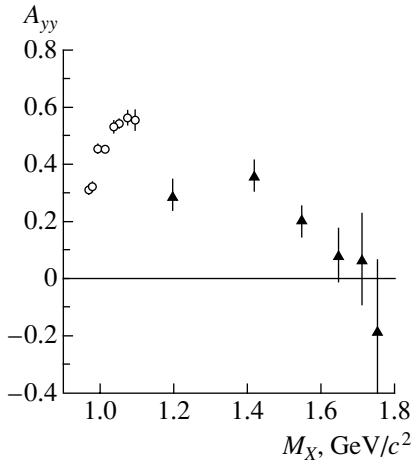

Fig. 8. Tensor analyzing power A_{yy} for $(d,d')X$ reactions according to (closed triangles) the present data on inelastic deuteron scattering on beryllium at 4.5 GeV/c for an emission angle of about 80 mrad and (open circles) the data from [14] for the reaction $^1\mathrm{H}(d,p)pn$ versus the quantity M that coincides with the missing mass M_X for (d,d') reactions and with the difference $M_X - m_p$ for the reaction $(d,p)pn$.

the contributions of the $F_{15}(1680)$ and $P_{13}(1720)$ resonances, whose longitudinal isoscalar form factors are also nonzero, which may significantly affect the t dependence of the tensor analyzing power. It should also be noted that, since we explore inclusive $(d,d')X$ processes, a few resonances can contribute at the above value of M_X because of their finite widths; at the same time, the theoretical predictions presented in Fig. 7 were obtained for the individual contributions of the $P_{11}(1440)$, $D_{13}(1520)$, $S_{11}(1535)$, and $S_{11}(1650)$ resonances. In view of this, exclusive (or semiexclusive) measurements involving the detection of resonance-decay products could aid in separating the contributions of various baryon resonances.

It is of interest to compare the present data on the tensor analyzing power A_{yy} for (d,d') reactions occurring on intranuclear nucleons and involving nucleon-resonance excitation with the tensor analyzing power for other inelastic processes. The parameter T_{20} for two-body deuteron breakup on hydrogen with proton emission at zero angle was measured in the experiment reported in [14]. In Fig. 8, the data obtained in the present experiment (closed triangles) are shown along with the values of A_{yy} for the reaction $^1\mathrm{H}(d,p)pn$ that were calculated on the basis of data from [14]. Along the abscissa, we plotted the quantity M that coincides with the missing mass M_X for (d,d') reactions and with the difference $M_X - m_p$ for the reaction $(d,p)pn$. It is surprising that, although the two processes are governed by the totally different mechanisms (the former was treated here on the basis of the multiple-scattering and the omega-meson-exchange model, while the latter should be described, under the kinematical conditions implemented in [14], by the one-nucleon-exchange diagram), the corresponding two data sets can be approximated, as can be seen from Fig. 8, by a single smooth dependence on the above variable M, which characterizes the degree of inelasticity of the reactions in question. It can be seen that, as the degree of inelasticity becomes greater, the quantity A_{yy} grows, attains a maximum, and then decreases.

The values of the vector analyzing power A_y are small and are characterized by large uncertainties (see table). In the vicinity of Roper resonance excitation, however, A_y takes a value of 0.155 ± 0.063, which is nonnegligible. Within the plane-wave impulse approximation (Fig. 5a), this can be considered as an indication of a significant role of the spin-dependent part of the elementary amplitude for $NN \to NP_{11}(1440)$ processes.

4. CONCLUSION

New data on the tensor analyzing power A_{yy} and the vector analyzing power A_y for the inelastic scattering $(d,d')X$ of 4.5-GeV/c deuterons on beryllium at an angle of about 80 mrad in the vicinity of the excitation of baryons with masses between 1.2 and 1.75 GeV/c^2 have been obtained. This corresponds to values of the 4-momentum transfer squared t between -0.17 and -0.90 (GeV/c)^2.

The new data on A_{yy}, together with data obtained previously for zero scattering angle [8, 10], presented versus t, show virtually no dependence on the primary momentum and the deuteron observation angle. It has also been found that A_{yy} is independent of the target atomic number A. These regularities indicate that rescattering, final-state interaction, and nuclear-medium effects, which depend on kinematical conditions, do not have a pronounced influence on the behavior of the tensor analyzing power.

A strong deviation of A_{yy} for $(d,d')X$ reactions from the PWIA predictions, as well as the behavior of the tensor analyzing power for elastic electron–deuteron scattering [25, 26] and elastic proton–deuteron scattering [27], is indicative of the sensitivity of this observable to the excitation of baryon resonances via double interaction.

The behavior of A_{yy} in the vicinity of the excitation of the $P_{11}(1440)$, $D_{13}(1520)$, and $S_{11}(1535)$ resonances is compatible with the predictions of the omega-meson-exchange model [13]; in the case of excitation of higher mass resonances, it may prove to be necessary to take into account, within this model, additional baryon resonances featuring nonzero longitudinal form factors. Moreover, the inclusion of

extra mechanisms, like double scattering [1, 7], exchanges of other mesons [32], or the excitation of N^* in the u channel [30, 31], may be required.

Polarization experiments in an exclusive implementation featuring the detection of resonance-decay products could contribute to obtaining deeper insights into the mechanisms that govern the excitation of various baryon resonances and into the spin properties of their interaction with nucleons.

ACKNOWLEDGMENTS

We are indebted to A.I. Malakhov, director of the Laboratory for High Energies at JINR, and V.N. Penev, deputy director of this laboratory, for their constant support of this study. We are also grateful to the personnel of the synchrophasotron and the POLARIS source for ensuring good conditions for performing the experiment. The assistance of L.V. Budkin, V.P. Ershov, V.V. Fimushkin, A.S. Nikiforov, Yu.K. Pilipenko, V.G. Perevozchikov, E.V. Ryzhov, A.I. Shirokov, and O.A. Titov in conducting the experiments is gratefully acknowledged. Thanks are also due to A.N. Prokof'ev and A.A Zhdanov for placing at our disposal scintillation counters for the polarimeter. We thank E. Tomasi-Gustafsson for help and stimulating discussions, as well as for critically reading the manuscript of this article.

REFERENCES

1. J. Banaigs, J. Berger, L. Goldzahl, *et al.*, Phys. Lett. B **45B**, 535 (1973).
2. Y. Akimov, R. Cool, L. Golovanov, *et al.*, Phys. Rev. Lett. **35**, 763 (1975).
3. L. S. Azhgireĭ, I. K. Vzorov, V. N. Zhmyrov, *et al.*, Yad. Fiz. **28**, 1017 (1978) [Sov. J. Nucl. Phys. **28**, 522 (1978)]; Yad. Fiz. **30**, 1578 (1979) [Sov. J. Nucl. Phys. **30**, 818 (1979)].
4. R. Baldini *et al.*, Nucl. Phys. A **379**, 477 (1982).
5. V. G. Ableev, G. G. Vorob'ev, L. Vizireva, *et al.*, Yad. Fiz. **37**, 348 (1983) [Sov. J. Nucl. Phys. **37**, 209 (1983)].
6. M. P. Combes *et al.*, Nucl. Phys. A **431**, 703 (1984).
7. L. S. Azhgireĭ, I. K. Vzorov, V. N. Zhmyrov, *et al.*, Yad. Fiz. **48**, 1758 (1988) [Sov. J. Nucl. Phys. **48**, 1058 (1988)].
8. L. S. Azhgirey, E. V. Chernykh, A. P. Kobushkin, *et. al.*, Phys. Lett. B **361**, 21 (1995).
9. Experiment LNS-E250 (unpublished).
10. L. S. Azhgirey, E. V. Chernykh, A. P. Kobushkin, *et al.*, JINR Rapid Commun., No. 2[88]-98, 17 (1988).
11. L. S. Azhgirey, V. V. Arkhipov, S. V. Afanas'ev, *et al.*, Yad. Fiz. **62**, 1796 (1999) [Phys. At. Nucl. **62**, 1673 (1999)].
12. M. P. Rekalo and E. Tomasi-Gustafsson, Phys. Rev. C **54**, 3125 (1996).
13. E. Tomasi-Gustafsson *et al.*, Phys. Rev. C **59**, 1526 (1999).
14. L. S. Azhgirey, V. V. Vikhrov, S. A. Zaporozhets, *et al.*, Yad. Fiz. **61**, 494 (1998) [Phys. At. Nucl. **61**, 432 (1998)].
15. S. V. Afanasiev, V. V. Arkhipov, L. S. Azhgirey, *et al.*, Phys. Lett. B **434**, 21 (1998).
16. N. G. Anishchenko *et al.*, in *Proceedings of 5th International Symposium on High Energy Spin Physics, Brookhaven, 1982,* AIP Conf. Proc. **95**, 445 (1983).
17. L. S. Zolin, A. G. Litvinenko, Yu. K. Pilipenko, *et al.*, Kratk. Soobshch. Ob'edin. Inst. Yad. Issled., No. 2[88]-98, 27 (1998).
18. C. F. Perdrisat *et al.*, Phys. Rev. Lett. **59**, 2840 (1987); V. Punjabi *et al.*, Phys. Rev. C **39**, 608 (1989); V. G. Ableev *et al.*, Pis'ma Zh. Éksp. Teor. Fiz. **47**, 558 (1988) [JETP Lett. **47**, 649 (1988)]; Kratk. Soobshch. Ob'edin. Inst. Yad. Issled., No. 4[43]-90, 5 (1990); T. Aono *et al.*, Phys. Rev. Lett. **74**, 4997 (1995).
19. L. S. Azhgireĭ, V. V. Vikhrov, A. A. Zhdanov, *et al.*, Prib. Tekh. Éksp., No. 1, 51 (1997).
20. L. S. Azhgirey, V. N. Zhmyrov, V. P. Ladygin, and G. D. Stoletov, Kratk. Soobshch. Ob'edin. Inst. Yad. Issled., No. 3[95]-99, 20 (1999).
21. V. P. Ladygin, Nucl. Instrum. Methods Phys. Res. A **437**, 98 (1999).
22. M. Lacombe, B. Loiseau, R. Vinh Mau, *et al.*, Phys. Rev. C **21**, 861 (1980); Phys. Lett. B **101B**, 139 (1981).
23. R. Machleidt, K. Holinde, and Ch. Elster, Phys. Rep. **149**, 1 (1987).
24. T. Udagawa, P. Oltmanns, F. Osterfeld, and S. W. Hong, Phys. Rev. C **49**, 3162 (1994); V. Dmitriev, Nucl. Phys. A **577**, 249c (1994).
25. M. Garçon, J. Arvieux, D. H. Beck, *et al.*, Phys. Rev. C **49**, 2516 (1994) and references therein.
26. D. Abbott *et al.*, nucl-ex/0001006.
27. V. Ghazikhanian, B. Aas, D. Adams, *et al.*, Phys. Rev. C **43**, 1532 (1991).
28. R. Bijker, F. Iachello, and A. Levitan, Ann. Phys. (N. Y.) **236**, 69 (1994); Phys. Rev. C **54**, 1935 (1996); Phys. Rev. D **55**, 2862 (1997).
29. P. L. Chung, F. Coester, B. D. Keister, and W. N. Polyzou, Phys. Rev. C **37**, 2000 (1988).
30. Yu. N. Uzikov, Yad. Fiz. **60**, 1771 (1997) [Phys. At. Nucl. **60**, 1616 (1997)].
31. L. S. Azhgireĭ and N. P. Yudin, Preprint No. P1-99-157, OIYaI (Joint Inst. for Nuclear Research, Dubna, 1999); Yad. Fiz. **63**, 2280 (2000) [Phys. At. Nucl. **63**, 2184 (2000)].
32. S. Hirenzaki, E. Oset, C. Djalali, and M. Morlet, Phys. Rev. C **61**, 044605 (2000).

Translated by A. Isaakyan

Physics of Atomic Nuclei, Vol. 64, No. 11, 2001, pp. 1971–1987. Translated from Yadernaya Fizika, Vol. 64, No. 11, 2001, pp. 2056–2072.

ELEMENTARY PARTICLES AND FIELDS
Theory

Solar Neutrinos in Models Involving an Extended Higgs Sector

O. M. Boyarkin* **and T. I. Bakanova**

Belarussian State Pedagogical University, Sovetskaya ul. 18, Minsk, 220050 Belarus

Received April 26, 2000; in final form, December 4, 2000

Abstract—Neutrino oscillations in matter and in a magnetic field are investigated within models involving an extended Higgs sector. The left–right model containing a bidoublet and two triplets of Higgs fields (LRM) and the general two-Higgs-doublet model (GTHDM) are chosen by way of example. It is shown that the interaction of leptons with physical Higgs bosons can substantially change the pattern of oscillations in these models in relation to the predictions of the Standard Model (SM). Upper limits on the Yukawa coupling constants and on the Higgs boson masses are found in order to obtain maximum corrections to the SM solar-matter potential V^{SM}. By using constraints on these parameters from the literature and those that are obtained here, it is possible to estimate corrections to V^{SM} that come exclusively from charged Higgs bosons. The maximum value of these corrections is 40% of V^{SM} within the LRM and 10% of V^{SM} within the GTHDM. The entire body of information about the contributions of physical Higgs bosons to the solar-matter potential can be obtained by studying the Lorentz structure of the amplitudes for the reactions $e^-\nu_l \to e^-\nu_{l'}$ at low energies. © *2001 MAIK "Nauka/Interperiodica".*

1. INTRODUCTION

At present, the entire body of experimental data indicates that the Standard Model describes correctly the interactions of elementary particles at energies achievable at currently existing accelerators. However, it is conceivable that we are still far from the true picture of the real world, with the Standard Model being an approximate theory that loses its predictive power as soon as energy reaches values of about a few hundred GeV. Moreover, numerous attempts at going beyond the Standard Model are also motivated by the quest of researchers for solving more consistently and more elegantly problems existing within the Standard Model. This can be exemplified by the problem in the neutrino sector of the theory. The structure of the Standard Model is such that, upon a spontaneous breakdown of symmetry, the neutrino remains a massless particle [a Dirac mass proportional to $\overline{\nu}_L\nu_R$ does not arise because there is no right-handed neutrino singlet in the theory, whereas the appearance of the Majorana mass proportional to $\nu_L^T C\sigma_2\nu_L$ is forbidden by $SU(2)_L$ invariance]. However, the results of experiments with cosmic and terrestrial neutrinos furnish compelling evidence in favor of a nonzero neutrino mass and mixing in the neutrino sector. The aforesaid is confirmed, in particular, by a discrepancy between the solar-neutrino flux predicted by the standard solar model, on one hand, and those that were measured by the Homestake, Kamiokande, GALLEX, and SAGE experiments [1], on the other hand. It should be noted that there exist solar models in which attempts are made to solve the neutrino problem without resort to types of neutrino behavior that are anomalous from the point of view of the Standard Model (vacuum oscillations, effects associated with the enhancement of oscillations in a medium and in a magnetic field, oscillations caused by lepton-flavor-violating currents, etc.). However, the most recent helioseismological data favor the standard solar model, strengthening our belief that the solar-neutrino problem must indeed be solved on the basis of models that predict a nonzero neutrino mass and the existence of the $\nu_e \to \nu_a$ neutrino-oscillation channel ($a = \mu, \tau$).

Earlier experiments [2] and recent results of the SuperKamiokande collaboration [3] on the fluxes of atmospheric neutrinos also suggest that the neutrino is massive. Data from these experiments are best explained under the assumption that the $\nu_\mu \to \nu_\tau$ oscillation channel is dominant. The possibility that a $\nu_\mu \to \nu_e$ admixture is present cannot be ruled out [4], because a description in terms of $\nu_\mu \to \nu_e$ oscillations exclusively also makes it possible to fit the theory to experimental data, albeit the quality of the resulting fit is much poorer.

There are two accelerator neutrino experiments that give grounds to believe that the neutrino has a nonzero mass and is a mixture of physical states. Specifically, experiments with the Los Alamos liquid

*e-mail: boyarkin@bspu.unibel.by

scintillation detector [5] and the KARMEN 2 experiment [6] indicate the presence of oscillations both in the $\overline{\nu}_\mu \to \overline{\nu}_e$ and in the $\nu_\mu \to \nu_e$ channel.

A more detailed investigation into the neutrino sector is expected from future high-statistics long-baseline oscillation experiments where a high-energy neutrino beam created at an accelerator travels a distance L in Earth's rock and is recorded by an underground detector. In the experiments currently performed by the CERN–Gran Sasso ICARUS and the Fermilab–Soudan MINOS collaboration (see [7] and [8], respectively), L is only 730 km, which is insufficient for a full development of the oscillations [9]. Presently, projects are being discussed (see, for example, [10] and references therein) in which a neutrino detector is arranged at the Laboratori Nazionali del Gran Sasso, while a neutrino source (muon collider producing a neutrino beam of energy in the range 10–30 GeV) is situated either at Fermilab ($L =$ 7400 km) or at KEK ($L = 8800$ km).

Thus, interest in theories where the left-handed neutrino develops a nonzero rest mass in a natural way is quite understandable. For such theories, we choose here the left–right model (LRM) featuring a bidoublet and two triplets of Higgs fields [11] and the model that is constructed on the basis of the Standard Model as its most general modification involving two doublets of Higgs fields (general two-Higgs-doublet model abbreviated here as GTHDM) [12]. The existence of lepton-flavor-violating currents at the tree level is a property common to these two models. The appearance of lepton-flavor-violating currents, both neutral and charged ones, is due to the interaction of physical Higgs bosons with leptons. For the first time, the effect of neutral lepton-flavor-violating currents on neutrino oscillations in matter was investigated in [13]. It turned out that limits on the parameters of neutrino oscillations change significantly upon taking into account these currents. In recent years, the idea of using lepton-flavor-violating currents to explain the results of experiments with cosmic and terrestrial neutrinos [14] has become ever more popular. It should be emphasized that, in theories involving massive neutrinos, mixing in the neutrino sector and the existence of lepton-flavor-violating currents are manifested as two facets of the same phenomenon that is associated with the choice of the Yukawa Lagrangian and the Higgs potential. Thus, the two effects exist in the theory simultaneously, so that any attempt at using them separately is a rough approximation.

The objective of the present study is to analyze the evolution of a neutrino beam in a medium and in a magnetic field with allowance for effects associated with lepton-flavor-violating currents and for mixing in the neutrino sector.

The ensuing exposition is organized as follows. In Section 2, we consider this problem within the LRM. In Section 3, the behavior of a neutrino flux is investigated on the basis of the GTHDM. In Section 4, constraints on the Yukawa coupling constants and on the masses of physical Higgs bosons are obtained by studying the channels of muon and tau-lepton decays. By using the resulting limits, we estimate the maximum values of corrections to the solar-matter potential in relation to Standard Model predictions. In the Conclusion, we analyze our results.

2. NEUTRINO OSCILLATIONS IN THE LRM

Left–right models relying on the gauge group $SU(2)_L \times SU(2)_R \times U(1)_{B-L}$ [15, 16] and involving the bidoublet $\Phi(1/2, 1/2, 0)$ and two triplets $\Delta_L(1, 0, 2)$ and $\Delta_R(0, 1, 2)$ of Higgs fields stand out among the extensions of the Standard Model. (i) A dynamical solution to the parity-violation problem in weak interactions, (ii) the emergence of a small left-handed-neutrino mass owing to the so-called seesaw mechanism, and (iii) the presence of elements among physical Higgs bosons that are common to these models and popular extensions of the Standard Model {minimal supersymmetric Standard Model [17], the model based on the gauge group $SU(3)_L \times U(1)_N$ [18], the superstring-motivated model based on the gauge group $SU(4) \times O(4)$ [19], and so on} are their main advantages. The present analysis is based on the asymmetric LRM ($g_L \neq g_R$) [20] featuring a potential of the most general form [21]. Thus, the results to be obtained will reproduce the spectrum of predictions of all possible LRM versions. Upon a spontaneous breakdown of symmetry, there arise, in the model, four doubly charged, four singly charged, four neutral scalar, and two neutral pseudoscalar Higgs bosons ($\Delta_{1,2}^{(\pm\pm)}$, $h^{(\pm)}$ and $\tilde{\delta}^{(\pm)}$, $S_{1,2,3,4}$, and $P_{1,2}$, respectively). The form and the strength of their interactions with fermions are completely determined by the choice of Yukawa Lagrangian $\mathcal{L}_{\rm Y}$ and potential V of the Higgs fields. The Yukawa Lagrangian describing the gauge-invariant interaction in the lepton sector is taken here in the form

$$\mathcal{L}_{\rm Y} = -\sum_{a,b}\{h_{ab}\bar{\Psi}_{aL}\Phi\Psi_{bR} + h'_{ab}\bar{\Psi}_{aL}\tilde{\Phi}\Psi_{bR} \quad (1)$$

$$+ if_{ab}[\Psi_{aL}^T C\sigma_2(\boldsymbol{\sigma}\cdot\boldsymbol{\Delta}_L)\Psi_{bL} + (L \to R)] + \text{conj.}\},$$

where Ψ_{aL} (Ψ_{aR}) is the left-handed (right-handed) lepton doublet, $\sigma_{1,2,3}$ are the Pauli matrices, C is the charge-conjugation matrix, $\tilde{\Phi} = \sigma_2\Phi^*\sigma_2$, a and b are the generation indices, h_{ab} and h'_{ab} are the bidoublet Yukawa coupling constants, and $f_{ab} = f_{ba}$ stands for the triplet Yukawa coupling constants.

From expression (1), it follows that the LRM will lead to lepton-flavor violation at the tree level. In the Standard Model, such a phenomenon does not occur since the lepton-mass matrix M_l is proportional to the matrix constructed from the Yukawa coupling constants, so that the diagonalization of the former entails the diagonalization of the interaction between the physical Higgs boson and leptons. In the LRM, the lepton mass matrix is the sum of four matrices (they are products of the Yukawa coupling constants and vacuum expectation values), which obviously cannot be diagonalized simultaneously. In order to demonstrate this, we note that, upon going over to the basis of states of physical Higgs bosons, we obtain, from (1), the interaction Lagrangians

$$\mathcal{L}_l^{dc} = -\sum_{a,b}\frac{f_{ab}}{2}[\overline{l_a^c}(1+\gamma_5)l_b c_{\theta_d} - \overline{l_a^c}(1-\gamma_5)l_b s_{\theta_d}]\Delta_1^{(++)} + (\Delta_1 \to \Delta_2, \theta_d \to \theta_d - \frac{\pi}{2}) + \text{conj.}, \quad (2)$$

$$\mathcal{L}_l^{sc} = \sum_{a,b}\Bigg\{ b\Big[\frac{h'_{ab}k_2 - h_{ab}k_1}{2k_+}\overline{\nu}_a(1-\gamma_5)l_b - \frac{h_{ab}k_2 - h'_{ab}k_1}{2k_+}\bar{N}_a(1+\gamma_5)l_b\Big]h^{(+)} + \frac{f_{ab}}{\sqrt{2}}\Big[\overline{l^c}_a(1+\gamma_5)\nu_b\Big(\frac{d\beta k_0^2}{(\alpha+\rho_1-\rho_3/2)v_R^2}h^{(+)} - d\tilde{\delta}^{(+)}\Big) + \overline{l_a^c}(1-\gamma_5)N_b\Big(\frac{ak_0}{v_R}h^{(+)} + \frac{a\beta k_0}{(\alpha+\rho_1-\rho_3/2)v_R}\tilde{\delta}^{(+)}\Big)\Big] + \text{conj.}\Bigg\}, \quad (3)$$

$$\mathcal{L}_l^{n} = -\frac{1}{\sqrt{2}k_+}\sum_a m_a\bar{l}_{aR}l_{aL}(S_1c_{\theta_0} - S_2s_{\theta_0}) - \frac{1}{\sqrt{2}k_+}\sum_{a,b}\bar{l}_{aR}l_{bL}[(h_{ab}k_1 - -h'_{ab}k_2) \times (S_1s_{\theta_0} + S_2c_{\theta_0}) + i(h_{ab}k_1 + h'_{ab}k_2)P_1] - \frac{1}{\sqrt{2}k_+}\sum_{a,b}\{\bar{N}_{aR}\nu_{bL}[h_{ab}(k_1c_{\theta_0} - k_2s_{\theta_0}) + h'_{ab}(k_2c_{\theta_0} + k_1s_{\theta_0})]S_1 - [h_{ab}(k_1s_{\theta_0} + k_2c_{\theta_0}) + h'_{ab}(k_2s_{\theta_0} - k_1c_{\theta_0})]S_2 - i(h_{ab}k_2 + h'_{ab}k_1)P_1\} - \frac{1}{\sqrt{2}}\sum_{a,b}f_{ab}[\overline{\nu}^c_{aL}\nu_{bL}(S_4 + iP_2) + \bar{N}^c_{aR}N_{bR}S_3] + \text{conj.}, \quad (4)$$

where

$$\langle\delta^0_{L,R}\rangle = \frac{v_{L,R}}{\sqrt{2}}, \quad \langle\Phi_1^0\rangle = k_1, \quad \langle\Phi_2^0\rangle = k_2,$$

$$k_\pm = \sqrt{k_1^2 \pm k_2^2}, \quad k_0 = \frac{k_-^2}{\sqrt{2}k_+}, \quad \alpha = \frac{\alpha_3 k_+^2}{2k_-^2},$$

$$\beta = \frac{k_+^2(\beta_1k_1 + 2\beta_3k_2)}{2k_-^2k_0},$$

$$a = \left[1 + \Big(1 + \frac{\beta^2}{(\alpha+\rho_1-\frac{\rho_3}{2})^2}\Big)\frac{k_0^2}{v_R^2}\right]^{-1/2},$$

$$b = \left(1 + \frac{k_0^2}{v_R^2}\right)^{-1/2},$$

$$d = \left[1 + \frac{\beta^2k_0^2}{(\alpha+\rho_1-\frac{\rho_3}{2})^2v_R^2}\right]^{-1/2};$$

$c_{\theta_0} = \cos\theta_0$ and $s_{\theta_0} = \sin\theta_0$, θ_0 being the mixing angle in the sector of neutral Higgs bosons; $c_{\theta_d} = \cos\theta_d$ and $s_{\theta_d} = \sin\theta_d$, θ_d being the mixing angle in the sector of doubly charged Higgs bosons; α_i, ρ_i, and β_i are constants appearing in the Higgs potential; and the index c denotes the charged-conjugation operation.

Since the neutrino is a Majorana particle in the LRM, the first and the fourth term in (3) can be rewritten, respectively, as

$$\sum_{a,b} b\lambda^*_{\nu a}\frac{h'_{ab}k_2 - h_{ab}k_1}{k_+}\overline{l_b^c}(1-\gamma_5)\nu_a h^{(+)} \quad (5)$$

and as

$$-\sum_{a,b}\lambda_{\nu a}\frac{df_{ab}}{\sqrt{2}}\overline{\nu}_a(1+\gamma_5)l_b\tilde{\delta}^{(+)}. \quad (6)$$

In deriving relations (5) and (6), we have taken into account the identity

$$\overline{\nu}_a(1-\gamma_5)l_b \equiv \overline{(\nu_a^c)^c}(1-\gamma_5)(l_b^c)^c \equiv -(\nu_a^c)^TC^{-1}(1-\gamma_5)C(\overline{l_b^c})^T \equiv \overline{l_b^c}(1-\gamma_5)\nu_a^c$$

and the condition that the Majorana spinor is self-conjugate,

$$\nu_a^c = \lambda^*_{\nu a}\nu_a, \quad (7)$$

where $\lambda_{\nu a}$ is the phase factor of ν_a. It should be recalled that not only do Yukawa coupling constants determine the interaction between leptons and physical Higgs bosons, but they also fix the parameters of neutrino oscillations [22], this being one of the most important properties of the LRM. This in turn means that, by investigating the processes of Higgs boson interaction only with charged leptons, we can obtain an entire body of required information about the values of the mixing angles and about the difference of the squares of the neutrino masses. For example, these can be the processes (see [15, 23] and references therein)

$$e^-e^- \to W^-W^-, \quad (8)$$

$$e^-\mu^+ \to W^-W^+, \quad (9)$$

$$e^-\mu^+ \to e^+\mu^-. \quad (10)$$

Thus, the LRM belongs to the class of models where the parameters of neutrino oscillations can be measured both by direct and by indirect methods.

Along with mass, the dipole magnetic moment is an important property of the neutrinos, the latter being induced by radiative corrections to the electromagnetic neutrino vertex. In the Standard Model where $m_\nu \neq 0$, this quantity is extremely small, since, on the internal neutrino line, helicity flip, which is necessary for the existence a nonvanishing magnetic moment, is due exclusively to the neutrino-mass term,

$$\mu_{\nu_a\nu_b} = \frac{3G_F}{16\sqrt{2}\pi^2}(m_{\nu_a} + m_{\nu_b})\sum_l \mathcal{U}^\dagger_{al}\mathcal{U}_{lb}\mu_\mathrm{B}, \quad (11)$$

where G_F is the Fermi constant, μ_B is the Bohr magneton, and $\nu_l = \sum_b \mathcal{U}_{lb}\nu_b$. Under the assumption that the tau-lepton mass is about a few MeV, we then obtain a value of $10^{-16}\mu_\mathrm{B}$ for $\mu_{\nu_{e(\mu)}\nu_\tau}$. The LRM belongs to the class of models that emerge as extensions of the Standard Model and which can lead, at some model-parameter values compatible with experimental data, to $\mu_{\nu_{e(\mu)}\nu_\tau}$ of about $10^{-12}\mu_\mathrm{B}$. Diagrams that induce a neutrino magnetic moment at the one-loop level can be divided into three classes: (i) diagrams involving virtual $W^\pm_{1,2}$ bosons, (ii) diagrams involving virtual $h^{(\pm)}$ and $\tilde{\delta}^{(\pm)}$ Higgs bosons, and (iii) diagrams involving $W^\pm_{1,2}$ bosons and $h^{(\pm)}$ and $\tilde{\delta}^{(\pm)}$ Higgs bosons in virtual states.

The contributions of diagrams belonging to the first and the second class are dominant. The neutrino magnetic moment caused by $W^\pm_1$-boson exchange in the basis of pure mass states is given by [24]

$$\mu^{WW}_{\nu_i\nu_j} = \frac{32\pi^2 e g_L g_R}{m^2_{W_1}}\sin 2\xi \sum_l m_l \mathcal{V}^\dagger_{i\nu_l}\mathcal{V}_{\nu_l j}, \quad (12)$$

where ξ is the mixing angle for charged gauge bosons and the 6×6 matrix $\mathcal{V}_{\alpha_l i}$ ($\alpha_l = \nu_l, N_l$) describes the transition from the flavor basis $\Psi^T_f = (\nu^T_e, N^T_e, \nu^T_\mu, N^T_\mu, \nu^T_\tau, N^T_\tau)$ to the basis of pure mass states.

The neutrino magnetic moment induced by the diagrams involving $\tilde{\delta}^{(\pm)}$ Higgs bosons in virtual states appears to be greater than the neutrino magnetic moment induced by the exchange of $h^{(\pm)}$ Higgs bosons and has the form [24]

$$\mu^{\tilde{\delta}\tilde{\delta}}_{\nu_a\nu_b} = \frac{e f_{ab}}{8\pi^2 m^2_{\tilde{\delta}}}\left[m_a f_{aa}\left(\ln\frac{m^2_{\tilde{\delta}}}{m^2_a} - 1\right)\right. \quad (13)$$

$$\left. + m_b f_{bb}\left(\ln\frac{m^2_{\tilde{\delta}}}{m^2_b} - 1\right)\right].$$

The expression for $\mu^{WW}_{\nu_i\nu_j}$ includes the factor $\sin\varphi_l$ (φ_l is the mixing angle between the light ν_l and the heavy N_l neutrino belonging to the same generation l). There exists a theoretical prejudice in favor of very small values of this angle (about 10^{-6}–10^{-5}). In this case, $\mu^{WW}_{\nu_i\nu_j}$ amounts to $10^{-15}\mu_\mathrm{B}$, provided that use is made of the upper limit of 3.1×10^{-2} on ξ. It was shown in [23], however, that, even if the seasaw relation

$$m_{\nu_l} m_{N_l} = m^2_l$$

holds, the angles φ_l can be rather large ($\sim 10^{-2}$). The necessary condition for this is that v_L is nonzero. At $\varphi_l \sim 10^{-2}$ and $\xi = \xi_\mathrm{max}$, $\mu^{WW}_{\nu_i\nu_j}$ is about $10^{-12}\mu_\mathrm{B}$.

Let us determine the maximum possible values of $\mu^{\tilde{\delta}\tilde{\delta}}_{\nu_a\nu_b}$ by using the existing constraints on the triplet Yukawa coupling constants and on the Higgs boson masses. Searches for the decay $\mu \to e\gamma$ lead to the constraint [25]

$$f_{\mu\mu}f_{e\mu} < 2\times 10^{-10}\left(\frac{m_\Delta}{\mathrm{GeV}}\right)^2, \quad (14)$$

where m_Δ is the mass of the lightest doubly charged Higgs boson. By assuming that $m_\Delta = 1$ TeV and by using the upper limit on $f_{\mu\mu}f_{e\mu}$, we obtain

$$\mu^{\tilde{\delta}\tilde{\delta}}_{\nu_e\nu_\mu} \approx 10^{-12}\mu_\mathrm{B} \quad (15)$$

at $m_{\tilde{\delta}} = 100$ GeV. It should be recalled that the mixing angles within a neutrino generation can be sizable only at large values of the Yukawa coupling constants [22].

Let us discuss the evolution of the solar-neutrino flux. We begin by considering the case of negligibly small values of the neutrino magnetic moment. The effect of heavy neutrinos on the oscillation pattern can be disregarded, because there is every reason to believe that their masses lie in the region around a few TeV. The interaction between left- and right-handed light neutrinos can be induced either by the neutrino magnetic moment or by lepton-flavor-violating currents. It will be shown below that, in the LRM, lepton-flavor-violating currents do not mix neutrinos of different helicities. For this reason, the evolution equations for left- and right-handed neutrinos will be independent of each other. We consider a neutrino system consisting of ν_{eL}, $\nu_{\mu L}$, and $\nu_{\tau L}$; further, we set the CP-violation phase to zero and choose the scheme of neutrino-generation mixing in the form

$$\begin{pmatrix}\nu_e\\ \nu_\mu\\ \nu_\tau\end{pmatrix} = \mathcal{U}\begin{pmatrix}\nu_1\\ \nu_2\\ \nu_3\end{pmatrix} \quad (16)$$

$$= \begin{pmatrix} 1 & 0 & 0 \\ 0 & c_{23} & s_{23} \\ 0 & -s_{23} & c_{23} \end{pmatrix} \begin{pmatrix} c_{13} & 0 & s_{13} \\ 0 & 1 & 0 \\ r - s_{13} & 0 & c_{13} \end{pmatrix} \times \begin{pmatrix} c_{12} & s_{12} & 0 \\ -s_{12} & c_{12} & 0 \\ 0 & 0 & 1 \end{pmatrix} \begin{pmatrix} \nu_1 \\ \nu_2 \\ \nu_3 \end{pmatrix},$$

where φ_{ik} is the mixing angle between ν_i and ν_k in a vacuum, $c_{ik} = \cos\varphi_{ik}$, and $s_{ik} = \sin\varphi_{ik}$.

In the ultrarelativistic limit $[E \gg \max(m_1, m_2, m_3)]$, the evolution equation for the case of motion in a vacuum has the form

$$i\frac{d}{dz}\begin{pmatrix} \nu_{eL} \\ \nu_{\mu L} \\ \nu_{\tau L} \end{pmatrix} = \mathcal{H}^v \begin{pmatrix} \nu_{eL} \\ \nu_{\mu L} \\ \nu_{\tau L} \end{pmatrix}, \qquad (17)$$

where

$$\mathcal{H}^v_{11} = \frac{1}{6E}\left[(3s^2_{13} - 1)\Delta m^2_{32} + (1 - 3c^2_{12}c^2_{13})\Delta m^2_{21}\right],$$

$$\mathcal{H}^v_{22} = \frac{1}{6E}[(3c_{13}s^2_{23} - 1)\Delta m^2_{32} + (1 - 3b^2_1)\Delta m^2_{21}],$$

$$\mathcal{H}^v_{12} = \frac{c_{13}}{2E}(s_{13}s_{23}\Delta m^2_{32} + c_{12}b_1\Delta m^2_{21}),$$

$$\mathcal{H}^v_{23} = \frac{1}{2E}(c^2_{13}c_{23}s_{23}\Delta m^2_{32} + b_1 b'_1\Delta m^2_{21}),$$

$$b_1 = c_{23}s_{12} + c_{12}s_{23}s_{13},$$

$$b'_1 = b_1\left(\varphi_{23} \to \varphi_{23} - \frac{\pi}{2}\right),$$

$$\Delta m^2_{ik} = m^2_i - m^2_k,$$

$$\mathcal{H}^v_{33} = \mathcal{H}^v_{22}\left(\varphi_{12} \to \varphi_{12} - \frac{\pi}{2}\right),$$

$$\mathcal{H}^v_{13} = \mathcal{H}^v_{12}\left(\varphi_{12} \to \varphi_{12} + \frac{\pi}{2}\right).$$

In a medium, the elements of the Hamiltonian $\mathcal{H}^v$ undergo changes owing to interactions with gauge bosons and Higgs bosons. Figures 1 and 2 show Feynman diagrams for elastic forward $\nu_{aL}e^-$ scattering. The parts of the interaction Lagrangian that are determined by relations (5) and (6) generate the diagrams in Fig. 2. If the arrows on a fermion line are directed oppositely, this means that it is not the spinor u but its charge-conjugate counterpart v that must be used to describe the respective charged fermion. Diagrams involving the exchanges of W_2 and Z_2 gauge bosons are disregarded here, because

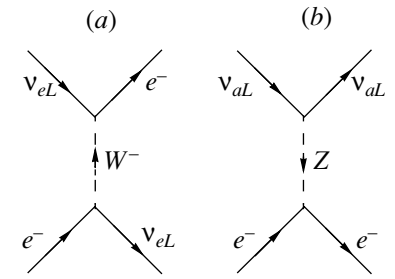

Fig. 1. Feynman diagrams for the process $e^-\nu_{aL} \to e^-\nu_{aL}$ in the Standard Model.

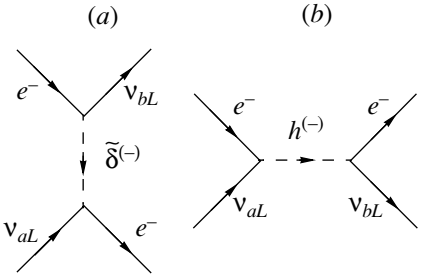

Fig. 2. LRM Feynman diagrams for the process $e^-\nu_{aL} \to e^-\nu_{bL}$ that are not present in the Standard Model.

corrections to the solar-matter potential that stem from such diagrams are at a level of 1% [26].

By using the Fierz transformation and performing averaging over solar matter, we find that the contribution to the solar-matter potential from the diagrams in Fig. 2 can be represented as

$$V^H_{ab} = \left(\frac{\alpha_{ea}\alpha_{eb}}{2m^2_h} - \frac{f_{ea}f_{eb}}{m^2_{\tilde{\delta}}}\right) n_e, \qquad (18)$$

where

$$\alpha_{ab} = \frac{h'_{ab}k_2 - h_{ab}k_1}{k_+}$$

and n_e (n_n) is the electron (neutron) density in solar matter.

The total contribution of the diagrams in Figs. 1 and 2 to the solar-matter potential is given by

$$V_{ee} = \frac{g^2_L}{4m^2_W}\left(\frac{1}{2}n_n - n_e\right) + V^H_{ee},$$

$$V_{aa} = \frac{g^2_L}{8m^2_W}n_n + V^H_{aa}, \quad V_{ab} = V^H_{ab}.$$

The evolution equation in the flavor basis has the form

$$i\frac{d}{dz}\Psi = \mathcal{H}^m\Psi, \qquad (19)$$

where

$$\mathcal{H}^m_{12} = \mathcal{H}^v_{12} + V^H_{e\mu}, \quad \mathcal{H}^m_{13} = \mathcal{H}^v_{13} + V^H_{e\tau},$$
$$\mathcal{H}^m_{23} = \mathcal{H}^v_{23} + V^H_{\mu\tau}, \quad V^{\rm SM} = -\sqrt{2}G_{\rm F}n_e,$$
$$\mathcal{H}^m_{11} = \mathcal{H}^v_{11} + V^{\rm SM} + V^H_{ee}, \quad \mathcal{H}^m_{22} = \mathcal{H}^v_{22} + V^H_{\mu\mu},$$
$$\mathcal{H}^m_{33} = \mathcal{H}^v_{33} + V^H_{\tau\tau},$$

and we have neglected the quantity proportional to the identity matrix.

Let us proceed to examine resonance transitions in the neutrino system for the case of motion in solar matter. Three resonance transitions are possible. They occur between the i and k states at densities $n_e(z)$ corresponding to the minimum of the difference

$$\Delta M^2_{ik} = M^2_i - M^2_k,$$

where the expressions for M^2_i are presented in the Appendix. Since the graphs of the functions $M^2_i(z)$ do not intersect, only two of the three possible resonances will be realized, depending on the structure parameters of the model. The approximate values of the resonance densities $n_e(z_r)$ can be found by equating the diagonal elements of the Hamiltonian $\mathcal{H}^m$:

$$\frac{1}{2E}\left[(s^2_{13} - c^2_{13}s^2_{23})\Delta m^2_{32} + (b^2_1 - c^2_{12}c^2_{13})\Delta m^2_{21}\right] \tag{20}$$
$$= \left(\sqrt{2}G_{\rm F} - \frac{\alpha^2_{ee} - \alpha^2_{\mu e}}{2m^2_h} + \frac{f^2_{ee} - f^2_{\mu e}}{m^2_{\tilde\delta}}\right) n_e,$$

$$\frac{1}{2E}[(s^2_{13} - c^2_{13}c^2_{23})\Delta m^2_{32} + (b'^2_1 - c^2_{12}c^2_{13})\Delta m^2_{21}] \tag{21}$$
$$= \left(\sqrt{2}G_{\rm F} - \frac{\alpha^2_{ee} - \alpha^2_{\tau e}}{2m^2_h} + \frac{f^2_{ee} - f^2_{\tau e}}{m^2_{\tilde\delta}}\right) n_e,$$

$$\frac{1}{2E}[c^2_{13}(s^2_{23} - c^2_{23})\Delta m^2_{32} + (b'^2_1 - b^2_1)\Delta m^2_{21}] \tag{22}$$
$$= \left(\frac{\alpha^2_{\tau e} - \alpha^2_{\mu e}}{2m^2_h} - \frac{f^2_{\tau e} - f^2_{\mu e}}{m^2_{\tilde\delta}}\right) n_e.$$

Equations (20), (21), and (22) are conditions under which the resonance transitions $\nu_{eL} \leftrightarrow \nu_{\mu L}$, $\nu_{eL} \leftrightarrow \nu_{\tau L}$, and $\nu_{\mu L} \leftrightarrow \nu_{\tau L}$, respectively, are realized. The dependence of the off-diagonal elements of the Hamiltonian $\mathcal{H}^m_{ab}$ on $n_e(z)$ can lead to interesting physical implications. We now assume that the conditions in (20) and (21) are satisfied. However, the conversion of muon neutrinos into tau neutrinos is not observed, since $\mathcal{H}^m_{23}$ vanishes at the density value corresponding to the resonance transition $\nu_{\mu L} \to \nu_{\tau L}$. Thus, we can see that, even at nonzero values of the mixing angle φ_{23}, there are still no tau neutrinos in the solar-neutrino flux.

In the case being considered, the probability of survival of left-handed electron neutrinos, $\mathcal{P}(\nu_{eL} \to \nu_{eL})$, can be obtained in an analytic form. Considering that the adiabatic approximation is not valid only in the regions where the resonance transitions are localized, we can represent the survival probability $\mathcal{P}(\nu_{eL} \to \nu_{eL})$ in the form

$$\mathcal{P}(\nu_{eL} \to \nu_{eL}) = \sum_{a,b} \mid \mathcal{U}_{ae}(\varphi^m_{nk}) \mid^2 \tag{23}$$
$$\times \mid \mathcal{U}_{be}(\varphi^m_{nk}) \mid^2 (p^S_{ab} + p^D_{ab}),$$

where φ^m_{nk} $(n, k = 1, 2, 3)$ are the mixing angles in matter at the point of ν_{eL} generation (their values are quoted in the Appendix) and p^S_{ab} ($p^D_{ab} = \sum_r p^S_{ar}p^S_{rb}$) is the probability of the resonance transition between ν_{aL} and ν_{bL} for a single (double) passage through the resonance region. With the aid of the method of complex trajectories proposed by Landau, we can find the expression for p^S_{ab} in the form [27]

$$p^S_{ab} = \exp\left[-\frac{1}{E}\,{\rm Im}\int\limits_{N_{ab}}^{\delta N_{ab}} \frac{\Delta M^2_{ab}(n^{ab}_e)}{\mid \dot N_{ab} \mid} dn_e\right], \tag{24}$$

where integration is performed in the upper complex half-plane of the variable $n_e(z)$. The quantities $n^{ab}_e = N_{ab} + i\delta N_{ab}$, where N_{ab} and δN_{ab} are the resonance electron densities and the resonance-transition widths, respectively, are found as complex solutions to the equations

$$\Delta M^2_{ab}(n^{ab}_e) = 0.$$

Under the condition that the resonances are isolated—that is, if the inequality

$$N_{ab} + \delta N_{ab} < N_{cd} - \delta N_{cd} \tag{25}$$

is satisfied—the resonance-transition probability can be calculated by using the approximate formula

$$p^S_{ab} = \exp\left(-\frac{\pi\delta N^2_{ab}}{16E \mid \dot N_{ab} \mid}\right), \tag{26}$$

where

$$\dot N_{ab} = dN_{ab}/dt.$$

In a rough approximation, the resonance width and the resonance electron density can be determined with the aid of the relations

$$\delta N_{ab} \sim \frac{2\mathcal{H}^m_{ab}}{V^0_{aa} - V^0_{bb}}, \quad N_{ab} \sim \frac{\mathcal{H}^v_{aa} - \mathcal{H}^v_{bb}}{V^0_{aa} - V^0_{bb}}, \tag{27}$$

where

$$V^0_{aa} = (-\sqrt{2}G_{\rm F})\delta_{ae} + \frac{\alpha^2_{ea}}{2m^2_h} - \frac{f^2_{ea}}{m^2_{\tilde\delta}}.$$

We further consider the evolution of the neutrino flux in solar matter, taking into account the effect of neutrino interaction with the magnetic field of the

Sun. For the sake of simplicity, we restrict ourselves to the two-flavor approximation, in which case the system under investigation is described by the wave function

$$\Psi^T = \left(\nu_{eL}^T, \nu_{XL}^T, \nu_{eR}^T, \nu_{XR}^T\right),$$

where $X = \mu, \tau$. For the axes z and x, we choose, respectively, the direction of the neutrino trajectory and the axis of rotation of the Sun. The magnetic field in the convection zone is then characterized by the geometric phase $\Phi(z)$ determined from the relation

$$B_x \pm iB_y = B_\perp \exp\left[\pm i\Phi(z)\right].$$

For the right-handed neutrinos, the diagrams in Fig. 3 make the following contribution to the solar-matter potential:

$$V_{ea}^R = -V_{ea}^H, \quad a = e, X. \tag{28}$$

In the flavor basis, the evolution equation for the system under consideration has the form

$$i\frac{d}{dz}\Psi = \mathcal{H}\Psi, \tag{29}$$

where

$$\mathcal{H} = \begin{pmatrix} \dfrac{\Delta m^2}{2E}s_\varphi^2 + V_{ee}^{mf} & \dfrac{\Delta m^2}{4E}s_{2\varphi} + V_{eX} & 0 & \mu_{eX}B_\perp \\ \dfrac{\Delta m^2}{4E}s_{2\varphi} + V_{eX} & \dfrac{\Delta m^2}{2E}c_\varphi^2 + V_{XX}^{mf} & -\mu_{Xe}B_\perp & 0 \\ 0 & -\mu_{Xe}^*B_\perp & \dfrac{\Delta m^2}{2E}s_\varphi^2 - V_{ee}^{mf} & \dfrac{\Delta m^2}{4E}s_{2\varphi} - V_{eX} \\ \mu_{Xa}^*B_\perp & 0 & \dfrac{\Delta m^2}{4E}s_{2\varphi} - V_{eX} & \dfrac{\Delta m^2}{2E}c_\varphi^2 - V_{XX}^{mf} \end{pmatrix}.$$

Here, μ_{ik} is the magnetic moment between the i and the k neutrino state, $V_{ll}^{mf} = V_{ll} + (1/2)(d\Phi/dt)$, $s_{2\varphi} = \sin 2\varphi$, $\Delta m^2 = m_1^2 - m_2^2$, and the notation φ_{eX} is used for φ. We recall that the neutrino magnetic moments diagonal in the lepton flavor are equal to zero owing to CPT invariance.

In the system under investigation, there can exist four resonance transitions that can occur under the conditions

$$\frac{\Delta m^2}{2E}c_{2\varphi} + V_{XX}^{mf} - V_{ee}^{mf} = 0 \quad (\nu_{eL} \leftrightarrow \nu_{XL}), \tag{30}$$

$$\frac{\Delta m^2}{2E}c_{2\varphi} - V_{XX}^{mf} - V_{ee}^{mf} = 0 \quad (\nu_{eL} \leftrightarrow \nu_{XR}), \tag{31}$$

$$\frac{\Delta m^2}{2E}c_{2\varphi} + V_{XX}^{mf} + V_{ee}^{mf} = 0 \quad (\nu_{eR} \leftrightarrow \nu_{XL}), \tag{32}$$

$$\frac{\Delta m^2}{2E}c_{2\varphi} - V_{XX}^{mf} + V_{ee}^{mf} = 0 \quad (\nu_{eR} \leftrightarrow \nu_{XR}). \tag{33}$$

By using expressions determining the eigenvalues of the Hamiltonian $\mathcal{H}$ and the mixing angles in matter (they are presented in the Appendix), we can obtain, with the aid of (23), the probability of survival of left-handed electron neutrinos. Since the neutrino flux can traverse three resonance regions, the sum in the expression for $\mathcal{P}(\nu_{eL} \to \nu_{eL})$ also includes the terms

$$p_{ab}^T = \sum_{c,d} p_{ac}^S p_{cd}^S p_{db}^S.$$

3. NEUTRINO OSCILLATIONS IN A MODIFICATION OF THE STANDARD MODEL WITH TWO DOUBLETS OF HIGGS FIELDS

For the first time, a model that is based on the $SU(2)_L \times U(1)_Y$ gauge group and which involves two doublets of Higgs fields,

$$\Phi_j\left(\frac{1}{2}, 1\right) = \begin{pmatrix} \Phi_j^+ \\ \Phi_j^0 \end{pmatrix}, \quad j = 1, 2$$

(two-Higgs-doublet model or THDM), was proposed in [28]. Models of this type can be grouped into two classes where the fermion flavor is either violated or conserved at the tree level. The Yukawa Lagrangian and the Higgs potential in the THDM1 and in the THDM2 possess an additional discrete symmetry [29] ensuring fermion-flavor conservation. In the THDM1, fermions corresponding to up and down doublet components develop masses owing to the vacuum expectation values of one of the doublets of Higgs fields. In the THDM2, the generation of masses of up and down fermions is associated with the vacuum expectation values of Φ_1 and Φ_2, respectively. A model that does not possess a discrete symmetry that prevents the violation of the fermion flavor at the tree level is referred to as the THDM3 or the general THDM (GTHDM). It should be recalled that nonzero nondiagonal Yukawa coupling constants lead to the existence of lepton-flavor-violating currents, on one hand, and are precisely

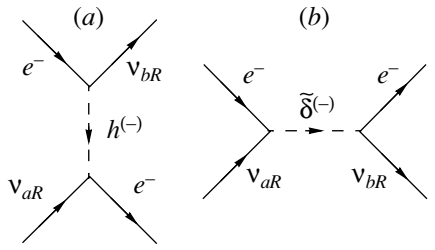

Fig. 3. Feynman diagrams describing the process $e^-\nu_{aR} \to e^-\nu_{bR}$ in the LRM.

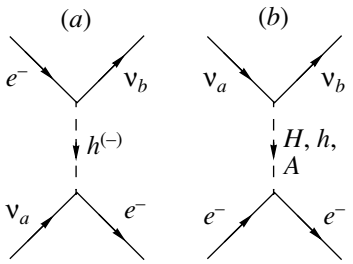

Fig. 4. Feynman diagrams for the process $e^-\nu_a \to e^-\nu_b$ within the GTHDM that involve $h^{(-)}$, h, H, and A exchanges.

those quantities that are responsible for mixing in the neutrino sector, on the other hand.

The Yukawa Lagrangian for the GTHDM is taken here in the commonly accepted form

$$\mathcal{L}_Y = -\sum_{a,b}(h^u_{ab}\bar{\Psi}_{aL}\tilde{\Phi}_1\nu_{bR} + h^d_{ab}\bar{\Psi}_{aL}\Phi_1 l_{bR} \quad (34)$$
$$+ h'^u_{ab}\bar{\Psi}_{aL}\tilde{\Phi}_2\nu_{bR} + h'^d_{ab}\bar{\Psi}_{aL}\Phi_2 l_{bR} + \text{conj.}),$$

where Ψ_{aL} is a left-handed lepton doublet, l_{aR} and ν_{aR} are right-handed lepton singlets, and $\tilde{\Phi}_{1,2} = i\sigma_2\Phi^*_{1,2}$. For the Higgs potential, we use the expression proposed in [30] and assume that it attains a minimum at

$$\Phi_j\left(\frac{1}{2},1\right) = \frac{1}{\sqrt{2}}\begin{pmatrix}0\\ v_j\end{pmatrix},$$

where

$$v_1^2 + v_2^2 = v^2 = (246\ \text{GeV})^2.$$

Upon a spontaneous breakdown of symmetry, we have the following physical Higgs bosons: two neutral CP-even scalars

$$\begin{pmatrix}H\\ h\end{pmatrix} = \begin{pmatrix}c_\alpha & s_\alpha\\ -s_\alpha & c_\alpha\end{pmatrix}\begin{pmatrix}\Phi_1^{0r}\\ \Phi_2^{0r}\end{pmatrix};$$

one neutral CP-odd scalar

$$A = -s_\beta\Phi_1^{0i} + c_\beta\Phi_2^{0i};$$

and two singly charged scalars

$$h^{(\pm)} = -s_\beta\Phi_1^{\pm} + c_\beta\Phi_2^{\pm},$$

where

$$\tan 2\alpha = \frac{v_1v_2(\lambda_3+\lambda_5)}{\lambda_2v_2^2 - \lambda_1v_1^2}, \quad \tan\beta = \frac{v_2}{v_1},$$

the superscript r (i) denotes the real (imaginary) part of the corresponding quantity, and λ_k are the parameters of the Higgs potential (see [30]).

By going over from the gauge basis to the basis of pure mass states, we obtain, from the Yukawa Lagrangian, the Lagrangians that describe the interaction of physical Higgs bosons with leptons and which have the form

$$\mathcal{L}_{h^{(\pm)}} = -\sqrt{2}v^{-1}\tan\beta\sum_a m_a\overline{\nu}_{aL}l_{aR}h^{(+)} \quad (35)$$
$$+\sum_{a,b}\kappa_{ab}\overline{\nu}_{aL}l_{bR}h^{(+)} + \text{conj.},$$

$$\mathcal{L}_{H,h,A} = \frac{1}{\sqrt{2}}\sum_{a,b}\Big\{\bar{l}_{aL}l_{bR}[(h^d_{ab}c_\alpha + h'^d_{ab}s_\alpha)H \quad (36)$$
$$+ (h'^d_{ab}c_\alpha - h^d_{ab}s_\alpha)h + i(h'^d_{ab}c_\beta - h^d_{ab}s_\beta)A]$$
$$+ (l\to\nu, d\to u) + \text{conj.}\Big\},$$

where $\kappa_{ab} = h'^d_{ab}c_\beta^{-1} + h^u_{ab}s_\beta - h'^u_{ab}c_\beta$. We note that the choice of Higgs sector ensures the Dirac character of neutrinos.

As in any gauge theory where the neutrino mass arises owing to a spontaneous breakdown of symmetry, there is a relationship between constants that determine the interaction of Higgs bosons with leptons, on one hand, and the neutrino-oscillation parameters, on the other hand. In the two-flavor approximation, the corresponding equations have the form

$$(h^u_{ee}v_1 + h'^u_{ee}v_2)/\sqrt{2} = m_1c_\varphi^2 + m_2s_\varphi^2, \quad (37)$$
$$(h^u_{XX}v_1 + h'^u_{XX}v_2)/\sqrt{2} = m_1s_\varphi^2 + m_2c_\varphi^2,$$
$$(h^u_{eX}v_1 + h'^u_{eX}v_2)/\sqrt{2} = c_\varphi s_\varphi(m_1 - m_2).$$

On the basis of Eqs. (35)–(37), we can conclude that, for the GTHDM, the parameters of neutrino oscillations can be measured by indirect methods in accelerator experiments. In contrast to the LRM, however, the total set of experiments must now include those where there are neutrino beams either in the initial or in the final state.

We now proceed to study solar neutrinos within the GTHDM. The contributions to the solar-matter potential come from diagrams involving virtual W^- and Z bosons (see Fig. 1) and from the diagrams in Fig. 4. By using the Fierz transformation and

performing averaging over solar matter, we arrive at the conclusion that diagrams featuring the exchange of $h^{(-)}$ bosons only modify the amplitudes for the forward elastic right-handed-neutrino scattering $e^-\nu_{aR} \to e^-\nu_{bR}$. The corresponding contribution to the solar-matter potential is given by

$$V_{ab}^{RR} = \frac{1}{4m_{h^{(-)}}^2}\kappa'_{ea}\kappa'_{eb}n_e, \tag{38}$$

where $\kappa'_{ab} = (-\sqrt{2}m_a v^{-1}\tan\beta)\delta_{ab} + \kappa_{ab}$.

On the other hand, the interaction with neutral Higgs bosons H, h, and A is responsible for the spin-flip elastic neutrino scattering

$$e^-\nu_{aL} \to e^-\nu_{bR}, \quad e^-\nu_{aR} \to e^-\nu_{bL}.$$

In averaging over matter, the contributions from the pseudoscalar Higgs boson disappear, and the eventual expression for that part of the solar-matter potential which is associated with the exchanges of neutral Higgs bosons has the form

$$V_{ab}^{LR} = V_{ab}^{RL} = \mathcal{B}_{ab}n_e, \tag{39}$$

where

$$\mathcal{B}_{ab} = \frac{1}{2}[(h^l_{ee}c_\alpha + h'^l_{ee}s_\alpha)(h^\nu_{ab}c_\alpha + h'^\nu_{ab}s_\alpha)m_H^{-2} + (h^l_{ee}s_\alpha - h'^l_{ee}c_\alpha)(h^\nu_{ab}s_\alpha - h'^\nu_{ab}c_\alpha)m_h^{-2}].$$

Thus, the interaction with neutral Higgs bosons leads to the effective neutrino-interaction Lagrangian

$$\mathcal{L}^{\text{eff}}_{H,h} = \overline{\nu}_{aL}\mathcal{B}_{ab}\nu_{bR}. \tag{40}$$

The form of expression (40) resembles that of the effective Lagrangian

$$\mathcal{L}^{\text{eff}}_m = \mu_{ab}\overline{\nu}_{aL}\sigma_{\lambda\rho}\mathcal{F}_{\lambda\rho}\nu_{bR}, \tag{41}$$

which involves the electromagnetic-field tensor $\mathcal{F}_{\lambda\rho}$ and which describes magnetic dipole interaction.

The GTHDM also belongs to the class of models where the neutrino magnetic moment may amount to about $10^{-12}\mu_B$. This occurs when the Yukawa coupling constants are great.

If the interactions specified by the Lagrangians in (40) and (41) are negligibly small, a system involving three sorts of left-handed neutrinos is described identically within the GTHDM and within the Standard Model [31].

For the case where the neutrino magnetic moment is on the order of $10^{-12}\mu_B$ or where the interaction V_{ab}^{LR} is great, we now consider the evolution of a neutrino flux. For the sake of simplicity, we restrict our analysis to the two-flavor approximation. Taking into account the interaction both with solar matter and with a magnetic field, we then obtain the evolution equation

$$i\frac{d}{dz}\begin{pmatrix}\nu_{eL}\\ \nu_{XL}\\ \nu_{eR}\\ \nu_{XR}\end{pmatrix} = \begin{pmatrix} \frac{\Delta m^2}{2E}s_\varphi^2 + V'^{LL}_{ee} & \frac{\Delta m^2}{4E}s_{2\varphi} & \tau_{ee} & \tau_{eX} \\ \frac{\Delta m^2}{4E}s_{2\varphi} & \frac{\Delta m^2}{2E}c_\varphi^2 + V'^{LL}_{XX} & \tau_{Xe} & \tau_{XX} \\ \tau^*_{ee} & \tau^*_{Xe} & \frac{\Delta m^2}{2E}s_\varphi^2 + V'^{RR}_{ee} & \frac{\Delta m^2}{4E}s_{2\varphi} + V^{RR}_{eX} \\ \tau^*_{eX} & \tau^*_{XX} & \frac{\Delta m^2}{4E}s_{2\varphi} + V^{RR}_{eX} & \frac{\Delta m^2}{2E}c_\varphi^2 + V'^{RR}_{XX} \end{pmatrix}\begin{pmatrix}\nu_{eL}\\ \nu_{XL}\\ \nu_{eR}\\ \nu_{XR}\end{pmatrix}, \tag{42}$$

where

$$V'^{LL}_{ee} = \sqrt{2}G_F\left(\frac{n_n}{2} - n_e\right) + \frac{\dot\Phi}{2},$$

$$V'^{LL}_{XX} = \frac{G_F n_n}{\sqrt{2}} + \frac{\dot\Phi}{2},$$

$$V'^{RR}_{ll} = V^{RR}_{ll} - \frac{\dot\Phi}{2}, \quad \tau_{ab} = \mu_{ab}B_\perp + V^{LR}_{ab}.$$

From (42), it follows that, depending on the values of the model parameters, three of the four possible resonance transitions can occur in the system being considered. Approximate values of the resonance electron density can be found from the equations

$$\frac{\Delta m^2}{2E}c_{2\varphi} - V'^{LL}_{ee} + V'^{LL}_{XX} = 0 \quad (\nu_{eL} \leftrightarrow \nu_{XL}), \tag{43}$$

$$\frac{\Delta m^2}{2E}c_{2\varphi} + V'^{RR}_{XX} - V'^{LL}_{ee} = 0 \quad (\nu_{eL} \leftrightarrow \nu_{XR}), \tag{44}$$

$$\frac{\Delta m^2}{2E}c_{2\varphi} - V'^{RR}_{ee} + V'^{LL}_{XX} = 0 \quad (\nu_{eR} \leftrightarrow \nu_{XL}), \tag{45}$$

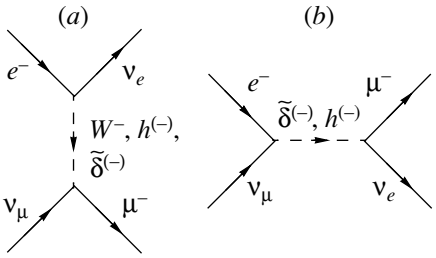

Fig. 5. Feynman diagrams for inverse muon decay within the LRM.

$$\frac{\Delta m^2}{2E}c_{2\varphi} + V'^{RR}_{XX} - V'^{RR}_{ee} = 0 \qquad (46)$$
$$(\nu_{eR} \leftrightarrow \nu_{XR}).$$

Thus, the interaction of leptons with physical Higgs bosons leads to the emergence of yet another resonance, namely,

$$\nu_{eR} \leftrightarrow \nu_{XR}.$$

Because of the very complicated form of the Hamiltonian in Eq. (42), only by invoking numerical methods can we determine the probability of survival of left-handed electron neutrinos.

4. CONSTRAINTS ON THE PARAMETERS OF THE HIGGS SECTOR

In this section, we will try to estimate corrections to the solar-matter potential that arise, in the models being considered, from the interaction with physical Higgs bosons. Complete information can be obtained in low-energy experiments studying elastic neutrino–electron scattering. In order to establish conclusively the $V-A$ structure of the amplitudes for such processes, it is necessary to detect simultaneously the charged lepton and the neutrino in the final state. Since the currently available experimental technique gives no way to perform such a measurement, we cannot be positive about the statement that the amplitudes for the reactions in question do indeed have the $V-A$ form. The situation is similar for the so-called direct lepton decays

$$\mu^- \to e^-\overline{\nu}_e\nu_\mu, \quad \tau^- \to e^-\overline{\nu}_e\nu_\tau \qquad (47)$$

and the so-called inverse lepton decays

$$\nu_\mu e^- \to \mu^-\nu_e, \quad \nu_\tau e^- \to \tau^-\nu_e. \qquad (48)$$

All the results of low-energy experiments for the processes in (47) and (48) can be parametrized in terms of the amplitudes $g^\gamma_{\lambda\lambda'}$ and the Fermi constant G_F as [32]

$$\frac{4G_\mathrm{F}}{\sqrt{2}}\sum g^\gamma_{\lambda\lambda'}\langle\overline{e}_\lambda \mid \Gamma_\gamma \mid \nu_{en}\rangle\langle\overline{\nu}_{Xm} \mid \Gamma_\gamma \mid X_{\lambda'}\rangle, \quad (49)$$

where $X = \mu, \tau$; the index γ specifies the interaction type ($\Gamma^S = 1$ for the scalar, $\Gamma^V = \gamma_\mu$ for the vector, and $\gamma^T = \sigma_{\mu\nu}/\sqrt{2}$ for the tensor interaction); the helicities of charged leptons (left-handed, right-handed) determine the subscripts λ and λ'; and the helicities of ν_e and ν_μ determine the subscripts n and m. Nine complex-valued amplitudes $g^\gamma_{\lambda\lambda'}$ and G_F form the set of 19 independent real-valued parameters, which are determined experimentally. We recall that, within the Standard Model, the amplitude g^V_{LL} must be equal to unity, while all the remaining amplitudes vanish.

Within the LRM, inverse muon (tau-lepton) decay is described by the diagrams in Fig. 5. The emergence of diagrams involving exchanges of $h^{(-)}$ Higgs bosons in the s channel is due to the Majorana nature of the neutrino. A comparison of the matrix elements corresponding to the diagrams in Fig. 5 with expression (49) leads to the relations

$$\frac{\alpha_{ee}\alpha_{XX}}{m_h^2} = 2\sqrt{2}G_\mathrm{F}g^S_{RR}, \qquad (50)$$

$$\frac{\alpha^2_{eX}}{m_h^2} = 4\sqrt{2}G_\mathrm{F}(g^V_{LL} - 1), \qquad (51)$$

$$\frac{f_{ee}f_{XX}}{m^2_{\tilde{\delta}}} = \sqrt{2}G_\mathrm{F}g^S_{LL}, \qquad (52)$$

$$\frac{f^2_{eX}}{m^2_{\tilde{\delta}}} = 2\sqrt{2}G_\mathrm{F}g^V_{RR}. \qquad (53)$$

We can see that, from the point of view of Fermi's four-fermion theory, the process in question as treated within the LRM is described by both vector and scalar currents. The nonzero amplitudes are g^V_{LL}, g^V_{RR}, g^S_{LL}, and g^S_{RR}. The experimental constraints on them from muon decay at a 90% C.L. are [33]

$$\mid g^V_{LL} \mid > 0.96, \ \mid g^V_{RR} \mid < 0.033, \qquad (54)$$
$$\mid g^S_{LL} \mid < 0.55, \ \mid g^S_{RR} \mid < 0.066.$$

From (50)–(54), it follows for the Yukawa coupling constants that (in GeV^{-2} units)

$$\frac{\alpha_{ee}\alpha_{\mu\mu}}{m_h^2} < 0.218 \times 10^{-5}, \qquad (55)$$

$$\frac{\alpha^2_{e\mu}}{m_h^2} < 0.264 \times 10^{-5}, \qquad (56)$$

$$\frac{f_{ee}f_{\mu\mu}}{m^2_{\tilde{\delta}}} < 0.907 \times 10^{-5}, \qquad (57)$$

$$\frac{f^2_{e\mu}}{m^2_{\tilde{\delta}}} < 0.109 \times 10^{-5}. \qquad (58)$$

We must now verify whether the inequalities in (55)–(58) are compatible with constraints that follow from other experiments. At present, only constraints on the triplet Yukawa coupling constants exist in the

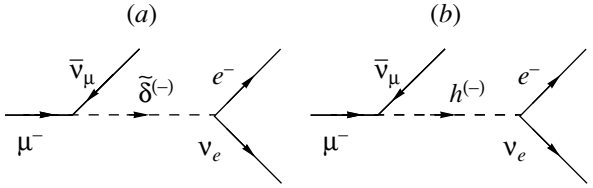

Fig. 6. LRM Feynman diagrams for the decay $\mu^- \to e^-\nu_e\overline{\nu}_\mu$.

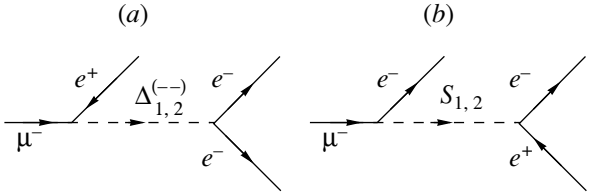

Fig. 7. LRM Feynman diagrams for the decay $\mu^- \to e^-e^+e^-$.

literature (see [15] and references therein). From the investigation of Bhabha scattering in experiments at SLAC and DESY, it follows that

$$\frac{f_{ee}^2}{m_\Delta^2} < 9.7 \times 10^{-6}\ \mathrm{GeV}^{-2}. \tag{59}$$

For the Yukawa coupling constants $f_{\mu\mu}$, a measurement of the $(g-2)_\mu$ factor yields the constraint

$$\frac{f_{\mu\mu}^2}{m_\Delta^2} < 2.5 \times 10^{-5}\ \mathrm{GeV}^{-2}. \tag{60}$$

It can be seen that an appropriate choice of mass values for the $\Delta^{(\pm\pm)}$ and $\tilde{\delta}^{(\pm)}$ bosons can reconcile the limits in (14), (59), and (60) with the constraint in (57). In the present analysis, we would like, however, to get rid of the uncertainty associated with the choice of the $\Delta^{(\pm\pm)}$-boson mass—that is, to have an upper limit on a quantity that is related to $f_{ee}f_{\mu\mu}/m_{\tilde{\delta}}^2$, which appears in the solar-matter potential. With this aim in view, we will now investigate muon decay through the channel

$$\mu^- \to e^-\nu_e\overline{\nu}_\mu. \tag{61}$$

The relevant Feynman diagrams are shown in Fig. 6. The decay width of a muon having left-hand circular polarization is given by

$$\Gamma_{\mu^-\to e^-\nu_e\overline{\nu}_\mu} = \frac{\sqrt{(f_{ee}f_{\mu\mu})^2 + f_{e\mu}^4}\,m_\mu^5}{96(2\pi)^3 m_{\tilde{\delta}}^4}. \tag{62}$$

Known experiments yield the constraint [34]

$$\frac{\Gamma_{\mu^-\to e^-\nu_e\overline{\nu}_\mu}}{\Gamma_{\mu^-\to \mathrm{all}}} < 1.2 \times 10^{-2}.$$

We then obtain

$$\frac{\sqrt{(f_{ee}f_{\mu\mu})^2 + f_{e\mu}^4}}{m_{\tilde{\delta}}^2} < 0.255 \times 10^{-5}\ \mathrm{GeV}^{-2}. \tag{63}$$

Obviously, the inequality in (63) is at odds with (57). This leads to the conclusion that data from searches for the decay $\mu^- \to e^-\nu_e\overline{\nu}_\mu$ reduce the upper limit on the amplitude g_{LL}^S to that in the constraint

$$|\, g_{LL}^S \,| < 0.155. \tag{64}$$

In deriving (64), we assumed that $f_{e\mu}^2 \ll f_{ee}f_{\mu\mu}$.

We will try to estimate the nondiagonal Yukawa coupling constants using data from searches for the decay

$$\mu^- \to e^-e^+e^-. \tag{65}$$

The diagrams that describe the decay process (65) in the second order of perturbation theory are displayed in Fig. 7. Assuming that the muon and the electrons are unpolarized and that $\theta_d = 0$, we can represent the decay width in the form

$$\Gamma_{\mu^-\to e^-e^+e^-} = \frac{\tau m_\mu^5}{96(2\pi)^3}, \tag{66}$$

where

$$\begin{aligned}\tau = {}& (f_{ee}f_{e\mu})^2\left(\frac{1}{m_{\Delta_1}^4} + \frac{1}{m_{\Delta_2}^4}\right)\\ &+ \frac{\alpha_{e\mu}^2}{4k_+^2}\left(\frac{m_e c_{\theta_0}s_{\theta_0} - \alpha_{ee}k_+ s_{\theta_0}^2}{m_{S_1}^2}\right.\\ &\left.- \frac{m_e s_{\theta_0}c_{\theta_0} + \alpha_{ee}k_+ c_{\theta_0}^2}{m_{S_2}^2}\right)^2\\ &+ \frac{4m_e f_{ee}f_{e\mu}\alpha_{e\mu}}{m_\mu k_+}\left(\frac{1}{m_{\Delta_1}^2} + \frac{1}{m_{\Delta_2}^2}\right)\\ &\times\left(\frac{m_e c_{\theta_0}s_{\theta_0} - \alpha_{ee}k_+ s_{\theta_0}^2}{m_{S_1}^2}\right.\\ &\left.- \frac{m_e s_{\theta_0}c_{\theta_0} + \alpha_{ee}k_+ c_{\theta_0}^2}{m_{S_2}^2}\right).\end{aligned}$$

From experiments, it follows that [34]

$$\frac{\Gamma_{\mu^-\to e^-e^+e^-}}{\Gamma_{\mu^-\to \mathrm{all}}} < 10^{-12}.$$

Setting $\alpha_{e\mu}$ to zero, we arrive at

$$f_{ee}f_{e\mu}\sqrt{\frac{1}{m_{\Delta_1}^4} + \frac{1}{m_{\Delta_2}^4}} < 2.33 \times 10^{-11}\ \mathrm{GeV}^{-2}. \tag{67}$$

For the inequalities in (67) and in (58) and (59) to be consistent, we must assume that the mass of the $\Delta_1^{(\pm\pm)}$ or of the $\Delta_2^{(\pm\pm)}$ boson is not less than 21 TeV and that the mass of the $\tilde{\delta}^{(\pm)}$ boson is simultaneously

about 100 GeV. Since the $\tilde{\delta}^{(\pm)}$ boson does not interact with quarks, there are no constraints on its mass from data on the decay $b \to s\gamma$. For its mass, it is therefore natural to use the upper limit of 100 GeV, which was obtained in LEP II experiments [35]. It should also be noted that there are no reasons that would forbid the existence of doubly charged Higgs bosons of mass about 21 TeV.

Let us proceed to discuss constraints on the bidoublet Yukawa coupling constants. The width with respect to the decay of a right-hand-polarized muon through the channel

$$\mu^- \to e^- \nu_e \overline{\nu}_\mu$$

is given by

$$\Gamma_{\mu^- \to e^- \nu_e \overline{\nu}_\mu} = \frac{[(\alpha_{ee}\alpha_{\mu\mu})^2 + \alpha_{e\mu}^4] m_\mu^5}{48(4\pi)^3 m_h^4}. \quad (68)$$

A comparison of the theoretical and experimental results leads to the conclusion that

$$\frac{\sqrt{(\alpha_{ee}\alpha_{\mu\mu})^2 + \alpha_{e\mu}^4}}{m_h^2} < 5.1 \times 10^{-6}\ \mathrm{GeV}^{-2}. \quad (69)$$

Disregarding $\alpha_{e\mu}$ in (69), we find that more stringent limits on $\alpha_{ee}\alpha_{\mu\mu}/m_h^2$ follow from data on inverse muon decay.

In order to determine limits on $\alpha_{e\mu}$ from data on the decay $\mu^- \to e^- e^+ e^-$, we have to make assumptions both on the S_2-boson mass and on the value of the constant $\alpha_{\mu\mu}$. Making the S_2-boson mass tend to 10 TeV, one can increase $\alpha_{e\mu}$ to values of about 2×10^{-1}, but a contradiction with (56) can be avoided only if the $h^{(\pm)}$-boson mass is less than 123 GeV. On one hand, that form of the Yukawa Lagrangian is taken to be commonly accepted which leads to the existence of interaction between quarks and the $h^{(\pm)}$ Higgs boson. It turns out that limits on its mass that follow from data on the decay $b \to s\gamma$ depend strongly on the choice of values for the LRM parameters and are about a few hundred GeV (see [36] and references therein). On the other hand, the Yukawa Lagrangian can be chosen in a form such that only neutral Higgs bosons interact with quarks [22]. This enables us to use the lower limit of 100 GeV [35] for the $h^{(\pm)}$-boson mass. It should be noted that, from the point of view of a precise determination of the quantities $\alpha_{e\mu}^2/m_h^2$ and $f_{e\mu}^2/m_{\tilde{\delta}}^2$, the most promising reactions are

$$e^-\gamma \to h^{(-)}\nu_\mu, \quad (70)$$

$$e^-\gamma \to \tilde{\delta}^{(-)}\nu_\mu. \quad (71)$$

They can be studied at e^+e^- colliders operating in the $e^-\gamma$ mode.

In the following, we will briefly discuss limits on the Yukawa coupling constants associated with the tau-lepton sector. The experimental constraints obtained by the CLEO collaboration in measuring the Michel parameters are less stringent than those for the muon case. At a 90% C.L., the constraints on $g^\gamma_{\lambda\lambda'}$ are [37]

$$|\, g_{LL}^V \,| < 1.0, \quad |\, g_{RR}^V \,| < 0.2, \quad (72)$$
$$|\, g_{LL}^S \,| < 1, \quad |\, g_{RR}^S \,| < 0.2.$$

From (72), it follows that (in GeV^{-2} units)

$$\frac{\alpha_{ee}\alpha_{\tau\tau}}{m_h^2} < 0.66 \times 10^{-5}, \quad (73)$$

$$\alpha_{e\tau} \approx 0, \quad (74)$$

$$\frac{f_{ee}f_{\tau\tau}}{m_{\tilde{\delta}}^2} < 3.3 \times 10^{-5}, \quad (75)$$

$$\frac{f_{e\tau}^2}{m_{\tilde{\delta}}^2} < 0.66 \times 10^{-5}. \quad (76)$$

The expression for the width with respect to the decay

$$\tau^- \to e^- e^+ e^- \quad (77)$$

can be obtained from (66) upon the substitution

$$f_{e\mu} \to f_{e\tau}, \quad \alpha_{e\mu} \to \alpha_{e\tau}, \quad m_\mu \to m_\tau.$$

The investigation of the decay process (77) by the CLEO collaboration [38] yielded the following result (at a 95% C.L.):

$$\mathrm{Br}(\tau^- \to e^- e^+ e^-) < 3.3 \times 10^{-6}.$$

Assuming that $\alpha_{e\tau}$ is equal to zero, we then obtain

$$f_{ee}f_{e\tau}\sqrt{\frac{1}{m_{\Delta_1}^4} + \frac{1}{m_{\Delta_2}^4}} < 1.8 \times 10^{-8}\ \mathrm{GeV}^{-2}. \quad (78)$$

If the $\Delta_1^{(\pm\pm)}$- or $\Delta_2^{(\pm\pm)}$-boson masses lie in the region around 3 TeV, the constraint in (78) yields

$$f_{ee}f_{e\tau} < 0.16, \quad (79)$$

whence we can conclude that the upper limit on $f_{ee}f_{e\tau}$ from (75) and (76) seems quite plausible. It should be emphasized that the quantities $\alpha_{e\tau}/m_h^2$ and $f_{e\tau}/m_{\tilde{\delta}}^2$ can be reliably determined with the aid of an $e^-\gamma$ collider by studying the reactions

$$e^-\gamma \to h^{(-)}\nu_\tau,$$
$$e^-\gamma \to \tilde{\delta}^{(-)}\nu_\tau.$$

In the majority of cases, processes involving cosmic and terrestrial neutrinos are analyzed on the basis of the Standard Model supplemented with a right-handed neutrino singlet in order to ensure a nonzero neutrino mass. In this case, the Yukawa Lagrangian reduces neutrino interaction with the physical Higgs boson (there is no such interaction in the usual version of the Standard Model). Since the strength of this interaction is proportional to the ratio of m_{ν_l} to

v (about 246 GeV)—that is, it is extremely small—the two versions of Standard Model differ only in the kinematical features of the neutrinos. The solar-matter potential in the Standard Model involving a right-handed neutrino singlet has the form

$$V^{\mathrm{SM}} = -\sqrt{2}G_{\mathrm{F}}n_e.$$

With the predictions of precisely this modification of the Standard Model, we will now compare the expressions for the solar-matter potential that were obtained within the LRM. We begin our analysis by considering the diagonal elements of the Hamiltonian from (19). If we assume that $\alpha_{ee} \approx \alpha_{\mu\mu}$ and $f_{ee} \approx f_{\mu\mu}$, then V^H_{ee} can amount to about 15.5% of V^{SM} in the case where the amplitudes g^S_{RR} and g^S_{LL} are of the same sign [see Eq. (54)]; in the case where these amplitudes are of opposite signs, the quantity V^H_{ee} can be as large as about 22% of V^{SM}. Since there is presently no information about α^2_{eX}/m^2_h, we can only assume that

$$\alpha_{e\mu} = \alpha_{e\tau} = 0. \tag{80}$$

With the aid of (58) and (76), we then obtain

$$V^H_{\mu\mu} < 6.6\%\, V^{\mathrm{SM}}, \quad V^H_{\tau\tau} < 40\%\, V^{\mathrm{SM}}.$$

For the nondiagonal elements of the Hamiltonian, the corrections are constrained by the inequalities

$$V^H_{e\mu} < 10\%\, V^{\mathrm{SM}}, \quad V^H_{e\tau} < 25\%\, V^{\mathrm{SM}},$$
$$V^H_{\mu\tau} < 16\%\, V^{\mathrm{SM}}.$$

We now perform a similar analysis for the GTHDM, where the inverse-muon-decay (tau-lepton-decay) process is described by diagrams involving the exchanges of W^- and $h^{(-)}$ bosons in the t channel (see Fig. 5) and diagrams involving the exchanges of H, h, and A bosons (see Fig. 8). The nonzero amplitudes are g^V_{LL}, g^V_{LR}, g^V_{RL}, and g^S_{RR}. They are related to the Yukawa coupling constants by the equations

$$\frac{4G_{\mathrm{F}}}{\sqrt{2}}g^S_{RR} = \frac{\kappa'_{ee}\kappa'_{XX}}{m^2_{h^{(-)}}}, \tag{81}$$

$$\frac{2G_{\mathrm{F}}}{\sqrt{2}}g^V_{RL} = \frac{2G_{\mathrm{F}}}{\sqrt{2}}g^V_{LR} = \frac{\lambda^l_{eX}\lambda^\nu_{eX}}{m^2_H} + \frac{\beta^l_{eX}\beta^\nu_{eX}}{m^2_h}, \tag{82}$$

where

$$\lambda^f_{ab} = h^f_{ab}c_\alpha + h'^f_{ab}s_\alpha, \quad \beta^f_{ab} = h'^f_{ab}c_\alpha - h^f_{ab}s_\alpha,$$
$$f = l, \nu, \quad a, b = e, X.$$

With the aid of available experimental data [34], we can obtain the constraints (the values in them are in GeV^{-2} units)

$$\frac{\kappa'_{ee}\kappa'_{\mu\mu}}{m^2_{h^{(-)}}} < 0.217 \times 10^{-5}, \tag{83}$$

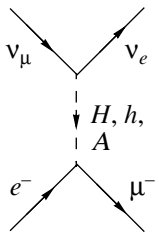

Fig. 8. GTHDM Feynman diagrams for the inverse muon decay that involve exchanges of neutral Higgs bosons.

$$\frac{\kappa'_{ee}\kappa'_{\tau\tau}}{m^2_{h^{(-)}}} < 0.66 \times 10^{-5}, \tag{84}$$

$$\frac{\lambda^l_{e\mu}\lambda^\nu_{e\mu}}{m^2_H} + \frac{\beta^l_{e\mu}\beta^\nu_{e\mu}}{m^2_h} < 0.99 \times 10^{-6}, \tag{85}$$

$$\frac{\lambda^l_{e\tau}\lambda^\nu_{e\tau}}{m^2_H} + \frac{\beta^l_{e\tau}\beta^\nu_{e\tau}}{m^2_h} < 0.28 \times 10^{-5}. \tag{86}$$

In our attempts at estimating the parameters of the Higgs sector that are discussed in the present study, we now invoke data on the decay processes

$$\mu^- \to e^-e^+e^-, \quad \tau^- \to e^-e^+e^-, \quad \mu^- \to e^-\nu_e\overline{\nu}_\mu$$

and try to find out whether their analysis may produce information of value for this purpose. The widths with respect to these decays are given by

$$\Gamma_{X^-\to e^-e^+e^-} = \frac{m^5_X}{96(4\pi)^3} \tag{87}$$
$$\times \left[\left(\frac{\lambda^l_{ee}\lambda^l_{eX}}{m^2_H} + \frac{\beta^l_{ee}\beta^l_{eX}}{m^2_h}\right)^2 + \frac{(\gamma^l_{ee}\gamma^l_{eX})^2}{m^4_A}\right],$$

$$\Gamma_{\mu^-\to e^-\nu_e\overline{\nu}_\mu} = \frac{m^5_\mu}{48(4\pi)^3} \tag{88}$$
$$\times \left[\frac{\kappa^4_{e\mu}}{m^4_{h^{(-)}}} + \left(\frac{\lambda^l_{e\mu}\lambda^\nu_{e\mu}}{m^2_H} + \frac{\beta^l_{e\mu}\beta^\nu_{e\mu}}{m^2_h}\right)^2 + \frac{(\gamma^l_{e\mu}\gamma^\nu_{e\mu})^2}{m^4_A}\right],$$

where $\gamma^f_{ab} = h'^f_{ab}c_\beta - h^f_{ab}s_\beta$. With the aid of experimental data, we can obtain (the numerical values in these results are in GeV^{-2} units)

$$\sqrt{\left(\frac{\lambda^l_{ee}\lambda^l_{e\mu}}{m^2_H} + \frac{\beta^l_{ee}\beta^l_{e\mu}}{m^2_h}\right)^2 + \frac{(\gamma^l_{ee}\gamma^l_{e\mu})^2}{m^4_A}} < 6.6 \times 10^{-11}, \tag{89}$$

$$\sqrt{\left(\frac{\lambda^l_{ee}\lambda^l_{e\tau}}{m^2_H} + \frac{\beta^l_{ee}\beta^l_{e\tau}}{m^2_h}\right)^2 + \frac{(\gamma^l_{ee}\gamma^l_{e\tau})^2}{m^4_A}} < 2.82 \times 10^{-7}, \tag{90}$$

$$\sqrt{\frac{\kappa^4_{e\mu}}{m^4_{h^{(-)}}} + \left(\frac{\lambda^l_{e\mu}\lambda^\nu_{e\mu}}{m^2_H} + \frac{\beta^l_{e\mu}\beta^\nu_{e\mu}}{m^2_h}\right)^2 + \frac{(\gamma^l_{e\mu}\gamma^\nu_{e\mu})^2}{m^4_A}} \tag{91}$$

$$< 5.1 \times 10^{-6}.$$

It can easily be seen that the constraints obtained within the GTHDM for the parameters of the Higgs sector are compatible. We will now evaluate the corrections to the solar-matter potential within the model being investigated. Assuming that $\kappa_{ee} \approx \kappa_{\mu\mu}$, we obtain

$$V_{ee}^{RR} < 3.3\%\, V^{\mathrm{SM}}.$$

On the basis of the definition of the constants κ_{ll}, we can state that their hierarchy can be the following:

$$\kappa_{\tau\tau} < \kappa_{\mu\mu} < \kappa_{ee}.$$

Even in the most conservative case of $\kappa_{ee} \approx \kappa_{\tau\tau}$, the quantity V_{ee}^{RR} may then amount to about 10% of V^{SM}. With the aid of relations (83) and (91), we can obtain

$$V_{\mu\mu}^{RR} < 8\%\, V^{\mathrm{SM}}, \quad V_{e\mu}^{RR} < 5\%\, V^{\mathrm{SM}}.$$

At present, we do not have at our disposal information required for determining $V_{\tau\tau}^{RR}$, $V_{e\tau}^{RR}$, and $V_{\mu\tau}^{RR}$. It will become possible to estimate V_{ab}^{RR} reliably in studying the reactions

$$e^-\gamma \to h^{(-)}\nu_e, h^{(-)}\nu_\tau, \quad \mu^-\gamma \to h^{(-)}\nu_\tau.$$

Attempts at estimating the contributions to the the solar-matter potential that are associated with neutral Higgs bosons have to deal with still greater uncertainties. Assuming that

$$\lambda_{ee}^l = \lambda_{eX}^l, \quad \beta_{ee}^l = \beta_{eX}^l$$

and using the inequalities in (89) and (90), we arrive at the conclusion that

$$V_{e\mu}^{LR} < 3\%\, V^{\mathrm{SM}}, \quad V_{e\tau}^{LR} < 8.5\%\, V^{\mathrm{SM}}.$$

Unfortunately, data required for estimating V_{ee}^{LR}, $V_{\mu\mu}^{LR}$, and $V_{\tau\tau}^{LR}$ are unavailable at present.

5. CONCLUSION

Within two extensions of the Standard Model—(i) LRM [$SU(2)_L \times SU(2)_R \times U(1)_{B-L}$ gauge group; a bidoublet and two triplets in the Higgs sector] and (ii) GTHDM [$SU(2)_L \times U(1)_Y$ gauge group; two doublets in the Higgs sector]—we have considered the propagation of a neutrino flux through a medium. Within either theory, the solar-matter potential undergoes considerable changes in relation to the Standard Model predictions owing to the interactions of leptons with physical Higgs bosons. In the LRM, these changes are generated by singly charged Higgs bosons. From the point of view of effective four-fermion interaction, this means the existence of charged currents not present in the Standard Model that involve both diagonal and off-diagonal components in the lepton flavor (flavor-conserving charged currents and flavor-violating charged currents, respectively). The existence of the latter leads to the mixing of neutrinos having identical helicities but different flavors. If the neutrino magnetic moment is disregarded, it is possible to obtain an analytic expression for the probability of survival of a left-handed electron neutrino, $\mathcal{P}(\nu_{eL} \to \nu_{eL})$, even in the three-flavor approximation, but if the magnetic moment is taken into account, this problem can be solved only in the two-flavor approximation.

Within the GTHDM, additional contributions to the solar-matter potential come both from singly charged and from neutral physical Higgs bosons H, h, and A. Neutral currents associated with H, h, and A bosons also involve lepton-flavor-conserving and lepton-flavor-violating components. The existence of the latter results in the mixing of neutrinos of different flavors and different helicities. Because of this, it is impossible to obtain $\mathcal{P}(\nu_{eL} \to \nu_{eL})$ analytically even at zero neutrino magnetic moment in the two-flavor approximation.

Thus, we can see that, while, in the Standard Model, the calculation of the survival probability for a left-handed electron neutrino of specific energy requires knowledge of the electron-density distribution in solar matter and values of oscillation parameters (neutrino mixing angles in a vacuum and the differences of the squared neutrino masses), in models involving an extended Higgs sector, we must additionally have at our disposal information about the interaction of Higgs bosons with leptons. We have investigated some channels of muon and tau-lepton decays and obtained a number of constraints on the Yukawa coupling constants and on the masses of physical Higgs bosons. The use of relevant limits available from the literature and of those derived here makes it possible to obtain more or less reliable estimates for maximum corrections to the solar-matter potential that come exclusively from the interaction of charged Higgs bosons with leptons. We can state that, within the LRM, corrections to the solar-matter potential can be as large as 40% of V^{SM} and 25% of V^{SM} for, respectively, diagonal ($\mathcal{H}_d$) and nondiagonal ($\mathcal{H}_{nd}$) elements of the Hamiltonian for the neutrino system. In the GTHDM, the deviations from the Standard Model predictions are less pronounced: for $\mathcal{H}_d$ and $\mathcal{H}_{nd}$, we have 10% of V^{SM} and 8.5% of V^{SM}, respectively. In order to deduce more precise information about corrections to the solar-matter potential within the extensions of the Standard Model that have been considered above, it is necessary to investigate the reactions

$$e^-\gamma \to h^{(-)}\nu_l, \quad e^-\gamma \to \tilde{\delta}^{(-)}\nu_l, \tag{92}$$

$$\mu^-\gamma \to \tilde{\delta}^{(-)}\nu_\tau, \quad \mu^-\gamma \to h^{(-)}\nu_\tau, \tag{93}$$

$$e^- \nu_l \to e^- \nu_{l'}. \quad (94)$$

Of course, the reactions in (94) stand out among these. The reasons for this are as follows: (i) They do not require the use of next-generation accelerators, because it is sufficient to investigate them at low energies. (ii) Analysis of the Lorentz structure of the amplitudes for these reactions will provide complete information about all possible corrections to the solar-matter potential. Knowing the solar-matter potential, we can proceed to revise constraints on oscillation parameters in any gauge theory involving an extended Higgs sector.

APPENDIX

Within the LRM, we have calculated the eigenvalues M_i^2 of the Hamiltonian and the mixing angles φ_{ik}^m for a neutrino beam propagating in matter.

At zero neutrino magnetic moment, M_i^2 in the three-flavor approximation is given by

$$M_1^2 = m_1^2 + \frac{C_1}{3} - \frac{1}{3}C_2\left(\cos q - \sqrt{3}\sin q\right), \quad (A.1)$$

$$M_2^2 = m_1^2 + \frac{C_1}{3} - \frac{1}{3}C_2\left(\cos q + \sqrt{3}\sin q\right), \quad (A.2)$$

$$M_3^2 = m_1^2 + \frac{C_1}{3} + \frac{2}{3}C_2\cos q,$$

where

$$D_{11} = 2E[c_{12}^2c_{13}^2V_{ee} + b_1^2V_{\mu\mu} + b_1'^2V_{\tau\tau} - 2c_{12}c_{13}(b_1V_{e\mu} - b_1'V_{e\tau}) - 2b_1b_1'V_{\mu\tau}],$$

$$D_{23} = 2E\big[c_{13}s_{13}s_{12}V_{ee} + s_{23}c_{13}b_2V_{\mu\mu} - c_{23}c_{13}b_2'V_{\tau\tau} + (s_{13}b_2 + c_{13}^2s_{23}s_{12})V_{e\mu} - (s_{13}b_2' + c_{13}^2c_{23}s_{12})V_{e\tau} - (c_{13}s_{23}b_2' - c_{13}c_{23}b_2)V_{\mu\tau}\big],$$

$$D_{12} = 2E\big\{c_{13}\big[c_{13}c_{12}s_{12}V_{ee} + (c_{12}b_2 - s_{12}b_1)V_{e\mu} + (s_{12}b_1' - c_{12}b_2')V_{e\tau}\big] - b_1b_2V_{\mu\mu} - b_1'b_2'V_{\tau\tau} + (b_1b_2' + b_2b_1')V_{\mu\tau}\big\},$$

$$D_{33} = 2E\big[s_{13}^2V_{ee} + c_{13}^2(s_{23}^2V_{\mu\mu} + c_{23}^2V_{\tau\tau}) + 2c_{13}(s_{13}s_{23}V_{e\mu} + s_{13}c_{23}V_{e\tau} + c_{13}c_{23}s_{23}V_{\mu\tau})\big],$$

$$D_{22} = D_{11}\left(\varphi_{12} \to \varphi_{12} + \frac{\pi}{2}\right),$$

$$D_{13} = D_{23}\left(\varphi_{12} \to \varphi_{12} - \frac{\pi}{2}\right),$$

$$b_2 = b_1\left(\varphi_{12} \to \varphi_{12} + \frac{\pi}{2}\right),$$

$$b_s = b_s'\left(\varphi_{23} \to \varphi_{23} - \frac{\pi}{2}\right) \quad (s = 1, 2),$$

$$S_{ik} = D_{ii} + D_{kk},$$

$$\Lambda_{ik} = D_{ii}D_{kk} - D_{ik}^2 \quad (i, k = 1, 2, 3),$$

$$C_0 = \Delta m_{21}^2\Lambda_{13} + \Delta m_{31}^2\Lambda_{12} + \Delta m_{21}^2\Delta m_{31}^2D_{11} + (2E)^3\sum_{a,b,c}\varepsilon_{abc}V_{ea}V_{\mu b}V_{\tau c} \quad (a, b, c, = e, \mu, \tau),$$

$$C_1 = \sum_i m_i^2 + 2E\sum_a V_{aa},$$

$$C_3 = \Delta m_{21}^2\Delta m_{31}^2 + \Delta m_{21}^2S_{31} + \Delta m_{31}^2S_{21} + \sum_{i<k}\Lambda_{ik},$$

$$C_2 = \pm\sqrt{|\,C_1^2 - 3C_3\,|},$$

$$q = \frac{1}{3}\arccos\left(\frac{9C_1C_3 - 2C_1^3 - 27C_0}{C_2^3}\right),$$

and the signs of C_3 and $9C_1C_3 - 2C_1^3 - 27C_0$ must be chosen to be identical.

For φ_{ik}^m, we have

$$\sin^2 2\varphi_{12}^m = \frac{\mathcal{A}_2\Delta M_{32}^2(\mathcal{A}_1\Delta M_{12}^2 - \mathcal{A}_2\Delta M_{32}^2)}{4\mathcal{A}_1^2\Delta M_{12}^4}, \quad (A.3)$$

$$\sin^2 2\varphi_{13}^m = \frac{\mathcal{A}_1(\Delta M_{32}^2\Delta M_{13}^2 - \mathcal{A}_1)}{4\Delta M_{32}^4\Delta M_{13}^4}, \quad (A.4)$$

$$\sin^2 2\varphi_{23}^m = \frac{4\Delta M_{23}^4[\mathcal{B}_1 + \mathcal{B}_2(\mathcal{B}_3 - M_1^2 - M_2^2)]^2}{\mathcal{A}_1^2(\Delta M_{32}^2 - \Delta M_{21}^2)^2}, \quad (A.5)$$

where

$$a_1 = c_{13}^2c_{12}s_{12}\Delta m_{12}^2 - b_1'b_2'\Delta m_{32}^2 + 2EV_{e\mu},$$

$$a_2 = c_{12}c_{13}s_{13}\Delta m_{12}^2 + c_{23}c_{13}b_1'\Delta m_{32}^2 + 2EV_{e\tau},$$

$$\mathcal{B}_1 = a_1a_2,$$

$$\mathcal{B}_2 = c_{13}s_{13}s_{12}\Delta m_{12}^2 - c_{23}c_{13}b_2\Delta m_{32}^2 + 2EV_{\mu\tau},$$

$$\mathcal{B}_3 = (s_{12}^2c_{13}^2 + s_{13}^2)\Delta m_{12}^2 + (b_2^2 + c_{13}^2c_{23}^2)\Delta m_{32}^2 - 2m_2^2 + 2E(V_{\mu\mu} + V_{\tau\tau}),$$

$$\mathcal{B}_4 = a_1^2 + a_2^2,$$

$$\mathcal{A}_1 = \mathcal{B}_4 + (\mathcal{B}_3 - M_1^2 - M_2^2)(\mathcal{B}_3 - 2M_3^2),$$

$$\mathcal{A}_2 = \mathcal{A}_1 + \Delta M_{31}^2(\mathcal{B}_3 - M_1^2 - M_2^2).$$

It should be emphasized that, in the LRM, both the eigenvalues of the Hamiltonian and the mixing angles in matter are dependent on φ_{23}. This immediately follows from the fact that ν_e, ν_μ, and ν_τ interact differently with physical Higgs bosons. We recall that, in the Standard Model, the quantities M_i^2 and φ_{ik}^m do not depend on φ_{23}.

The inclusion of the neutrino magnetic moment complicates the calculations, and only in the two-flavor approximations have we been able to obtain a

solution in radicals. The eigenvalues of the Hamiltonian for the system being considered are given by

$$M_1^2 = \frac{1}{2}(m_1^2 + m_2^2) + \sqrt{z_1} - \sqrt{z_2} + \sqrt{z_3}, \quad \text{(A.6)}$$
$$M_2^2 = \frac{1}{2}(m_1^2 + m_2^2) - \sqrt{z_1} + \sqrt{z_2} + \sqrt{z_3},$$
$$M_3^2 = \frac{1}{2}(m_1^2 + m_2^2) - \sqrt{z_1} - \sqrt{z_2} - \sqrt{z_3},$$
$$M_4^2 = \frac{1}{2}(m_1^2 + m_2^2) + \sqrt{z_1} + \sqrt{z_2} - \sqrt{z_3},$$

where

$$z_i = y_i + p', \quad y_1 = 2p\cos\alpha,$$
$$y_{2,3} = -p[\cos\alpha \pm \sqrt{3}\sin\alpha],$$
$$p = \pm\sqrt{|\,-3p'^2 + \frac{r}{16}\,|},$$
$$p' = \frac{1}{6}\left[\frac{1}{2}\Delta m_{12}^4 + V_1^2 + V_2^2 + 2(V_0^2 + \mu_{ea}^2 B_\perp^2)\right],$$
$$r = 2(\Delta m_{12}^2)^2(V_1^2 + V_2^2) + (V_1^2 - V_2^2)^2$$
$$+ 4V_0^2[4\mu_{ea}^2 B_\perp^2 + (V_1 + V_2)^2] + 4\mu_{ea}^2 B_\perp^2 (V_1 - V_2)^2,$$
$$q' = \Delta m_{12}^2(V_2^2 - V_1^2),$$
$$q = \frac{-128p'^3 + 4p'r - q'^2}{64},$$
$$\alpha = \frac{1}{3}\arccos\left(\frac{q}{2(p/3)^3}\right),$$
$$V_1 = 2E(V_{ee}^{mf} c_\varphi^2 + V_{XX}^{mf} s_\varphi^2 + 2V_{eX} c_\varphi s_\varphi),$$
$$V_2 = V_1(\varphi \to \varphi + \frac{\pi}{2}),$$
$$V_0 = 2E(V_{ee}^{mf} - V_{XX}^{mf}) c_\varphi s_\varphi + 2EV_{eX}(s_\varphi^2 - c_\varphi^2).$$

Since we have four resonance transitions in this case, the number of the mixing angles in matter is also equal to four. We parametrize the rotation matrix $\mathcal{U}_m$ as

$$\mathcal{U}^m = \begin{pmatrix} c_{12}^m & s_{12}^m & 0 & 0 \\ -s_{12}^m & c_{12}^m & 0 & 0 \\ 0 & 0 & c_{34}^m & s_{34}^m \\ 0 & 0 & -s_{34}^m & c_{34}^m \end{pmatrix} \begin{pmatrix} c_{14}^m & 0 & 0 & s_{14}^m \\ 0 & c_{23}^m & s_{23}^m & 0 \\ 0 & -s_{23}^m & c_{23}^m & 0 \\ -s_{14}^m & 0 & 0 & c_{14}^m \end{pmatrix}.$$

The mixing angles are then determined by the relations

$$\tan^2\varphi_{14}^m = \frac{(1 - \sqrt{1 - d_3^2})\mathcal{P}_2^{(+-)}}{(1 + \sqrt{1 - d_3^2})\mathcal{P}_1^{(++)}}, \quad \text{(A.7)}$$
$$\tan^2\varphi_{23}^m = \frac{(1 - \sqrt{1 - d_3^2})\mathcal{P}_2^{(-+)}}{(1 + \sqrt{1 - d_3^2})\mathcal{P}_1^{(--)}},$$
$$\tan^2\varphi_{12}^m = \frac{\mathcal{P}_1^{(--)}}{\mathcal{P}_1^{(++)}}, \quad \tan^2\varphi_{34}^m = \frac{\mathcal{P}_1^{(-+)}}{\mathcal{P}_1^{(+-)}}, \quad \text{(A.8)}$$

where

$$d_1 = \frac{2V_0}{\Delta M_{21}^2}, \quad d_2 = \frac{2V_0}{\Delta M_{43}^2},$$
$$d_3 = \frac{4\mu_{eX} B_\perp}{\Delta M_{21}^2\sqrt{1 - d_1^2} + \Delta M_{43}^2\sqrt{1 - d_2^2}},$$
$$\mathcal{P}_s^{(qq')} = \frac{1}{4}(1 + q\sqrt{1 - d_s^2}\cos 2\varphi + q' d_s \sin 2\varphi),$$
$$q, q' = \pm 1, \quad s = 1, 2.$$

REFERENCES

1. R. Davis, Prog. Part. Nucl. Phys. **32**, 13 (1994); KAMIOKANDE Collab. (Y. Fukuda *et al.*), Phys. Rev. Lett. **77**, 1683 (1996); Super-KAMIOKANDE Collab. (Y. Fukuda *et al.*), Phys. Rev. Lett. **82**, 1810 (1999); GALLEX Collab. (W. Hampel *et al.*), Phys. Lett. B **388**, 384 (1996); SAGE Collab. (J. N. Abdurashitov *et al.*), Phys. Rev. Lett. **77**, 4708 (1996).
2. R. Beccker-Szendy *et al.*, Phys. Rev. D **46**, 3720 (1992).
3. Super-KAMIOKANDE Collab. (Y. Fukuda *et al.*), Phys. Rev. Lett. **81**, 1562 (1998); Phys. Lett. B **433**, 9 (1998); **467**, 185 (1999).
4. G. L. Fogli, E. Lisi, A. Marrone, and G. Scioscia, hep-ph/9808205.
5. LSND Collab. (C. Athanassopoulos *et al.*), Phys. Rev. Lett. **77**, 3082 (1996); **81**, 1774 (1998).
6. K . Eitel *et al.*, Nucl. Phys. B (Proc. Suppl.) **70**, 210 (1999).
7. P. Picchi and F. Pietropaolo, hep-ph/9812222.
8. The MINOS Collab., Neutrino Oscillation Physics at Fermilab. The NuMI-MINOS Project, Report NUMI-L-375, May 1998.
9. P. Lipari, hep-ph/9903481.
10. A. Bueno, M. Campanelli, and A. Rubbia, Preprint CERN-EP/99-74; V. Barger, S. Geer, and K. Whisnant, FERMILAB-PUB-99-187-T; hep-ph/9906487.
11. J. C. Pati and A. Salam, Phys. Rev. D **10**, 275 (1974); R. N. Mohapatra and J. C. Pati, Phys. Rev. D **11**, 566 (1975); Phys. Rev. D **11**, 2558 (1975); G. Senjanovich and R. N. Mohapatra, Phys. Rev. D **12**, 1502 (1975).
12. M. Sher, Phys. Rep. **179**, 273 (1989).
13. L. Wolfenstein, Phys.Rev. D **17**, 2369 (1978).
14. P. I. Krastev and J. N. Bahkall, hep-ph/9703267; M. C. Gonsalez-Garcia *et al.*, hep-ph/9809531; Loretta M. Johnson and Douglas W. McKay, hep-ph/9805311.
15. R. N. Mohapatra and D. Sidhu, Phys. Rev. Lett. **38**, 667 (1977); R. N. Mohapatra and G. Senjanovic, Phys. Rev. D **23**, 165 (1981); R. N. Mohapatra, in *Unification and Supersymmetry* (Springer-Verlag, New York, 1986), p. 345.

16. S. Rajpoot, Phys. Rev. D **40**, 3795 (1989); R. M. Francis, M. Frank, and C. S. Kalman, Phys. Rev. D **43**, 2369 (1991).
17. H. P. Nilles, Phys. Rep. **110**, 1 (1984); H. Haber and G. Kane, Phys. Rep. **117**, 75 (1985).
18. M. Singer, J. W. F. Valle, and J. Shechter, Phys. Rev. D **22**, 738 (1980); M. Singer and J. W. F. Valle, Phys. Rev. D **28**, 540 (1983); P. H. Frampton, Phys. Rev. Lett. **69**, 2889 (1992); R. Foot, H. N. Long, and Tuan A. Tran, Phys. Rev. D **50**, R34 (1994).
19. B. C. Allanach *et al.*, Phys. Rev. D **56**, 2362 (1997).
20. R. N. Mohapatra, Prog. Part. Nucl. Phys. **26**, 165 (1991); O. M. Boyarkin, Acta Phys. Pol. B **23**, 1031 (1992); Phys. Rev. D **50**, 2247 (1994).
21. N. G. Deshpande *et al.*, Phys. Rev. D **44**, 837 (1991).
22. G. G. Boyarkina and O. M. Boyarkin, Eur. Phys. J. C **13**, 99 (2000).
23. G. G. Boyarkina and O. M. Boyarkin, Yad. Fiz. **61**, 757 (1998) [Phys. At. Nucl. **61**, 683 (1998)].
24. M. Fukugita and T. Yanagida, *Physics and Astrophysics of Neutrino,* Ed. by M. Fukugita and A. Suzuki (Springer-Verlag, Tokyo, 1994).
25. R. N. Mohapatra, Phys. Rev. D **46**, 2990 (1992).
26. O. M. Boyarkin, Phys. Rev. D **53**, 5298 (1996).
27. C. W. Kim, S. Nussinov, and W. K. Sze, Phys. Lett. B **184**, 403 (1987).
28. T. D. Lee, Phys. Rev. D **8**, 1226 (1973).
29. S. L. Glashow and S. Weinberg, Phys. Rev. D **15**, 1958 (1977).
30. G. C. Branco *et al.*, Nucl. Phys. B **259**, 306 (1985); T. P. Cheng and M. Sher, Phys. Rev. D **35**, 3484 (1987); L. J. Hall and S. Weinberg, Phys. Rev. D **48**, 979 (1993); D. Atwood *et al.*, Phys. Rev. Lett. **75**, 3800 (1995); Phys. Rev. D **53**, 1199 (1996); **55**, 3156 (1997).
31. Palash B. Pal, Int. J. Mod. Phys. A **7**, 5387 (1992).
32. W. Fetscher, H. J. Gerber, and K. F. Johnson, Phys. Lett. B **173**, 102 (1986).
33. B. Balke *et al.*, Phys. Rev. D **37**, 587 (1988).
34. Review of Particle Physics, Eur. Phys. J. C **15**, 1 (2000).
35. ICHEP-2000, Osaka, Aug. 2000.
36. Gautan Bhattacharyya and Amitava Raychaudhuri, CERN-TH/95-118, 1995.
37. W. Lohmann and J. Raab, DESY 95-188, 1995.
38. CLEO Collab. (J. Bartelt *et al.*), Phys. Rev. Lett. **73**, 1890 (1994).

Translated by A. Isaakyan

Physics of Atomic Nuclei, Vol. 64, No. 11, 2001, pp. 1988–1994. Translated from Yadernaya Fizika, Vol. 64, No. 11, 2001, pp. 2073–2079.

ELEMENTARY PARTICLES AND FIELDS
Theory

Structure Function $F_2^p(x, Q^2)$ at Small x within the Generalized Regge Eikonal Approach

V. A. Petrov* **and A. V. Prokudin****

Institute for High Energy Physics, Protvino, Moscow oblast, 142284 Russia

Received April 21, 2000; in final form, February 14, 2001

Abstract—The small-x behavior of the proton structure function $F_2^p(x, Q^2)$ is investigated within a generalized Regge eikonal model that takes automatically into account the unitarity condition for processes involving off-shell particles. A good quality of description of experimental data for $x < 10^{-2}$ is achieved, and the assumption that data on $F_2^p(x, Q^2)$ that were obtained at the HERA collider can be described by using classical universal Regge trajectories is validated. In doing this, hypothetical hard trajectories with large intercepts are not used. The x and Q^2 slopes and the effective intercept are considered as functions of x and Q^2. © *2001 MAIK "Nauka/Interperiodica".*

1. INTRODUCTION

There exist a great number of models describing the small-x behavior of the proton structure function $F_2^p(x, Q^2)$ in terms of a so-called soft Pomeron [1] or in terms of a hard Pomeron [2]. Below, we essentially adduce new arguments in favor of a soft Pomeron within a general approach that takes into account the unitarity condition for processes involving virtual particles. This approach disregards completely the possibilities of calculations within perturbative QCD, but this does not of course mean that we ignore QCD as a basis of the theory of strong interactions.

2. EXTENSION OF THE REGGE EIKONAL MODEL TO PROCESSES INVOLVING VIRTUAL PARTICLES

We begin formulating the model from the unitarity condition

$$\mathrm{Im}T(s, \mathbf{b}) = |T(s, \mathbf{b})|^2 + \eta(s, \mathbf{b}),$$

where $T(s, \mathbf{b})$ is the scattering amplitude in the impact-parameter space, $\sqrt{s}$ is the c.m. collision energy, $\mathbf{b}$ is the impact parameter, and $\eta(s, \mathbf{b})$ stands for the contribution of inelastic channels. Within the eikonal model, the amplitude can be represented in the form

$$T(s, \mathbf{b}) = \frac{e^{2i\delta(s,\mathbf{b})} - 1}{2i} \quad . \tag{1}$$

In terms of the eikonal $\delta(s, \mathbf{b})$, the unitarity condition takes the simple form

$$\mathrm{Im}\delta(s, \mathbf{b}) \geq 0, \ s > s_{\mathrm{inel}}. \tag{2}$$

In the Regge pole approximation, the eikonal function in the t space (here, t is the momentum transfer) is given by

$$\hat{\delta}(s, t) = c\Big(\frac{s}{s_0}\Big)^{\alpha(0)} e^{t\frac{\rho^2}{4}}, \tag{3}$$

where c is a dimensionless constant, $s_0 = 1\ \mathrm{GeV}^2$,

$$\rho^2 = 4\alpha'(0)\ln\frac{s}{s_0} + r^2 \tag{4}$$

is the Reggeon radius, and r^2 (GeV^{-2}) is the bare radius of hadrons involved in the reaction being considered.

Thus, the eikonal function has a simple pole in the J plane, and the corresponding Regge trajectory is taken in the linear approximation at small t; that is,

$$\alpha(t) = \alpha(0) + \alpha'(0)t. \tag{5}$$

In order to go over from t to b space, we use the Fourier–Bessel transformation

$$\hat{f}(t) = 4\pi s \int_0^\infty db^2 J_0(b\sqrt{-t}) f(b), \tag{6}$$

$$f(b) = \frac{1}{16\pi s} \int_{-\infty}^0 dt J_0(b\sqrt{-t})\hat{f}(t). \tag{7}$$

By using (7), we obtain the well-known b representation for the eikonal function:

$$\delta(s, b) = \frac{c}{s_0}\Big(\frac{s}{s_0}\Big)^{\alpha(0)-1} \frac{e^{-\frac{b^2}{\rho^2}}}{4\pi\rho^2}. \tag{8}$$

In this approach, the Pomeron is the leading pole of the eikonal function.

*e-mail: petrov@mx.ihep.su
**e-mail: prokudin@th1.ihep.su

For cross sections, we use the following normalization conditions:

$$\sigma_{\rm tot} = \frac{1}{s}{\rm Im}T(s, t=0),$$
$$\sigma_{\rm el} = 4\pi \int\limits_0^\infty db^2 |T(s,b)|^2, \qquad (9)$$
$$\frac{d\sigma}{dt} = \frac{|T(s,t)|^2}{16\pi s^2}.$$

A generalization of the eikonal representation (in general, this is correct beyond the Regge eikonal approach as well) to the case of off-shell particles can be obtained by means of the following consideration. The amplitude $T(s,t)$ can be recast into the form

$$T(q', p'|q, p) \qquad (10)$$
$$= \hat{\delta}(q', p'|q, p) + i \int d^3q'' d^3p'' d^3q''' d^3p''' (2\pi)^4$$
$$\times \delta(q' + p' - q'' - p'')(2\pi)^4 \delta(q''' + p''' - q - p)$$
$$\times \delta(p', q'|q'', p'') L(q'', p''|q''', p''') \delta(q''', p'''|q, p),$$

where q, p and q', p' are the particle momenta, respectively, before and after a scattering event; for identical particles of mass m, we have

$$T(s,t) = T(q', p'|q, p)\Big|_{q'^2=q^2=p'^2=p^2=m^2}, \qquad (11)$$
$$\hat{\delta}(s,t) = \hat{\delta}(q', p'|q, p)\Big|_{q'^2=q^2=p'^2=p^2=m^2},$$
$$s = (p+q)^2 = (p'+q')^2,$$
$$t = (p-p')^2 = (q-q')^2,$$
$$d^3p = \frac{d\mathbf{p}}{(2\pi)^3 \cdot 2p_0} \equiv \frac{d^4p}{(2\pi)^4}\Theta(p_0) \cdot 2\pi\delta(p^2 - m^2),$$
$$\sum_{n=2}^{\infty} \frac{2(2i\delta(s,b))^{n-2}}{n!} \equiv L(s,b),$$
$$L(s,t) = 4s \int d^2b e^{ikb} L(s,b).$$

The representation in (10) can be illustrated by the following diagram:

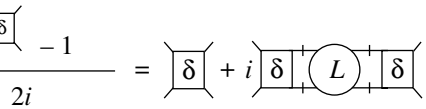

A further step, which is of paramount importance indeed, consists in letting some external momenta go off the mass shell. We assume that $q^2 \neq m^2$ and $q'^2 \neq m^2$ (that is, two of the interacting particles are off the mass shell, as they are in the process $\gamma^* p \to \gamma^* p$). The representation in (10) then takes the form

$$T^{**} = \hat{\delta}^{**} + i\hat{\delta}^* \circ L \circ \hat{\delta}^*, \qquad (12)$$

where asterisks label off-shell particles and the symbol "$\circ$" denotes integration as in (10). The off-shell amplitude can be related to the on-shell amplitude as [3]

$$T^{**}(s,b) = \delta^{**}(s,b) \qquad (13)$$
$$- \frac{\delta^*(s,b)\delta^*(s,b)}{\delta(s,b)} + \frac{\delta^*(s,b)\delta^*(s,b)}{\delta(s,b)\delta(s,b)} T(s,b).$$

The decomposition in (12) can obviously be illustrated with the aid of the following diagram:

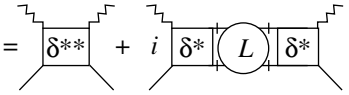

The case where only one particle is off the mass shell is considered in a similar way. We assume that $q^2 \neq m^2$. Equation (10) can then be recast into the form

$$T^* = \hat{\delta}^* + i\hat{\delta}^* \circ L \circ \hat{\delta}\,, \qquad (14)$$

or

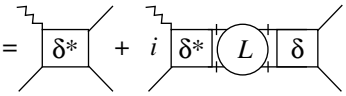

The amplitudes T^* and T are obviously related by the equation

$$T^*(s,b) = \frac{\delta^*(s,b)}{\delta(s,b)} T(s,b). \qquad (15)$$

Let us choose a specific realization of the eikonal function in the presence of virtual particles. In terms of the operator-product-expansion method, the eikonal is actually associated (in the spirit of the well-known Chew–Yang approach, but with allowance for the latest achievements) with the contribution of the leading twist 2, whence it follows that, at fixed $x \simeq Q^2/(s+Q^2)$ values, the violation of scaling is weak (non-power-law). Taking this and formula (8) into account, we parametrize the eikonal in the form

$$\delta^*_\pm(s,b) = \xi_\pm \frac{c_*(Q^2)}{s_0 + Q^2 - m^2} \qquad (16)$$
$$\times \left(\frac{s + Q^2 - m^2}{s_0 + Q^2 - m^2}\right)^{\alpha(0)-1} \frac{e^{-b^2/\rho_*^2}}{4\pi\rho_*^2}.$$

Here, $\xi_\pm$ are the signature factors;

$$\rho_*^2 = 4\alpha'(0) \ln \frac{s + Q^2 - m^2}{s_0 + Q^2 - m^2} + r_N^2 + r_*^2(Q^2)\,; \qquad (17)$$

and

$$\delta^{**}_{\pm}(s,b) = \xi_{\pm}\frac{c_{**}(Q^2)}{s_0+Q^2-m^2} \times \Big(\frac{s+Q^2-m^2}{s_0+Q^2-m^2}\Big)^{\alpha(0)-1}\frac{e^{-b^2/\rho^2_{**}}}{4\pi\rho^2_{**}}, \quad (18)$$

where

$$\rho^2_{**} = 4\alpha'(0)\ln\frac{s+Q^2-m^2}{s_0+Q^2-m^2} + r_N^2 + r^2_{**}(Q^2) \quad (19)$$

and r_N, r_*, and r_{**} are radii associated with the corresponding vertices. We assume that the coefficients $c_*(Q^2)$ and $c_{**}(Q^2)$ weakly depend (in a non-power-law way) on Q^2. Below, we describe the properties of the model in various kinematical regimes.

2.1. Total Cross Section

According to the representation in (10), we obtain

$$\sigma^{**}_{\rm tot} = \frac{1}{s}{\rm Im}T^{**}(s,t=0)\ . \quad (20)$$

We have

$$\sigma^{**}_{\rm tot} \to \frac{(s/Q^2)^{\Delta}}{Q^2} \times \Big[c_{**}(Q^2) - \frac{c_*(Q^2)^2}{c}\Big(\frac{s_0}{Q^2}\Big)^{1+\Delta}\frac{\rho^2}{\rho^2_*}\Big] \quad (21)$$

in the Regge regime ($s \gg Q^2$) and

$$\sigma^{**}_{\rm tot} \to \frac{c_{**}(Q^2)}{Q^2}\Big(\frac{1}{x}\Big)^{\Delta} - \frac{c_*(Q^2)^2}{2c}\frac{1}{Q^2}\Big(\frac{1}{x}\Big)^{\Delta}\Big(\frac{s_0}{Q^2}\Big)^{1+\Delta}\frac{\ln\dfrac{Q^2(1-x)}{s_0 x}}{\ln(1/x)}. \quad (22)$$

in the Bjorken regime ($s \simeq Q^2(1-x)/x$; x is fixed).

We can now demonstrate an interesting phenomenon that is observed in our model, the stripping of the Pomeron. Such an effect also occurs in the model considered in [4], in which case the effective intercept

$$\Delta(Q^2) = \Delta_0\left(1+\frac{2Q^2}{Q^2+d}\right), \quad (23)$$

where d (GeV^2) is a parameter, depends only on Q^2 and grows with increasing Q^2 ($\Delta(Q^2=0) = \Delta_0 \sim 0.08$, $\Delta(Q^2\to\infty) \sim 0.24$).

Let us assume that the structure function is described by the formula

$$F_2^p(x,Q^2) = f(Q^2)\Big(\frac{1}{x}\Big)^{\Delta_{\rm eff}(Q^2)}, \quad (24)$$

where $\Delta_{\rm eff}(Q^2)$ is the effective intercept, which does not of course correspond to the Regge trajectory, since it depends on the photon virtuality Q^2. We now use (22) and, at fixed (and sufficiently small) x, find that, in our model, the effective intercept can be represented as

$$\Delta_{\rm eff}(x,Q^2) \simeq \Delta + \frac{(s_0/Q^2)^{1+\Delta}}{\ln^2(1/x)}f(x,Q^2), \quad (25)$$

where

$$f(x,Q^2) = \frac{c_*(Q^2)\ln(Q^2/s_0)}{2\,c\,c_{**}(Q^2) - \dfrac{c_*(Q^2)(s_0/Q^2)^{1+\Delta}\ln(Q^2/s_0)\,x}{\ln(1/x)}}. \quad (26)$$

In expression (25), the right-hand side tends to Δ with increasing Q^2. Thus, we obtain the following effect: with increasing photon virtuality Q^2, the unitary corrections decrease; at sufficiently small x, the proton structure function can be described by the Born term of the eikonal expansion, so that the effective intercept in (24) will be equal to the Pomeron intercept.

In our model, the effective intercept depends, in contrast to what takes place in (23), on x and $\Delta_{\rm eff}(x, Q^2\to\infty) \sim 0.1$ as well.

Thus, we obtain a method for measuring the Pomeron intercept and for testing our model.

The total cross section exhibits a power-law behavior in the Regge limit, but this does not mean the violation of the Froissart–Martin bound [5], since this bound cannot be obtained for this case. But if we recover the mass-shell conditions for particles, we will recover the normal logarithmic asymptotic behavior of the cross section as well, $\sigma \sim \ln^2(s/s_0)$. In the Bjorken limit, we have a strong (power-law) violation of scaling in the second term, which, however, does not represent the contribution of higher twists because it has a nonintegral power. It is interesting to note that, if the entire dependence on virtuality in the eikonal strictly factorized, the total cross section would obey the Froissart–Martin bound off the mass shell (with respect to the s dependence) as well. However, there is generally no such factorization.

2.2. Elastic-Scattering Cross Section

For elastic-scattering cross section, we arrive at [see (10)]

$$\sigma^*_{\rm el} = 4\pi\int\limits_0^{\infty} db^2\Big|\frac{\delta^*}{\delta}T(s,b)\Big|^2. \quad (27)$$

Since $q'^2 = \mu^2$, where μ is the mass of the product particle, it is natural to assume that $s_0 = \mu^2$. As a result, we obtain

$$\sigma^*_{\rm el} \to 16\pi\alpha'(0)\Delta\Big(\frac{c_*}{c}\Big)^2\Big(\frac{\mu^2}{Q^2}\Big)^{2+2\Delta}\Big(\ln\frac{s}{\mu^2}\Big)^2 \quad (28)$$

Parameter values obtained by fitting experimental data

$\Delta_{\mathbf{P}}$	0.11578 (fix.)	$\alpha'_{\mathbf{P}}$ [GeV^{-2}]	0.27691 (fix.)
c^{**}	7.7247 ± 4.1474	c^*	2.4350 ± 2.7259
c_1^*	$(0.42154 \pm 0.58348) \times 10^{-1}$	r^2 [GeV^{-2}]	62.152 ± 81.490
Q_0^2 [GeV^2]	1.0 (fix.)	W_0 [GeV]	1.8869 ± 0.87862

in the Regge regime and

$$\sigma_{\rm el}^* \to 8\pi\alpha'(0)\Big(\frac{c_*}{c}\Big)^2\Big(\frac{\mu^2}{Q^2}\Big)^{2+2\Delta}\frac{(\ln(Q^2/x))^2}{\ln(1/x)} \quad (29)$$

in the Bjorken regime.

It is interesting to note that

$$\frac{\sigma_{\rm el}^*}{\sigma_{\rm tot}^{**}} \to 0 \quad (30)$$

in contrast to the limit of 1/2 for the case where all particles are on the mass shell. We are now ready to proceed to describe the proton structure function $F_2^p(x,Q^2)$.

3. MODEL FOR $F_2^p(x,Q^2)$

The proton structure function $F_2^p(x,Q^2)$ is related to the transverse cross section $\sigma_T^{**}(W,Q^2)$ for the process $\gamma^* + p \to X$ by the equation

$$\sigma_T^{**}(W,Q^2) = \frac{4\pi^2\alpha}{Q^2(1-x)} \times \frac{1+\dfrac{4m_p^2x^2}{Q^2}}{1+R(x,Q^2)}F_2^p(x,Q^2), \quad (31)$$

where $W^2 = \dfrac{Q^2}{x} - Q^2 + m_p^2$ and $R(x,Q^2) = \dfrac{\sigma_L^{**}}{\sigma_T^{**}}$. Since the ratio $R(x,Q^2)$ is assumed to be small, we set it to zero; that is, we assume that the total cross section coincides with the transverse cross section.

In the ensuing analysis, we restrict ourselves to the case of x values as small as $x < 10^{-2}$; this is done in order that we could use the asymptotic formula (21), which explicitly demonstrates unitarization effects in our model. By using (13), (16), and (18), we can recast Eq. (21) into the form ($s \equiv W^2$; $\Delta_{\mathbf{P}} \equiv \Delta$ is the Pomeron intercept)

$$\sigma_{\rm tot}^{**} \to \frac{((W^2+Q^2-m_p^2)/(W_0^2+Q^2-m_p^2))^{\Delta_{\mathbf{P}}}}{(W_0^2+Q^2-m_p^2)} \times \Big[c_{**}(Q^2) - \frac{c_*^2(Q^2)}{c}\Big(\frac{W_0^2-\mu^2-m_p^2}{W_0^2+Q^2-m_p^2}\Big)^{1+\Delta_{\mathbf{P}}}\frac{\rho^2}{\rho_*^2}\Big]. \quad (32)$$

In deriving this formula, we assumed that the γ^*p scattering amplitude is proportional to the amplitude for the scattering of a virtual vector meson by a proton [6] and that this effective vector meson is ρ_0; that is,

$$T_{\gamma^*p\to\gamma^*p}(W,Q^2,t) = kT_{\rho_0^*p\to\rho_0^*p}(W,Q^2,t), \quad (33)$$

where k is a constant.

We note that the asymptotic behavior given by (32) takes place at $Q^2 = 0$—that is, for real photons. Although the photons are real in this case, the vector mesons are off the mass shell. Therefore, the Froissart–Martin bound is not violated. But if we take into account electromagnetic interaction in all orders in $\alpha_{\rm em}$, $\sigma_{\gamma p}$ will be infinite because of long-range interactions in the t channel.

Because we use asymptotic formulas, we neglect the real part of the Pomeron signature factor (since it is proportional to $\Delta_{\mathbf{P}} \simeq 0.1$) and set the signature factor to i.

The parametrizations for c_{**} and c_* are

$$c_{**}(Q^2) = \frac{c^{**}}{((Q_0^2+Q^2)/Q_0^2)^{\Delta}}, \quad (34)$$

$$c_*(Q^2) = \frac{c^* + c_1^*\ln\left(\dfrac{Q_0^2+Q^2}{Q_0^2}\right)^3}{((Q_0^2+Q^2)/Q_0^2)^{\Delta}},$$

$$c = c_*(-\mu^2),$$

where $Q_0^2 = 1.0$ GeV^2; $\mu = 0.77$ GeV (ρ-meson mass); and c^{**}, c^*, and c_1^* are numerical parameters.

In principle, the Q^2 dependence of the coefficients $c_{*(*)}$ can be taken into account with the aid of perturbative QCD (by introducing some additional assumptions). However, we refrain from doing this here and rely on purely phenomenological fits for the coefficients. In order to clarify the role of perturbative QCD, we are going to use it in subsequent studies. The parametrizations of the radii ρ^2 and ρ_*^2 are

$$\rho_*^2(W,Q^2) = 4\alpha'(0) \times \ln\frac{W^2+Q^2-m_p^2}{W_0^2+Q^2-m_p^2} + r^2/(Q_0^2+Q^2), \quad (35)$$

$$\rho^2(W) = \rho_*^2(W,-\mu^2)\ ,$$

where r and W_0^2 (GeV^2) are parameters and $Q_0^2 = 1.0$ GeV^2.

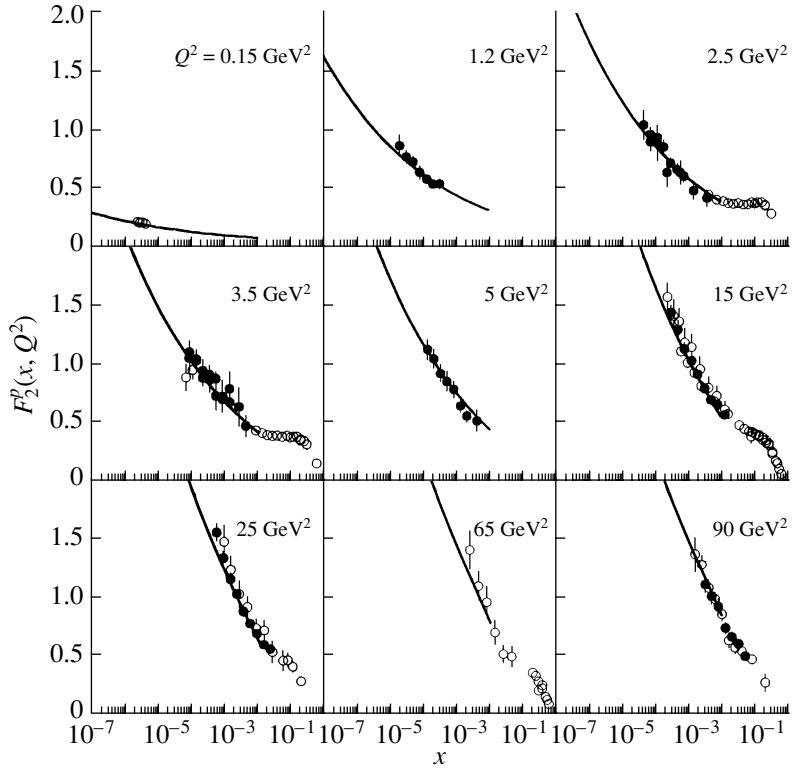

Fig. 1. Experimental data on the proton structure function $F_2^p(x, Q^2)$ at low Q^2 and model predictions

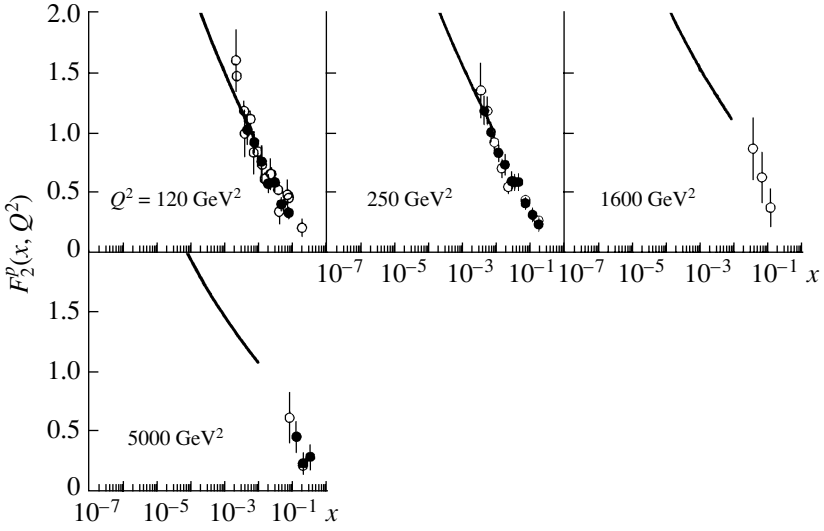

Fig. 2. Experimental data on the proton structure function $F_2^p(x, Q^2)$ at high Q^2 and model predictions.

For the proton structure function $F_2^p(x, Q^2)$, we finally obtain

$$F_2^p(x,Q^2) = \frac{1}{4\pi^2\alpha}\frac{Q^2(1-x)}{1+\dfrac{4m_p^2x^2}{Q^2}} \qquad (36)$$
$$\times \frac{((W^2+Q^2-m_p^2)/(W_0^2+Q^2-m_p^2))^{\Delta_{\mathbf{P}}}}{(W_0^2+Q^2-m_p^2)}$$
$$\times \left[c_{**}(Q^2) - \frac{c_*^2(Q^2)}{c}\left(\frac{W_0^2-\mu^2-m_p^2}{W_0^2+Q^2-m_p^2}\right)^{1+\Delta_{\mathbf{P}}} \frac{\rho^2}{\rho_*^2}\right].$$

For $Q^2 \gg W_0^2$ and $1/x \gg 1$, the asymptotic expression for the structure function is

$$F_2^p(x,Q^2) \simeq \left(\frac{1}{x}\right)^{\Delta}\left[c_{**}(Q^2) - \frac{c_*^2(Q^2)}{c} \qquad (37)\right.$$

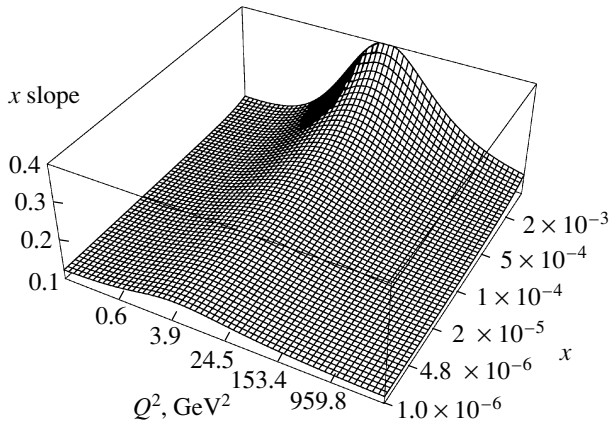

Fig. 3. Slope $\frac{\partial ln F_2^p(x,Q^2)}{\partial \ln(1/x)}$ in the coordinate x as a function of x and Q^2.

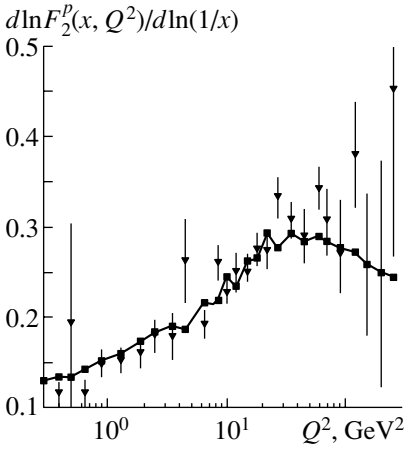

Fig. 4. Effective intercept measured experimentally, along with model predictions. Closed boxes on the curve indicate points where the slope $\frac{\partial \ln F_2^p(x,Q^2)}{\partial \ln(1/x)}$ was calculated.

$$\times \left(\frac{\ln(Q^2/W_0^2)}{\ln(1/x)} + 1 \right) \left(\frac{W_0^2}{Q^2} \right)^{1+\Delta} \Bigg].$$

4. RESULTS

It was mentioned above that, in our fit, we use data for $x < 10^{-2}$; thus, we select 401 points of the complete set of 1265 points. Having five free parameters, we obtained $\chi^2/\mathrm{NDF} = 1.0098$. (The fitted parameter values are quoted in the table. Data on the intercept and the slope of the Pomeron trajectory were borrowed from the study reported in [7] and devoted to describing nucleon–nucleon scattering.)

The results of fitting are presented in Figs. 1 and 2.

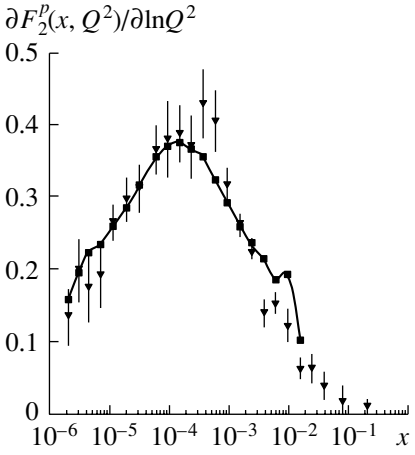

Fig. 5. Slope $\frac{\partial F_2^p(x,Q^2)}{\partial \ln Q^2}$ in the coordinate Q. Closed boxes on the curve indicate points where the slope was calculated within the model.

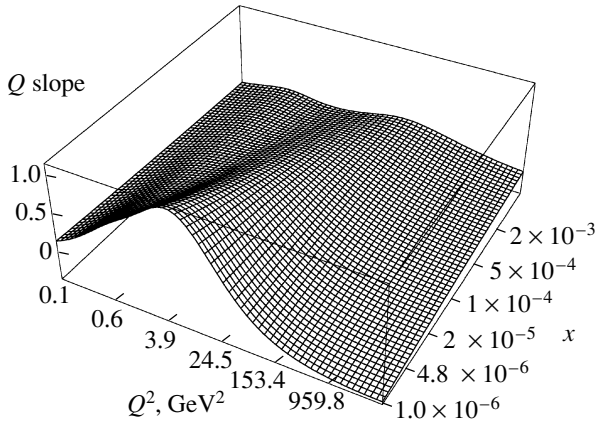

Fig. 6. Slope $\frac{\partial F_2^p(x,Q^2)}{\partial \ln Q^2}$ in the coordinate Q as a function of x and Q^2.

4.1. x Slope or $\partial \ln F_2^p(x, Q^2)/\partial \ln(1/x)$

Data on $F_2^p(x, Q^2)$ show a tendency toward a fast growth with decreasing x—this is the so-called HERA effect. Our model assumes that this effect will become weaker with increasing Q^2 (Fig. 3). This was also predicted within the dipole-Pomeron model [1b]. We suppose that new experimental data in the region specified by the inequalities $100 \le Q^2 \le 1000$ GeV^2 and $x \le 10^{-2}$ will contribute to proving or disproving this prediction.

The effective intercept, which is measured experimentally under the assumption that $F_2^p \propto (1/x)^{\Delta_{\mathrm{eff}}(Q^2)}$, can be approximately associated with the x slope if the slope depends weakly on x. We have calculated the slope; the results of these calculations

are shown in Fig. 4, along with experimental data. We emphasize that we have calculated the effective slope; that is, we have not included experimental data on it in the fitting process. As can be seen, the experimental data are well described by our model.

4.2. Q Slope or $\partial F_2^p(x,Q^2)/\partial \ln Q^2$

Data on the Q slope show a peak in the region $Q^2 \sim 1$–5 GeV^2. This maximum is often interpreted as a transition from the Regge behavior to the perturbative regime of QCD. We have performed relevant calculations within our model; the results are displayed in Fig. 5. As can be seen, the specific behavior of the Q slope is quite consistent with the Regge regime. We also want to emphasize that the definition of the transition region depends on the path in the two-dimensional surface of $\partial F_2^p(x,Q^2)/\partial \ln Q^2$, and this can lead to an x dependence for the position of the maximum [1b]. In order to demonstrate this effect, we present a figure that illustrates the slope calculated within our model (Fig. 6).

5. CONCLUSION

The proton structure function $F_2^p(x,Q^2)$ at small x has been described within the generalized Regge eikonal approach. No additional Regge poles with Q^2-dependent intercepts are required for describing experimental data. Experimental data on the x and Q slopes have also been well described. The model predicts the weakening of the effect obtained at the HERA collider (the same prediction was made within the dipole-Pomeron model [1b]).

ACKNOWLEDGMENTS

We are grateful to E. Martynov and A. Kaidalov for stimulating discussions and to A. De Roeck for placing experimental data at our disposal. One of the authors (A.V. Prokudin) is indebted to the Department of the Theoretical Physics at the International Centre for Theoretical Physics (ICTP, Trieste, Italy) for the invitation and hospitality at ICTP, where part of this work was performed.

REFERENCES

1. (a) K. Adel, F. Barreiro, and F. J. Ynduráin, Nucl. Phys. B **495**, 211 (1997); E. Martynov, in *Proceedings of the Conference "Handron-94," Uzhgorod, 1994,* Ed. by G. Bugroy, L. Jenkovszky, E. Martynov (Naukova Dumka, Kiev, 1994), p. 311; E. Martynov, in *Proceedings of the VI Blois Conference on Elastic and Diffractive Scattering, Blois, France, 1995,* Ed. by P. Chiapetta, M. Haguenauer, and J. Trân Thanh Vân (Editions Frontières, Paris, 1996), p. 203; L. Jenkovszky, E. Martynov, and F. Paccanoni, PFDP 95/TH/21, Padova University (1995); W. Buchmuller and D. Haidt, DESY 96-061 (1996); hep-ph/9605428; D. Schildknecht and H. Spiesberger, BI-TP 97/25, hep-ph/9707447; (b) P. Desgrolard *et al.,* Phys. Lett. B **309**, 191 (1993); P. Desgrolard, A. Lengyel, and E. Martynov, Eur. Phys. J. C **7**, 655 (1999).
2. A. Capella *et al.,* Phys. Lett. B **337**, 358 (1994); H. Abramowicz *et al.,* Phys. Lett. B **269**, 465 (1991); H. Abramowicz and A. Levy, DESY 97-251; hep-ph/9712415; A. Donnachie, in *Proceedings of the Summer School on Hadronic Aspects of Collider Physics, Zuoz, 1994,* Ed. by E. P. Locher (PSI-Proc., Villigen, 1994), p. 135; M. Bertini, M. Giffon, and E. Predazzi, Phys. Lett. B **349**, 561 (1995); A. Donnachie and P. V. Landshoff, Phys. Lett. B **437**, 408 (1998); C. Merino, A. B. Kaidalov, and D. Pertermann, hep-ph/9911331.
3. V. Petrov, in *Proceeding of the VI Blois Workshop* (Editions Frontières, Paris, 1995), p. 139; Nucl. Phys. B (Proc. Suppl.) **54**, 160 (1997).
4. A. Capella, A. Kaidalov, C. Merino, and J. Trân Thanh Vân, Phys. Lett. B **337**, 358 (1994).
5. M. Froissart, Phys. Rev. **123**, 1053 (1961); A. Martin, Phys. Rev. **129**, 993 (1963).
6. N. M. Kroll, T. D. Lee, and B. Zumino, Phys. Rev. **157**, 1376 (1967).
7. V. Petrov and A. Prokudin, in *Proceedings of the International Conference on Elastic and Diffractive Scattering, Protvino, Russia, 1999* (World Sci., Singapore, 2000), p. 95.

Translated by A. Isaakyan

Physics of Atomic Nuclei, Vol. 64, No. 11, 2001, pp. 1995–2005. From Yadernaya Fizika, Vol. 64, No. 11, 2001, pp. 2080–2090.

ELEMENTARY PARTICLES AND FIELDS
Theory

Comparison of the k_T-Factorization Approach and the QCD Parton Model for Charm and Beauty Hadroproduction*

M. G. Ryskin[**], **Yu. M. Shabelski**[1),***], **and A. G. Shuvaev**[****]

Petersburg Nuclear Physics Institute, Russian Academy of Sciences, Gatchina, 188300 Russia

Received September 12, 2000; in final form, February 28, 2001

Abstract—We compare numerical predictions of the conventional QCD parton model and of the k_T-factorization approach (semihard theory) for heavy-quark production in high-energy hadron collisions. The total production cross sections and one-particle rapidity and p_T distributions, as well as two-particle correlations, are considered. The distinction between the predictions of the two approaches is not very large, while the shapes of the distributions are slightly different. © *2001 MAIK "Nauka/Interperiodica".*

1. INTRODUCTION

Investigation of heavy-quark production in high-energy hadron collisions is an important method for studying the quark–gluon structure of hadrons. Realistic estimates of the cross section for heavy-quark production, as well as the correlations of two product heavy quarks (heavy-flavor hadrons), are necessary for planning experiments at existing and future accelerators, as well as in cosmic-ray physics.

The description of hard interactions in hadron collisions within QCD is possible only with the help of some phenomenology, which reduces the hadron–hadron interaction to the parton–parton one via the formalism of the hadron structure functions. The cross sections of hard processes in hadron–hadron interactions can be written as the convolutions of squared matrix elements of the subprocess calculated within QCD with parton distributions in colliding hadrons.

The most popular and technically simplest approach is the so-called QCD collinear approximation or parton model (PM). In this model, all particles involved are assumed to be on the mass shell, carrying only longitudinal momenta, and the cross section is averaged over two transverse polarizations of the incident gluons. The virtualities q^2 of the initial partons are taken into account only through their structure functions. The cross sections of QCD subprocess are calculated usually in the leading order (LO), as well as in the next-to-leading order (NLO) [1–5]. The transverse momenta of the incident partons are neglected in the QCD matrix elements. This is the direct analogy of the Weizsäcker–Williams approximation in QED. It allows one to describe quite reasonably experimental data on the total cross sections and one-particle distributions of product heavy flavors; however, it cannot reproduce, say, the azimuthal correlations [6] of two heavy quarks or the distributions over the total transverse momentum of heavy-quark pairs [7], which are determined by the transverse momenta of the incident partons.

There is an attempt at incorporating the transverse momenta of the incident partons by a random shift of these momenta (k_T kick) [7] according to certain exponential distributions. This allows one to describe quantitatively two-particle correlations [7], but creates the problems in the simultaneous description of one-particle longitudinal and transverse momentum distributions [8].

Another possibility to incorporate the incident parton transverse momenta is referred to as the k_T-factorization approach [9–13], or the theory of semihard interactions [14–19]. Here, the Feynman diagrams are calculated taking account of the virtualities and of all possible polarizations of the incident partons. In the small-x domain (x is the fraction of the momentum of incident hadron which is carried out by the parton under consideration in the infinite-momentum frame), there are no grounds to neglect the transverse momenta of the gluons, q_{1T} and q_{2T}, in comparison with the quark mass and transverse momenta, p_{iT}. Moreover, at very high energies and very high p_{1T}, the main contribution to the cross sections comes from the region of $q_{1T} \sim p_{1T}$ or $q_{2T} \sim p_{1T}$. The QCD matrix elements of the subprocesses are rather complicated in such an approach. We have

*This article was submitted by the authors in English.

[1)]Abdus Salam International Centre for Theoretical Physics, Strada Costiera 11, I-34014 Trieste, Italy.

[**]e-mail: ryskin@thd.pnpi.spb.ru

[***]e-mail: shabelsk@thd.pnpi.spb.ru

[****]e-mail: shuvaev@thd.pnpi.spb.ru

calculated them in the LO. On the other hand, the multiple emission of soft gluons is included here. That is why there arises the question of which approach is more constructive.

The majority of the published papers on k_T factorization have presented no numerical results or presented rather incomplete ones. Old sets of structure functions have been used, and, sometimes, the parton model results obtained with a particular set are compared with k_T-factorization results based on another set.

In [20], we presented a comparison of results obtained with the help of the k_T-factorization approach and the parton model. The main goal of [20] was to demonstrate the differences in the qualitative and numerical predictions coming from the matrix elements. To simplify the calculations and to avoid various additional dependences, we used a gluon distribution which had only a reasonable qualitative behavior and a fixed value of α_s.

The objective of this study is to present a comparison between the results of the conventional parton model and the k_T-factorization approach for the quantities which are measured experimentally. For this reason, we use the realistic gluon distribution GRV94 [21] compatible with the most recent data (see discussion in [22]).

Below, we briefly repeat the basic formalism of the approaches used, discuss the values of the parameters, and present numerical results on charm and beauty production obtained in the LO (and qualitatively in NLO) parton model and in the k_T-factorization approach.

2. CONVENTIONAL PARTON-MODEL APPROACH

The conventional PM expression for the calculation of heavy-quark-hadroproduction cross sections has the factorized form [23]

$$\sigma(AB \to Q\bar{Q}) = \sum_{ij} \int dx_i dx_j G_{A/i}(x_i, \mu_F) \quad (1)$$
$$\times\, G_{B/j}(x_j, \mu_F) \hat{\sigma}(ij \to Q\bar{Q}),$$

where $G_{A/i}(x_i, \mu_F)$ and $G_{B/j}(x_j, \mu_F)$ are the structure functions of partons i and j in the colliding hadrons A and B with invariant energy s_{AB}, μ_F is the factorization scale (i.e., virtualities of incident partons), and $\hat{\sigma}(ij \to Q\bar{Q})$ is the cross section of the subprocess that is calculated in perturbative QCD. The latter cross section can be written as a sum of LO and NLO contributions,

$$\hat{\sigma}(ij \to Q\bar{Q}) = \frac{\alpha_s^2(\mu_R)}{m_Q^2}\Big(f_{ij}^{(o)}(\rho) \quad (2)$$
$$+ 4\pi\alpha_s(\mu_R)\Big[f_{ij}^{(1)}(\rho) + \bar{f}_{ij}^{(1)}(\rho)\ln(\mu^2/m_Q^2)\Big]\Big),$$

where α_s is QCD coupling constant, μ_R is the renormalization scale, and $f_{ij}^{(o)}$, as well as $f_{ij}^{(1)}$ and $\bar{f}_{ij}^{(1)}$, depends only on the single variable

$$\rho = \frac{4m_Q^2}{\hat{s}}, \hat{s} = x_i x_j s_{AB}; \quad (3)$$

therefore, $\hat{s}$ is the invariant energy of colliding partons. {In the factor $\ln(\mu^2/m_Q^2)$, we assume $\mu_R = \mu_F = \mu$ following [1]. In the case of different values of μ_R and μ_F, which is preferable for describing experimental data from [7], Eq. (2) becomes more complicated.}

Expression (1) corresponds to the process shown schematically in Fig. 1. The main contribution to the cross section at small x is known to come from gluons, $i = j = g$.

Usually in the PM, the values

$$\mu_F = \mu_R = m_Q \quad (4)$$

are used for the total cross sections and

$$\mu_F = \mu_R = m_T = \sqrt{m_Q^2 + p_{QT}^2} \quad (5)$$

for the one-particle distributions [7]. However, we calculate the total cross sections of heavy-quark production as the integrals over their p_T distrubutions, i.e., with scales (5).

Both in the parton model and in the k_T-factorization approach, we take

$$m_c = 1.4\ \text{GeV}, \qquad m_b = 4.6\ \text{GeV} \quad (6)$$

for the values of short-distance perturbative quark masses [24, 25].

Another important problem of PM is the collinear approximation. The transverse momenta of the incident partons, q_{iT} and q_{jT}, are assumed to be zero, and their virtualities are taken into account only through the structure functions; the cross section $\hat{\sigma}(ij \to Q\bar{Q})$ is assumed to be independent of these virtualities. Naturally, this approximation significantly simplifies the calculations.

The conventional NLO parton-model approach with collinear approximation works quite reasonably for one-particle distributions and for the total cross sections; at the same time, it is in serious disagreement with data on heavy-quark correlations (without introducing a k_T kick [7]).

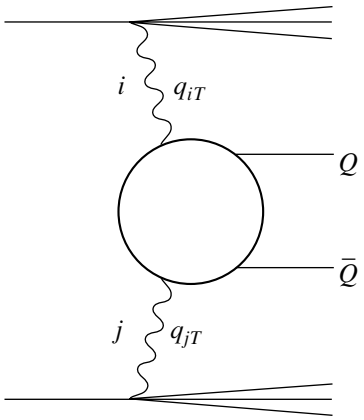

Fig. 1. Heavy-quark production in hadron–hadron collisions. The LO parton model corresponds to the case where $q_{1T} = q_{2T} = 0$.

3. HEAVY-QUARK PRODUCTION IN THE k_T-FACTORIZATION APPROACH

In the k_T-factorization approach, the transverse momenta of the incident gluons in the small-x region result from the $\alpha_s \ln k_T^2$ diffusion in the gluon evolution. The diffusion is described by the function $\varphi(x, q^2)$ giving the gluon distribution at a fixed fraction of the longitudinal momentum of the initial hadron, x, and of the gluon virtuality, q^2. At very low x, the leading $\log(1/x)$ accuracy seems reasonable; therefore, the function $\varphi(x, q^2)$ can be approximately determined [14] via the derivative of the usual structure function:

$$\varphi(x, q^2) = 4\sqrt{2}\pi^3 \frac{\partial[xG(x, q^2)]}{\partial q^2}. \qquad (7)$$

This definition of $\varphi(x, q^2)$ enables us to treat correctly effects arising from the gluon virtualities.

Although φ is generally a function of three variables, x, q_T, and q^2, the transverse momentum dependence is comparatively weak since $q_T^2 \approx -q^2$ for small x in the leading log approximation (LLA) in agreement with q^2 dependences of structure functions. Note that, due to QCD scaling violation, $\varphi(x, q^2)$ for realistic structure functions increases faster with decreasing x. Therefore, at smaller x, larger q_T becomes important in numerical calculations.

The exact expression for the q_T gluon distribution can be obtained as a solution to the evolution equation, which, in contrast to the PM case, is nonlinear due to interactions between the partons in the small-x region. The calculations [26] of the q_T gluon distribution in the leading order by using Balitsky–Fadin–Kuraev–Lipatov (BFKL) theory [27] result in

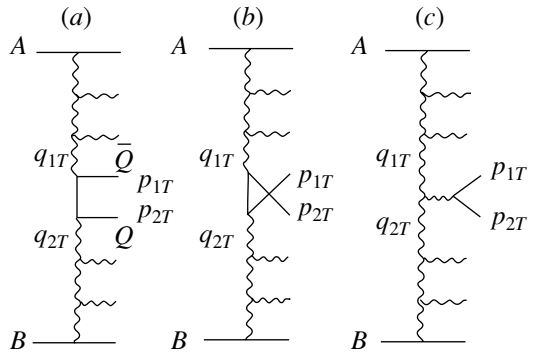

Fig. 2. Low-order QCD diagrams (a–c) for heavy-quark production in hadron A–hadron B collisions via gluon–gluon fusion.

deviations from our $\varphi(x, q^2)$ function given by (7) by only about 10–15%.

Here, we deal with a matrix element that takes into account the gluon virtualities and polarizations. Since it is much more complicated than in the PM, we consider only the LO of the subprocess $gg \to Q\bar{Q}$, which gives the main contribution to the heavy-quark-production cross section at small-x (see the diagrams in Fig. 2). The lower and upper ladder blocks represent the two-dimensional gluon functions $\varphi(x_1, q_1^2)$ and $\varphi(x_2, q_2^2)$.

Strictly speaking, Eq. (7) may be justified only in the leading $\log(1/x)$ limit. To restore the unintegrated parton distribution $f_a(x, q_T, \mu)$ (i.e., the probability of finding a parton a with transverse momentum q_T that initiates our hard process with factorization scale μ) based on the conventional (integrated) parton density $a(x, q_1^2)$, we have to consider the Dokshitzer–Gribov–Lipatov–Altarelli–Parisi (DGLAP) evolution[2)]

$$\frac{\partial a}{\partial \ln q_1^2} = \frac{\alpha_s}{2\pi}\left[\int_x^{1-\Delta} \sum_{a'} P_{aa'}(z) a'\left(\frac{x}{z}, q_1^2\right) dz \right. \qquad (8)$$
$$\left. - a(x, q_1^2) \sum_{a'} \int_0^{1-\Delta} P_{a'a}(z') dz' \right]$$

[here, $a(x, q_1^2)$ denotes $xg(x, q_1^2)$ or $xq(x, q_1^2)$, and $P_{aa'}(z)$ are the splitting functions].

The first term on the right-hand side of (8) describes the number of partons δ_a emitted in the interval $q_1^2 < q_T^2 < q_1^2 + \delta q_1^2$, while the second (virtual) term reflects the fact that the parton a disappears after splitting.

[2)]For $g \to gg$ splitting, we must insert the factor z' into the last integral in Eq. (8) to take into account the identity of the product gluons.

The second contribution may be resummed to give the survival probability T_a that the parton a with transverse momentum q_T remains intact in the evolution up to the factorization scale:

$$T_a(q_T,\mu) \tag{9}$$
$$= \exp\left[-\int\limits_{q_T^2}^{\mu^2}\frac{\alpha_s(p_T)}{2\pi}\frac{dp_T^2}{p_T^2}\sum_{a'}\int\limits_0^{1-\Delta}P_{a'a}(z')dz'\right].$$

Thus, the unintegrated distribution $f_a(x,q_T,\mu)$ has the form

$$f_a(x,q_T,\mu) \tag{10}$$
$$= \left[\frac{\alpha_s}{2\pi}\int\limits_x^{1-\Delta}P_{aa'}(z)a'\left(\frac{x}{z},q_T^2\right)dz\right]T_a(q_T,\mu),$$

where the cutoff $\Delta = q_T/\mu$ is used in Eqs. (8)–(10) [28, 29].

In the leading $\log(1/x)$ (i.e., BFKL) limit, the virtual DGLAP contribution is neglected. Thus, $T_a = 1$, and one comes back to (7)

$$f_a^{\mathrm{BFKL}}(x,q_T,\mu) = \frac{\partial a(x,\lambda^2)}{\partial\ln\lambda^2}, \lambda = q_T. \tag{11}$$

In the double log limit, Eq. (10) can be written in the form

$$f_a^{\mathrm{DDT}}(x,q_T,\mu) \tag{12}$$
$$= \frac{\partial}{\partial\ln\lambda^2}\left[a(x,\lambda^2)T_a(\lambda,\mu)\right]_{\lambda=q_T},$$

which was first proposed in [30]. In this limit, the derivative $\partial T_a/\partial\ln\lambda^2$ cancels the second term on the right-hand side of (8) (see [29] for a more detailed discussion).

Finally, the probability $f_a(x,q_T,\mu)$ is related to the BFKL function $\varphi(x,q_T^2)$ as

$$\varphi(x,q^2) = 4\sqrt{2}\pi^3 f_a(x,q_T,\mu). \tag{13}$$

Note that, owing to a virtual DGLAP contribution, the derivative $\partial a(x,q_1^2)/\partial q_1^2$ can be negative for not overly small x values. This shortcoming of (11) is overcome partly in the case of (12). Unfortunately, the cutoff Δ used in a conventional DGLAP computation does not depend on the scale μ. To obtain an integrated parton distributions it is enough to put any small $\Delta \ll 1$.[3)]

[3)]There is a cancellation between the real and virtual soft gluon double log contributions in the DGLAP equation, written for the integrated partons (including all $k_T \le \mu$). The emission of a soft gluon with momentum fraction $(1-z)\to 0$ does not affect the x distribution of parent partons. Thus, the virtual and real contributions originated from $1/(1-z)$ singularity of the splitting function $P(z)$ cancel each other. On the contrary, in the unintegrated case, the emission of soft gluon (with $q_T' > k_T$) alters the transverse momentum of parent (t-channel) parton. Equation (12) includes this effect through the derivative $\partial T(k_T^2,\mu^2)/\partial k_T^2$.

On the other hand, in the survival probability (9), we have to use the true (within the leading log approximation) value $\Delta = q_T/\mu$. Thus, for a rather large q_T (of the order of μ) and x, even the Dokshitzer–Dyakonov–Troyan (DDT) form (12) is not sufficiently precise. Only expression (10) with the same cutoff Δ in a real DGLAP contribution and in the survival probability (9) ensures positiveness of the unintegrated probability $f_a(x,q_T,\mu)$ in the entire interval $0 < x < 1$.

Of course, just by definition, we have $f_a(x,q_T,\mu) = 0$ when the transverse momentum q_T becomes larger than the factorization scale μ.

In what follows, we use the Sudakov decomposition for the quark momenta $p_{1,2}$ through the momenta of colliding hadrons, p_A and p_B ($p_A^2 = p_B^2 \simeq 0$), and the transverse momenta $p_{1,2T}$, that is,

$$p_{1,2} = x_{1,2}p_B + y_{1,2}p_A + p_{1,2T}. \tag{14}$$

The differential cross section of heavy-quark hadroproduction has the form[4)]

$$\frac{d\sigma_{AB}}{dy_1^*dy_2^*d^2p_{1T}d^2p_{2T}} = \frac{1}{(2\pi)^8}\frac{1}{s^2} \tag{15}$$
$$\times\int d^2q_{1T}d^2q_{2T}\delta(q_{1T}+q_{2T}-p_{1T}-p_{2T})$$
$$\times\frac{\alpha_s(q_1^2)}{q_1^2}\frac{\alpha_s(q_2^2)}{q_2^2}\varphi(y,q_1^2)\varphi(x,q_2^2)|M_{QQ}|^2.$$

Here, $s = 2p_Ap_B$, $q_{1,2T}$ are the gluon transverse momenta, $y_{1,2}^*$ are the quark rapidities in the hadron–hadron c.m. frame,

$$x_1 = \frac{m_{1T}}{\sqrt{s}}e^{-y_1^*}, x_2 = \frac{m_{2T}}{\sqrt{s}}e^{-y_2^*}, x = x_1 + x_2,$$
$$y_1 = \frac{m_{1T}}{\sqrt{s}}e^{y_1^*}, y_2 = \frac{m_{2T}}{\sqrt{s}}e^{y_2^*}, y = y_1 + y_2, \tag{16}$$
$$m_{1,2T}^2 = m_Q^2 + p_{1,2T}^2,$$

and $|M_{QQ}|^2$ is the square of the matrix element for the heavy-quark pair hadroproduction.

In LLA kinematics, we have

$$q_1 \simeq yp_A + q_{1T}, \quad q_2 \simeq xp_B + q_{2T}, \tag{17}$$

so that

$$q_1^2 \simeq -q_{1T}^2, \quad q_2^2 \simeq -q_{2T}^2. \tag{18}$$

(The more accurate relations are $q_1^2 = -\dfrac{q_{1T}^2}{(1-y)}$ and $q_2^2 = -\dfrac{q_{2T}^2}{(1-x)}$, but we are working in the kinematics where $x, y \sim 0$.)

The matrix element M is calculated in the Born approximation of QCD (for details, see [18, 20]) without standard simplifications of the parton model.

[4)]We set the argument of α_s to the gluon virtuality, which is very close to the BLM scheme [31] (see also [17]).

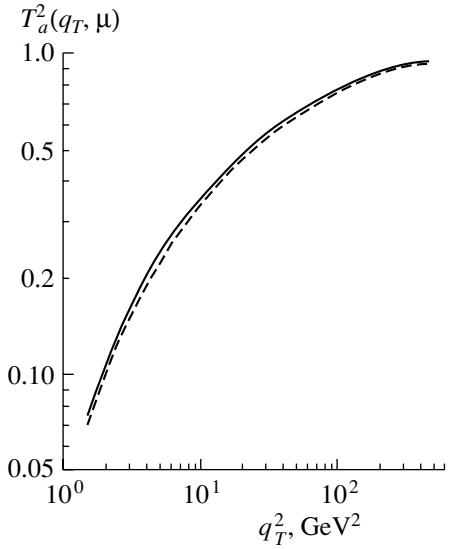

Fig. 3. The role of the T factor (9) in the calculation of (solid curve) charm and (dashed curve) beauty production with $p_T = 20$ GeV at $\sqrt{s} = 14$ TeV.

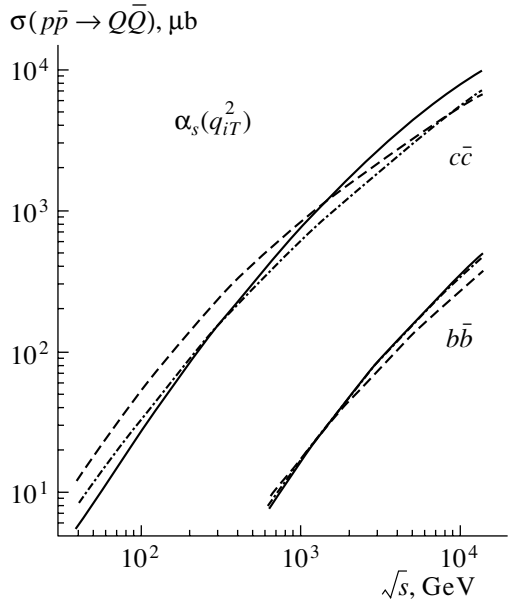

Fig. 4. Total cross sections for charm and beauty hadroproduction in the k_T-factorization approach with the unintegrated gluon distribution $f_g(x, q_T, \mu)$ given by (10) for μ^2 values in (9) equal to (solid curves) $\hat{s}$ and (dash-dotted curves) $\hat{s}/4$ and (dashed curves) in the LO PM.

3. TOTAL CROSS SECTIONS AND ONE-PARTICLE DISTRIBUTIONS

Equation (15) enables us to calculate straightforwardly all distributions concerning one-particle or pair production. One-particle calculations, as well as correlations between two produced heavy quarks, can easily be obtained by using, say, the VEGAS code [32].

However, there exists an important problem that comes from the infrared region. Since the functions $\varphi(x, q_2^2)$ and $\varphi(y, q_1^2)$ are unknown at small values of q_2^2 and q_1^2 (smaller than some Q_0^2 value), we use the direct consequence of (7) [32],

$$xG(x, q^2) = xG(x, Q_0^2) + \frac{1}{4\sqrt{2}\pi^3}\int\limits_{Q_0^2}^{q^2} \varphi(x, q_1^2) dq_1^2, \tag{19}$$

and rewrite the integrals in (15) as

$$\int d^2q_{1T} d^2q_{2T} \delta(q_{1T} + q_{2T} - p_{1T} - p_{2T}) \tag{20}$$
$$\times \frac{\alpha_s(q_1^2)}{q_1^2}\frac{\alpha_s(q_2^2)}{q_2^2}\varphi(y, q_1^2)\varphi(x, q_2^2)|M_{QQ}|^2$$
$$= (4\sqrt{2}\pi^3\alpha_s(m_T^2))^2 xG(x, Q_0^2) yG(y, Q_0^2)$$
$$\times T^2(Q_0^2, \mu^2)\left(\frac{|M_{QQ}|^2}{q_1^2 q_2^2}\right)_{q_{1,2}\to 0}$$
$$+ 4\sqrt{2}\pi^3\alpha_s(m_T^2) xG(x, Q_0^2) T(Q_0^2, \mu^2)$$
$$\times \int\limits_{Q_0^2}^{\infty} dq_{1T}^2 \delta(q_{1T} - p_{1T} - p_{2T})\frac{\alpha_s(q_1^2)}{q_1^2}$$
$$\times \varphi(y, q_1^2)\left(\frac{|M_{QQ}|^2}{q_2^2}\right)_{q_2\to 0}$$
$$+ 4\sqrt{2}\pi^3\alpha_s(m_T^2) yG(y, Q_0^2) T(Q_0^2, \mu^2)$$
$$\times \int\limits_{Q_0^2}^{\infty} dq_{2T}^2 \delta(q_{2T} - p_{1T} - p_{2T})\frac{\alpha_s(q_2^2)}{q_2^2}$$
$$\times \varphi(x, q_2^2)\left(\frac{|M_{QQ}|^2}{q_1^2}\right)_{q_1\to 0} + \int\limits_{Q_0^2}^{\infty} d^2q_{1T}$$
$$\times \int\limits_{Q_0^2}^{\infty} d^2q_{2T} \delta(q_{1T} + q_{2T} - p_{1T} - p_{2T})$$
$$\times \frac{\alpha_s(q_1^2)}{q_1^2}\frac{\alpha_s(q_2^2)}{q_2^2}\varphi(y, q_1^2)\varphi(x, q_2^2)|M_{QQ}|^2,$$

where the unintegrated gluon distributions are taken from (13).

The first contribution in (20), with the averaging of the matrix element over the directions of the two-dimensional vectors q_{1T} and q_{2T}, is identical to the

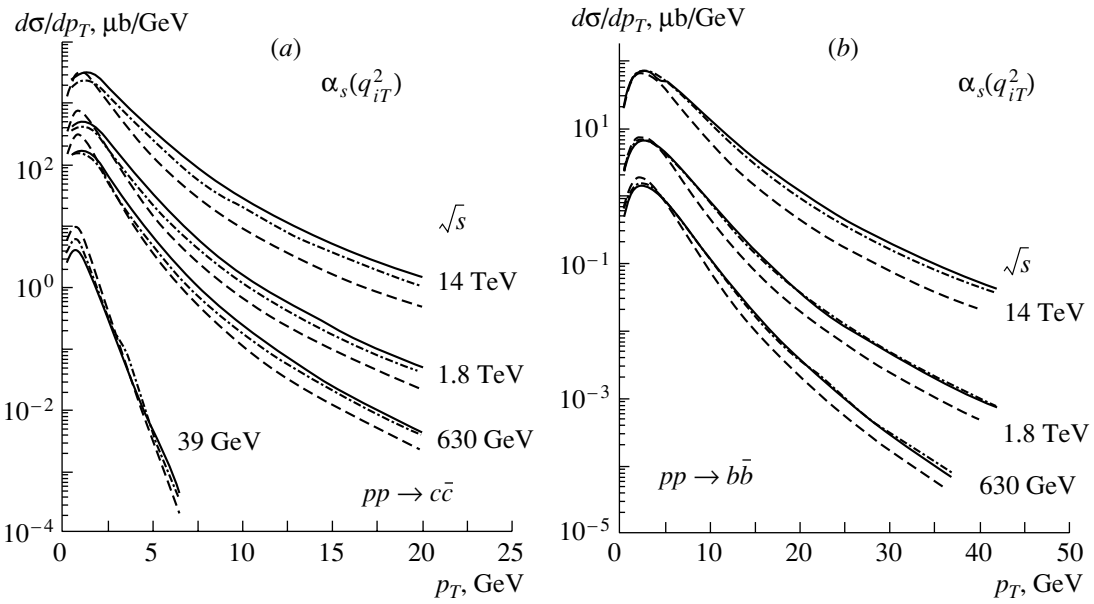

Fig. 5. Transverse momentum distributions of (*a*) c quarks and (*b*) b quarks produced at various energies. The dashed curves represent the results of the LO PM. The solid curves were calculated with the unintegrated gluon distribution $f_g(x, q_T, \mu)$ given by (10) for μ^2 values in (9) equal to $\hat{s}$, while the dash-dotted curves were calculated for $\mu^2 = \hat{s}/4$.

conventional LO PM expression, with QCD scales $\mu_R^2 = m_T^2$ and $\mu_F^2 = Q_0^2$ multiplied by the "survival" probability $T^2(Q_0^2, \mu^2)$ not to have transverse momenta $q_{1,2,T} > Q_0$. The sum of the product-heavy-quark transverse momenta is exactly zero here.

The next three terms contain the corrections to the PM related to the gluon polarizations, virtualities, and transverse momenta in the matrix element. The relative contribution of the corrections depends strongly on the initial energy. If it is not sufficiently high, the first term in (20) dominates, and all results nearly coincide [after taking into account (19)] with the conventional LO PM predictions. In the case of very high energy, the opposite situation takes place—the first term in (20) can be considered as a small correction—and our results differ from the conventional ones. It is necessary to note that the absolute and the relative values of all terms in (20) strongly depend on the T-factor inclusion [i.e., when we use (9), (10), (13), or (7)].

Before the numerical comparison, it is necessary to note that the NLO PM actually results only in a normalization factor in the case of one-particle distributions, the shapes of LO and LO + NLO distributions being almost the same (see [3–5, 34]). This means that we can calculate the K factor

$$K = \frac{\sigma(LO) + \sigma(NLO)}{\sigma(LO)}, \qquad (21)$$

say, from the results for the total production cross sections, and restrict ourselves only to LO calculations of p_T, or rapidity distributions, multiplying them by the K factors.

The numerical values of the K factors depend [35] on the structure functions used, quark masses, QCD scales, and initial energy, the dependence on the renormalization scale μ_R being especially important. This seems to be evident, because the LO contribution is proportional to α_s^2, whereas the NLO contribution is proportional to α_s^3. However, the more important dependence at high energies, when small-ρ values dominate, comes from the structure of (2). In the limit $\rho \to 0$, the functions $f_{gg}^{(1)}$ and $\bar{f}_{gg}^{(1)}$ have constant limits [1], $f_{gg}^{(1)}(\rho \to 0) \approx 0.1$ and $\bar{f}_{gg}^{(1)}(\rho \to 0) \approx -0.04$, so due to (2) the K factor at high energies depends strongly on the ratio μ/m_Q.

First of all, we consider the role of the T factors (9). In Fig. 3, we show their values which were calculated as the ratios of the values of the last term of (20) to the same values calculated with $T_a(q_{1T}, \mu) = 1$ for the cases of charm and beauty production at $\sqrt{s} = 14$ TeV and $\mu^2 = \hat{s}$ as functions of q_{1T}. The values of heavy-quark transverse momenta were fixed at 20 GeV. In both cases, the values of $T_a(q_{1T})$ are rather small at small q_{1T} and $T_a(q_{1T}) \to 1$ for $p_T \ll q_{1T}$.

Let us now compare the numerical results predicted by the parton model and by the k_T-factorization approach.

The energy dependences of the total cross sections of $c\bar{c}$- and $b\bar{b}$-pair production are presented in Fig. 4.

As was mentioned, at comparatively small energies the first term in (20) dominates and the results of the k_T-factorization approach should be close to the LO PM prediction. Actually, the first results are even smaller owing to the presence of the T factor in (10). However, the k_T-factorization approach predicts a stronger energy dependence than the LO PM, both for $c\bar{c}$ and for $b\bar{b}$ production. This can be explained by additional contributions appearing at very high energies in the k_T-factorization approach (see [20]).

The one-particle p_T distributions, $d\sigma/dp_T$ calculated within the k_T-factorization approach and within the LO PM are presented in Fig. 5. In all cases, the k_T-factorization approach predicts broader distributions. The average values of p_T of the product heavy quarks are rather different in these two approaches, as one can see from the table.

This seems very natural because, in contrast to the case of the LO PM, a large p_T of one heavy quark can be compensated not only by the p_T of another heavy quark but also by the initial gluons (i.e., by hard gluon-jet emission).

The rapidity distributions of product heavy quarks presented in Fig. 6 show that the main part of the difference between the k_T-factorization approach and the LO PM comes from the central region.

4. TWO-PARTICLE CORRELATIONS

We saw from the preceding section that there is only a small difference in our results for the total cross sections and one-particle distributions obtained in the k_T-factorization approach and in the LO PM. The predictions of the NLO parton model for these quantities differ from the LO PM only by a normalization factor of 2–2.5 [3–5, 34]. Thus, the difference between our predictions and the NLO PM should be small.

The calculations of two-particle correlations in the different approaches are more informative. The simplest quantity here is the distribution of the product heavy-quark pair with respect to their total transverse momentum p_{pair}. In the LO, we obviously have $p_{\text{pair}} = p_{1T} + p_{2T} = q_{1T} + q_{2T}$; if $q_{1T} = q_{2T} = 0$, then $d\sigma/dp_{\text{pair}}$ is a delta function of zero. Thus, the p_{pair} distributions give direct information about the transverse-momentum distribution of incident partons.

It is clear that, if $q_{iT} \ll p_{iT}$, then the distributions in p_{pair} should be narrower than the one-particle p_T distributions. In this case, the Weizsäcker–Williams approximation should be valid, and one can believe that the parton model reflects the real dynamics of the interaction. In the opposite case, $q_{iT} \sim p_{iT}$, the large transverse momentum of the product heavy quark can be compensated not by the other quark, but by a high-p_T gluon. We have shown in [20] that about 70–80% of the total cross section for high-p_T quark production at high energies originates from such processes, when the heavy-quark propagator is close to the mass shell.

Mean charm- and beauty-quark transverse momenta $\langle p_T \rangle$ (in GeV) in the k_T-factorization approach with $\mu^2 = \hat{s}$ and in the LO parton model

$\sqrt{s}$, TeV	LO PM		k_T factorization	
	$c\bar{c}$	$b\bar{b}$	$c\bar{c}$	$b\bar{b}$
14	1.78	4.53	2.23	5.47
1.8	1.48	3.96	1.91	4.54

We have calculated $d\sigma/dp_{\text{pair}}$ for (a) charm and (b) beauty production in the k_T-factorization approach using the unintegrated gluon distribution (9), (10), and (13) with the scale values of $\mu^2 = \hat{s}$ and $\mu^2 = \hat{s}/4$ (only for $\sqrt{s} = 14$ TeV). Our results for pair production at various initial energies are shown by solid curves in Fig. 7. For the sake of comparison, the one-particle p_T-distributions taken from Fig. 5, which were obtained in the same k_T-factorization approach and with the same T factor, are shown by the dashed curves. Since we set $Q_0^2 = 1$ GeV^2 in (20), we cannot distinguish between the initial gluons with q_T equal to, say, 0.1 and 0.9 GeV; therefore, our first bin in the distribution $d\sigma/dp_{\text{pair}}$ has the width of 2 GeV, which explains some irregular behavior of the solid curves at low p_T. Naturally, all solid and dashed curves are normalized equally at the same energy.

At comparatively small energies of $\sqrt{s} = 39$ GeV and even at $\sqrt{s} = 630$ GeV, the distributions $d\sigma/dp_{\text{pair}}$ are narrower than the one-particle distributions $d\sigma/dp_T$. This means that the transverse momenta of the product heavy quarks compensate each other almost completely. However, the situation changes drastically with increasing initial energy. From comparatively small p_T, the difference between the curves decreases with energy. At $\sqrt{s} = 14$ TeV, the distributions are similar in the cases of both $c\bar{c}$ and $b\bar{b}$ production. This means that the production mechanism changes in the energy region being discussed. At $\sqrt{s} = 14$ TeV, the transverse momentum of the product heavy quark is balanced more probably by one or a few gluons (see also [20]), because the contribution with large virtuality in the quark propagator is more suppressed in relation to the large virtuality in the gluon propagator.

The behavior under discussion depends on the scale μ^2 in the T factor (9). The results of a similar calculation at $\sqrt{s} = 14$ TeV with $\mu^2 = \hat{s}/4$ are shown

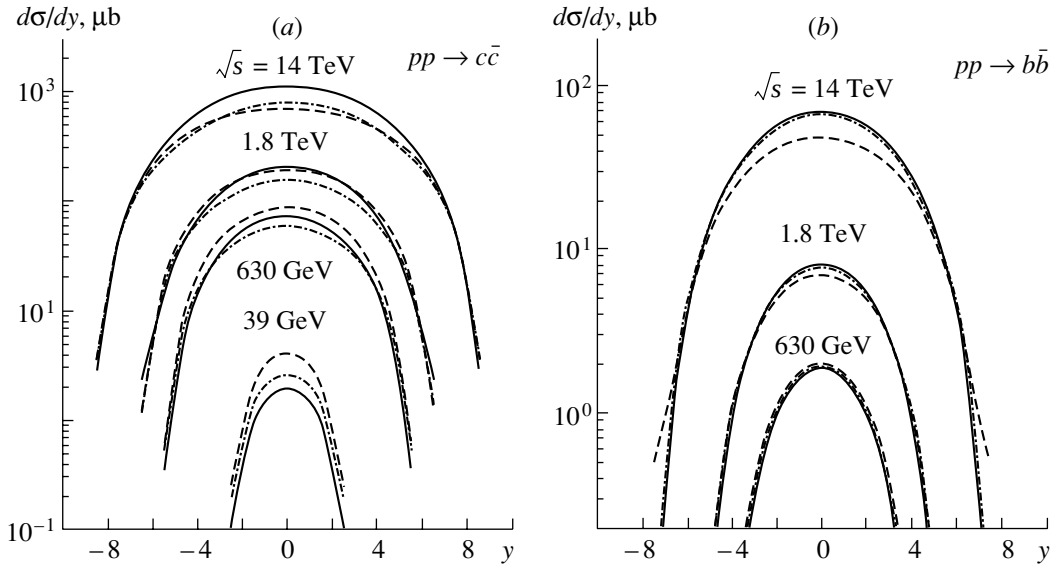

Fig. 6. Rapidity distributions of (*a*) c and (*b*) b quarks produced at various energies. The dashed curves represent the results of the LO PM. The solid curves were calculated with the unintegrated gluon distribution $f_g(x, q_T, \mu)$ given by (10) for μ^2 values in (9) equal to $\hat{s}$, while the dash-dotted curves were calculated at $\mu^2 = \hat{s}/4$.

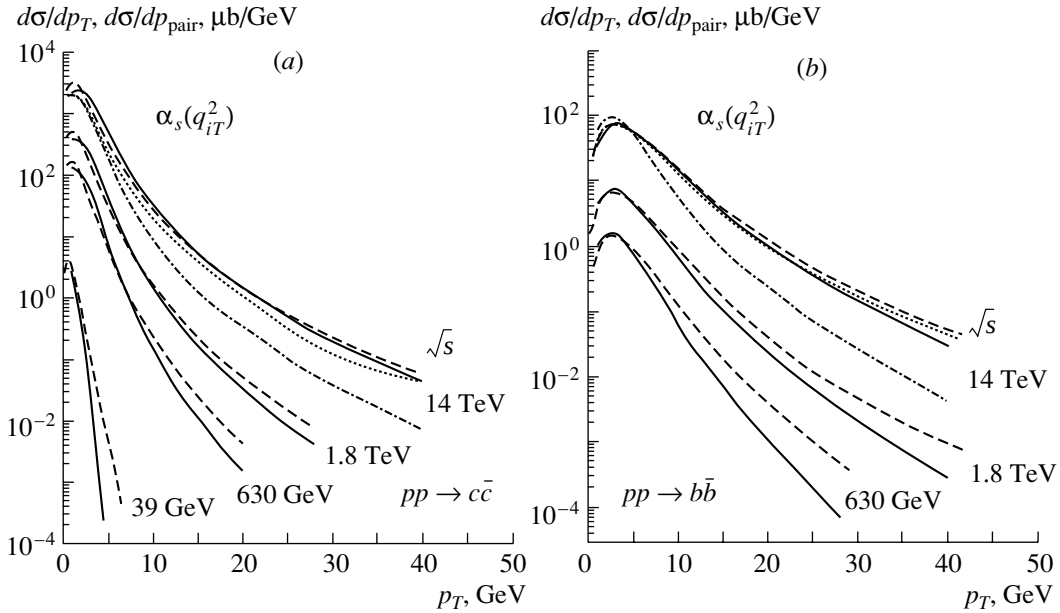

Fig. 7. Distributions of the total transverse momentum p_{pair} for (*a*) c and (*b*) b quarks produced at various energies (solid curves) according to the calculations with the unintegrated gluon distribution $f_g(x, q_T, \mu)$ given by (9) and (10) for μ^2 values in (9) equal to $\hat{s}$. The dashed curves show the one-particle (single) p_T distributions for the same μ^2 from Fig. 5. The dash-dotted and dotted curves represent the results of the same calculations for pair and single production at $\sqrt{s} = 14$ TeV with $\mu^2 = \hat{s}/4$.

in Fig. 7 for pair and single production (dash-dotted and dotted curves, respectively). Here, the difference between these two curves is more significant and becomes larger at lower energies.

The distributions of the product heavy-quark pair as a function of the rapidity gap $\Delta y = |y_Q - y_{\bar{Q}}|$ between the quarks are presented in Fig. 8. Here, the difference between the LO PM and the k_T-factorization predictions is not large again every-

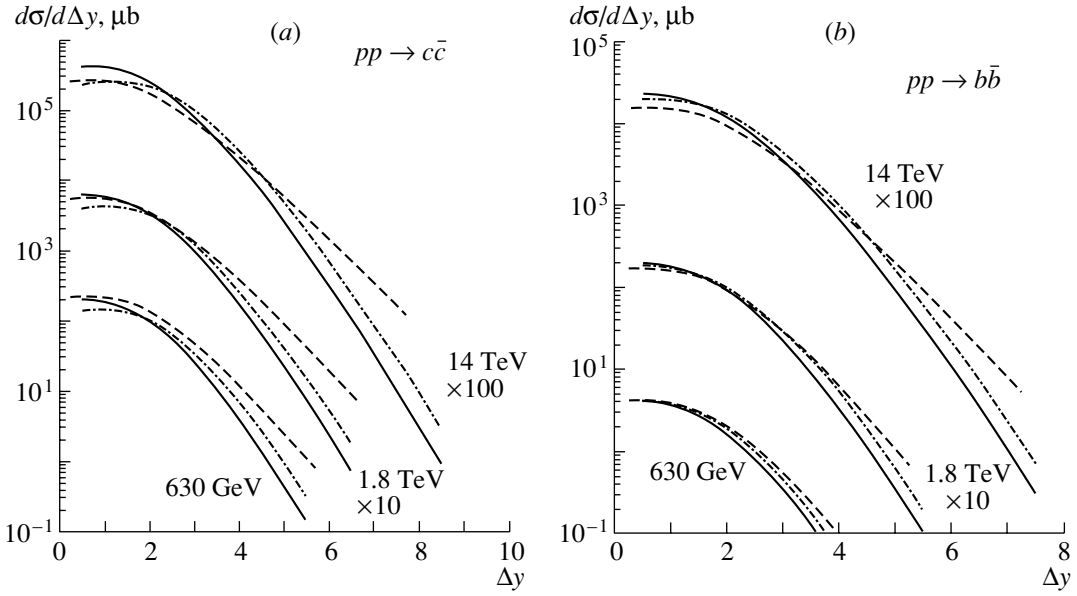

Fig. 8. Distributions of the rapidity difference between two (a) c or (b) b quarks produced at various energies according to calculations in the k_T-factorization approach with the unintegrated gluon distribution $f_g(x, q_T, \mu)$ given by (9) and (10) for μ^2 values in (9) equal to (solid curves) $\hat{s}$ and (dash-dotted curves) $\hat{s}/4$. The dashed curves represent the LO PM predictions.

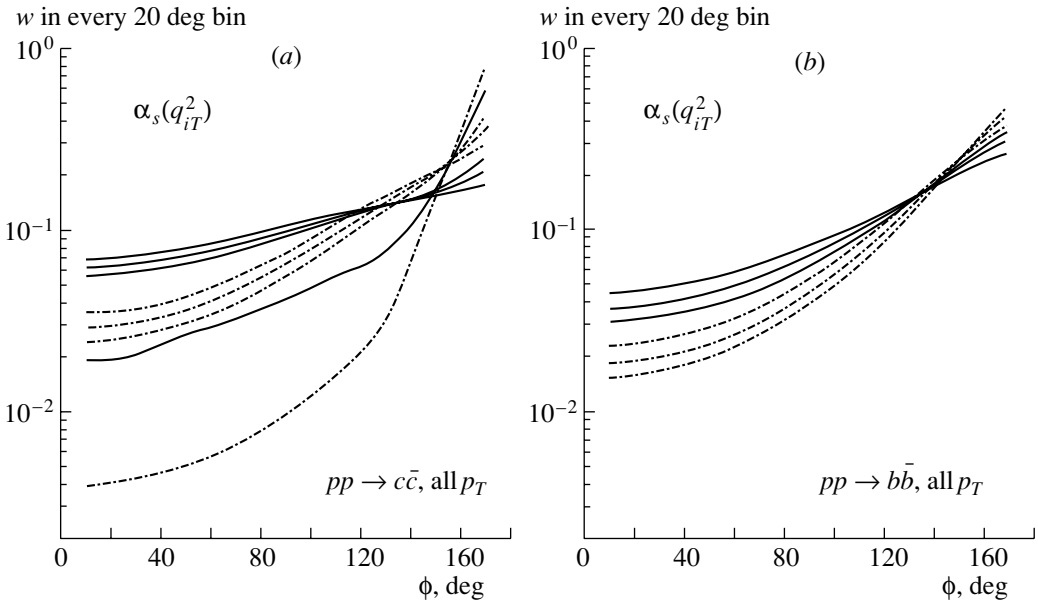

Fig. 9. Calculated azimuthal correlations of (a) charm and (b) beauty pair production for (solid curves) $\mu^2 = \hat{s}$ and (dash-dotted curves) $\mu^2 = \hat{s}/4$ at the energies equal to $\sqrt{s} = 14$ TeV, 1.8 TeV, 630 GeV, and 39 GeV (the latter one only for charm production) from top to bottom in the left part of the figures.

where, with the exception of the region of very large Δy.

Another interesting correlation is the distribution in the azimuthal angle ϕ, which is defined as the opening angle between the two product heavy quarks that is projected onto the plane that is perpendicular to the beam and which is defined as the xy plane. In the LO PM, the sum of the product-heavy-quark momenta projected onto this plane is exactly zero, and the angle between them is always 180°. In the case of the NLO PM, the ϕ distribution is nontrivial [6]; however, the predicted distribution (without including the k_T kick) is narrower in comparison with the fixed target data [7].

The theoretical and the experimental investigation of such distributions are very important for checking our understanding of the processes under consideration. The problem is that, in the case of one-particle inclusive distributions for heavy-quark production in hadron collisions, the sum of LO and NLO contributions of PM virtually coincides [3–5, 34] with the LO contribution multiplied by K factors. Therefore, agreement with experimental data can be achieved for too small or too large an NLO contribution by fitting one parameter, which can work as a normalization factor (say, the QCD scale). The deviation of azimuthal correlations from the trivial $\delta(\phi-\pi)$ distribution comes from the NLO correction to the PM. However, the standard NLO contributions are not sufficiently large for describing data, and only a comparatively large intrinsic transverse momentum of incoming partons (k_T kick) allows us to describe [7] data.

Preliminary results for the azimuthal correlations in the k_T-factorization approach were considered in [19]. The main distinction between information coming from $d\sigma/dp_{\rm pair}$ and $d\sigma/d\phi$ distributions is due to a comparatively slow heavy quark. It makes a negligibly small contribution to the $d\sigma/dp_{\rm pair}$ in the first case; in the second case, each quark contributes to the distribution $d\sigma/d\phi$ almost independently of its momentum, so that all corrections coming from quark confinement, hadronization, and resonance decay can be important.

As was discussed above, the first contribution in (20) is identical to the conventional LO PM, where the angle between the momenta of the product heavy quarks is always 180°. However, the angle between the momenta of two heavy hadrons can be slightly different from this value because of hadronization processes. To take this into account, we assume that, in this first contribution, the probability of finding a hadron pair with azimuthal angle $180^\circ-\phi$ is determined by the expression

$$w_1(\phi)=\frac{p_h}{\sqrt{p_h^2+p_T^2}}, \qquad (22)$$

where $p_h=0.2$ GeV is the transverse momentum in the azimuthal plane coming from the hadronization process. The other contributions in (20) result in a more or less broad ϕ distribution; therefore, we neglect their small modification due to hadronization.

The k_T-factorization-approach predictions for the azimuthal correlation of heavy quarks produced in pp collisions are presented in Fig. 9, and one can see that they change drastically when the initial energy increases from fixed target to the collider region.

5. CONCLUSION

We have compared the conventional LO PM and the k_T-factorization approach for heavy-quark hadroproduction at collider energies using a realistic gluon (parton) distribution. Both the transverse momenta and rapidity distributions have been considered, as well as two-particle correlations, such as the distribution in the rapidity gap between two heavy quarks, their azimuthal correlations, and the distributions of the total transverse momentum of the product heavy-quark pair ($p_{\rm pair}$).

It was shown in [20] that the contribution of the domain with strong q_T ordering ($q_{1,2T}\ll m_T=\sqrt{m_Q^2+p_T^2}$) in the k_T-factorization approach coincides with the LO PM prediction. In addition, a numerically large contribution appears at high energies in the k_T-factorization approach in the region $q_{1,2T}\geq m_T$. It is kinematically related to the events where the transverse momentum of heavy quark Q is balanced not by the momentum of the antiquark $\bar{Q}$ but by the momentum of the nearest gluon.

This configuration is associated with the NLO (or even NNLO, if $q_{1,2T}\geq m_T$) corrections in terms of the PM with fixed number of flavors, i.e., without the heavy quarks in the evolution. Indeed, as was mentioned in [1], up to 80% of the whole NLO cross section originates from events where the heavy-quark transverse momentum is balanced by the nearest gluon jet. Thus, the large "NLO" contribution, especially at large p_T, is explained by the fact that the virtuality of the t-channel (or the u-channel) quark becomes small in the region around $q_T\simeq p_T$, and the singularity of the quark propagator $1/((\hat{p}-\hat{q})-m_Q)$ in the "hard" QCD matrix element $M(q_{1T},q_{2T},p_{1T},p_{2T})$ reveals itself.

The double logarithmic Sudakov-type form factor T in the definition of unintegrated parton density (10) comprises an important part of the virtual loop NLO (with respect to the PM) corrections. Thus, we demonstrate that the k_T-factorization approach collects, even at the LO, a major part of the contributions that play the role of the NLO (and even NNLO) corrections to the conventional PM. Therefore, we hope that a higher order (in α_s) correction to k_T factorization would be rather small.

Another advantage of this approach is that a nonzero transverse momentum of $Q\bar{Q}$ system ($p_{\rm pair}=p_{1T}+p_{2T}=q_{1T}+q_{2T}$) is naturally achieved in k_T factorization. We have calculated the $p_{\rm pair}$ distribution and compared it with the single-quark p_T spectrum. At low energies, the typical values of $p_{\rm pair}$ are much lesser than the heavy-quark p_T, in accordance with the collinear approximation. However, for the CERN Large Hadron Collider energy,

both spectra become close to each other, indicating that the transverse momentum of the second heavy quark is relatively small. The typical value of this momentum ($p_{\text{pair}} = k_T$ kick) depends on the parton structure functions (densities). It increases with initial energy (k_T kick increases with decreasing momentum fractions x and y carried by incoming partons) and with the transverse momenta of heavy quarks, p_T. Thus, it becomes possible to describe a nontrivial azimuthal correlation without introducing a large "phenomenological" intrinsic transverse momentum of the partons.

It is necessary to note that significant values of the parton transverse momenta q_{1T} and q_{2T} increase in our calculations with increasing $p_T^{\min}$ of the detected b quark. In the language of k_T kick, this means that the values of $\langle k_T^2 \rangle$ also increase.

A more detailed study of heavy-quark correlations in the k_T-factorization approach, the role of DL factor $T(k_T^2, \mu^2)$, and the value of scale μ in the T factor will be published elsewhere.

ACKNOWLEDGMENTS

The above calculations were carried out at the International Centre for Theoretical Physics (Trieste). Y.M. Shabelski is grateful to Prof. S. Randjbar-Daemi for providing this possibility and to the staff for creating good working conditions. We are grateful to Yu.L. Dokshitzer, G.P. Korchemsky, and M.N. Mangano for discussions.

This work is supported by NATO (grant no. OUTR.LG 971390) and by the Russian Foundation for Basic Research (project no. 01-02-17095).

REFERENCES

1. P. Nason, S. Dawson, and R. K. Ellis, Nucl. Phys. B **303**, 607 (1988).
2. G. Altarelli *et al.,* Nucl. Phys. B **308**, 724 (1988).
3. P. Nason, S. Dawson, and R. K. Ellis, Nucl. Phys. B **327**, 49 (1989).
4. W. Beenakker, H. Kuijf, W. L. van Neerven, and J. Smith, Phys. Rev. D **40**, 54 (1989).
5. W. Beenakker, W. L. van Neerven, R. Meng, *et al.,* Nucl. Phys. B **351**, 507 (1991).
6. M. N. Mangano, P. Nason, and G. Ridolfi, Nucl. Phys. B **373**, 295 (1992).
7. S. Frixione, M. N. Mangano, P. Nason, and G. Ridolfi, Preprint CERN-TH/97-16 (1997); hep-ph/9702287.
8. Yu. M. Shabelski, Talk given at HERA Monte Carlo Workshop, DESY, Hamburg, 1998; hep-ph/9904492.
9. S. Catani, M. Ciafaloni, and F. Hautmann, Phys. Lett. B **242**, 97 (1990); Nucl. Phys. B **366**, 135 (1991).
10. J. C. Collins and R. K. Ellis, Nucl. Phys. B **360**, 3 (1991).
11. G. Marchesini and B. R. Webber, Nucl. Phys. B **386**, 215 (1992).
12. S. Catani and F. Hautmann, Phys. Lett. B **315**, 475 (1993); Nucl. Phys. B **427**, 475 (1994).
13. S. Camici and M. Ciafaloni, Nucl. Phys. B **467**, 25 (1996); Phys. Lett. B **396**, 406 (1997).
14. L. V. Gribov, E. M. Levin, and M. G. Ryskin, Phys. Rep. **100**, 1 (1983).
15. E. M. Levin and M. G. Ryskin, Phys. Rep. **189**, 267 (1990).
16. E. M. Levin, M. G. Ryskin, Yu. M. Shabelski, and A. G. Shuvaev, Yad. Fiz. **53**, 1059 (1991) [Sov. J. Nucl. Phys. **53**, 657 (1991)].
17. E. M. Levin, M. G. Ryskin, Yu. M. Shabelski, and A. G. Shuvaev, Yad. Fiz. **54**, 1420 (1991) [Sov. J. Nucl. Phys. **54**, 867 (1991)].
18. M. G. Ryskin, Yu. M. Shabelski, and A. G. Shuvaev, Z. Phys. C **69**, 269 (1996).
19. Yu. M. Shabelski and A. G. Shuvaev, Eur. Phys. J. C **6**, 313 (1999).
20. M. G. Ryskin, Yu. M. Shabelski, and A. G. Shuvaev, Yad. Fiz. **64**, 123 (2001) [Phys. At. Nucl. **64**, 120 (2001)]
21. M. Gluck, E. Reya, and A. Vogt, Z. Phys. C **67**, 433 (1995).
22. M. Gluck, E. Reya, and A. Vogt, Eur. Phys. J. C **5**, 461 (1998).
23. J. C. Collins, D. E. Soper, and G. Sterman, Nucl. Phys. B **308**, 833 (1988).
24. S. Narison, Phys. Lett. B **341**, 73 (1994); hep-ph/9503234.
25. P. Ball, M. Beneke, and V. M. Braun, Phys. Rev. D **52**, 3929 (1995).
26. J. Blümlein, Preprint 95-121, DESY (Hamburg, 1995).
27. E. A. Kuraev, L. N. Lipatov, and V. S. Fadin, Zh. Éksp. Teor. Fiz. **72**, 377 (1977) [Sov. Phys. JETP **45**, 199 (1977)].
28. G. Marchesini and B. R. Webber, Nucl. Phys. B **310**, 461 (1988).
29. M. A. Kimber, A. D. Martin, and M. G. Ryskin, Eur. Phys. J. C **12**, 655 (2000).
30. Yu. L. Dokshitzer, D. I. Dyakonov, and S. I. Troyan, Phys. Rep. **58**, 270 (1980).
31. S. J. Brodsky, G. P. Lepage, and P. B. Mackenzie, Phys. Rev. D **28**, 228 (1983).
32. G. P. Lepage, J. Comput. Phys. **27**, 192 (1978).
33. J. Kwiechinski, Z. Phys. C **29**, 561 (1985).
34. M. N. Mangano, P. Nason, and G. Ridolfi, Nucl. Phys. B **405**, 507 (1993).
35. Liu Wenjie, O. P. Strogova, L. Cifarelli, and Yu. M. Shabelski, Yad. Fiz. **57**, 900 (1994) [Phys. At. Nucl. **57**, 844 (1994)].

Physics of Atomic Nuclei, Vol. 64, No. 11, 2001, pp. 2006–2019. From Yadernaya Fizika, Vol. 64, No. 11, 2001, pp. 2091–2104.

ELEMENTARY PARTICLES AND FIELDS
Theory

Strong Decays of a Scalar Glueball in a Scale-Invariant Chiral Quark Model*

M. K. Volkov and V. L. Yudichev

Joint Institute for Nuclear Research, Dubna, Moscow oblast, 141980 Russia

Received August 16, 2000; in final form, March 22, 2001

Abstract—An effective meson Lagrangian including a scalar glueball is constructed on the basis of $U(3) \times U(3)$ chiral symmetry. The glueball is introduced in the meson Lagrangian by using the principle of scale invariance of an effective Lagrangian and the dilaton model. The singlet–octet mixing of scalar-meson states is described by means of the 't Hooft interaction. The contribution of scalar and pseudoscalar anomalies to the breakdown of scale invariance is taken into account. The mixing of quarkonia with the glueball is described. The mass spectrum of scalar mesons, together with the glueball, and also their strong decay widths are calculated. From a comparison of the results with experimental data, it follows that $f_0(1500)$ is rather a glueball, whereas $f_0(1710)$ is a quarkonium. This is in accord with the results obtained in our previous study, where radially excited scalar-meson states were described. It is shown that the ρ meson plays an important role in the description of glueball decays. © *2001 MAIK "Nauka/Interperiodica".*

1. INTRODUCTION

The self-interaction of gluons, a feature peculiar to QCD, gave an idea that gluons can form bound states that can propagate as particles in space. Unfortunately, because of theoretical problems, an exact answer to the question of whether these states really exist or not has not yet been obtained. However, from recent lattice simulations [1–3], one can conclude that, most probably, glueballs are real objects of our world. Having assumed that glueballs exist, one can try to construct a model to describe their interaction with other mesons and their properties (such as masses and decay widths) and to identify them with observed resonances.

An exact microscopic description of bound gluon states cannot be constructed systematically within QCD. In this situation, QCD-motivated phenomenological models are a tool that can help to deal with glueballs, as well as with quarkonia, which form most of the observed meson states. However, using these models to describe glueballs, we encounter many difficulties concerning, e.g., the ambiguity of the ways of including glueballs in models and the identification of experimentally observed meson states. This explains the variety of points of view on this problem.

First of all, we do not know the exact mass of a glueball. From the quenched QCD lattice simulations, Weingarten (see, e.g., [1, 3]) concluded that the lightest scalar glueball is expected around 1.7 GeV. Amsler [4] considered the state $f_0(1500)$ as a candidate for a scalar glueball. QCD sum rules [5] and the K-matrix method [6] showed that both $f_0(1500)$ and $f_0(1710)$ are mixed states with a large admixture of the glueball component.

All bound isoscalar $q\bar{q}$ states are subject to mixing with glueballs, and their spectrum has many interpretations made by various authors. For example, Palano [7] suggested a scenario in which the states $a_0(980)$, $K_0^*(1430)$, $f_0(980)$, and $f_0(1400)$ form a nonet. The state $f_0(1500)$ is considered as a scalar glueball. Törnqvist *et al.* [8] considered the states $f_0(980)$ and $f_0(1370)$ as manifestations of the ground and excited $s\bar{s}$ states and the state $f_0(400–1200)$ as the ground $u\bar{u}$ state. Eef van Beveren *et al.* [9] treated the states $f_0(400–1200)$ and $f_0(1370)$ as ground $u\bar{u}$ states and the states $f_0(980)$ and $f_0(1500)$ as ground $s\bar{s}$ states. Two states for each $q\bar{q}$ system occur owing to pole doubling, which takes place for scalar mesons in their model. Shakin *et al.* [10, 11] found from a nonlocal confinement model that the $f_0(980)$ resonance is the ground $u\bar{u}$ state and that $f_0(1370)$ is the ground $s\bar{s}$ state. The state $f_0(1500)$ is considered as a radial excitation of $f_0(980)$. They believe that the mass of scalar glueball is 1770 MeV.

In [12], following the methods given in [13–16], we showed that all experimentally observed scalar-meson states with masses in the interval from 0.4 to 1.71 GeV can be interpreted as members of two scalar-meson nonets—the ground-state nonet

*This article was submitted by the authors in English.

(lighter than 1 GeV) and its first radial excitation (heavier than 1 GeV). We considered all scalar mesons as $q\bar{q}$ bound states and took into account singlet–octet mixing caused by the 't Hooft interaction. In [12], we obtained a scalar–isoscalar state with a mass of 1600 MeV and had to choose to which of the experimentally observed states, $f_0(1500)$ or $f_0(1710)$, we should ascribe it. From our analysis of the strong decay rates calculated in our model, we found that $f_0(1710)$ fits in the nonet of quarkonia better than $f_0(1500)$. Therefore, we supposed that the state $f_0(1500)$ contains a greater admixture of the scalar glueball (see [5, 6]). However, the final decision should be made after including the scalar glueball into the model and after taking account of its mixing with quarkonia. In the present study, which is devoted to solving this problem, from the analysis of strong decay widths of the glueball we again arrive at an analogous conclusion.[1)]

To describe the properties of the glueball and its interaction with quarkonia, one should introduce a scalar–isoscalar dilaton field χ in our model, in addition to the quarkonia that have already been described [12]. For this purpose, one can make use of the idea of approximate scale invariance of the effective Lagrangians based on the dilaton model. Such models were studied by many authors (see, e.g., [17–21]). Unfortunately, there is no unique way to introduce the dilaton field in a chiral Lagrangian. This explains the large number of models dealing with glueballs.

The guideline one should follow in introducing the dilaton field in an effective meson Lagrangian is to reproduce the Ward identity associated with the scale anomaly. The latter leads to the following equation for the vacuum expectation value of the divergence of the dilatation current:

$$\langle \partial_\mu S^\mu \rangle = \mathcal{C}_g - \sum_{q=u,d,s} m_q^0 \langle \bar{q}q \rangle, \qquad (1)$$

$$\mathcal{C}_g = \left(\frac{11}{24} N_c - \frac{1}{12} N_f \right) \left\langle \frac{\alpha}{\pi} G_{\mu\nu}^2 \right\rangle, \qquad (2)$$

where N_c is the number of colors; N_f is the number of flavors; $\langle \frac{\alpha}{\pi} G_{\mu\nu}^2 \rangle$ and $\langle \bar{q}q \rangle$ are the gluon and the quark condensate, respectively; and m_q^0 is the current quark mass.

In this paper, we are going to use the most natural method of introducing the dilaton field in the effective Lagrangian by requiring that, in the chiral limit, our Lagrangian be scale-invariant except for the dilaton potential and terms induced by gluon anomalies. To realize this program, one should multiply all dimensional parameters of the original Lagrangian (without the dilaton) by a corresponding power of the dilaton field divided by its vacuum expectation value χ_c. Thus, instead of the four-quark coupling constant G, the 't Hooft coupling constant K, the ultraviolet cutoff Λ (necessary for regularizing the divergent integrals coming from quark loops), and the constituent quark masses m_q ($q = u, s$), one should use $G(\chi_c/\chi)^2$, $K(\chi_c/\chi)^5$, $\Lambda(\chi/\chi_c)$, and $m_q(\chi/\chi_c)$.

The current quark masses m_q^0 are not multiplied by the dilaton field and violate scale invariance explicitly, as this takes place in QCD. Their contribution to the divergence of dilatation current is determined by quark condensates and disappears in the chiral limit [see (1)].

The scale invariance is also broken by those terms in the effective Lagrangian that are induced by the pseudoscalar and scalar gluon anomalies and are given by [22, 23]

$$L_{\rm an} = -h_\phi \phi_0^2 + h_\sigma \sigma_0^2, \qquad (3)$$

where h_ϕ and h_σ are constants and the fields ϕ_0 and σ_0 ($\langle \sigma_0 \rangle \neq 0$) are defined as follows: $\phi_0 = \sqrt{2/3}\phi_u - \sqrt{1/3}\phi_s$, and $\sigma_0 = \sqrt{2/3}\sigma_u - \sqrt{1/3}\sigma_s$; here, σ_u ($\langle \sigma_u \rangle \neq 0$) and ϕ_u consist of $u(d)$ quarks, and σ_s ($\langle \sigma_s \rangle \neq 0$) and ϕ_s consist of s quarks.

These terms appear due to the 't Hooft interaction. When restoring scale invariance of the effective Lagrangian by inserting dilaton fields (the procedure of the restoration of scale invariance is given in Section 3), these terms must be treated separately. Moreover, it turns out that these terms determine most of quarkonium–glueball mixing.

Omitting, for a moment, the 't Hooft interaction in our approach, we require the Lagrangian to be scale-invariant in the chiral limit both before and after the spontaneous breaking of chiral symmetry (SBCS), except for the dilaton potential. This property can be obtained by considering (after bosonization when the effective Lagrangian is expressed in terms of bosonic scalar and pseudoscalar fields σ and ϕ) the shift of the scalar-meson field σ

$$\sigma = \sigma' - m\frac{\chi}{\chi_c} \qquad (m^0 = 0), \qquad (4)$$

where $\langle \sigma' \rangle_0 = 0$ and $\langle \sigma \rangle_0 = -m$, guaranteeing that relation (1) is satisfied. The nonzero vacuum expectation value of σ appears as a result of SBCS, and thus the constituent quark mass m is produced. In the case of nonvanishing current quark masses, (4) changes by including an additional (nonscaled) mass term m^0 in the expression on the right-hand side:

$$\sigma = \sigma' - m\frac{\chi}{\chi_c} + m^0. \qquad (5)$$

[1)]However, radially excited states have not yet been considered.

The structure of the paper is as follows. In Section 2, we derive the usual $U(3) \times U(3)$ flavor symmetric effective Lagrangian with the 't Hooft interaction and without dilaton fields. In Section 3, the dilaton field is introduced in the effective Lagrangian obtained in Section 2. In Section 4, the gap equations are investigated, the quadratic (in fields) terms are deduced, and the mixing matrix for scalar–isoscalar states is introduced. In Section 5, the numerical estimates for the model parameters are given. The main strong decays of scalar–isoscalar mesons are calculated in Section 6. It is shown there that the ρ meson plays an important role in the decay of a glueball into four pions. Finally, we discuss our results in the Conclusion.

2. CHIRAL EFFECTIVE LAGRANGIAN WITH 'T HOOFT INTERACTION

A $U(3) \times U(3)$ chiral Lagrangian with the 't Hooft interaction was investigated in paper [24]. It consists of three terms (see below). The first term represents the free-quark Lagrangian, the second is composed of four-quark vertices as in the NJL model, and the last one describes the six-quark 't Hooft interaction [25] that is necessary to solve the $U_A(1)$ problem:

$$L = \bar{q}(i\hat{\partial} - m^0)q \tag{6}$$
$$+ \frac{G}{2}\sum_{a=0}^{8}[(\bar{q}\lambda_a q)^2 + (\bar{q}i\gamma_5\lambda_a q)^2]$$
$$- K\left\{\det[\bar{q}(1+\gamma_5)q] + \det[\bar{q}(1-\gamma_5)q]\right\}.$$

Here, G and K are coupling constants; $\lambda_a (a = 1, ..., 8)$ are the Gell-Mann matrices; $\lambda_0 = \sqrt{2/3}\ \mathbf{1}$, with $\mathbf{1}$ being the identity matrix; and m^0 is a current quark mass matrix with diagonal elements m_u^0, m_d^0, and m_s^0 ($m_u^0 \approx m_d^0$).

The standard bosonization procedure for local quark models consists in replacing the four-quark vertices by Yukawa coupling of quarks to bosonic fields, which enables one to perform integration with respect to quark fields. The final effective bosonic Lagrangian appears then as a result of the calculation of the quark determinant. To realize this program, it is necessary, using the method described in [24–27], to go over from Lagrangian (6) to an intermediate Lagrangian that contains only four-quark vertices

$$L = \bar{q}(i\hat{\partial} - \bar{m}^0)q \tag{7}$$
$$+ \frac{1}{2}\sum_{a,b=1}^{9}[G_{ab}^{(-)}(\bar{q}\tau_a q)(\bar{q}\tau_b q)$$
$$+ G_{ab}^{(+)}(\bar{q}i\gamma_5\tau_a q)(\bar{q}i\gamma_5\tau_b q)],$$

where

$$\tau_a = \lambda_a \quad (a = 1, ..., 7), \quad \tau_8 = (\sqrt{2}\lambda_0 + \lambda_8)/\sqrt{3},$$
$$\tau_9 = (-\lambda_0 + \sqrt{2}\lambda_8)/\sqrt{3}, \tag{8}$$
$$G_{11}^{(\pm)} = G_{22}^{(\pm)} = G_{33}^{(\pm)} = G \pm 4Km_s I_1^\Lambda(m_s),$$
$$G_{44}^{(\pm)} = G_{55}^{(\pm)} = G_{66}^{(\pm)} = G_{77}^{(\pm)} = G \pm 4Km_u I_1^\Lambda(m_u),$$
$$G_{88}^{(\pm)} = G \mp 4Km_s I_1^\Lambda(m_s), \quad G_{99}^{(\pm)} = G,$$
$$G_{89}^{(\pm)} = G_{98}^{(\pm)} = \pm 4\sqrt{2}Km_u I_1^\Lambda(m_u),$$
$$G_{ab}^{(\pm)} = 0 \quad (a \neq b; \quad a, b = 1, \ldots, 7),$$
$$G_{a8}^{(\pm)} = G_{a9}^{(\pm)} = G_{8a}^{(\pm)} = G_{9a}^{(\pm)} = 0 \quad (a = 1, \ldots, 7),$$

and $\bar{m}^0$ is a diagonal matrix composed of the modified current quark masses

$$\bar{m}_u^0 = m_u^0 - 32Km_u m_s I_1^\Lambda(m_u) I_1^\Lambda(m_s), \tag{9}$$
$$\bar{m}_s^0 = m_s^0 - 32Km_u^2 I_1^\Lambda(m_u)^2. \tag{10}$$

Here, m_u and m_s are constituent quark masses, and the integrals

$$I_n^\Lambda(m_a) = \frac{N_c}{(2\pi)^4}\int d_e^4 k \frac{\theta(\Lambda^2 - k^2)}{(k^2 + m_a^2)^n} \tag{11}$$
$$(n = 1, 2; a = u, s)$$

are calculated in the Euclidean metric and regularized by a simple $O(4)$-symmetric ultraviolet cutoff Λ. For $I_1^\Lambda(m_a)$, one gets

$$I_1^\Lambda(m_a) = \frac{N_c}{16\pi^2}\left(\Lambda^2 - m_a^2 \ln\left(\frac{\Lambda^2}{m_a^2} + 1\right)\right), \tag{12}$$

where m_a represents a corresponding constituent quark mass, m_u or m_s. Note that we have already introduced the notation of constituent quark masses here, although they will be consistently considered only later, when discussing mass gap equations (see (50) and (51) below) and the related shift of scalar-meson fields. However, as we want to use an effective four-fermion interaction instead of the original six-quark one, we have to use full quark propagators with constituent quark masses to calculate quark loop corrections for the constant G [see (8)]. For the definition of the constituent quark masses, see (14) and (15) below.

In addition to the one-loop corrections to the constant G at four-quark vertices, we modified the current quark masses m_a^0 [see (9) and (10)]. This is done to avoid the problem of double counting of the 't Hooft contribution in gap equations which was encountered in [27]. After the redefinition of the constant G and of the current quark masses, we can guarantee that, in the large-N_c limit, the mass spectrum of mesons and the gap equations, derived from the new Lagrangian with modified four-quark vertices and current quark

masses, are the same as those obtained from the original Lagrangian with six-quark vertices.

Now we can bosonize Lagrangian (7). By introducing auxiliary scalar σ and pseudoscalar ϕ fields, we obtain [13, 14, 24]

$$\mathcal{L}(\sigma,\phi) \tag{13}$$
$$= -\frac{1}{2}\sum_{a,b=1}^{9}\left(\sigma_a (G^{(-)})^{-1}_{ab}\sigma_b + \phi_a (G^{(+)})^{-1}_{ab}\phi_b\right)$$
$$- i\,\mathrm{tr}\ln\left\{i\hat{\partial} - \bar{m}^0 + \sum_{a=1}^{9}\tau_a(\sigma_a + i\gamma_5\phi_a)\right\}.$$

As we expect, the chiral symmetry is spontaneously broken owing to strong attraction of quarks in the scalar channel, and the scalar–isoscalar fields acquire nonzero vacuum expectation values $\langle\sigma_a\rangle_0 \neq 0$ $(a = 8, 9)$. These values are related to basic model parameters G, m^0, and Λ via gap equations, as will be shown in the next section. Therefore, we first have to shift the σ fields by a proper value so that the new fields have zero vacuum expectation values:

$$\sigma_a = \sigma'_a - \mu_a + \bar{\mu}^0_a, \qquad \langle\sigma'_a\rangle_0 = 0, \tag{14}$$

where $\mu_a = 0 \quad (a = 1,\ldots,7)$, $\mu_8 = m_u$, and $\mu_9 = -m_s/\sqrt{2}$ and $\bar{\mu}^0_a = 0 \quad (a = 1,\ldots,7)$, $\bar{\mu}^0_8 = \bar{m}^0_u$, and $\bar{\mu}^0_9 = -\bar{m}^0_s/\sqrt{2}$. After this shift, we obtain

$$\mathcal{L}(\sigma',\phi) = L_G(\sigma',\phi) \tag{15}$$
$$- i\,\mathrm{tr}\ln\left\{i\hat{\partial} - m + \sum_{a=1}^{9}\tau_a(\sigma'_a + i\gamma_5\phi_a)\right\},$$

where

$$L_G(\sigma',\phi) \tag{16}$$
$$= -\frac{1}{2}\sum_{a,b=1}^{9}(\sigma'_a - \mu_a + \bar{\mu}^0_a)\left(G^{(-)}\right)^{-1}_{ab}$$
$$\times(\sigma'_b - \mu_b + \bar{\mu}^0_b) - \frac{1}{2}\sum_{a,b=1}^{9}\phi_a\left(G^{(+)}\right)^{-1}_{ab}\phi_b,$$

and m is a diagonal matrix of constituent quark masses for different flavors. From Lagrangian (15), we take only those terms (in momentum space) which are linear, squared, cubic, and quadruple in scalar and pseudoscalar fields,[2)]

$$\mathcal{L}(\sigma',\phi) = L_G(\sigma',\phi) \tag{17}$$
$$+ \mathrm{tr}\left[I_2^\Lambda(m)((\partial_\mu\sigma')^2 + (\partial_\mu\phi)^2) - 4mI_1^\Lambda(m)\sigma'\right.$$
$$+ 2I_1^\Lambda(m)(\sigma'^2 + \phi^2) - 4m^2 I_2^\Lambda(m)\sigma'^2$$
$$+ 4mI_2^\Lambda(m)\sigma'(\sigma'^2 + \phi^2) - I_2^\Lambda(m)(\sigma'^2 + \phi^2)^2$$
$$\left. + I_2^\Lambda(m)[\sigma' - m,\phi]^2_-\right],$$
$$\sigma' = \sum_{a=1}^{9}\sigma_a\tau_a, \qquad \phi = \sum_{a=1}^{9}\phi_a\tau_a, \tag{18}$$

where "tr" means a calculation of the trace over τ-matrix expressions and $[\ldots]_-$ stands for a commutator. Hereafter, the coordinate derivatives are denoted as $\partial_\mu \equiv \partial/\partial x_\mu$, and the sum over μ is assumed in (17). The argument of I_1^Λ and I_2^Λ is rather formal. Instead of the matrix m, one should put either m_u or m_s; as well, an appropriate g_a, defined in (24) below, should be taken in place of g, depending on the sort of mesons. In the case of strange mesons, for the integral I_2^Λ, one should use $I_2^\Lambda(m_u, m_s)$ defined below in (25). Which one to choose and how to calculate "tr" are explained in detail in [13]. The expression for $I_1^\Lambda(m_a)$ in the Euclidean metric is given in (12). The integrals $I_2^\Lambda(m_a)$ are also calculated in Euclidean spacetime

$$I_2^\Lambda(m_a) = \frac{N_c}{16\pi^2}\left(\ln\left(\frac{\Lambda^2}{m_a^2} + 1\right) - \frac{\Lambda^2}{\Lambda^2 + m_a^2}\right). \tag{19}$$

Then, we renormalize the fields in (17), so that the kinetic terms of the effective Lagrangian are of the conventional form, and diagonalize the isoscalar sector,

$$\bar{\mathcal{L}}(\sigma^r,\phi^r) = \bar{L}_G(\sigma^r,\phi^r) \tag{20}$$
$$+ \mathrm{tr}\left[\frac{1}{4}((\partial_\mu\sigma^r)^2 + (\partial_\mu\phi^r)^2) - 4mgI_1^\Lambda(m)\sigma^r\right.$$
$$+ 2g^2 I_1^\Lambda(m)(\sigma^{r\,2} + Z\phi^{r\,2}) + \frac{1}{4}[m,\phi^r]^2_- - m^2\sigma^{r\,2}$$
$$+ mg\sigma^r(\sigma^{r\,2} + Z\phi^{r\,2}) - \frac{g}{2}[m,\phi^r]_-[\sigma^r,\phi^r]_-$$
$$\left. - \frac{g^2}{4}((\sigma^{r\,2} + Z\phi^{r\,2})^2 - [\sigma^r,\phi^r]^2_-)\right],$$
$$\sigma^r = \sum_{a=1}^{9}\sigma^r_a\tau_a, \qquad \phi^r = \sum_{a=1}^{9}\phi^r_a\tau_a. \tag{21}$$

For $\bar{L}_G$, we have

$$\bar{L}_G(\sigma^r,\phi^r) \tag{22}$$
$$= -\frac{1}{2}\sum_{a,b=1}^{9}(g_a\sigma^r_a - \mu_a + \bar{\mu}^0_a)\left(G^{(-)}\right)^{-1}_{ab}$$

[2)] Despite that the scalar fields are of the main interest in this paper, we still need pseudoscalar fields to fix the model parameters.

$$\times (g_b\sigma_b^r - \mu_b + \bar{\mu}_b^0) - \frac{Z}{2}\sum_{a,b=1}^{9} g_a\phi_a^r \left(G^{(+)}\right)^{-1}_{ab} g_b\phi_b^r.$$

Here, we have introduced the Yukawa coupling constants g_a:

$$\sigma_a' = g_a\sigma_a^r, \qquad \phi_a = \sqrt{Z}g_a\phi_a^r, \tag{23}$$

$$g_1^2 = g_2^2 = g_3^2 = g_8^2 = g_u^2 = [4I_2^\Lambda(m_u)]^{-1}, \tag{24}$$
$$g_4^2 = g_5^2 = g_6^2 = g_7^2 = [4I_2^\Lambda(m_u, m_s)]^{-1},$$
$$g_9^2 = g_s^2 = [4I_2^\Lambda(m_s)]^{-1},$$

$$I_2^\Lambda(m_u, m_s) = \frac{N_c}{(2\pi)^4} \tag{25}$$

$$\times \int d_e^4k \frac{\theta(\Lambda^2 - k^2)}{(k^2 + m_u^2)(k^2 + m_s^2)} = \frac{3}{(4\pi)^2(m_s^2 - m_u^2)}$$
$$\times \left[m_s^2 \ln\left(\frac{\Lambda^2}{m_s^2} + 1\right) - m_u^2 \ln\left(\frac{\Lambda^2}{m_u^2} + 1\right)\right],$$

$$Z = \left(1 - \frac{6m_u}{M_{A_1}^2}\right)^{-1} \approx 1.44, \tag{26}$$

where we have taken into account π-A_1 transitions leading to an additional Z factor, with M_{A_1} being the mass of an axial-vector meson (see [13]). The renormalized scalar and pseudoscalar fields in (20)–(23) are labeled with the superscript r.

The mass formulas for isovectors and isodublets follow immediately from (20). One just has to look up the coefficients at ${\sigma^r}^2$ and ${\phi^r}^2$. There are still nondiagonal terms in (22) in the isoscalar sector. This problem is solved by choosing the proper mixing angles, both for the scalars and for the pseudoscalars (see, e.g., [24]). As we are going to introduce the glueball field, the mixing with scalar–isoscalar quarkonia will change the situation. One has to consider the mixing among three states, which cannot be described by a single angle. For simplicity, in our estimations we resort to a numerical diagonalization procedure, not to the algebraic one. Concerning the pseudoscalar sector, one can avail oneself of the results given in [24]. All what concerns dealing with the glueball is discussed in the next section.

3. NAMBU–JONA-LASINIO MODEL WITH DILATON

As we have already mentioned above, we introduce the glueball field into our effective Lagrangian, obtained in the preceding section, as a dilaton. For this purpose, we use the following principle. Insofar as the QCD Lagrangian is scale-invariant in the chiral limit, we suppose that our effective meson Lagrangian, motivated by QCD, has also to be scale-invariant both before and after SBCS in the case when the current quark masses are equal to zero. As a result, we come to the following prescription: the dimensional model parameters G, Λ, K, and m_a are replaced by the following rule: $G \to G(\chi_c/\chi)^2$, $K \to K(\chi_c/\chi)^5$, $\Lambda \to \Lambda(\chi/\chi_c)$, $m_a \to m_a(\chi/\chi_c)$, where χ is the dilaton field with the vacuum expectation value χ_c. But there are terms that break scale invariance. They are the terms containing current quark masses, the scale anomaly of QCD reproduced by the dilaton potential, and terms of the type $h_\phi\phi_0^2$ and $h_\sigma\sigma_0^2$ [see (3)] induced by gluon anomalies in the meson Lagrangian.

As was mentioned in the preceding section, the current quark masses break scale invariance and should not therefore be multiplied by dilaton fields. The modified current quark masses $\bar{m}^0$ are not multiplied by dilaton fields either. In particular, this transforms formula (14) to what follows:

$$\sigma_a = \sigma_a' - \mu_a\frac{\chi}{\chi_c} + \bar{\mu}_a^0. \tag{27}$$

Finally, we arrive at the Lagrangian

$$\bar{\mathcal{L}}(\sigma^r, \phi^r, \chi) = \mathcal{L}(\chi) + L_{\rm kin}(\sigma^r, \phi^r) \tag{28}$$
$$+ \bar{L}_G(\sigma^r, \phi^r, \chi) + L_{1-\rm loop}(\sigma^r, \phi^r, \chi)$$
$$+\Delta L_{\rm an}(\sigma^r, \phi^r, \chi).$$

Here, $\mathcal{L}(\chi)$ is the pure dilaton Lagrangian

$$\mathcal{L}(\chi) = \frac{1}{2}(\partial_\nu\chi)^2 - V(\chi) \tag{29}$$

with the potential

$$V(\chi) = B\left(\frac{\chi}{\chi_0}\right)^4 \left[\ln\left(\frac{\chi}{\chi_0}\right)^4 - 1\right] \tag{30}$$

that has a minimum at $\chi = \chi_0$, and the parameter B representing the vacuum energy density when there are no quarks. The curvature of the potential at its minimum determines the bare glueball mass

$$m_g = \frac{4\sqrt{B}}{\chi_0}. \tag{31}$$

The part $L_{\rm kin}(\sigma^r, \phi^r)$ of Lagrangian (28) contains the pure kinetic terms

$$L_{\rm kin}(\sigma^r, \phi^r) = \frac{1}{2}\sum_{a=1}^{9}\left((\partial_\nu\sigma_a^r)^2 + (\partial_\nu\phi_a^r)^2\right). \tag{32}$$

The next term reads

$$\bar{L}_G(\sigma^r, \phi^r, \chi) = -\frac{1}{2}\left(\frac{\chi}{\chi_c}\right)^2 \tag{33}$$
$$\times \sum_{a,b=1}^{9}\left(g_a\sigma_a^r - \mu_a\frac{\chi}{\chi_c} + \bar{\mu}_a^0\right)\left(G^{(-)}\right)^{-1}_{ab}$$
$$\times \left(g_b\sigma_b^r - \mu_b\frac{\chi}{\chi_c} + \bar{\mu}_b^0\right) - \frac{Z}{2}\left(\frac{\chi}{\chi_c}\right)^2$$

$$\times \sum_{a,b=1}^{9} g_a \phi_a^r \left(G^{(+)}\right)^{-1}_{ab} g_b \phi_b^r.$$

The sum of one-loop quark diagrams is denoted as $L_{1-\mathrm{loop}}(\sigma^r, \phi^r, \chi)$

$$L_{1-\mathrm{loop}}(\sigma^r, \phi^r, \chi) = \mathrm{tr}\Bigg[-4mgI_1^\Lambda(m)\sigma^r \left(\frac{\chi}{\chi_c}\right)^3 \tag{34}$$

$$+ 2g^2 I_1^\Lambda(m)({\sigma^r}^2 + Z{\phi^r}^2)\left(\frac{\chi}{\chi_c}\right)^2$$

$$- m^2{\sigma^r}^2\left(\frac{\chi}{\chi_c}\right)^2 + mg\frac{\chi}{\chi_c}\sigma^r({\sigma^r}^2 + Z{\phi^r}^2)$$

$$- \frac{g^2}{4}\left((\sigma^r{}^2 + Z\phi^r{}^2)^2 - [\sigma^r, \phi^r]^2\right)$$

$$-\frac{g}{2}[m, \phi^r]_-[\sigma^r, \phi^r]_-\Bigg].$$

As one can see, expanding (33) in a power series in χ, we can extract a term that is of order χ^4. It can be absorbed by the term in the pure dilaton potential that has the same degree of χ. Obviously, this leads only to a redefinition of the constants B and χ_0, which anyway are not known from the very beginning. Moreover, saying in advance, terms like χ^4 do not contribute to the divergence of the dilatation current (1) because of their scale invariance.

If the procedure of the scale invariance restoration of this Lagrangian is implemented, the part induced by gluon anomalies also becomes scale-invariant. To avoid this, one should subtract this part in the scale-invariant form and add it in a scale-breaking (SB) form. This is achieved by including the term ΔL_{an}:

$$\Delta L_{\mathrm{an}} = -L_{\mathrm{an}}\left(\frac{\chi}{\chi_c}\right)^2 + L_{\mathrm{an}}^{\mathrm{SB}}. \tag{35}$$

The term L_{an} was introduced in (3). In L_{an}, we will use the renormalized fields σ_0^r and ϕ_0^r instead of σ_0 and ϕ_0, however, taking into account the effects of a nonzero vacuum expectation value of σ_0. Let us define the scale-breaking term $L_{\mathrm{an}}^{\mathrm{SB}}$. The coefficients h_σ and h_ϕ in (3) can be determined by comparing them with the terms in (33) that describe the singlet–octet mixing. We obtain

$$h_\phi = -\frac{3}{2\sqrt{2}} g_u g_s Z (G^{(+)})^{-1}_{89}, \tag{36}$$

$$h_\sigma = \frac{3}{2\sqrt{2}} g_u g_s (G^{(-)})^{-1}_{89}.$$

If these terms were to be made scale-invariant, one should insert $(\chi/\chi_c)^2$ into them. However, as the gluon anomalies break scale invariance, we introduce the dilaton field into these terms in a more complicated way. The inverse matrix elements $(G^{(+)})^{-1}_{ab}$ and $(G^{(-)})^{-1}_{ab}$,

$$(G^{(+)})^{-1}_{89} = \frac{-4\sqrt{2}m_u K I_1^\Lambda(m_u)}{G_{88}^{(+)}G_{99}^{(+)} - (G_{89}^{(+)})^2}, \tag{37}$$

$$(G^{(-)})^{-1}_{89} = \frac{4\sqrt{2}m_u K I_1^\Lambda(m_u)}{G_{88}^{(-)}G_{99}^{(-)} - (G_{89}^{(-)})^2}, \tag{38}$$

are determined by two different interactions. The numerators are fully defined by the 't Hooft interaction that leads to anomalous terms (3) breaking scale invariance; therefore, we do not introduce here dilaton fields. The denominators are determined by constant G describing the main four-quark interaction, and the dilaton field is inserted into it, according to the prescription given in the beginning of this section. Finally, we come to the following form of $L_{\mathrm{an}}^{\mathrm{SB}}$:

$$L_{\mathrm{an}}^{\mathrm{SB}} \tag{39}$$

$$= \left(-h_\phi {\phi_0^r}^2 + h_\sigma\left(\sigma_0^r - F_0\frac{\chi}{\chi_c} + F_0^0\right)^2\right)\left(\frac{\chi}{\chi_c}\right)^4,$$

$$F_0 = \frac{\sqrt{2}m_u}{\sqrt{3}g_u} + \frac{m_s}{\sqrt{6}g_s}, F_0^0 = \frac{\sqrt{2}\bar{m}_u^0}{\sqrt{3}g_u} + \frac{\bar{m}_s^0}{\sqrt{6}g_s}. \tag{40}$$

From it, we immediately obtain the term ΔL_{an}:

$$\Delta L_{\mathrm{an}} = \left(h_\phi {\phi_0^r}^2 - h_\sigma\left(\sigma_0^r - F_0\frac{\chi}{\chi_c} + F_0^0\right)^2\right) \tag{41}$$

$$\times \left(\frac{\chi}{\chi_c}\right)^2\left(1 - \left(\frac{\chi}{\chi_c}\right)^2\right).$$

Let us now consider the vacuum expectation value of the divergence of the dilatation current calculated from the potential of the effective meson–dilaton Lagrangian:

$$\langle \partial_\mu S^\mu\rangle = \left(\sum_{a=8}^{9}\sigma_a^r\frac{\partial V}{\partial \sigma_a^r} + \chi\frac{\partial V}{\partial \chi} - 4V\right)\Bigg|_{\substack{\chi=\chi_c \\ \sigma_a^r=0}} \tag{42}$$

$$= 4B\left(\frac{\chi_c}{\chi_0}\right)^4 - 2h_\sigma\left(F_0 - F_0^0\right)^2 - \sum_{q=u,d,s}\bar{m}_q^0\langle\bar{q}q\rangle.$$

Here, $V = V(\chi) + \bar{V}(\sigma^r, \phi^r, \chi)$, and $\bar{V}(\sigma^r, \phi^r, \chi)$ is the potential part of Lagrangian $\bar{\mathcal{L}}(\sigma^r, \phi^r, \chi)$ that does not contain the pure dilaton potential. The expression given in (42) is simplified by using the following relation between the quark condensates and integrals $I_1^\Lambda(m_u)$ and $I_1^\Lambda(m_s)$:

$$4m_q I_1^\Lambda(m_q) = -\langle\bar{q}q\rangle_0 \qquad (q = u, d, s). \tag{43}$$

Table 1. Masses of the physical scalar-meson states $\sigma_{\rm I}$, $\sigma_{\rm II}$, and $\sigma_{\rm III}$; values of the parameters χ_c and χ_0; bag constant B; and (bare) glueball mass M_g

$M_{\sigma_{\rm III}}$, MeV	$\sigma_{\rm I}$	$\sigma_{\rm II}$	$\sigma_{\rm III}$	χ_c	χ_0	B, GeV^4	M_g, MeV
1500	400	1100	1500	206	190	0.009	1447
1710	400	1100	1710	180	166	0.009	1665

These integrals are related to the constants $G^{(-)}_{ab}$ through the gap equations, as will be shown in the next section [see (47) and (48) below]. Comparing the QCD expression (1) with (42), one can see that the term $\sum m^0_q\langle\bar qq\rangle$ in (1) is canceled by the corresponding contribution in (42). Equating the right-hand sides of (1) and (42),

$$\mathcal{C}_g - \sum_{q=u,d,s} m^0_q\langle\bar qq\rangle = 4B\left(\frac{\chi_c}{\chi_0}\right)^4 \qquad (44)$$
$$- 2h_\sigma\left(F_0 - F^0_0\right)^2 - \sum_{q=u,d,s}\bar m^0_q\langle\bar qq\rangle,$$

we obtain the correspondence

$$\mathcal{C}_g = 4B\left(\frac{\chi_c}{\chi_0}\right)^4 \qquad (45)$$
$$+ \sum_{a,b=8}^{9}(\bar\mu^0_a - \mu^0_a)(G^{(-)})^{-1}_{ab}(\mu_b - \bar\mu^0_b)$$
$$- 2h_\sigma\left(F_0 - F^0_0\right)^2,$$

where $\mu^0_8 = m^0_u$ and $\mu^0_9 = -m_s/\sqrt{2}$. This equation relates the gluon condensate, whose value is taken from other models (see, e.g., [28]), to the model parameter B. The next step is to investigate the gap equations.

4. EQUATIONS

As usual, gap equations follow from the requirement that the terms linear in σ^r and χ' be absent in our Lagrangian:

$$\left.\frac{\delta\bar{\mathcal{L}}}{\delta\sigma^r_8}\right|_{(\phi^r,\sigma^r,\chi')=0} = 0, \quad \left.\frac{\delta\bar{\mathcal{L}}}{\delta\sigma^r_9}\right|_{(\phi^r,\sigma^r,\chi')=0} = 0, \quad (46)$$
$$\left.\frac{\delta\bar{\mathcal{L}}}{\delta\chi}\right|_{(\phi^r,\sigma^r,\chi')=0} = 0.$$

Here, the field $\chi' = \chi - \chi_c$ with a zero vacuum expectation value $\langle\chi'\rangle_0 = 0$ is associated with the glueball field. In further calculations, the Lagrangian is expanded in power series of χ'. As a result, we obtain the equations

$$(m_u - \bar m^0_u)(G^{(-)})^{-1}_{88} \qquad (47)$$
$$- \frac{m_s - \bar m^0_s}{\sqrt{2}}(G^{(-)})^{-1}_{89} - 8m_uI^\Lambda_1(m_u) = 0,$$
$$(m_s - \bar m^0_s)(G^{(-)})^{-1}_{99} \qquad (48)$$
$$-\sqrt{2}(m_u - \bar m^0_u)(G^{(-)})^{-1}_{98} - 8m_sI^\Lambda_1(m_s) = 0,$$
$$4B\left(\frac{\chi_c}{\chi_0}\right)^3\frac{1}{\chi_0}\ln\left(\frac{\chi_c}{\chi_0}\right)^4 \qquad (49)$$
$$+ \frac{1}{\chi_c}\left(\sum_{a,b=8}^{9}\bar\mu^0_a(G^{(-)})^{-1}_{ab}(\bar\mu^0_b - 3\mu_b)\right)$$
$$- \frac{2h_\sigma}{\chi_c}\left(F_0 - F^0_0\right)^2 = 0.$$

Using (9) and (10), one can rewrite equations (47) and (48) in the well-known form [27]

$$m^0_u = m_u - 8Gm_uI^\Lambda_1(m_u) \qquad (50)$$
$$- 32Km_um_sI^\Lambda_1(m_u)I^\Lambda_1(m_s),$$
$$m^0_s = m_s - 8Gm_sI^\Lambda_1(m_s) \qquad (51)$$
$$- 32K(m_uI^\Lambda_1(m_u))^2.$$

To define the masses of quarkonia and the glueball, we consider that part of Lagrangian (28) which is quadratic in fields σ^r and χ' and which we denote by $L^{(2)}$:

$$L^{(2)}(\sigma,\phi,\chi') \qquad (52)$$
$$= -\frac{1}{2}\{g^2_8[(G^{(-)})^{-1}_{88} - 8I^\Lambda_1(m_u)] + 4m^2_u\}{\sigma^r}^2_8$$

Table 2. Elements of the matrix b describing mixing in the scalar–isoscalar sector

	$\sigma_{\rm I}$	$\sigma_{\rm II}$	$\sigma_{\rm III}$
$\sigma_{\rm III} \equiv f_0(1500)$			
σ^r_u	0.939	0.240	0.247
σ^r_s	−0.214	0.968	−0.128
χ'	−0.270	0.067	0.960
$\sigma_{\rm III} \equiv f_0(1710)$			
σ^r_u	0.948	0.232	0.216
σ^r_s	−0.216	0.971	−0.099
χ'	−0.233	0.047	0.971

$$-\frac{1}{2}\{g_9^2[(G^{(-)})^{-1}_{99}-8I_1^\Lambda(m_s)]+4m_s^2\}{\sigma^r}_9^2$$
$$-g_8g_9(G^{(-)})^{-1}_{89}\sigma_8^r\sigma_9^r-\frac{M_g^2}{2}{\chi'}^2$$
$$+\sum_{a,b=8}^{9}\frac{\bar\mu_a^0}{\chi_c}(G^{(-)})^{-1}_{ab}g_b\sigma_b^r\chi'$$
$$+\frac{4h_\sigma(F_0-F_0^0)}{\chi_c\sqrt{3}}\left(\sigma_9^r-\sigma_8^r\sqrt{2}\right)\chi',$$

where

$$M_g^2=\chi_c^{-2}(4\mathcal{C}_g+\sum_{a,b=8}^{9}\bar\mu_a^0(G^{(-)})^{-1}_{ab} \tag{53}$$
$$\times(2\bar\mu_b^0-\mu_b)+\sum_{a,b=8}^{9}4\mu_a^0(G^{(-)})^{-1}_{ab}(\mu_b-\bar\mu_b^0)$$
$$-h_\sigma 4F_0^2+4h_\sigma(F_0^0)^2)$$

is the glueball mass before taking account of mixing effects.

From this Lagrangian, after diagonalization, we obtain the masses of three scalar-meson states, $\sigma_{\rm I}$, $\sigma_{\rm II}$, and $\sigma_{\rm III}$, and a matrix of mixing coefficients b that relates the nondiagonalized fields $\sigma_8\equiv\sigma_u$, $\sigma_9\equiv\sigma_s$, and χ' to the physical ones $\sigma_{\rm I}$, $\sigma_{\rm II}$, and $\sigma_{\rm III}$:

$$\begin{pmatrix}\sigma_u\\ \sigma_s\\ \chi'\end{pmatrix}=\begin{pmatrix}b_{\sigma_u\sigma_{\rm I}} & b_{\sigma_u\sigma_{\rm II}} & b_{\sigma_u\sigma_{\rm III}}\\ b_{\sigma_s\sigma_{\rm I}} & b_{\sigma_s\sigma_{\rm II}} & b_{\sigma_s\sigma_{\rm III}}\\ b_{\chi'\sigma_{\rm I}} & b_{\chi'\sigma_{\rm II}} & b_{\chi'\sigma_{\rm III}}\end{pmatrix}\begin{pmatrix}\sigma_{\rm I}\\ \sigma_{\rm II}\\ \sigma_{\rm III}\end{pmatrix}. \tag{54}$$

5. MODEL PARAMETERS AND NUMERICAL ESTIMATES

The basic parameters of our model are G, K, Λ, m_u, and m_s. Once the dilaton fields have been introduced, they retain their values [13, 24]:

$$m_u=280\ {\rm MeV}, m_s=420\ {\rm MeV}, \Lambda=1.26\ {\rm GeV},$$
$$G=4.38\ {\rm GeV}^{-2}, K=11.2\ {\rm GeV}^{-5}. \tag{55}$$

Moreover, three new parameters, χ_0, χ_c, and B, appear. To fix the new parameters, one should use Eqs. (45) and (49) and the physical glueball mass. As a result, we obtain

$$\chi_0=\chi_c\exp\left(-\frac{\sum_{a,b=8}^{9}\bar\mu_a^0(G^{(-)})^{-1}_{ab}(3\mu_b-\bar\mu_b^0)+2h_\sigma\left(F_0-F_0^0\right)^2}{4[\mathcal{C}_g-\sum_{a,b=8}^{9}(\bar\mu_a^0-\mu_a^0)(G^{(-)})^{-1}_{ab}(\mu_b-\bar\mu_b^0)+2h_\sigma\left(F_0-F_0^0\right)^2]}\right), \tag{56}$$

$$B=\frac{\mathcal{C}_g-\sum_{a,b=8}^{9}(\bar\mu_a^0-\mu_a^0)(G^{(-)})^{-1}_{ab}(\mu_b-\bar\mu_b^0)+2h_\sigma\left(F_0-F_0^0\right)^2}{4}\left(\frac{\chi_0}{\chi_c}\right)^4. \tag{57}$$

We adjust the parameter χ_c so that the mass of the heaviest scalar meson, $\sigma_{\rm III}$, would be either 1500 or 1710 MeV. The result of our fit for both cases is given in Table 1. One will also find the mixing coefficients in Table 2.

6. DECAY WIDTHS

Once all parameters have been fixed, we can estimate the decay widths for the main strong decay modes of scalar mesons: $\sigma_l\to\pi\pi$, KK, $\eta\eta$, $\eta\eta'$, and 4π, where $l={\rm I},{\rm II},{\rm III}$.

Note that, in the energy region under consideration ($\sim$1500 MeV), we work on the brim of the validity of exploiting the chiral symmetry that was used to construct our effective Lagrangian. Thus, we can consider our results to be rather qualitative.

Let us start with the lightest scalar–isoscalar-meson state $\sigma_{\rm I}$ associated with $f_0(400-1200)$. This state decays into pions. This is the only strong decay mode, because $\sigma_{\rm I}$ is too light for other channels to be open. The amplitude describing its decay into pions has the form

$$A_{\sigma_{\rm I}\to\pi^+\pi^-}=2A^g_{\pi^+\pi^-}b_{\chi'\sigma_{\rm I}}+2A^ub_{\sigma_u\sigma_{\rm I}}, \tag{58}$$

$$A^g_{\pi^+\pi^-}=-\frac{M_\pi^2}{\chi_c},\quad A^u=2g_um_uZ, \tag{59}$$

where $A^g_{\pi^+\pi^-}$ is the contribution from the glueball component and A^u is the contribution from the $(\bar uu)$ quarkonium one. The coefficients $b_{\chi'\sigma_{\rm I}}$ and $b_{\sigma_u\sigma_{\rm I}}$ represent the corresponding elements of the 3×3 mixing matrix for scalar–isoscalar states (see Table 2). Both contributions have identical signs and are added to the width of $\sigma_{\rm I}$.

To calculate the decay width of a meson into two mesons, one can use the formula

$$\Gamma=\frac{|A|^2}{16\pi M^3}\frac{\lambda^{1/2}(M^2,M_1^2,M_2^2)}{r}, \tag{60}$$

where A is the amplitude of the process, M is the mass of the decaying particle, M_1 and M_2 are masses of secondary particles, and r is the dimension of the

permutation symmetry group in the phase space of final states. The function $\lambda(x,y,z)$ is defined as [29]

$$\lambda(x,y,z) = (x-y-z)^2 - 4yz. \quad (61)$$

For the decay of $\sigma_{\rm I}$ into pions, formula (60) can be rewritten in the simpler form

$$\Gamma_{\sigma_{\rm I}\to\pi^+\pi^-} = \frac{|A_{\sigma_{\rm I}\to\pi^+\pi^-}|^2}{16\pi M_{\sigma_{\rm I}}}\sqrt{1-\frac{4M_\pi^2}{M_{\sigma_{\rm I}}^2}}. \quad (62)$$

Using isotopic symmetry, we obtain the total width

$$\Gamma_{\sigma_{\rm I}\to\pi\pi} = \frac{3}{2}\Gamma_{\sigma_{\rm I}\to\pi^+\pi^-} \approx 820\ \text{MeV} \quad (63)$$

for the case where the model parameters are fixed for the state $\sigma_{\rm III}$ identified with $f_0(1500)$ and

$$\Gamma_{\sigma_{\rm I}\to\pi\pi} \approx 830\ \text{MeV} \quad (64)$$

for the case of $\sigma_{\rm III} \equiv f_0(1710)$. The experimental value is known with a large uncertainty and is reported to lie in the interval from 600 to 1000 MeV [29].

The amplitude describing the decay of the state $\sigma_{\rm II}$, which we identify with $f_0(980)$, into pions also consists of two parts

$$A_{\sigma_{\rm II}\to\pi^+\pi^-} = 2A^g_{\pi^+\pi^-}b_{\chi'\sigma_{\rm II}} + 2A^u b_{\sigma_u\sigma_{\rm II}}. \quad (65)$$

Here, the glueball contribution is small again and the quarkonium determines the decay width; however, in this case both contributions are opposite in sign and slightly compensate each other. The width of the state $\sigma_{\rm II}$ is close to that obtained in the model without glueballs [24]. We obtain

$$\Gamma_{\sigma_{\rm II}\to\pi\pi} \approx 28\ \text{MeV} \quad (66)$$

if $\sigma_{\rm III} \equiv f_0(1500)$ and

$$\Gamma_{\sigma_{\rm II}\to\pi\pi} \approx 26\ \text{MeV} \quad (67)$$

if $\sigma_{\rm III} \equiv f_0(1710)$. For the decay of $\sigma_{\rm II}$ into pions, the experiment gives a value lying within the range 30–70 MeV [30].

Let us now proceed to consider the decays of $\sigma_{\rm III}$. The process $\sigma_{\rm III} \to \pi^+\pi^-$ is given by the amplitude

$$A_{\sigma_{\rm III}\to\pi^+\pi^-} = 2A^g_{\pi^+\pi^-}b_{\chi'\sigma_{\rm III}} + 2A^u b_{\sigma_u\sigma_{\rm III}}, \quad (68)$$

which consists of two parts. The first part represents the contribution from the pure glueball. This contribution is small (since it is proportional to the pion mass squared), and the process is determined by the second part that describes the decay of the quarkonium component. As a result, the width of the decay $\sigma_{\rm III} \to \pi\pi$ is

$$\Gamma_{\sigma_{\rm III}\to\pi\pi} = \frac{3}{2}\Gamma_{\sigma_{\rm III}\to\pi^+\pi^-} \approx 14\ \text{MeV} \quad (69)$$

if $\sigma_{\rm III} \equiv f_0(1500)$ and

$$\Gamma_{\sigma_{\rm III}\to\pi\pi} \approx 8\ \text{MeV} \quad (70)$$

if $\sigma_{\rm III} \equiv f_0(1710)$.

In the case of $K\bar{K}$ channels, the contribution of the pure glueball is also proportional to the kaon mass squared and is rather large in relation to the pion case. The amplitude of the decay $\sigma_{\rm III} \to K^+K^-$ consists of three parts:

$$A_{\sigma_{\rm III}\to K^+K^-} = A^g_{KK}b_{\chi'\sigma_{\rm III}} + A^u_{KK}b_{\sigma_u\sigma_{\rm III}} + A^s_{KK}b_{\sigma_s\sigma_{\rm III}}, \quad (71)$$

where the pure glueball decay into K^+K^- is given by the amplitude

$$A^g_{KK} = -\frac{2M_K^2}{\chi_c}. \quad (72)$$

The quarkonium contributions are

$$A^u_{KK} = 2g_u Z \times \left(\frac{m_u+m_s}{2}\left(\frac{F_\pi}{F_K}\right)^2 + \frac{m_s(m_u-m_s)}{m_u+m_s}\right), \quad (73)$$

$$A^s_{KK} = -4\sqrt{2}g_s Z \times \left(\frac{m_u+m_s}{2}\left(\frac{F_s}{F_K}\right)^2 + \frac{m_u(m_s-m_u)}{m_u+m_s}\right), \quad (74)$$

where F_π and F_K are the pion and kaon weak decay constants, respectively, and $F_s = m_s/(g_s\sqrt{Z})$. In the case where $\sigma_{\rm III}$ is $f_0(1500)$, we have

$$\Gamma_{\sigma_{\rm III}\to K\bar{K}} = \Gamma_{\sigma_{\rm III}\to K^+K^-} + \Gamma_{\sigma_{\rm III}\to K^0\bar{K}^0} = 2\Gamma_{\sigma_{\rm III}\to K^+K^-} \approx 29\ \text{MeV}; \quad (75)$$

in the other case [$\sigma_{\rm III} \equiv f_0(1710)$],

$$\Gamma_{\sigma_{\rm III}\to K\bar{K}} \approx 60\ \text{MeV}. \quad (76)$$

The amplitude of the decay of $\sigma_{\rm III}$ into $\eta\eta$ and $\eta\eta'$ can also be considered in the same manner. The only complication is singlet–octet mixing in the pseudoscalar sector and additional vertices coming from $\Delta L_{\rm an}$. The corresponding amplitude is

$$A_{\sigma_{\rm III}\to\eta\eta} = 2A^g_{\eta\eta}b_{\chi'\sigma_{\rm III}} + 2A^u\sin^2\bar{\theta}b_{\sigma_u\sigma_{\rm III}} + 2A^s\cos^2\bar{\theta}b_{\sigma_s\sigma_{\rm III}} + 2A^{\rm an}_\phi\sin^2\theta b_{\chi'\sigma_{\rm III}}, \quad (77)$$

$$A^g_{\eta\eta} = -\frac{M_\eta^2}{\chi_c}, \quad (78)$$

$$A^{\rm an}_\phi = -\frac{2h_\phi}{\chi_c}, \quad (79)$$

where $\bar{\theta} = \theta - \theta_0$, with θ being the singlet–octet mixing angle in the pseudoscalar channel, $\theta \approx -19^\circ$ [24], and θ_0 being the ideal mixing angle, $\tan\theta_0 = 1/\sqrt{2}$. Therefore, the decay width is

$$\Gamma_{\sigma_{\rm III}\to\eta\eta} \approx 25\ \text{MeV} \quad (80)$$

if $\sigma_{\rm III} \equiv f_0(1500)$ and

$$\Gamma_{\sigma_{\rm III}\to\eta\eta} \approx 43\ \text{MeV} \quad (81)$$

if $\sigma_{\rm III} \equiv f_0(1710)$. For the decay of $\sigma_{\rm III}$ into $\eta\eta'$, we have the amplitude

$$A_{\sigma_{\rm III}\to\eta\eta'} = -A^u\sin 2\bar{\theta}b_{\sigma_u\sigma_{\rm III}} \quad (82)$$

$$+ A^s \sin 2\bar{\theta} b_{\sigma_s \sigma_{\rm III}} - A^{\rm an}_\phi \sin 2\theta b_{\chi' \sigma_{\rm III}}.$$

The direct decay of a bare glueball into $\eta\eta'$ is absent here. This process occurs only due to the mixing of the glueball and scalar–isoscalar quarkonia and the anomaly contribution. The decay widths are as follows:

$$\Gamma_{\sigma_{\rm III} \to \eta\eta'} \sim 10 \text{ MeV} \tag{83}$$

for $\sigma_{\rm III} \equiv f_0(1500)$ and

$$\Gamma_{\sigma_{\rm III} \to \eta\eta'} \approx 30 \text{ MeV} \tag{84}$$

for $\sigma_{\rm III} \equiv f_0(1710)$. The estimate for the decay $f_0(1500)$ into $\eta\eta'$ is very rough, because the decay is allowed only owing to a finite width of the resonance, since its mass lies slightly below the $\eta\eta'$ threshold. The calculation is made for the mass of $f_0(1500)$ plus its half-width. For $f_0(1710)$, we have a more reliable estimate, since its mass is large enough for the decay to be possible.

Up to this moment, we considered only decays into a pair of mesons. For the state $\sigma_{\rm III}$, there is a possibility to decay into four pions. This decay can occur through intermediate σ ($f_0(400–1200)$) resonance.

The decay through the σ resonance can be represented as two processes: with two resonances $\sigma_{\rm III} \to \sigma\sigma \to 4\pi$ and one resonance $\sigma_{\rm III} \to \sigma 2\pi \to 4\pi$. The vertices determining these decays follow from Lagrangian (28). The decay of a glueball into two σ is given by the amplitude

$$A_{\sigma_{\rm III} \to \sigma\sigma} \approx 2A^g_{\sigma\sigma} b_{\chi' \sigma_{\rm III}} + 3Z^{-1} A^u b_{\sigma_u \sigma_{\rm III}} b^2_{\sigma_u \sigma_{\rm I}} + 2A^{\rm an}_\sigma b_{\chi' \sigma_{\rm III}} b^2_{\sigma_u \sigma_{\rm I}}, \tag{85}$$

where $A^g_{\sigma\sigma}$ is the pure glueball amplitude[3)]

$$A^g_{\sigma\sigma} \approx -\frac{M^2_{\sigma_u}}{\chi_c}, \tag{86}$$

and the anomaly amplitude $A^{\rm an}_\sigma$ coming from $\Delta L_{\rm an}$ is

$$A^{\rm an}_\sigma = \frac{2h_\sigma}{3\chi_c}. \tag{87}$$

The total amplitude describing the decay into four pions through two σ resonances is

$$A_{\sigma_{\rm III} \to \sigma\sigma \to 2\pi^+ 2\pi^-} = 2A_{\sigma_{\rm III} \to \sigma\sigma} A^2_{\sigma \to \pi^+\pi^-} (\Delta_\sigma(s_{12}) \Delta_\sigma(s_{34}) + \Delta(s_{14}) \Delta(s_{23})), \tag{88}$$

where the function $\Delta_\sigma(s)$ appears owing to the resonant structure of the processes,

$$\Delta_\sigma(s) = (s - M^2_{\sigma_{\rm I}} + iM_{\sigma_{\rm I}} \Gamma_{\sigma_{\rm I}})^{-1}, \tag{89}$$

where $\Gamma_{\sigma_{\rm I}} \approx \Gamma_{\sigma \to \pi\pi}$ is the decay width of the $\sigma_{\rm I}$ resonance [see (63)]. This function depends on the invariant mass squared s_{ij} defined as

$$s_{ij} = (k_i + k_j)^2 \qquad (i, j = 1, \ldots, 4). \tag{90}$$

Here, i and j label the momenta k_i of the pions $\pi^+(k_1)$, $\pi^-(k_2)$, $\pi^+(k_3)$, and $\pi^-(k_4)$.

Let us now consider the decay into 4π through one σ resonance. The amplitude describing this process is as follows:

$$A_{\sigma_{\rm III} \to \sigma 2\pi} = A^g_{\sigma 2\pi} (b_{\sigma_u \sigma_{\rm I}} b_{\chi' \sigma_{\rm III}} + b_{\sigma_u \sigma_{\rm III}} b_{\chi' \sigma_{\rm I}}) + A^u_{\sigma 2\pi} b_{\sigma_u \sigma_{\rm III}} b_{\sigma_u \sigma_{\rm I}}. \tag{91}$$

The glueball amplitude is

$$A^g_{\sigma 2\pi} = \frac{4m_u g_u Z}{\chi_c}, \tag{92}$$

while, for the quarkonium amplitude, we have

$$A^u_{\sigma 2\pi} = -4g^2_u Z. \tag{93}$$

The glueball contribution prevails over the quarkonium one in magnitude and is opposite in sign.

The amplitude describing the decay $\sigma_{\rm III} \to 2\pi^+ 2\pi^-$ through one σ resonance is

$$A_{\sigma_{\rm III} \to \sigma 2\pi \to 2\pi^+ 2\pi^-} = -A_{\sigma_{\rm III} \to \sigma 2\pi} A_{\sigma \to \pi^+\pi^-} (\Delta_\sigma(s_{12}) + \Delta_\sigma(s_{34}) + \Delta_\sigma(s_{14}) + \Delta_\sigma(s_{23})). \tag{94}$$

The total amplitude of the decay into $2\pi^+ 2\pi^-$ via σ resonances is obtained as a cumulative contribution from both one and two intermediate σ mesons:

$$A_{\sigma_{\rm III} \to 2\pi^+ 2\pi^-} = A_{\sigma_{\rm III} \to \sigma\sigma \to 2\pi^+ 2\pi^-} + A_{\sigma_{\rm III} \to \sigma 2\pi \to 2\pi^+ 2\pi^-}. \tag{95}$$

The amplitude describing the decay into $2\pi^0 \pi^+ \pi^-$ has the form

$$A_{\sigma_{\rm III} \to 2\pi^0 \pi^+ \pi^-} = A_{\sigma_{\rm III} \to \sigma\sigma \to 2\pi^0 \pi^+ \pi^-} + A_{\sigma_{\rm III} \to \sigma 2\pi \to 2\pi^0 \pi^+ \pi^-}, \tag{96}$$

where

$$A_{\sigma_{\rm III} \to \sigma\sigma \to 2\pi^0 \pi^+ \pi^-} = 4A_{\sigma_{\rm III} \to \sigma\sigma} A_{\sigma \to 2\pi^0} A_{\sigma \to \pi^+\pi^-} \Delta_\sigma(s_{12}) \Delta_\sigma(s_{34}), \tag{97}$$

$$A_{\sigma_{\rm III} \to \sigma 2\pi \to 2\pi^0 \pi^+ \pi^-} = -2A_{\sigma_{\rm III} \to \sigma 2\pi} A_{\sigma \to 2\pi^0} (\Delta_\sigma(s_{12}) + \Delta_\sigma(s_{34})). \tag{98}$$

In this case, k_1 and k_2 are momenta of the two π^0 and s_{12} is their invariant mass squared. The indices 3 and 4 stand for π^+ and π^-, respectively. The amplitude $A_{\sigma \to 2\pi^0}$ is equal to $0.5A_{\sigma \to \pi^+\pi^-}$.

In the case of the decay into $4\pi^0$, we have

$$A_{\sigma_{\rm III} \to 4\pi^0} = A_{\sigma_{\rm III} \to \sigma\sigma \to 4\pi^0} + A_{\sigma_{\rm III} \to \sigma 2\pi \to 4\pi^0}, \tag{99}$$

where

$$A_{\sigma_{\rm III} \to \sigma\sigma \to 4\pi^0} \tag{100}$$

[3)] To obtain an approximate estimate for the glueball contribution, we used the mass of σ_u state before diagonalization [see the term with $\sigma^{r\ 2}_8$ in (52)].

$$= 4A_{\sigma_{\rm III}\to\sigma\sigma}A^2_{\sigma\to 2\pi^0}(\Delta_\sigma(s_{12})\Delta_\sigma(s_{34}) + \Delta_\sigma(s_{13})\Delta_\sigma(s_{24}) + \Delta_\sigma(s_{14})\Delta_\sigma(s_{23})),$$

$$A_{\sigma_{\rm III}\to\sigma 2\pi\to 2\pi^0\pi^+\pi^-} = -2A_{\sigma_{\rm III}\to\sigma 2\pi}A_{\sigma\to 2\pi^0}(\Delta_\sigma(s_{12}) + \Delta_\sigma(s_{13}) + \Delta_\sigma(s_{14}) + \Delta_\sigma(s_{23}) + \Delta_\sigma(s_{24}) + \Delta_\sigma(s_{34})). \quad (101)$$

Let us give numerical estimates for these decay modes. The width with respect to glueball decay into four particles is calculated using the prescription given in [29],

$$\Gamma_{4\pi} = \frac{1}{64(2\pi)^6 r M^2_{\sigma_{\rm III}}}\int\limits_{s^-_{123}}^{s^+_{123}} ds_{123}\int\limits_{s^-_{12}}^{s^+_{12}} ds_{12}\int\limits_{s^-_{34}}^{s^+_{34}} ds_{34}\int\limits_{s^-_{23}}^{s^+_{23}} ds_{23}\int\limits_{-1}^{1}\frac{|A_{\sigma_{\rm III}\to 4\pi}|^2 d\zeta}{\sqrt{\lambda(s_{123},s_{12},M^2_\pi)(1-\zeta^2)}}, \quad (102)$$

where $A_{\sigma_{\rm III}\to 4\pi}$ is the amplitude describing one of the processes discussed above and $M_{\sigma_{\rm III}}$ is the mass of $\sigma_{\rm III}$. The symmetry factor r is determined by the number of identical particles in the final state. The corresponding two-particle invariant masses are defined in (90) except for s_{123}, the invariant mass of three pions,

$$s_{123} = (k_1 + k_2 + k_3)^2. \quad (103)$$

The cosine between the plane spanned by the 3-momenta $\mathbf{k}_1$ and $\mathbf{k}_2$ and the plane spanned by $\mathbf{k}_3$ and $\mathbf{k}_4$ in the rest frame of three mesons ($\mathbf{k}_1 + \mathbf{k}_2 + \mathbf{k}_3 = 0$) is denoted by ζ. The limits of integration are as follows:

$$s^-_{123} = 9M^2_\pi, \quad s^+_{123} = (M_{\sigma_{\rm III}} - M_\pi)^2, \quad (104)$$

$$s^-_{12} = 4M^2_\pi, \quad s^+_{12} = (\sqrt{s_{123}} - M_\pi)^2,$$

$$s^\pm_{34} = 2M^2_\pi + \frac{1}{2s_{123}}\left[(s_{123} + M^2_\pi - s_{12})\times(M^2_{\sigma_{\rm III}} - M^2_\pi - s_{123}) \pm \sqrt{\lambda(s_{123},s_{12},M^2_\pi)\lambda(M^2_{\sigma_{\rm III}},s_{123},M^2_\pi)}\right],$$

$$s^\pm_{23} = 2M^2_\pi + \frac{1}{2s_{12}}\left[s_{12}(s_{123} - M^2_\pi - s_{12}) \pm \sqrt{\lambda(s_{12},M^2_\pi,M^2_\pi)\lambda(s_{123},s_{12},M^2_\pi)}\right].$$

Formula (102) is similar to that given in [31]; however, we used here different kinematical variables. As a result, we find for the decay into 4π that

$$\Gamma_{\sigma_{\rm III}\to 2\pi^+2\pi^-} \approx 2.2\ \text{MeV}, \quad (105)$$

$$\Gamma_{\sigma_{\rm III}\to 2\pi^0\pi^+\pi^-} \approx 1.2\ \text{MeV}, \quad \Gamma_{\sigma_{\rm III}\to 4\pi^0} \approx 0.1\ \text{MeV}$$

if $\sigma_{\rm III} \equiv f_0(1500)$. The total width is

$$\Gamma^{\rm tot}_{\sigma_{\rm III}\to 4\pi} \approx 3.5\ \text{MeV}; \quad (106)$$

in the other case [$\sigma_{\rm III} \equiv f_0(1710)$], we have

$$\Gamma_{\sigma_{\rm III}\to 2\pi^+2\pi^-} \approx 6\ \text{MeV}, \quad (107)$$

$$\Gamma_{\sigma_{\rm III}\to 2\pi^0\pi^+\pi^-} \approx 3.3\ \text{MeV}, \quad \Gamma_{\sigma_{\rm III}\to 4\pi^0} \approx 0.3\ \text{MeV}.$$

The total width is

$$\Gamma^{\rm tot}_{\sigma_{\rm III}\to 4\pi} \approx 10\ \text{MeV}. \quad (108)$$

As one can see, these values are very small.

The other possibility of the state $\sigma_{\rm III}$ to decay into four pions is to produce two intermediate ρ resonances ($\sigma_{\rm III}\to 2\rho\to 4\pi$). In contrast to the decay through scalar resonances, where strong compensations take place, no compensation occurs in the process with ρ resonances, and it turns out that the decay through ρ determines most of the decay width of $\sigma_{\rm III}$.

To calculate the amplitude describing the process $\sigma_{\rm III}\to 2\rho$, we need a piece of the Lagrangian with ρ-meson fields. Although we did not consider vector mesons in the source Lagrangian, an extended version of the NJL model [13] contains the vector and axial-vector fields. Taking the mass term for ρ mesons from [13] and including dilaton fields in it according to the principle of scale invariance, we obtain

$$\frac{M^2_\rho}{2}\left(\frac{\chi}{\chi_c}\right)^2(2\rho^+_\mu\rho^-_\mu + \rho^0_\mu\rho^0_\mu), \quad (109)$$

where $M_\rho = 770$ MeV is the ρ-meson mass. From this, we derive the vertex describing the decay $\sigma_{\rm III}\to\rho\rho$:

$$\frac{M^2_\rho}{\chi_c}b_{\chi'\sigma_{\rm III}}\chi'(2\rho^+_\mu\rho^-_\mu + \rho^0_\mu\rho^0_\mu). \quad (110)$$

The decay of a ρ meson into pions is described by the amplitude

$$g_\rho(p_1 - p_2)^\mu, \quad (111)$$

where $g_\rho = 6.14$ is the ρ-meson decay constant and p_1 and p_2 are the momenta of π^+ and π^-. Finally, we arrive at the following formula for the amplitude of the process $\sigma_{\rm III}\to\rho^0\rho^0\to 2\pi^+2\pi^-$:

$$A_{\sigma_{\rm III}\to\rho^0\rho^0\to 2\pi^+2\pi^-} = \frac{M^2_\rho g^2_\rho b_{\chi'\sigma_{\rm III}}}{\chi_c} \quad (112)$$

Table 3. Partial and total decay widths (in MeV) of the scalar-meson states $f_0(400–1200)$ and $f_0(980)$ and of the glueball for two cases [$\sigma_{\rm III} \equiv f_0(1500)$ and $\sigma_{\rm III} \equiv f_0(1710)$] and experimental values of decay widths of $f_0(1500)$ and $f_0(1710)$ [30]

	$\Gamma_{\pi\pi}$	$\Gamma_{K\bar{K}}$	$\Gamma_{\eta\eta}$	$\Gamma_{\eta\eta'}$	$\Gamma_{4\pi}$	$\Gamma_{\rm tot}$	$\Gamma_{\rm tot}^{\rm exp}$
$f_0(400–1200)$	820	–	–	–	–	820	600–1200
$f_0(980)$	28	–	–	–	–	28	40–100
$f_0(1500)$	14	29	25	10	~ 140	~ 220	112
$f_0(1710)$	8	60	43	30	~ 1000	~ 1100	130

$$\times \Big((s_{13}+s_{24}-s_{14}-s_{23})\Delta_\rho(s_{12})\Delta_\rho(s_{34}) + (s_{13}+s_{24}-s_{12}-s_{34})\Delta_\rho(s_{14})\Delta_\rho(s_{23}) \Big).$$

The function $\Delta_\rho(s)$ has the form

$$\Delta_\rho(s) = (s - M_\rho^2 + iM_\rho\Gamma_\rho)^{-1}, \qquad (113)$$

where $\Gamma_\rho = 150$ MeV is the decay width of the ρ resonance.

The decay into $2\pi^0\pi^+\pi^-$ occurs through a pair of charged ρ resonances: ρ^+ and ρ^-. The amplitude of this process is the same as for the decay with intermediate ρ^0. The decay into $4\pi^0$ cannot go via ρ resonances.

In an extended NJL model [13], there are no vertices describing the decay of a quarkonium into ρ mesons. As a result, only the glueball part determines the decay of $\sigma_{\rm III}$ into four pions through ρ resonances, unlike the case with σ resonances. This leads to a large decay rate through ρ mesons (in contrast to decays through σ).

Let us now give the numerical estimates for the decay into four pions. In the case where $\sigma_{\rm III} \equiv f_0(1500)$, we have

$$\Gamma_{\sigma_{\rm III}\to\rho\rho\to 2\pi^+2\pi^-} \approx 50\ {\rm MeV}, \qquad (114)$$
$$\Gamma_{\sigma_{\rm III}\to\rho\rho\to 2\pi^0\pi^+\pi^-} \approx 90\ {\rm MeV},$$

with the total width being

$$\Gamma^{\rm tot}_{\sigma_{\rm III}\to 4\pi} \approx 140\ {\rm MeV}. \qquad (115)$$

In the other case ($\sigma_{\rm III} \equiv f_0(1710)$), we obtain

$$\Gamma_{\sigma_{\rm III}\to\rho\rho\to 2\pi^+2\pi^-} \approx 350\ {\rm MeV}, \qquad (116)$$
$$\Gamma_{\sigma_{\rm III}\to\rho\rho\to 2\pi^0\pi^+\pi^-} \approx 650\ {\rm MeV},$$

$$\Gamma^{\rm tot}_{\sigma_{\rm III}\to 4\pi} \approx 1\ {\rm GeV}. \qquad (117)$$

We can now estimate the total width of the state $\sigma_{\rm III}$. If $\sigma_{\rm III}$ is identified with $f_0(1500)$, we have

$$\Gamma^{\rm tot}_{\sigma_{\rm III}} \approx 220\ {\rm MeV}, \qquad (118)$$

which is in qualitative agreement with the experimental value of 112 MeV [30], and, in the other case ($\sigma_{\rm III} \equiv f_0(1710)$), we obtain

$$\Gamma^{\rm tot}_{\sigma_{\rm III}} \approx 1.1\ {\rm GeV}, \qquad (119)$$

which is in a glaring contradiction with experimental data. In the last case [$f_0(1710)$], ρ mesons can show up as on-mass-shell decay products at large probability. The decay width is estimated at about 1 GeV. The absence of this decay mode in experimental observations is a reason that $f_0(1710)$ is not a glueball.

Our estimates for the decay widths of the scalar-meson states $\sigma_{\rm I}$, $\sigma_{\rm II}$, and $\sigma_{\rm III}$ are collected in Table 3.

7. CONCLUSION

In the approach presented here, we assume that (with the exception of the dilaton potential and the 't Hooft interaction) scale invariance holds for the effective Lagrangian before and after SBCS in the chiral limit. On the other hand, we take into account effects of scale-invariance breaking that come from three sources: the terms with current quark masses, the dilaton potential reproducing the scale anomaly of QCD, and term $L_{\rm an}$ induced by gluon anomalies [see (3) in the Introduction].

Scale-invariance breaking that is associated with the term $L_{\rm an}$ was not taken into account in our previous paper [32].[4)] This led to a small quarkonium–glueball mixing proportional to current quark masses disappearing in the chiral limit. If the term $\Delta L_{\rm an}$ is taken into account in (28), the quarkonium–glueball mixing becomes much greater and does not disappear in the chiral limit, being proportional to constituent quark masses (quark condensates). This corresponds to the results obtained from QCD in [33]. This contribution to the quarkonium–glueball mixing proves to have a decisive effect on the strong decay widths of scalar mesons.

[4)] Note that there was wrong sign of the term in formula (43) that describes the quarkonium–glueball mixing, which led to incorrect estimates for the decay widths of the scalar glueball.

For the scalar-meson states $f_0(400-1200)$ and $f_0(980)$, we obtain a good agreement with experimental data [30]. Their decay widths are determined by quarkonium parts of decay amplitudes.

Strong decays of the scalar-meson state $\sigma_{\rm III}$ ("glueball") are considered for two different masses: 1500 and 1710 MeV. In the $\pi\pi$ channel, the contribution from quarkonia prevails over that from the glueball and thereby determines the decay rate. In the case of KK, $\eta\eta$, and $\eta\eta'$ channels, there are noticeable compensations among decay amplitudes between the glueball and quarkonium contributions.

A similar situation with compensations takes place in the decay into 4π with intermediate σ mesons. Here, we have a strong compensation among the glueball and quarkonium contributions. But there is the possibility for the state $\sigma_{\rm III}$ to decay through ρ resonances. In this case, no compensation occurs since there is no quarkonium component, and this channel determines a major part of the total decay width of $\sigma_{\rm III}$.

We performed calculations for both candidates for the scalar glueball state, $f_0(1500)$ and $f_0(1710)$, and found that $f_0(1500)$ is rather the glueball. The main decay mode is that into four pions. The decay rate into a pair of kaons is next by order of magnitude and is followed by the $\eta\eta$, $\eta\eta'$, and $\pi\pi$ decay modes.

The total width of the third scalar–isoscalar state is estimated to be about 220 MeV for $M_{\sigma_{\rm III}} = 1500$ MeV and 1.2 GeV for $M_{\sigma_{\rm III}} = 1710$ MeV. The experimental width of $f_0(1500)$ is 112 MeV, and that of $f_0(1710)$ is 130 MeV. Unfortunately, the detailed data on the branching ratios of $f_0(1500)$ and $f_0(1710)$ are controversial and not reliable [30].

Our calculations are rather qualitative. However, they allow us to conclude that $f_0(1500)$ is a scalar glueball state, whereas $f_0(1710)$ is a quarkonium for the following reasons: (i) The total decay width of the glueball in our model fits its experimental value better if $f_0(1500)$ is assumed to be the glueball, rather than $f_0(1710)$. (ii) As follows from our calculations, the main decay mode of the scalar glueball is that into four pions. This is true for the state $f_0(1500)$. A decay of $f_0(1710)$ into four pions, however, was not seen in experiment. (iii) Moreover, a direct decay into a pair of ρ mesons on their mass shell is possible for a scalar glueball with the mass about 1.7 GeV. It has not been observed either. Our conclusion concerning the nature of $f_0(1710)$ as a quarkonium state is in agreement with the conclusion drawn in [12].

We are going to use this approach in our future work for describing both glueballs and ground and radially excited scalar-meson nonets which lie in the energy interval from 0.4 to 1.71 GeV.

ACKNOWLEDGMENTS

We are grateful to Prof. A.A. Andrianov, Prof. D. Ebert, Dr. A.E. Dorokhov, Dr. S.B. Gerasimov, and Dr. N.I. Kochelev for stimulating discussions.

This work was supported by Russian Foundation for Basic Research (grant no. 00-02-17190).

REFERENCES

1. J. Sexton, A. Vaccarino, and D. Weingarten, Phys. Rev. Lett. **75**, 4563 (1995).
2. W. Lee and D. Weingarten, Phys. Rev. D **59**, 094508 (1999).
3. A. Vaccarino and D. Weingarten, hep-lat/9910007.
4. C. Amsler *et al.,* Phys. Lett. B **353**, 425 (1995); C. Amsler and F. Close, Phys. Lett. B **353**, 385 (1995).
5. S. Narison, Nucl. Phys. B **509**, 312 (1998).
6. V. V. Anisovich, D. V. Bugg, and A. V. Sarantsev, Phys. Rev. D **58**, 111503 (1998).
7. A. Palano, Nucl. Phys. B (Proc. Suppl.) **39**, 287 (1995).
8. N. A. Törnqvist and M. Roos, Phys. Rev. Lett. **76**, 1575 (1996).
9. Eef van Beveren and G. Rupp, hep-ph/9806246.
10. L. S. Celenza, B. Huang, H. Wang, and C. M. Shakin, Preprint No. BCCNT:99/111/283, Brooklin Coll. (New York, 1999).
11. L. S. Celenza, Shun-fu Gao, Bo Huangsheng Wang, and C. M. Shakin, Phys. Rev. C **61**, 035201 (2000).
12. M. K. Volkov and V. L. Yudichev, Int. J. Mod. Phys. A **14**, 4621 (1999); Fiz. Élem. Chastits At. Yadra **31**, 576 (2000) [Phys. Part. Nucl. **31**, 282 (2000)]; Yad. Fiz. **63**, 1924 (2000) [Phys. At. Nucl. **63**, 1835 (2000)].
13. M. K. Volkov, Ann. Phys. (N.Y.) **157**, 282 (1984); Fiz. Élem. Chastits At. Yadra **17**, 433 (1986) [Sov. J. Part. Nucl. **17**, 186 (1986)]; D. Ebert and H. Reinhardt, Nucl. Phys. B **271**, 188 (1986); M. K. Volkov, Fiz. Élem. Chastits At. Yadra **24**, 81 (1993) [Phys. Part. Nucl. **24**, 35 (1993)].
14. M. K. Volkov and D. Ebert, Yad. Fiz. **36**, 1265 (1982) [Sov. J. Nucl. Phys. **36**, 736 (1982)]; Z. Phys. C **16**, 205 (1983).
15. M. K. Volkov and C. Weiss, Phys. Rev. D **56**, 221 (1997).
16. M. K. Volkov, Yad. Fiz. **60**, 2094 (1997) [Phys. At. Nucl. **60**, 1920 (1997)].
17. G. Ripka and M. Jaminon, Ann. Phys. (N.Y.) **218**, 51 (1992); M. Jaminon and G. Rapha, Nucl. Phys. A **564**, 551 (1993).
18. J. Cugnon, M. Jaminon, and B. van den Bosche, Nucl. Phys. A **598**, 515 (1996); M. Jaminon and B. van den Bosche, Nucl. Phys. A **619**, 285 (1997).
19. K. Kusaka, M. K. Volkov, and W. Weise, Phys. Lett. B **302**, 145 (1993).

20. A. A. Andrianov, V. A. Andrianov, V. Yu. Novozhilov, and Yu. V. Novozhilov, Pis'ma Zh. Éksp. Teor. Fiz. **43**, 557 (1986) [JETP Lett. **43**, 719 (1986)]; A. A. Andrianov, V. A. Andrianov, D. Ebert, and T. Feldmann, Int. J. Mod. Phys. A **12**, 5589 (1997); A. A. Andrianov and V. A. Andrianov, Z. Phys. C **55**, 435 (1992); A. A. Andrianov, V. A. Andrianov, Yu. V. Novozhilov, and V. Yu. Novozhilov, Phys. Lett. B **186**, 401 (1987).
21. J. Ellis and J. Lánik, Phys. Lett. B **150B**, 289 (1985); Phys. Lett. B **175**, 83 (1986); J. Lánik, Acta Phys. Slov. **35**, 343 (1985); B. A. Campbell, J. Ellis, and K. A. Olive, Nucl. Phys. B **345**, 57 (1990).
22. C. Rosenzweig, J. Schechter, and G. Trahern, Phys. Rev. D **21**, 3388 (1980).
23. M. K. Volkov, Fiz. Élem. Chastits At. Yadra **13**, 1070 (1982) [Sov. J. Part. Nucl. **13**, 446 (1982)].
24. M. K. Volkov, M. Nagy, and V. L. Yudichev, Nuovo Cimento A **112**, 225 (1999).
25. A. E. Dorokhov and N. I. Kochelev, Z. Phys. C **37**, 377 (1988); Yad. Fiz. **52**, 214 (1990) [Sov. J. Nucl. Phys. **52**, 135 (1990)]; Fiz. Élem. Chastits At. Yadra **23**, 1192 (1992) [Sov. J. Part. Nucl. **23**, 522 (1992)].
26. H. Vogl and W. Weise, Prog. Part. Nucl. Phys. **27**, 195 (1991).
27. S. P. Klevansky, Rev. Mod. Phys. **64**, 649 (1992).
28. D. J. Broadhurst *et al.*, Phys. Lett. B **329**, 103 (1994); B. V. Geshkenbein, Yad. Fiz. **58**, 1873 (1995) [Phys. At. Nucl. **58**, 1771 (1995)]; S. Narison, Phys. Lett. B **387**, 162 (1996).
29. E. Byckling and K. Kajantie, *Particle Kinematics* (Wiley, London, 1973).
30. Particle Data Group (C. Caso *et al.*), Eur. Phys. J. C **3**, 1 (1998).
31. R. Kumar, Phys. Rev. **185**, 1865 (1969).
32. D. Ebert, M. Nagy, M. K. Volkov, and V. L. Yudichev, Eur. Phys. J. A **8**, 567 (2000).
33. M. A. Shifman, Phys. Rep. **209**, 341 (1991).

Physics of Atomic Nuclei, Vol. 64, No. 11, 2001, pp. 2020–2026. Translated from Yadernaya Fizika, Vol. 64, No. 11, 2001, pp. 2105–2112.

ELEMENTARY PARTICLES AND FIELDS
Theory

Gluon Cluster Solution in Effective Yang–Mills Theory

O. V. Pavlovskiĭ*

Institute of Theoretical Problems of Microscopic Physics, Moscow State University, Vorob'evy gory, Moscow, 119899 Russia

Received April 5, 2000; in final form, October 30, 2000

Abstract—A finite-energy classical solution in effective Yang–Mills theory specified by a nonstandard Lagrangian is obtained. The effect of vacuum polarization on the formation of gluon clusters is discussed.

1. INTRODUCTION

Investigation of nontrivial solutions to classical field equations has been actively performed since the mid-1970, when stable finite-energy classical solutions having nontrivial topology (monopoles and instantons) were discovered [1–3]. Such solutions, which had the form of clusters—compact lumps of energy whose density vanishes at spatial infinity—were investigated in detail; in particular, important mathematical results concerning the existence and stability of these solutions in various field models were obtained [4] and nontrivial physical effects following from the existence of such solutions were revealed [5, 6].

At the same time, it was found that, in the physical case of $3+1$ spacetime dimensions, scale invariance forbids the existence of such static finite-energy cluster solutions in the matter-field-free non-Abelian theory of classical Yang–Mills fields [7]. In [8], it was shown that not only static but also periodic solutions of the type being discussed do not exist in classical non-Abelian Yang–Mills theory. This gives every reason to state that there is no classical glueball defined as a finite-energy gluon cluster object [9]. In this context, it became clear that the existence of, say, a monopole solution [1, 2] in $3+1$ spacetime dimensions is due to a nontrivial interaction with scalar Higgs fields. Also, unstable spherically symmetric solutions of the cluster type (sphalerons) [10], which determine the height of the potential barrier between two topologically nonequivalent vacua, were found in the theory of classical Yang–Mills fields interacting with classical Higgs fields [10, 11].

In addition, stable topologically nontrivial solutions that possess an electric charge (dions) [12] were investigated in Yang–Mills theory involving Higgs fields. The existence and the stability of such solutions are also due to a nontrivial interaction of non-Abelian fields with scalar Higgs fields.

Nonstatic stable solutions of the cluster type, q spheres, were also considered in the literature [13] (see also [14] and references therein). The existence and the stability of such solutions were due to their charge. Solutions of such types were actively discussed within effective hadron models like the quark bag model [13, 14].

In view of the aforesaid, cluster solutions in the theory of non-Abelian fields may appear only as the result of going beyond pure Yang–Mills theory. This is possible, for example, owing to interaction with matter fields, as is observed in the case of monopoles and dions. In the present study, it will be shown that the inclusion of quantum vacuum-polarization effects in the presence of a classical gluon field can also lead to the formation of such solutions. This is suggested by the study of Schwinger [15], who considered the case of QED. Indeed, he showed that the effect of such polarization phenomena on a classical solution can effectively be taken into account by supplementing the Lagrangian of the original classical theory with additional terms of higher order in fields. He also proved that, in the problem of the singular classical self-energy of the electron, this modification to the Lagrangian plays the role of regularization for this singularity. In the present study, we will attempt to use Schwinger's idea of taking into account vacuum polarization for the case of non-Abelian gauge fields and will show that these phenomena lead to the formation of compact static spherically symmetric objects.

As was indicated above, there are no nontrivial stable finite-energy classical solutions in pure non-Abelian Yang–Mills theory free from matter fields. However, infinite-energy solutions of this type do exist. An analysis of, say, static spherically symmetric

*e-mail: ovp@goa.bog.msu.su

classical solutions in $SU(2)$ Yang–Mills theory of the chromomagnetic type ($A_0 = 0$) reveals that typical solutions occur in a vacuum state at the origin and at infinity and take singular values on a sphere of finite radius. Because of this singularity, such solutions possess an infinite energy [16, 17].

By using the analogy with the aforementioned problem of the electron self-energy, we will show that, in just the same way as in the case of QED, the modified Lagrangian that takes into account polarization phenomena will also regularize the singularity of the self-energy of such an object (here, this singularity is not localized at a point, as was in the case of electrodynamics, but it is distributed over a sphere of finite radius).

In the present study, we rely on the approach proposed and developed in [18–26]. Within this approach, quantum fluctuations and polarization phenomena are taken into account in a gauge-invariant way by supplementing original Yang–Mills theory with additional modifying terms that involve higher covariant derivatives with respect to the field A^a_μ. As a result, there arises an effective field theory, whereas the classical field is treated as a field that is averaged over quantum fluctuations: $A_{\text{eff}} = \langle A_0 \rangle$ [20–22]. Such nonstandard Lagrangians for Yang–Mills fields naturally arose in attempts at constructing the low-energy limit of QCD on the basis of solutions to the Schwinger–Dyson equation [18, 20]. Similar analyses were performed in [25, 26]. Investigations along these lines resulted in deriving effective gauge-invariant Lagrangians that describe the infrared behavior of the asymptotic expressions for strongly connected Green's functions. In the first approximation, these Lagrangians contained terms of the $f^{abc}(F_{\mu\nu})^a(F^\nu{}_\rho)^b(F^{\rho\mu})^c$ and $(D_\rho F_{\mu\nu})^a(D^\rho F^{\mu\nu})^a$ types. Further, some classical solutions for such effective Lagrangians were analyzed in [22]. The hope for describing color-particle confinement was associated with these solutions. Classical solutions in Yang–Mills theories specified by nonstandard Lagrangians were also investigated in [27].

In the present study, we consider the simplest modification to Yang–Mills theory; namely, the standard Lagrangian

$$\mathcal{L} = -\frac{1}{4}(F_{\mu\nu})^a(F^{\mu\nu})^a \qquad (1)$$

is supplemented here with a modifying term that involves higher covariant derivatives and which is equal, apart from a total divergence, to

$$\Delta\mathcal{L} = f^{abc}(F_{\mu\nu})^a(F^\nu{}_\rho)^b(F^{\rho\mu})^c \qquad (2)$$
$$= (D_\rho F_{\mu\nu})^a(D^\rho F^{\mu\nu})^a - (D^\mu F_{\mu\nu})^a(D_\rho F^{\rho\nu})^a,$$

where $(F_{\mu\nu})^a = \partial_\mu A^a_\nu - \partial_\nu A^a_\mu + f^{abc}A^b_\mu A^c_\nu$ is the strength tensor for the Yang–Mills fields A^a_μ of the $SU(N)$ gauge group and f^{abc} are the structure constants of this group. The covariant derivative then has the form $(D_\mu)^{ab} = \delta^{ab}\partial_\mu + f^{abc}A^c_\mu$.

This modification is chosen because it leads to equations containing derivatives to powers not higher than two, which makes it possible to analyze them in greatest detail.

Moreover, the above additional term has a clear physical meaning within the gauge-invariant approach proposed in [28], where Yang–Mills theory is reformulated in terms of bimetric gravity; as a result, it can be demonstrated [29] that this addition to the standard Lagrangian is the cosmological Λ term, which is well known from the general theory of relativity. In [29], it is shown that this additional term arises naturally in regularizing the self-energy of singular solutions in Yang–Mills theory. Such a regularization is necessary in using these solutions as a natural gluon-bag model for fermions. The hadron model constructed on the basis of such a gluon bag was considered in detail elsewhere [17].

Similar Lagrangians appear not only within the aforementioned approaches. For example, modifying terms of this type in the Lagrangian were obtained in [30, 31] by the method of dimensional reduction from the gravitational action functional in spaces of higher dimensions. Analogous investigations were performed in [32, 33]. That similar Lagrangians arise within different approaches gives sufficient grounds to believe that theories specified by such Lagrangians play an important role in physics and require a thorough study.

In the present study, we consider the problem of existence of finite-energy classical solutions in the Yang–Mills theory involving the nonstandard additional term (2) in the Lagrangian. In order to simplify relevant calculations, we analyze the case of the $SU(2)$ gauge group and examine static magnetic-type solutions ($A_0 = 0$) associated with the Wu–Yang substitution [34].

The ensuing exposition is organized as follows. In Section 2, we briefly recall basic formulas from classical Yang–Mills theory specified by nonstandard Lagrangians, introduce the required notation, and derive equations for a subsequent investigation. Section 3 is devoted to proving the existence of finite-energy solutions and to describing the properties of such solutions. In Section 4, we summarize the basic results of the present study and outline prospects for further investigations.

2. COMPENDIUM OF INFORMATION ABOUT CLASSICAL THEORY OF YANG–MILLS FIELDS WITH NONSTANDARD LAGRANGIANS

As was indicated in the Introduction, we will consider the classical theory of non-Abelian gauge fields that is specified by the Lagrangian

$$\mathcal{L}^\varepsilon = -\frac{1}{4}(F_{\mu\nu})^a(F^{\mu\nu})^a - \frac{\varepsilon^2}{6}\epsilon^{abc}(F_{\mu\nu})^a(F^\nu{}_\rho)^b(F^{\rho\mu})^c = -\frac{1}{4}(F_{\mu\nu})^a(F^{\mu\nu})^a - \frac{\varepsilon^2}{6}(F_{\mu\nu})^a(G^{\mu\nu})^a, \tag{3}$$

where ε is the effective coupling constant having dimensions of inverse mass and $(G^{\mu\nu})^a = \epsilon^{abc}(F^\nu{}_\rho)^b(F^{\rho\mu})^c$. By using the variational principle, we arrive at the field equation

$$D^{ab}_\mu(F^{\mu\nu} - \varepsilon^2 G^{\mu\nu})^b = 0. \tag{4}$$

The energy–momentum tensor can be found by the standard formula

$$T^\nu{}_\mu = \partial_\mu A^a_\rho \frac{\partial\mathcal{L}^\varepsilon}{\partial(\partial_\nu A^a_\rho)} - \delta^\nu{}_\mu\mathcal{L}^\varepsilon = -(F^{\nu\rho} - \varepsilon^2 G^{\nu\rho})^a\partial_\mu A^a_\rho - \delta^\nu{}_\mu\mathcal{L}^\varepsilon. \tag{5}$$

We further symmetrize expression (5) by supplementing it with a total divergence of the form

$$\partial_\rho[(F^{\nu\rho} - \varepsilon^2 G^{\nu\rho})^a A^a_\mu] \tag{6}$$

and, with the aid of the field Eq. (4), eventually obtain

$$T^\nu{}_\mu = -(F^{\nu\rho} - \varepsilon G^{\nu\rho})^a(F_{\mu\rho})^a - \delta^\nu{}_\mu\mathcal{L}^\varepsilon. \tag{7}$$

Let us now consider the Wu–Yang spherically symmetric substitution [34]

$$A^a_0 = 0, \qquad A^a_i = \epsilon_{aij}n_j\frac{1 - H(r)}{r}, \tag{8}$$

where $n_i = x_i/r$. As a result, $F_{\mu\nu}$ and $G_{\mu\nu}$ will take the form

$$(F_{0\nu})^a = 0, \quad (F_{ij})^a = \epsilon_{ijk}\left[(\delta_{ak} - n_a n_k)\frac{H'(r)}{r} + n_a n_k\frac{H(r)^2 - 1}{r^2}\right], \tag{9}$$

$$(G_{0\nu})^a = 0, \quad (G_{ij})^a = \epsilon_{ijk}\left[(\delta_{ak} - n_a n_k) \times \frac{H'(r)(H(r)^2 - 1)}{r^3} + n_a n_k\left(\frac{H'(r)}{r}\right)^2\right]. \tag{10}$$

The field Eq. (4) leads to the relation

$$\left(1 - \frac{\varepsilon^2}{r^2}(H(r)^2 - 1)\right)r^2H''(r) = H(r)\Big(H(r)^2 - 1\Big) + \frac{\varepsilon^2}{r^2}\Big((rH'(r))^2H(r) - 2rH'(r)(H(r)^2 - 1)\Big), \tag{11}$$

while the energy of the corresponding field configuration is

$$E^\varepsilon = \int T^{00}d^3x = 4\pi\int\limits_0^\infty\left[\left(1 - \frac{\varepsilon^2}{r^2}(H(r)^2 - 1)\right) \times \big(H'(r)\big)^2 + \frac{(H(r)^2 - 1)^2}{2r^2}\right]dr = \int\limits_0^\infty E(r)dr. \tag{12}$$

3. FINITE-SELF-ENERGY SOLUTION

Let us now proceed to investigate solutions to Eq. (11). We will be interested in solutions characterized by finite values of the energy given by Eq. (12). This imposes specific constraints on the behavior of the function $H(r)$ at the origin of coordinates and at infinity. The presence of the factor

$$\Phi[H](r) = \Big(r^2 - \varepsilon^2(H(r)^2 - 1)\Big) \tag{13}$$

in front of the highest derivative $H''(r)$ is one of the features of Eq. (11) that have far-reaching consequences. Suppose that, at some value of r_s, a solution H_s to Eq. (11) occurs in a region where the factor $\Phi[H_s](r_s)$ is small; it will be shown below that, in this region, $H_s(r)$ will exhibit a singular behavior that is determined by this small factor in front of the highest derivative. It can easily be seen that the region where $\Phi[H] \sim 0$ is specified by a small vicinity of the function

$$\tilde{H}(r) = \pm\sqrt{1 + r^2/\varepsilon^2}. \tag{14}$$

Let us now assume that the solution $H_s(r)$ is near $\tilde{H}(r)$ or $|\tilde{H}(r) - H_s(r)| < \delta \sim 0$. By using conventional procedures, we can determine the asymptotic behavior of $H_s(r)$ in this region. The result is

$$H_s(r) \overset{r\to R\pm 0}{\longrightarrow} \pm\sqrt{1 + R^2/\varepsilon^2} - C\,(R - r)^{2/3} + o(R - r), \tag{15}$$

where C is an arbitrary constant (a positive or a negative one) and R is the point at which the functions $\tilde{H}(r)$ and $H_s(r)$ intersect. Here, we also note that the derivative of this function,

$$H'_s(r) \overset{r\to R\pm 0}{\longrightarrow} \frac{2}{3}C\,(R - r)^{-1/3} + o(1), \tag{16}$$

is singular at the point R. At the same time, the density of the energy of this field configuration is finite at the point R, namely,

$$E(r)|_{r=R} \sim 4\pi \left(\pm \frac{8\varepsilon^2}{9R^2} \sqrt{1 + R^2/\varepsilon^2}\, C^3 + \frac{R^2}{2\varepsilon^4} \right); \tag{17}$$

therefore, the self-energy functional (12) is finite for solutions of the above type. In the following, we will investigate the set of solutions having a singularity of the form in (15).

Equation (11) is a complicated nonlinear second-order differential equation, whose solutions can be investigated only by numerical or approximate methods. In order to perform such investigations, it is necessary to know the asymptotic behavior of solutions to this equation at the origin of coordinates and at infinity. As was noted above, the solutions in question must satisfy the condition requiring that the self-energy integral (12) be finite. Such an investigation yielded the following asymptotic expressions. For $r \to 0$,

$$H(r) \simeq e + a_1 r^2 + a_1^2 \frac{2\varepsilon^2 a_1 + 3e}{10(1 - 2e a_1 \varepsilon^2)} r^4 + o(r^6), \tag{18}$$

where $e = \pm 1$ and a_1 is an arbitrary constant. Equation (11) possesses a discrete symmetry: its form is invariant under the substitution $H(r) \to -H(r)$. In terms of expression (18), this substitution corresponds to the simultaneous sign reversals $a_1 \to -a_1$ and $e \to -e$. The case of $e = -1$ and $a_1 > 0$ is of particular importance for the ensuing analysis. For $r \to \infty$, we similarly have

$$\begin{aligned} H(\rho) \simeq 1 + a_2 \rho + \frac{3}{4} a_2^2 \rho^2 + \frac{11}{20} a_2^3 \rho^3 \qquad (19) \\ + \frac{193 a_2^2 - 240\varepsilon^2}{480} a_2^2 \rho^4 + \frac{329 a_2^2 - 1280\varepsilon^2}{1120} a_2^3 \rho^5 \\ + o(\rho^6), \quad \rho = 1/r, \end{aligned}$$

where a_2 is an arbitrary constant. Below, we will consider solutions whose asymptotic behavior is given by (19) with $a_2 > 0$.

Prior to proceeding to describe directly solutions to Eq. (11) that have the asymptotic behavior (18) on the left and the asymptotic behavior (19) on the right, we would like to note yet another important fact. In Eq. (11), we make the scale transformation

$$r = \frac{\varepsilon}{\varepsilon_N} r_N. \tag{20}$$

As a result, we obtain an equation of the same structure at a different parameter value, $\varepsilon = \varepsilon_N$. Thus, we see that, if a set of solutions $\{H_{\varepsilon_1}(r)\}$ at some value ε_1 is known, a set of solutions for any other value ε_2 can be obtained by means of the substitution in (20), which is equivalent to

$$\{H_{\varepsilon_1}(r)\} \overset{r \to \frac{\varepsilon_1}{\varepsilon_2} r}{\longrightarrow} \left\{ H_{\varepsilon_2}(r) = H_{\varepsilon_1}\left(\frac{\varepsilon_1}{\varepsilon_2} r \right) \right\}. \tag{21}$$

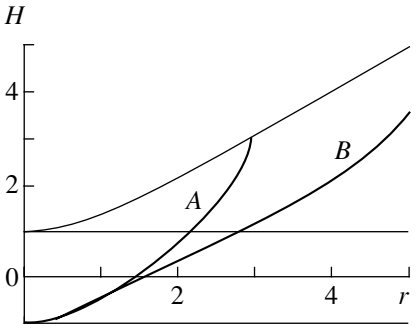

Fig. 1. Effect of the additional term in Lagrangian (3) on the classical solution. Thin lines represent the function $\tilde{H}(r)$ and the vacuum solutions $H = \pm 1$.

In the subsequent analysis, we fix the parameter ε, setting it, for example, to unity, and vary the boundary conditions—that is, a_1 and a_2. In accordance with (20), all quantities that have dimensions of length are measured in ε units.

Let us now proceed to describe directly a numerical investigation of solutions $H(r)$ whose asymptotic behavior is given by (18) and (19). Solutions $H_<(r)$ whose asymptotic behavior at the origin of coordinates is specified by (18) (at $e = -1$ and $a_1 > 0$) will be referred to as internal ones. With increasing r, they grow monotonically at any $a_1 > 0$, reaching the function $\tilde{H}(r)$ (14); at the point $r = R$ of their intersection, the asymptotic behavior of these solutions is given by (15). In Fig. 1, the behavior of solutions to Eq. (11) is illustrated at various values of the parameter ε. The A- and the B-labeled curve represent, respectively, the solution to Eq. (11) at the parameter value of $\varepsilon = 1$ and the solution that takes the asymptotic form (18) near the origin of coordinates and which corresponds to the value of $\varepsilon = 0$ (it should be recalled that, in Fig. 1, r is measured in ε units). The latter case, which was investigated, for example, in [17] is that of a solution to the usual Yang–Mills equation without polarization effects. From the figure, we can see that, as the amplitude of $H(r)$ grows, which entails the growth of the energy density, the role of the additional term in the Lagrangian given by (3) becomes more pronounced. That, at the point $r = R$, the solution at $\varepsilon = 1$ exhibits a critical behavior corresponding to the asymptotic form in (15) is directly related to the presence of this term.

A similar monotonic behavior is characteristic of the external solution $H_>(r)$ whose asymptotic form at

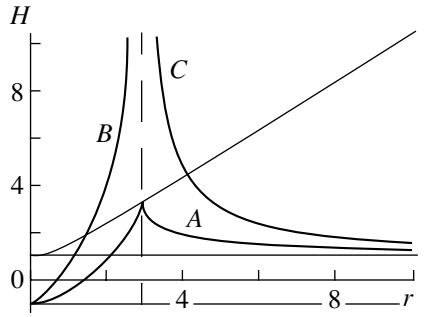

Fig. 2. (A) Finite-energy solution (here, $\varepsilon = 1$ and $a_1 = 0.544$; the radius of the singularity is $r_1 = 2.95$); (B, C) singular solutions at $\varepsilon = 0$. Thin lines represent the function $\tilde{H}(r)$ and the vacuum solutions $H = \pm 1$.

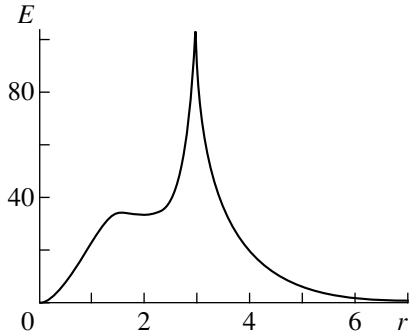

Fig. 3. Energy-density distribution.

infinity is given by (19) (at $a_2 > 0$). The above raises the important question of how the solution $H_<(r)$, for one, can be extended to the right beyond the singular point at $r = R$. This is a challenging problem that requires going beyond the mathematical model formulated here. From the mathematical point of view, we are dealing, in this case, with solutions noncontinuable to the right (left), which are well known in the literature [35]. Since the point at which the solution $H(r)$ is singular is an essential singularity, it cannot be removed by means of coordinate transformations; nor is it possible to solve the problem at hand by popular methods of the theory of functions of complex variables. The arising difficulty is associated with the loss of uniqueness in the boundary-value problem formulated here for Eq. (11). A recourse to an additional physical principle that would make it possible to choose, among the set of solutions to Eq. (11), that which corresponds to the actual physical situation is a possible way out of the situation.

In order to reveal the required physical principle and to recover the uniqueness of the boundary-value problem, we recall that the c-number Yang–Mills field being investigated is essentially the original gluon field averaged over quantum fluctuations; hence, solutions in this effective theory must approximate real objects of the original theory. Such objects must be characterized by continuous physical features like the energy density; therefore, it is natural to require that approximate solutions in the effective theory specified by the Lagrangian in (3) meet the same conditions. As will be shown below, the condition requiring that the energy density be continuous is sufficient for unambiguously fixing the sought solution over the entire space. It is interesting to note that, in the case under consideration, this condition actually results in that there is a critical (limiting) energy-density value $E^{\rm cr}$ above which no solution can exist because of polarization effects.

If we adopt the requirement that the energy density be continuous, the above mathematical difficulties are resolved in a remarkable way, and it proves to be possible to match unambiguously the internal and the external solution. We will say that we have been able to construct a solution over the entire space if we have found two solutions, an internal and an external one, that ensure the same critical energy-density value $E^{\rm cr}$ at a given surface, which is a sphere of radius $r = R$ in our spherically symmetric case; that is,

$$E(r)_<|_{r=R} = E(r)_>|_{r=R} \quad \longrightarrow \quad C_< = C_>. \quad (22)$$

It turns out that, by using the condition in (22), it is possible to obtain, for any ε, a solution $H(r)$ that is tangential to the function $\tilde{H}(r)$ (14) at one point $r = R$, the condition in (22) being sufficient for unambiguously fixing such a solution at fixed ε (that is, for fixing such features of the solution as R, a_1, and a_2). Figure 2 shows a solution obtained numerically at $\varepsilon = 1$ (function A), r in Fig. 2 being measured in ε units; also shown in this figure is a solution at $\varepsilon = 0$, which has a singularity at the point $r = R$ (functions B and C). With the aid of expression (12), one can obtain the graph of the energy density for the field configuration being studied (see Fig. 3). The energy density $E(r)$ in Fig. 3 is measured in $1/\varepsilon$ units. We can see that, in what is concerned with the energy density, the resulting solution is a spherically symmetric shell, with the entire energy of such a configuration being concentrated in the vicinity of this shell.

Let us now address the question of the energy of the field configuration that we obtained and of its dependence on the parameter ε. Considering that the matching condition is invariant under the transformations in (21), which relate solutions at different values of ε, and using expression (12) for the energy of such field configurations, we can obtain

$$E^{\varepsilon} = \frac{1}{\varepsilon} E^{\varepsilon=1}, \quad (23)$$

where $E^{\varepsilon=1}$ is the energy of the field configuration at $\varepsilon = 1$. Relation (23) does not seem surprising since the original Yang–Mills theory was scale-invariant and since its modification specified by Eq. (3) has led to the emergence of the dimensional parameter ε and, hence, to the emergence of a scale for massive solutions. By using numerical methods, one can find that, at $\varepsilon = 1$, such a configuration has the energy of $E^{\varepsilon=1} = 110.75$; in order to assess the energy and the effective radius R of such solutions, it is now necessary to have at our disposal a physical estimate of the parameter ε. According to the estimates presented in [21], $1/\varepsilon \simeq 0.59\pi$ GeV. The object explored in the present study will then have an energy of about 200 GeV (more precisely, $M \simeq 205$ GeV) and the effective radius of $R \simeq 0.3$ fm.

To conclude this section, we note that an analysis similar to that described above was performed for solutions to Eq. (11) that obey the asymptotic condition (18) on the left at $e = -1$ and $a_1 > 0$. Just like the solutions studied above, they grow monotonically at any $a_1 > 0$ with increasing r, reaching the function $\tilde{H}(r)$ (14); at the point R of intersection with it, their asymptotic behavior is given by (15). We were, however, unable to find a solution on the right that has a singularity at the same point R, which satisfies the matching condition (22) at this point, and which has the asymptotic form (19) at infinity (this form corresponds to a finite-energy solution).

4. DISCUSSION AND CONCLUSION

Solutions to the classical equations of Yang–Mills theory have been investigated here with allowance for averaging over quantum fluctuations and for vacuum polarization in the vicinity of such solutions. It was shown in a number of studies [18–20, 25, 26] that, in the first approximation, these phenomena can be taken into account by supplementing the standard Lagrangian of Yang–Mills theory with a modifying term $\Delta\mathcal{L}$ involving higher covariant derivatives. This approach is manifestly invariant under Lorentz and gauge transformations; it is also advantageous in that the resulting theory proves to be local.

In the present study, it has been shown that this approach predicts the existence of massive gluon clusters whose mass is about a few hundred GeV and whose effective radius is about a few tenths of fm. Such objects owe their existence to a modification of the Lagrangian of the theory via supplementing it with a modifying term that is associated with vacuum-polarization phenomena, their mass being directly dependent on the dimensional quantity ε, which appears in the Lagrangian in front of the modifying term. In conventional Yang–Mills theory, such objects would have an infinite mass.

In Section 3, the effect of polarization phenomena on a classical field has been considered for the specific example of Wu–Yang parametrization describing spherically symmetric solutions for the case of the $SU(2)$ color group. This effect is illustrated in Fig. 1. It turns out that, for an internal solution issuing from the vacuum state at the origin of coordinates, the role of polarization effects becomes more pronounced with increasing gluon-field energy density [with increasing function $H(r)$ in Fig. 1]. At some point $r = R$, $E[H_\varepsilon](r)$ eventually reaches a critical energy-density value $E^{\mathrm{cr}} < \infty$ at which H_ε has a singularity. It has been shown that a similar pattern is observed for an external solution as well: starting from the vacuum solution at infinity, the field energy density grows and also reaches a critical value.

It seems that the only physically meaningful way to relate the internal and the external solution is to choose boundary conditions at the origin and at infinity in such way as to ensure coincidence of the critical values E^{cr} that the internal and the external solution take at a sphere of radius R. This corresponds to the intuitively comprehensible requirement that physical features of the system like the energy-density distribution be continuous. On the basis of this requirement, it has proved to be possible to construct such a solution over the entire space (curve A in Fig. 2), to calculate its mass, and to determine its effective radius.

From the point of view of soliton theory, the solution that we have obtained is a quantum soliton, its mass being in inverse proportion to the effective coupling constant ε, which reflects the intensity of polarization phenomena.

In conclusion, we note that similar solutions were recently found in non-Abelian Born–Infeld theory [36]. In the Wu–Yang parametrization, these static spherically symmetric solutions satisfy the following boundary-value problem: the sought solutions issue from the vacuum state $H = -1$ at the origin of coordinates and go over into the topologically nonequivalent vacuum $H = 1$ at infinity. In Born–Infeld theory, such solutions were interpreted as sphalerons characterized by the Chern–Simons topological number of $Q = 1/2$. From the theory of sphalerons, it is well known [10, 11] that unstable classical solutions determine the height of the potential barrier between topologically nonequivalent vacua in non-Abelian field theory. Investigation of such solutions is of paramount importance for a semiclassical analysis of the nontrivial structure of the ground state of this theory. It should also be noted that the solution investigated in the present article is singular on a sphere of finite radius, and this is the point where it differs substantially from the aforementioned solutions in non-Abelian Born–Infeld theory [36]. It is well

known, however, that the theory that is specified by the Lagrangian in Eq. (3) and which has been studied here can be considered as the first approximation in the coupling constant of non-Abelian Born–Infeld theory [37], which in turn has a direct bearing on brane theory [38–40]. In view of this, the solution that we have obtained may be of interest for those theories as well.

It is also worth noting that a solution in the effective theory has been obtained only in the first approximation and that the effect of higher order terms on the possible existence of the gluon clusters considered above has yet to be investigated. Moreover, only the fields of the $SU(2)$ color group have been studied in the present article. Since the $SU(2)$ group is a subgroup of $SU(3)$, the spectrum of solutions for the general $SU(3)$ color group of course contains the solutions investigated here. It is conceivable, however, that there exist solutions for the general group $SU(3)$ that are not reduced to those for $SU(2)$. But the most important question of all is that of physical implications of the possible existence of such objects.

5. ACKNOWLEDGMENTS

This work was supported by the Russian Foundation for Basic Research (project no. 96-15-96674).

REFERENCES

1. G. 't Hooft, Nucl. Phys. B **79**, 276 (1974).
2. A. N. Polyakov, Pis'ma Zh. Éksp. Teor. Fiz. **20**, 430 (1974) [JETP Lett. **20**, 194 (1974)].
3. A. A. Belavin, A. M. Polyakov, A. S. Schwartz, and Yu. S. Tyupkin, Phys. Lett. B **59B**, 85 (1975).
4. G. H. Derrick, J. Math. Phys. **5**, 1252 (1964).
5. V. A. Rubakov, Pis'ma Zh. Éksp. Teor. Fiz. **33**, 658 (1981) [JETP Lett. **33**, 644 (1981)].
6. C. Callan, Phys. Rev. D **25**, 2141 (1982); **26**, 2058 (1982).
7. S. Deser, Phys. Lett. B **64B**, 463 (1976).
8. H. Pagels, Phys. Lett. B **68B**, 466 (1977).
9. S. Coleman, Commun. Math. Phys. **55**, 113 (1977).
10. F. R. Klinkhamer and N. S. Manton, Phys. Rev. D **30**, 2212 (1984).
11. L. G. Yaffe, Phys. Rev. D **40**, 3463 (1989).
12. B. Julia and A. Zee, Phys. Rev. D **11**, 2227 (1975).
13. R. Friedberg, T. D. Lee, and A. Sirlin, Phys. Rev. D **13**, 2739 (1976); Nucl. Phys. B **115**, 1, 36 (1976).
14. T. D. Lee and Y. Pang, Phys. Rep. **221**, 251 (1992).
15. J. Schwinger, Phys. Rev. **82**, 664 (1951).
16. F. A. Lunev, Phys. Lett. B **311**, 273 (1993).
17. F. A. Lunev and O. V. Pavlovskiĭ, Teor. Mat. Fiz. **117**, 163 (1998).
18. A. I. Alekseev, B. A. Arbuzov, and V. A. Baĭkov, Teor. Mat. Fiz. **52**, 187 (1982).
19. A. I. Alekseev and B. A. Arbuzov, Teor. Mat. Fiz. **59**, 80 (1984).
20. A. I. Alekseev and B. A. Arbuzov, Phys. Lett. B **242**, 103 (1990).
21. A. I. Alekseev and B. A. Arbuzov, Teor. Mat. Fiz. **65**, 202 (1985).
22. A. I. Alekseev, A. S. Vshivtsev, and A. V. Tatarintsev, Teor. Mat. Fiz. **77**, 266 (1988).
23. A. I. Alekseev, A. S. Vshivtsev, and V. K. Perez-Fernandez, Izv. Vyssh. Uchebn. Zaved., Fiz. **33** (4), 82 (1990).
24. A. G. Lavkin, Yad. Fiz. **55**, 1146 (1992) [Sov. J. Nucl. Phys. **55**, 644 (1992)].
25. M. Baker and F. Zachariasen, Phys. Lett. B **108B**, 206 (1982).
26. M. Baker, J. S. Ball, and F. Zachariasen, Nucl. Phys. B **209**, 445 (1983).
27. S. Baskal and T. Dereli, J. Phys. G **19**, 477 (1993).
28. F. A. Lunev, Phys. Lett. B **295**, 99 (1992); Teor. Mat. Fiz. **94**, 66 (1993).
29. O. V. Pavlovsky, in *Proceedings of the 10th International Seminar "Quarks'98," Suzdal, 1998* (INR RAS, Moscow, 1999).
30. E. H. Simmons, Phys. Lett. B **226**, 132 (1989).
31. E. H. Simmons, Phys. Lett. B **246**, 471 (1990).
32. K. Arthur, G. M. O'Brien, and D. H. Tchrakian, J. Math. Phys. **38**, 4403 (1997).
33. K. Fujii, Lett. Math. Phys. **12**, 363 (1986).
34. T. T. Wu and C. N. Yang, in *Properties of Matter under Unusual Conditions,* Ed. by H. Mark and S. Fernback (Interscience, New York, 1969).
35. B. P. Demidovich, *Lectures on Stability Theory* (Nauka, Moscow, 1967).
36. D. Gal'tsov and R. Kerner, Phys. Rev. Lett. **84**, 5955 (2000).
37. D. Brecher and M. J. Perry, Nucl. Phys. B **527**, 121 (1998).
38. A. A. Tseytlin, Nucl. Phys. B **501**, 41 (1997).
39. G. Gibbons, Nucl. Phys. B **514**, 603 (1998).
40. J. P. Gauntlett, J. Gomis, and P. K. Townsend, JHEP **01**, 003 (1998).

Translated by A. Isaakyan

Physics of Atomic Nuclei, Vol. 64, No. 11, 2001, pp. 2027–2031. Translated from Yadernaya Fizika, Vol. 64, No. 11, 2001, pp. 2113–2117.

ELEMENTARY PARTICLES AND FIELDS
Theory

Production of P-Wave Charmonium States in Two-Particle Decays of B_c Mesons

V. A. Saleev*

Samara State University, ul. Akademika Pavlova 1, Samara, 443011 Russia

Received July 28, 2000; in final form, January 30, 2001

Abstract—On the basis of the model of hard one-gluon exchange, the two-particle hadronic decays of B_c mesons into S- and P-wave charmonium states, $B_c \to X_{c\bar{c}}\pi(\rho)$, are considered at high momentum transfers and in the nonrelativistic approximation. It is shown that the width with respect to B_c-meson decay into S-wave charmonium states is two times greater than the width with respect to B_c-meson decay into P-wave states and that the yield of J/ψ mesons in the cascade processes of B_c-meson decay via the formation and radiative decay of P-wave charmonium states is approximately 8% of the yield of directly produced J/ψ mesons. © *2001 MAIK "Nauka/Interperiodica".*

1. INTRODUCTION

Information about B_c mesons can be obtained most directly from their decays producing J/ψ mesons in the final state [1]. At present, B_c mesons are sought in two main decay channels,

$$B_c \to J/\psi + l + \nu_l \tag{1}$$

and

$$B_c \to J/\psi + \pi(\rho). \tag{2}$$

The first observation of the B_c meson by the CDF collaboration at Tevatron [2] was based on an analysis of the semilepton decay mode (1). Although the width with respect to the decay process (2) is less than the width with respect to the decay process (1), two-particle hadronic decays may appear to be more promising from the point of view of isolating a signal from B_c-meson production and of determining the B_c-meson mass. First, all final-state particles in decays (2) are detectable hadrons, and this makes it possible to determine precisely the features of the B_c meson. Second, the momentum transfer to the spectator quark is much greater in decays (2) than in decays (1). Allowance for this effect considerably increases the theoretical estimate of the $B_c \to J/\psi\pi(\rho)$ decay width in relation to that calculated within the spectator model, where the decay width is controlled by the overlap integral of the nonrelativistic wave functions of the initial- and final-state quarkonium. In [3] and, more recently, in [4], it was found that, within the model of hard one-gluon exchange, one can expect a nearly fourfold increase in the theoretical estimate of the $B_c \to J/\psi\pi(\rho)$ decay width. In the present study, we consider the following two-particle hadronic decay of the B_c meson into the S- and P-wave states of charmonium ($X_{c\bar{c}}$):

$$B_c \to X_{c\bar{c}} + \pi(\rho). \tag{3}$$

It will be shown that the width with respect to two-particle hadronic B_c-meson decay producing a J/ψ meson in the final state increases further by about 8% upon taking into account the contribution of cascade processes leading to J/ψ-meson production via the radiative decays of P-wave charmonium ($X_{c\bar{c}}$) states generated in B_c-meson decays along with either a π or a ρ meson.

2. HARD-EXCHANGE MODEL

In the nonrelativistic approximation, we disregard the binding energy of quarks and antiquarks in the B_c meson and in the charmonium $X_{c\bar{c}}$. The B_c-meson mass is then equal to the sum of the b- and the c-quark mass, $m_1 = m_b + m_c$; accordingly, the charmonium mass is $m_2 = 2m_c$. Furthermore, the quark and the antiquark in the B_c meson or in $X_{c\bar{c}}$ move at the same 4-velocities,

$$v_1 = \frac{p_1}{m_1} = \frac{p_{\bar{b}}}{m_b} = \frac{p_c}{m_c}, \tag{4}$$

$$v_2 = \frac{p_2}{m_2} = \frac{p_{\bar{c}}}{m_c} = \frac{p'_c}{m_c}. \tag{5}$$

In order to secure this condition for the quark and the antiquark in $X_{c\bar{c}}$ after weak $\bar{b}$ decay [$\bar{b} \to \bar{c}\pi(\rho)$], the 4-momentum transfer k to the spectator c quark must be quite high, with the virtuality being

$$|k^2| = \frac{m_2}{4m_1}((m_1 - m_2)^2 - m_3^2) \gg \Lambda^2_{\mathrm{QCD}}, \tag{6}$$

*e-mail: saleev@ssu.samara.ru

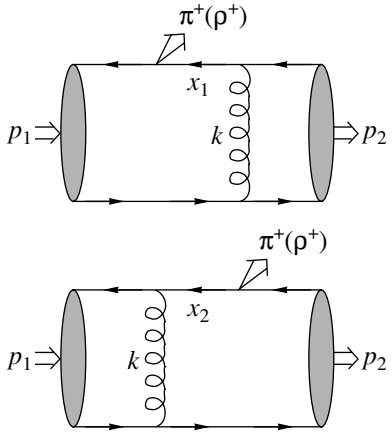

Diagrams describing the decay process $B_c \to X_{c\bar{c}}\pi(\rho)$.

where m_3 stands for the π- or the ρ-meson mass. For various S- and P-wave $X_{c\bar{c}}$ states of mass $m_2 =$ 3.0–3.5 GeV, $|k^2|$ lies in the range 1.0–1.2 GeV^2. So high a value of the momentum transfer violates the condition that ensures the applicability of the spectator model and which requires a significant overlap of the wave functions for the initial- and the final-state heavy meson.

Here, use is made of the general covariant formalism proposed in [5] for calculating the cross sections for the production of S- and P-wave heavy quarkonia and their decay widths at high momentum transfers between the quarks involved. In the leading nonrelativistic approximation in the relative momentum of the quark and the antiquark in quarkonia, the expression for the amplitude of the decay of the $(\bar{b}c)$ bound state into the $(\bar{c}c)$ bound state in this approach has the form

$$A(p_1,p_2) = \int \frac{d\mathbf{q}_1}{(2\pi)^3} \sum_{L_{1z}S_{1z}} \Psi_{L_{1z}S_{1z}}(\mathbf{q}_1) \quad (7)$$
$$\times \langle L_1 L_{1z}; S_1 S_{1z} | J_1 J_{1z}\rangle \int \frac{d\mathbf{q}_2}{(2\pi)^3} \sum_{L_{2z}S_{2z}} \Psi_{L_{2z}S_{2z}}(\mathbf{q}_2)$$
$$\times \langle L_2 L_{2z}; S_2 S_{2z} | J_2 J_{2z}\rangle \mathcal{M}(p_1,p_2,q_1,q_2),$$

where p_1 (p_2), J_1 (J_2), L_1 (L_2), and S_1 (S_2) are, respectively, the 4-momentum, the total angular momentum, the total orbital angular momentum, and the total spin of the initial (final) bound state; $\mathcal{M}(p_1,p_2,q_1,q_2)$ is the quantity that is obtained from the hard amplitude of the decay process (3) by cutting off the fermion lines of the initial and the final meson (see figure); and $\Psi_{L_zS_z}(\mathbf{q})$ stands for the nonrelativistic wave functions of the initial and the final meson.

We now introduce the operators $\Gamma_{SS_z}(p,q)$ that project the state of a free quark–antiquark pair onto the bound state with fixed quantum numbers. To first-order terms in the relative momentum q of the quark and the antiquark, they can be represented as

$$\Gamma_{S_1S_{1z}}(p_1,q_1) \quad (8)$$
$$= \frac{\sqrt{m_1}}{4m_cm_b}\left(\frac{m_c}{m_1}\hat{p}_1 - \hat{q}_1 + m_c\right)\hat{A}_1$$
$$\times \left(\frac{m_b}{m_1}\hat{p}_1 + \hat{q}_1 - m_b\right),$$

where $\hat{A}_1 = \gamma_5$ for $S_1 = 0$ and $\hat{A}_1 = \hat{\varepsilon}(S_{1z})$ for $S_1 =$ 1, and as

$$\Gamma^\dagger_{S_2S_{2z}}(p_2,q_2) \quad (9)$$
$$= \frac{\sqrt{m_2}}{4m_c^2}\left(\frac{m_c}{m_2}\hat{p}_2 + \hat{q}_2 - m_c\right)\hat{A}_2$$
$$\times \left(\frac{m_c}{m_2}\hat{p}_2 - \hat{q}_2 + m_c\right),$$

where $\hat{A}_2 = \gamma_5$ for $S_2 = 0$ and $\hat{A}_2 = \hat{\varepsilon}(S_{2z})$ for $S_2 =$ 1; here, $\varepsilon(S_{1z,2z})$ is the polarization vector of the spin-1 particle. It should be noted that the color factor $\delta^{ij}/\sqrt{3}$, which takes into account the fact that the quark and the antiquark in the meson are in the color-singlet state, is omitted in the above expressions for the projection operators $\Gamma_{SS_z}(p,q)$.

Using the projection operators (8) and (9), we can represent the amplitude $\mathcal{M}(p_1,p_2,q_1,q_2)$ in the form

$$\mathcal{M}(p_1,p_2,q_1,q_2) \quad (10)$$
$$= \mathrm{tr}\left[\Gamma^\dagger_{S_2S_{2z}}(p_2,q_2)\gamma^\beta\Gamma_{S_1S_{1z}}(p_1,q_1)\mathcal{O}_\beta\right],$$

where, in the case of a π meson in the final state, we have

$$\mathcal{O}_\beta = \mathcal{O}^1_\beta + \mathcal{O}^2_\beta, \quad (11)$$

$$\mathcal{O}^1_\beta = \frac{G_\mathrm{F}}{\sqrt{2}}\frac{16}{3}\pi\alpha_s V_{bc} f_\pi a_1 \hat{p}_3 \quad (12)$$
$$\times (1-\gamma_5)\left(\frac{-\hat{x}_1 + m_c}{x_1^2 - m_c^2}\right)\frac{\gamma_\beta}{k^2},$$

$$\mathcal{O}^2_\beta = \frac{G_\mathrm{F}}{\sqrt{2}}\frac{16}{3}\pi\alpha_s V_{bc} f_\pi a_1 \frac{\gamma_\beta}{k^2} \quad (13)$$
$$\times \left(\frac{-\hat{x}_2 + m_b}{x_2^2 - m_b^2}\right)\hat{p}_3(1-\gamma_5).$$

Here,

$$\hat{x}_1 = \frac{m_b}{m_1}\hat{p}_1 + \hat{q}_1 - \hat{p}_3, \quad \hat{x}_2 = \frac{m_c}{m_2}\hat{p}_2 + \hat{q}_2 + \hat{p}_3,$$
$$\hat{k} = \frac{m_c}{m_2}\hat{p}_2 - \frac{m_c}{m_1}\hat{p}_1 - \hat{q}_1 + \hat{q}_2,$$

p_3 is the momentum of the π meson, f_π is its leptonic-decay constant, the factor a_1 takes into account hard gluon corrections to the effective four-fermion vertex [6], α_s is the strong-interaction constant, G_F is the

effective constant of four-fermion interaction, and V_{bc} is an element of the Kobayashi–Maskawa matrix. Since q_1/m_1 and q_2/m_2 are small, we can expand $\mathcal{M}(p_1,p_2,q_1,q_2)$ in a Taylor series near the point $q_1 = q_2 = 0$,

$$\mathcal{M}(p_1,p_2,q_1,q_2) = \mathcal{M}(p_1,p_2,0,0) + q_{1\alpha}\frac{\partial\mathcal{M}}{\partial q_{1\alpha}}\bigg|_{q_{1,2}=0} + q_{2\alpha}\frac{\partial\mathcal{M}}{\partial q_{2\alpha}}\bigg|_{q_{1,2}=0} + \frac{1}{2}q_{1\alpha}q_{1\beta}\frac{\partial^2\mathcal{M}}{\partial q_{1\alpha}\partial q_{2\beta}}\bigg|_{q_{1,2}=0} + \dots . \quad (14)$$

Here, each term corresponds to the transition $B_c \to X_{c\bar{c}}$ featuring fixed quantum numbers of the bound states $(\bar{b}c)$ and $(\bar{c}c)$—namely, $L_1 = 0$ and $L_2 = 0$ for the first term, $L_1 = 1$ and $L_2 = 0$ for the second term, $L_1 = 0$ and $L_2 = 1$ for the third term, and so on. For the S- and P-wave states of the initial and the final quarkonium, the amplitude $\mathcal{A}(p_1,p_2)$ depends, apart from $\mathbf{q}^2$ terms, on the nonrelativistic radial wave function $R_s(0)$ for the B_c meson and on the derivative $R'_p(0)$ of the charmonium radial wave function at the coordinate origin as

$$\int \frac{d\mathbf{q}}{(2\pi)^3}\Psi_{00}(\mathbf{q}) = \frac{R_s(0)}{\sqrt{4\pi}}, \quad (15)$$

$$\int \frac{d\mathbf{q}}{(2\pi)^3}\Psi_{1L_z}(\mathbf{q})q_\alpha = -i\sqrt{\frac{3}{4\pi}}R'_p(0)\varepsilon_\alpha(p,L_z), \quad (16)$$

where $\varepsilon_\alpha(p,L_z)$ is the polarization 4-vector of the spin-1 particle. In the case of charmonium produced in the $^1P_1$ state, we have

$$\sum_{L_{2z}} \varepsilon^\alpha(p_2,L_{2z})\langle 1L_{2z},00|1J_{2z}\rangle = \varepsilon^\alpha(p_2,J_{2z}). \quad (17)$$

In this case, summation over charmonium polarizations yields

$$\sum_{J_{2z}=-1}^{1} \varepsilon^\alpha(p_2,J_{2z})\varepsilon^\beta(p_2,J_{2z}) = \mathcal{P}^{\alpha\beta}(p_2), \quad (18)$$

where

$$\mathcal{P}^{\alpha\beta}(p_2) = -g^{\alpha\beta} + \frac{p_2^\alpha p_2^\beta}{m_2^2}$$

and $g^{\alpha\beta}$ means the standard metric tensor $[\mathrm{diag}(g^{\alpha\beta}) = (1,-1,-1,-1)]$. In the case where the $^3P_J(J = 0,1,2)$ state is produced, we arrive at

$$\sum_{S_{2z},L_{2z}} \varepsilon^\alpha(p_2,L_{2z})\langle 1L_{2z},1S_{2z}|J_2,J_{2z}\rangle\varepsilon^\beta(p_2,S_{2z}) = \begin{cases} \frac{1}{\sqrt{3}}(g^{\alpha\beta} - \frac{p_2^\alpha p_2^\beta}{m_2^2}) \text{ for } J_2 = 0 \\ \frac{i}{\sqrt{2}m_2}\varepsilon^{\alpha\beta\mu\nu}p_{2\mu}\varepsilon_\nu(p_2,J_{2z}) \text{ for } J_2 = 1 \\ \varepsilon^{\alpha\beta}(p_2,J_{2z}) \text{ for } J_2 = 2, \end{cases} \quad (19)$$

where $\varepsilon^{\alpha\beta\mu\nu}$ is a completely antisymmetric rank-4 tensor and $\varepsilon^{\alpha\beta}(p_2,J_{2z})$ is the polarization tensor for the spin-2 particle. The sum over polarizations for the $^3P_2$ state is given by [7]

$$\sum_{J_{2z}=-2}^{2} \varepsilon_{\alpha\beta}(p_2,J_{2z})\varepsilon^*_{\mu\nu}(p_2,J_{2z}) = \frac{1}{2}\big(\mathcal{P}_{\alpha\mu}(p_2)\mathcal{P}_{\beta\nu}(p_2) + \mathcal{P}_{\alpha\nu}(p_2)\mathcal{P}_{\beta\mu}(p_2)\big) - \frac{1}{3}\mathcal{P}_{\alpha\beta}(p_2)\mathcal{P}_{\mu\nu}(p_2). \quad (20)$$

From the above expressions that describe the decay process (3) with a π meson in the final state, we can obtain the analogous expressions for the decay process with a ρ meson in the final state by making the substitution $f_\pi\hat{p}_3 \to m_\rho f_\rho\hat{\varepsilon}_3$ in the amplitude in (10), where ε_3^μ is the ρ-meson polarization 4-vector.

3. RESULTS OF THE CALCULATION

Without discussing the details of rather standard calculations, we present below our results for the widths with respect to decays of a pseudoscalar meson B_c into final states involving various S- and P-wave states of the charmonium $X_{c\bar{c}}$ and a π or a ρ meson. The results have the simplest form for the decay $B_c \to X_{c\bar{c}}\pi$. Since $m_\pi \ll m_c, m_b$, the π-meson mass can be disregarded. Owing to this, we can obtain simple analytic formulas for the decay widths. The results are

$$\Gamma(B_c \to J/\psi\pi) = \frac{128}{9\pi}F\frac{|R_2(0)|^2}{m_2^3}\frac{(1+x)^3}{(1-x)^5}, \quad (21)$$

$$\Gamma(B_c \to \eta_c\pi) = \frac{32}{9\pi}F\frac{|R_2(0)|^2}{m_2^3}\frac{(1+x)^3}{(1-x)^5} \times (x^2-2x+3)^2, \quad (22)$$

$$\Gamma(B_c \to h_c\pi) = \frac{128}{3\pi}F\frac{|R'_2(0)|^2}{m_2^5}\frac{(1+x)^3}{(1-x)^7} \times (x^2-x+2)^2, \quad (23)$$

$$\Gamma(B_c \to \chi_{c0}\pi) = \frac{128}{9\pi}F\frac{|R'_2(0)|^2}{m_2^5}\frac{(1+x)^3}{(1-x)^7} \times (3x^3-12x^2+14x-7)^2, \quad (24)$$

$$\Gamma(B_c \to \chi_{c1}\pi) = \frac{256}{3\pi}F\frac{|R'_2(0)|^2}{m_2^5}\frac{(1+x)^3}{(1-x)^5} \quad (25)$$

Ratios of the widths of B_c meson with respect to decays into the P-wave states of charmonium $\Gamma(B_c \to X_{c\bar{c}}\pi(\rho))$ to the decay width $\Gamma(B_c \to J/\psi\pi(\rho))$

$X_{c\bar{c}}$	$^{2S+1}X_J$	$\frac{\Gamma(B_c \to X_{c\bar{c}}\pi)}{\Gamma(B_c \to J/\psi\pi)}$	$\frac{\Gamma(B_c \to X_{c\bar{c}}\rho)}{\Gamma(B_c \to X_{c\bar{c}}\pi)}$
J/ψ	$^3S_1$	1.00	4.0
η_c	$^1S_0$	1.17	3.2
h_c	$^1P_1$	0.50	3.7
χ_{c0}	$^3P_0$	0.29	3.6
χ_{c1}	$^3P_1$	0.10	5.6
χ_{c2}	$^3P_2$	0.28	4.3

$$\times (x^2 - x - 1)^2,$$

$$\Gamma(B_c \to \chi_{c2}\pi) = \frac{256}{9\pi} F \frac{|R_2'(0)|^2}{m_2^5} \frac{(1+x)^5}{(1-x)^7}, \quad (26)$$

where

$$x = \frac{m_2}{m_1} \text{ and } F = \alpha_s^2 G_F^2 V_{bc}^2 f_\pi^2 |R_1(0)|^2 a_1^2;$$

$R_1(0)$ and $R_2(0)$ are the nonrelativistic radial wave functions for, respectively, the B_c meson and the S-wave charmonium $X_{c\bar{c}}$ at the origin; and $R_2'(0)$ is the derivative of the radial wave function for the P-wave charmonium $X_{c\bar{c}}$ at the origin. The present numerical calculations were performed with the following set of parameter values: $G_F = 1.166 \times 10^{-5}$ GeV^{-2}, $\alpha_s = 0.33$, $V_{bc} = 0.04$, $f_\pi = 0.13$ GeV, $m_\pi = 0.14$ GeV, $f_\rho = 0.22$ GeV, $m_\rho = 0.77$ GeV, $m_{B_c} = 6.3$ GeV, $m_\psi = 3.1$ GeV, $m_{\eta_c} = 2.98$ GeV, $m_{h_c} = 3.5$ GeV, $m_{\chi_{c0}} = 3.4$ GeV, $m_{\chi_{c1}} = 3.5$ GeV, $m_{\chi_{c2}} = 3.55$ GeV, $|R_{s1}(0)|^2 = 1.27$ GeV^3, $|R_{s2}(0)|^2 = 0.94$ GeV^3, and $|R_{p2}'(0)|^2 = 0.08$ GeV^5.

The results obtained here for the widths of the B_c meson with respect to decays into J/ψ and η_c agree with those obtained in [3, 4]. For example, the $B_c \to J/\psi\pi$ decay width calculated in the present study is

$$\Gamma(B_c \to J/\psi + \pi) = 7.5 \times 10^{-6} a_1^2 \text{ eV}. \quad (27)$$

The widths of the B_c meson with respect to decays into other states of the charmonium $X_{c\bar{c}}$ can be expressed in terms of (27) by using the results from the table.

It is interesting to note that, in the case where a π (ρ) meson is produced in the final state, the total width of the B_c meson with respect to decays into ^3P_J states is about 30% (40%) of the total width of the B_c meson with respect to decays into the S-wave states of J/ψ and η_c. So large a contribution of P-wave charmonium states to the width with respect to the two-particle hadronic decay of the B_c meson leads to a noticeable enlargement in the width of the B_c meson with respect to decay into J/ψ through the cascade decays of P-wave charmonia, $\chi_{c0,c1,c2} \to J/\psi\gamma$. The branching ratios for the radiative decays of P-wave charmonia into J/ψ are well known: $\mathrm{Br}(\chi_{c0} \to J/\psi + \gamma) = 0.007$, $\mathrm{Br}(\chi_{c1} \to J/\psi + \gamma) = 0.27$, and $\mathrm{Br}(\chi_{c2} \to J/\psi + \gamma) = 0.14$ [8]. Using the results obtained here (see table), we arrive at

$$\frac{\Gamma(B_c \to \chi_{c0,c1,c2}\pi \to J/\psi\gamma)}{\Gamma(B_c \to J/\psi\pi)} = 0.068, \quad (28)$$

$$\frac{\Gamma(B_c \to \chi_{c0,c1,c2}\rho \to J/\psi\gamma)}{\Gamma(B_c \to J/\psi\rho)} = 0.082. \quad (29)$$

Summing the decay widths for the cases of a π and a ρ meson in the final state, we find that, in the two-particle hadronic decays of B_c mesons, J/ψ particles are produced in the cascade processes through the decays of P-wave states approximately 12.7 times more rarely than in the direct process $B_c \to J/\psi\pi(\rho)$. It should be noted that, in the semileptonic decays of B_c mesons with J/ψ in the final state, the contribution of the cascade mechanism of J/ψ production through radiative decays of P-wave charmonia is about 1/20 of the contribution of the direct-production mechanism [9].

The estimation of the $B_c \to J/\psi\pi(\rho)$ decay width within potential models [10] yields

$$\mathrm{Br}(B_c \to J/\psi\pi) + \mathrm{Br}(B_c \to J/\psi\rho) = 0.8\%. \quad (30)$$

Within the hard-exchange model considered here, we obtain

$$\mathrm{Br}(B_c \to J/\psi\pi) + \mathrm{Br}(B_c \to J/\psi\rho) = 3.0\% \quad (31)$$

for the direct decays at $a_1 = 1.1$ and

$$\mathrm{Br}(B_c \to J/\psi\pi\gamma) + \mathrm{Br}(B_c \to J/\psi\rho\gamma) = 0.24\% \quad (32)$$

for the cascade decays of B_c into J/ψ via the production of $\chi_{c0,c1,c2}$.

4. CONCLUSION

It has been shown that the width with respect to the two-particle hadronic decay of the B_c meson into J/ψ accompanied by either a π or a ρ meson is nearly four times greater in the hard-gluon-exchange formalism than in the spectator model. Allowance for the contribution from the cascade processes of B_c decays through the production of P-wave charmonium states that is followed by their radiative decay into $J/\psi + \gamma$ leads to a further increase in the calculated yield of J/ψ from the decays under consideration by about 8%. This effect is modest, but it increases the probability of observing the B_c meson in the experiments performed at the FNAL and LEP accelerators.

ACKNOWLEDGMENTS

I am grateful to V.V. Kiselev and A.K. Likhoded for interest in this study and enlightening discussions on B_c-meson physics.

This work was supported in part by the program Universities of Russia—Fundamental Research (project no. 02.01.03) and by the Ministry for Higher Education of the Russian Federation (project no. 98-0-6.2-53).

REFERENCES

1. S. S. Gershteĭn *et al.*, Usp. Fiz. Nauk **165**, 3 (1995) [Phys. Usp. **38**, 1 (1995)]; hep-ph/9803433.
2. CDF Collab. (F. Abe *et al.*), hep-ex/9805034.
3. V. V. Kiselev, Phys. Lett. B **372**, 326 (1996); hep-ph/9605451.
4. O. N. Pakhomova and V. A. Saleev, hep-ph/9911313; Yad. Fiz. **63**, 2091 (2000) [Phys. At. Nucl. **63**, 1999 (2000)].
5. B. Guberina *et al.,* Nucl. Phys. B **174**, 317 (1980).
6. A. J. Buras, Nucl. Phys. B **434**, 606 (1995).
7. L. Bergström, Phys. Rev. D **43**, 2157 (1991).
8. Particle Data Group (R. M. Barnett *et al.*), Phys. Rev. D **54**, 1 (1996).
9. D. Scora and N. Isgur, CEBAF-TH-94-14 (1994).
10. C.-H. Chang and Y.-Q. Chen, Phys. Rev. D **49**, 3399 (1994).

Translated by O. Chernavskaya

Physics of Atomic Nuclei, Vol. 64, No. 11, 2001, pp. 2032–2036. Translated from Yadernaya Fizika, Vol. 64, No. 11, 2001, pp. 2118–2123.

ELEMENTARY PARTICLES AND FIELDS
Theory

Relativistically Invariant Method for Constructing the One- and the Two-Parton Density Matrix

A. V. Shchelkachev

Institute for High Energy Physics, Protvino, Moscow oblast, 142284 Russia

Received February 28, 2000; in final form, October 31, 2000

Abstract—By representing the hadron as a system consisting of one or two partons and a multiparton core, which in turn is treated as a parton of variable mass, a relativistically invariant density matrix for this system is constructed by performing integration with respect to this mass. The proposed approach makes it possible to establish simple relations between the density-matrix elements and to validate or interpret more clearly assumptions adopted by various authors in parton models. © *2001 MAIK "Nauka/Interperiodica".*

1. INTRODUCTION

A method is described in this article for dealing with relativistic quark-parton models of the hadron that are proposed for analyzing deep-inelastic scattering.

The hadron is treated here as a system consisting of one or two partons and a core having a variable mass and containing the remaining partons.

As was mentioned in [1], where the reader can find introductory information about the method developed here, the density matrix that is nondiagonal in discrete spin indices and in continuous momentum variables is generally required for describing the structure of hadrons. Conventional distribution functions are diagonal elements of this matrix.

We begin constructing the hadron wave function with the aid of expressions from [2]. Owing to relativistic invariance, the expressions for density-matrix elements contain a comparatively small number of unknown functions depending, in the one-parton case, on one variable—the invariant fireball mass, which in turn is a function of two usual parton variables, x and k.

These functions can be sought on the basis of theoretical considerations by proceeding from QCD or by constructing quasipotentials. In the present study, however, we do not introduce the interaction of partons; instead, we consider the possibility of determining the required functions from experimental data and later use them to describe other experiments. By way of example, it is shown in Section 2 that the density matrix can be determined from experiments studying the deep-inelastic scattering of electrons or muons on longitudinally polarized protons. In Section 3, it is demonstrated that one can make predictions for scattering on a proton whose spin is transversely oriented in the rest frame.

In Section 4, it is proven that the expressions obtained in Section 2 for partons of half-integer spin can be applied, nearly without modifications, to the case where the parton spin is equal to unity, both for zero-mass gluons and for massive vector diquarks. The description of scalar diquarks is trivial. The expressions for the three-particle system of two partons and a fireball are presented further in that section. The end of the section is devoted to deriving a relation between the usual structure functions $F_{1,2}(x)$ and $g_{1,2}(x)$ and the elements of the one-particle density matrix introduced in Section 2.

The basic results of this study are briefly summarized in the Conclusion.

2. DENSITY MATRIX FOR FREE QUARKS

In this section, we construct the density matrix for the parton with a half-integer spin in the proton. We assume that all partons are free and that all gluons and quarks but one that is singled out are contained in a fireball of mass W that can vary in a certain interval. Integration with respect to W is performed over all possible values.

First, we write basic kinematical relations.

We consider the quark in a proton of 4-momentum $(P_0, 0, 0, P)$, where $P_0 = \sqrt{M^2 + P^2}$, M being the proton mass, and introduce the variables x and $\mathbf{k}_T$ to describe the quark 4-momentum $(q_{(P)0}, \mathbf{k}_T, q_{(P)L})$, where $q_{(P)0} = \sqrt{\mu^2 + \mathbf{k}_T^2 + q_{(P)L}^2}$, with μ being the quark mass; here, the subscript L labels the longitudinal component, and the subscript P indicates that the corresponding quantity is considered in the reference frame where the proton has the momentum P. We also denote by $x = (q_{(P)0} + q_{(P)L})/(P_0 + P)$ the usual light-front variable.

Constraints on the mass W and on $k^2 \equiv k_T^2$ are obtained from the energy-conservation law in the proton rest frame,

$$\sqrt{\mu^2 + k^2 + q_{(R)L}^2} + \sqrt{W^2 + k^2 + q_{(R)L}^2} = M. \quad (1)$$

All components of the quark momentum in the rest frame (it is denoted by the symbol R) are determined from the usual Lorentz transformations

$$q_{(R)0} = (q_{(P)0} - \beta q_{(P)L})/\sqrt{1-\beta^2},$$
$$q_{(R)L} = (-\beta q_{(P)0} + q_{(P)L})/\sqrt{1-\beta^2},$$

where $\beta = P/P_0$. From (1), we can easily obtain $0 \le W \le (M-\mu)$ and

$$0 \le k^2 \le \left(\frac{M^2-\mu^2}{2M}\right)^2. \quad (2)$$

According to [2], the wave function for a particle having a mass M and involving a quark of mass μ and helicity λ_1 and a fireball of fixed mass W and helicity λ_2 has the form

$$|\mathbf{P}=0\ \Sigma[MJ]\mu\lambda_1 W\lambda_2\rangle = N_J \int d^2\omega \bar{D}^J_{\Sigma\lambda}(\phi,\theta,0) \times |\mathbf{P}=0;\phi,\theta,M,\mu\lambda_1,W\lambda_2\rangle, \quad (3)$$
$$\lambda = \lambda_1 - \lambda_2,\ \ N_J = \sqrt{(2J+1)/4\pi},$$
$$d^2\omega = \sin\theta d\theta d\phi,$$

where J is the total angular momentum; Σ is its projection onto a given axis (we choose the z axis); and $\bar{D}^j_{m_1m_2}(\alpha,\beta,\gamma)$ are usual rotation-matrix elements determined by the Euler angles α, β, and γ.

The functions $|\mathbf{P}=0;\phi,\theta,M,\mu\lambda_1,W\lambda_2\rangle$ describe that state of two particles, a quark and a fireball, in the reference frame comoving with their center of mass (hadron) in which the first particle of helicity λ_1 moves in the direction determined by the polar angles ϕ and θ, while the second particle of helicity λ_2 moves in the opposite direction. The momenta of the two particles are equal in magnitude:

$$q_{(R)}^2 \equiv k^2 + q_{(R)L}^2 = \frac{1}{4M^2}(M^4 + W^4 + \mu^4 - 2M^2W^2 - 2M^2\mu^2 - 2W^2\mu^2). \quad (4)$$

In order to obtain the hadron wave function in the required reference frame (its velocity with respect to the hadron rest frame along the z axis is equal to V), it is necessary to perform the Lorentz transformation $\hat{L}_z(V)$ and, if required, a rotation $\hat{R}(\Phi,\Theta,0)$ in (3). The mass W is still fixed, the angular momentum J transforms into the spin S, and its projection Σ transforms into the helicity Λ:

$$|\mathbf{P}\Lambda[MS]\mu\lambda_1 W\lambda_2\rangle = \hat{R}(\Phi,\Theta,0)\hat{L}_z(V)N_S \times \int d^2\omega \bar{D}^S_{\Lambda\lambda}(\phi,\theta,0)|\mathbf{P}=0;\phi,\theta,M,\mu\lambda_1,W\lambda_2\rangle. \quad (5)$$

The operators $\hat{R}$ and $\hat{L}$ on the right-hand side of Eq. (5) act according to the usual rules on the single-particle states $|q_{(R)},\phi,\theta,\lambda_1\rangle$ and $|-q_{(R)},\phi,\theta,\lambda_2\rangle$. Upon the transformation, the particle wave functions must be expanded in states of specific helicities in the new reference frame. The corresponding expressions from [3] will be quoted in the next section. By performing integration over all possible values of W and summation over all allowed values of λ_2 in (5), we find that the general expression that describes the quark state in the hadron has the form

$$|\mathbf{P}\Lambda[MS]\mu\lambda_1\rangle = \sum_{\lambda_2}\int dW g_{\lambda_2}(W)|\mathbf{P}\Lambda[MS]\mu\lambda_1 W\lambda_2\rangle. \quad (6)$$

If the quark and the fireball do not interact, we can assume that the weight function g depends only on the total angular momentum of the fireball and not on its projection onto the direction of motion. In the case of noninteracting particles, the density matrix, which is diagonal in W, can be represented as

$$\hat{\rho}_{\lambda_1\lambda_1'}(\mathbf{P},\Lambda,M,S) = \int dW \sum_{\lambda_2\lambda_2'} \rho^2{}_{\lambda_2\lambda_2'}(W) \times |\mathbf{P}\Lambda[MS]\mu\lambda_1 W\lambda_2\rangle\langle\mathbf{P}\Lambda[MS]\mu\lambda_1' W\lambda_2'|. \quad (7)$$

The elements of the density matrix (or conventional distribution functions, which are diagonal elements of this matrix) are obtained upon going over from the integration variables W, θ, and ϕ to the integration variables x, k^2, and ϕ. Usually, the matrix elements are assumed to be independent of ϕ, in which case it is possible to perform integration with respect to ϕ explicitly from the outset and, thereupon, to go over from integration with respect to W and θ to integration with respect to k^2 and x. We can determine the weight function $g_\lambda(W)$ in (6) and the weight function $\rho^2_{\lambda\lambda'}(W)$ in (7) (in just the same way as distribution functions in the usual parton models) from experimental data or calculate them theoretically under some additional assumptions. In doing this, we can avoid calculating the cumbersome determinants $D(W,\theta)/D(k^2,x)$. Since it follows from (4) that, at fixed W, the absolute value of the particle momentum in the hadron rest frame $q_{(R)}$ is also fixed, we can first go over from integration with respect to $\cos\theta = \pm\sqrt{q_{(R)}^2 - k^2}/q_{(R)}$, where a plus sign is taken for $0 \le \theta \le \pi/2$ and a minus sign is taken for $\pi/2 \le \theta \le \pi$, to integration with respect to k^2. We obtain

$$d(\cos\theta)/d(k^2) = 1/(2q_{(R)L}q_{(R)}).$$

Changing the order of integration with respect to W and k^2 and using the relation

$$W^2 = M^2 + \mu^2 - M^2x - (k^2+\mu^2)/x, \quad (8)$$

we can easily go over from integration with respect to W to integration with respect to x.

In this calculation, we use the relations

$$q_{(R)L} = \frac{1}{2}xM - \frac{k^2+\mu^2}{2xM}, \tag{9}$$

$$q^2_{(R)} = \frac{1}{4}\left\{x^2M^2 + \frac{(k^2+\mu^2)^2}{x^2M^2} + 2k^2 - 2\mu^2\right\}, \tag{10}$$

$$q_{(R)0} = \frac{1}{2}xM + \frac{k^2+\mu^2}{2xM}. \tag{11}$$

In expressions (3) and (5)–(7), we make the following substitution in the functions $\bar{D}^S_{\Lambda\lambda_1}(\cos\theta,\phi)$:

$$\cos\theta = q_{(R)L}/q_{(R)}.$$

If $\mu \neq 0$, then

$$\mu^2/M^2 \leq x \leq 1,$$

while k^2 varies within the interval

$$0 \leq k^2 \leq M^2(1-x)(x-\mu^2/M^2).$$

For the other order of integration, we have

$$0 \leq k^2 \leq \left(\frac{M^2-\mu^2}{2M}\right)^2, \tag{12}$$

$$\frac{M^2+\mu^2}{2M^2} - \sqrt{\left(\frac{M^2-\mu^2}{2M^2}\right)^2 - \frac{k^2}{M^2}} \tag{13}$$

$$\leq x \leq \frac{M^2+\mu^2}{2M^2} + \sqrt{\left(\frac{M^2-\mu^2}{2M^2}\right)^2 - \frac{k^2}{M^2}}.$$

For half-integer values of the hadron and the parton (quark) spin, the spin of the fireball can be equal only to zero or unity. Therefore, only two functions of W that correspond to these values of spin appear in (6) and (7). There are well-known expressions for the functions $\bar{D}^S_{\Lambda\lambda_1}(\cos\theta,\phi)$ in terms of $\exp(i\Lambda\phi)$ and the functions $d^S_{\Lambda\lambda}$ depending only on θ. If one quark-parton is singled out, two of these functions are equal to $\cos(\theta/2)$, while the other two are equal to $\pm\sin(\theta/2)$.

3. DESCRIPTION OF EXPERIMENTAL DISTRIBUTION FUNCTIONS

In order to compare, at least at a qualitative level, the predictions of the proposed model for the nondiagonal free-parton density matrix with experimental distribution functions, it is necessary to average diagonal density-matrix elements by performing integration with respect to k^2. For a nonzero quark mass μ, the resulting expressions are rather cumbersome. To a considerable extent, this is because the functions describing a quark state of specific helicity in the hadron rest frame do not correspond to states of conserved helicities in the reference frame where the proton momentum is equal to P. Therefore, the functions used in the above formulas to describe the states of free quarks must be expressed in terms of linear combinations of the functions corresponding to conserved helicities in the P frame. We can easily do this by introducing, for each quark state, the Lorentz 4-vector

$$s = \left\{\frac{(\mathbf{q}\cdot\boldsymbol{\xi})}{\mu}, \boldsymbol{\xi} + \frac{(\mathbf{q}\cdot\boldsymbol{\xi})\mathbf{q}}{\mu(\mu+q_0)}\right\},$$

where $\boldsymbol{\xi}$ corresponds to the direction of the quark spin in its rest frame [4]. The quark states of specific helicity in the hadron rest frame or in the P frame will then correspond to the vectors

$$s_{(f)} = \pm\left\{\frac{q_{(f)}}{\mu}, \frac{q_{(f)0}}{\mu q_{(f)}}\mathbf{k}_T, \frac{q_{(f)0}}{\mu q_{(f)}}q_{(f)L}\right\}, \tag{14}$$

where a plus and a minus sign correspond to a positive and a negative helicity, respectively; for the hadron rest frame, $(f) = (R)$, while, for the P frame, $(f) = (P)$. The quantities $q_{(P)0}$ and $q_{(P)L}$ are obtained from known $q_{(R)0}$ and $q_{(R)L}$ by means of the ordinary Lorentz transformation with $\beta = P/P_0$. We recall that $q^2_{(f)} = q^2_{(f)L} + \mathbf{k}^2$. From (9) and (11), we obtain

$$q_{(P)L} = \frac{1}{2}x(P_0+P) - \frac{k^2+\mu^2}{2x(P_0+P)}, \tag{15}$$

$$q_{(P)0} = \frac{1}{2}x(P_0+P) + \frac{k^2+\mu^2}{2x(P_0+P)}. \tag{16}$$

If the angle between the vectors $\boldsymbol{\xi}_R$ and $\boldsymbol{\xi}_P$ is α in the quark rest frame, the wave functions $\Psi^{(\pm)}_R$ and $\Psi^{(\pm)}_P$, which describe the states of a quark with a positive or a negative helicity in the R and the P frame, satisfy the relations [3]

$$\Psi^{(+)}_R = \cos\frac{\alpha}{2}\,\Psi^{(+)}_P + \sin\frac{\alpha}{2}\,\Psi^{(-)}_P,$$

$$\Psi^{(-)}_R = -\sin\frac{\alpha}{2}\,\Psi^{(+)}_P + \cos\frac{\alpha}{2}\,\Psi^{(-)}_P.$$

The cosine $\cos\alpha \equiv (\boldsymbol{\xi}_R\cdot\boldsymbol{\xi}_P)$ is also equal to the invariant scalar product:

$$\cos\alpha = -(s_{(R)}s_{(P)}).$$

Expression (14) is the 4-vector $s_{(R)}$ in the hadron rest frame, while $s_{(P)}$ is defined in the P frame. In order to calculate $\cos\alpha$, it is therefore necessary to apply the Lorentz transformation with $\beta = P/P_0$ to $s_{(R)}$. Assuming that

$$A(x,k^2) = (P_0+P)Mx^2 + \frac{(k^2+\mu^2)^2}{(P_0+P)Mx^2} + \frac{2P_0}{M}\left(k^2-\mu^2\right),$$

we arrive at

$$-(s_{(R)}s_{(P)}) = \frac{A(x,k^2)}{\sqrt{A^2(x,k^2) + 16k^2\mu^2\dfrac{P^2}{M^2}}}. \quad (17)$$

In this study, we do not aim at performing a detailed comparison with experimental data—our objective is to demonstrate the potential of the proposed model. Therefore, we consider below the case of zero quark mass, where helicity is conserved in going over to any reference frame. As a result, all expressions are substantially simplified, and the variable x varies in the interval from 0 to 1.

Functions that characterize the state of a proton that has a longitudinal polarization in the rest frame (its direction coincides with the proton momentum P) will be labeled with the subscript S; the subscript T will be used for the transverse polarization, orthogonal to the momentum P. If the polarization of the quark-parton is insignificant, the result obtained upon summation over the corresponding indices is $\rho_S(x) = \rho_T(x) \equiv \rho(x)$, where

$$\rho(x) = C\int\limits_0^{M^2x(1-x)} d(k^2)\cdot 2\frac{\sigma_1(W^2)+\sigma_0(W^2)/2}{M^2\left(x+\dfrac{k^2}{M^2x}\right)^2}. \quad (18)$$

Here, C is a constant that is independent of dynamical variables,

$$W^2 = M^2\left(1-x-\frac{k^2}{M^2x}\right),$$

and the functions $\sigma_{1,0}$ correspond to the contributions of two possible fireball states of angular momenta 1 and 0.

If we are interested in the distribution of quarks with definite helicity, the function

$$\Delta\rho_S(x) = C\int\limits_0^{M^2x(1-x)} d(k^2)\quad \frac{\left(x-\dfrac{k^2}{M^2x}\right)\sigma_0(W^2)}{M^2\left(x+\dfrac{k^2}{M^2x}\right)^3} \quad (19)$$

for longitudinally polarized protons and the function

$$\Delta\rho_T(x) = C\int\limits_0^{M^2x(1-x)} d(k^2)\quad \frac{\dfrac{2k}{M}\sigma_0(W^2)}{M^2\left(x+\dfrac{k^2}{M^2x}\right)^3} \quad (20)$$

for the hadron transversely polarized in its rest frame must be added to the function $\rho(x)$ for positively polarized quarks or subtracted from it for negatively polarized quarks.

Any pair of relations (18), (19), or (20) is a set of integral equations. If, for example, $\rho(x)$ and $\Delta\rho_S(x)$ are known from experimental data, $\sigma_1(W^2)$ and $\sigma_0(W^2)$ can be determined by solving these equations (exactly or approximately), whereupon it is possible to predict the values of the function $\Delta\rho_T(x)$ by using relation (20). Given $\sigma_1(W^2)$ and $\sigma_0(W^2)$, we can also make many other predictions.

The quantities $\sigma_1(W^2)$ and $\sigma_0(W^2)$ can be parametrized in the form

$$\sigma_{1,0} = \left(W^2\right)^\nu H_n^{1,0}(W^2),$$

where $H_n^{1,0}(W^2)$ are polynomials of degree n and ν is a rational number. Its value and the coefficients in H_n are variable parameters.

This parametrization makes it possible to express $\rho(x)$ and $\Delta\rho_{S,T}$ in terms of a hypergeometric function or, for integral values of ν, in terms of a combination of rational functions and logarithms. By varying two constants in H_n, one can arrive at results in agreement with experimental data, but, as was mentioned above, a detailed comparison with experimental data will be performed elsewhere.

4. DENSITY MATRIX FOR TWO PARTONS

Since there exist partons of various kinds, it is reasonable to begin this section by briefly considering vector partons. The general expressions (6) and (7) are valid both for zero-mass gluons and for massive vector diquarks (as a matter of fact, they are valid for particles of arbitrary spin). If a spin-1 vector parton is singled out, the spin of the fireball can also assume only two values, 3/2 and 1/2. Since the wave functions or the density-matrix elements for a hadron that consists of free partons depend only on the fireball spin, an increase in the number of the possible spin projections onto a specific axis does not lead to an increase in the number of unknown functions determining the density-matrix elements. Instead of the two functions $\sigma_1(W^2)$ and $\sigma_0(W^2)$, which describe the state with the selected quark, there appear the two functions $\sigma_{1/2}(W^2)$ and $\sigma_{3/2}(W^2)$. The functions $\bar{D}^S_{\Lambda\lambda}(\theta,\phi,0)$ have the same structure.

Analysis of the two-parton case amounts to singling out one more parton from the fireball. Thus, we describe the hadron as a system formed by a fireball of variable mass and spin and two partons that do not interact with each other.

In the hadron rest frame, we have

$$|\mathbf{P}=0\ \Sigma[MJ]; w_{12}S\mu_1\lambda_1,\mu_2\lambda_2;\lambda_{12}W\lambda_3\rangle \quad (21)$$
$$= N_JN_S\int d^2\omega_A\int d^2\omega_B\bar{D}^J_{\Sigma\lambda_A}(\omega_A)\bar{D}^S_{\lambda_{12}\lambda}(\omega_B)$$
$$\times|\mathbf{P}=0;\phi_A,\theta_A,M;\phi_B,\theta_B,w_{12}S\lambda_1\lambda_2;W\lambda_3\rangle,$$

where Σ, J, and M are the same quantities as in (3); $\mu_{1,2}$ and $\lambda_{1,2}$ are, respectively, the masses and the

helicities of the partons that were singled out; S, λ_{12}, and w_{12} are the spin, the helicity, and the invariant mass of the two-parton system; W and λ_3 are, respectively, the mass and the helicity of the fireball; $\phi_{A,B}$ and $\theta_{A,B}$ are the angles in the subsystems; N_J and N_S are the known normalization factors (see [2]); and

$$\lambda = \lambda_1 - \lambda_2, \quad \lambda_A = \lambda_{12} - \lambda_3.$$

The functions $\hat{D}^J_{\Sigma\lambda_A}$ in (21) are identical to those in the preceding case; however, the functions $\hat{D}^S_{\lambda_{12}\lambda}(\omega_B)$ have a more complicated form since the spin S can be equal to 3/2 or 1. The explicit expressions for these functions can be found in [2] (or in any handbook on angular-momentum theory).

Given the two-particle density matrix, it is possible to calculate the one-particle density matrix, whence it follows that the parametrizations of unknown functions must be consistent in the two cases. Therefore, it is reasonable to compare the results with experimental data simultaneously. Since the calculations in the two-particle case are cumbersome, a comparison is postponed to a forthcoming publication.

We can use (7) to calculate the differential cross sections for the deep-inelastic electromagnetic scattering of partons by a hadron, $E^l d\sigma/d^3p^l$ (where E^l and $\mathbf{p}^l$ are the lepton energy and momentum), for the hadron spin parallel, antiparallel, and orthogonal (in the rest frame) to the lepton spin. A comparison of the resulting formulas with the usual expressions for these quantities in terms of the functions $F_{1,2}(x)$ and $g_{1,2}(x)$ would permit expressing F_k and g_k in terms of the diagonal elements of the density matrix. We can obtain a sufficiently accurate approximation by expressing, in the known formulas, the quark distributions in terms of the diagonal elements of the density matrix [1].

By way of example, we indicate that, at high momentum transfers, simple substitutions can be made in the well-known expressions

$$2xF_1(x,Q^2) = \sum_a e_a^2 x[q_a^\uparrow(x,Q^2) + q_a^\downarrow(x,Q^2)],$$

$$g_1(x,Q^2) = \frac{1}{2}\sum_a e_a^2[q_a^\uparrow(x,Q^2) - q_a^\downarrow(x,Q^2)],$$

where the subscripts a correspond to the quark flavors and functions $q_a^{\uparrow,\downarrow}$ describe quarks whose spins are parallel or antiparallel to the nucleon spin. A high precision can be achieved by replacing the distribution functions by the integrals of the density-matrix elements diagonal in k^2. For a first approximation, we can set $k^2 = 0$ and assume that

$$q_a^\uparrow = \rho^2_{(a)1/2,1/2}, \quad q_a^\downarrow = \rho^2_{(a)-1/2,-1/2}.$$

5. CONCLUSION

The proposed method makes it possible to establish many interesting relations between distribution functions and density-matrix elements by using only the property of relativistic invariance. We can generalize this method by introducing the interaction between the quark and the fireball and by describing it by various quasipotentials. An account of the quasipotential method can be found in [5–7].

We can validate or interpret clearly the results obtained by means of the Wilson expansion [8] or by other methods [9–11]. These problems will be considered in more detail elsewhere.

We emphasize once again that, even in the simplest form, the proposed model can readily describe a wide variety of experimental data to a fairly high precision.

REFERENCES

1. A. V. Shchelkachev, in *Proceedings of the XVIII Workshop on High Energy Physics and Field Theory, IHEP, Protvino, Russia, 1996,* Ed. by V. A. Petrov, A. P. Samokhin, and R. N. Rogalyov, p. 250.
2. J. Werle, *Relativistic Theory of Reactions (Model-Independent Methods)* (PWN, Warsaw, 1966; Atomizdat, Moscow, 1969).
3. A. V. Shchelkachev, Teor. Mat. Fiz. **96**, 3 (1993).
4. L. B. Okun, *Leptons and Quarks* (Nauka, Moscow, 1981; North-Holland, Amsterdam, 1984).
5. V. G. Kadyshevsky, Nucl. Phys. B **6**, 125 (1968).
6. A. A. Logunov, V. I. Savrin, N. E. Tyurin, and O. A. Khrustalev, Teor. Mat. Fiz. **6**, 157 (1971).
7. A. A. Arkhipov and V. I. Savrin, Teor. Mat. Fiz. **16**, 328 (1973); **19**, 320 (1974).
8. K. Wilson, Phys. Rev. **179**, 1499 (1969).
9. R. L. Jaffe and X. Ji, Phys. Rev. D **43**, 724 (1991).
10. L. L. Frankfurt and M. Stricman, Phys. Rep. **160**, 235 (1988).
11. S. J. Brodsky, L. L. Frankfurt, J. F. Gunion, *et al.*, Phys. Rev. D **50**, 3134 (1994).

Translated by M. Kobrinsky

Physics of Atomic Nuclei, Vol. 64, No. 11, 2001, pp. 2037–2042. Translated from Yadernaya Fizika, Vol. 64, No. 11, 2001, pp. 2124–2129.

ELEMENTARY PARTICLES AND FIELDS
Theory

Effect of Parton Shadowing on the Distributions of Global Observables

P. I. Zarubin, M. V. Savina, and S. V. Shmatov*

Joint Institute for Nuclear Research, Dubna, Moscow oblast, 141980 Russia

Received June 13, 2000; in final form, October 25, 2000

Abstract—The effect of parton shadowing on the distributions of global observables (total transverse energy E_T and charged-particle multiplicity $n_{\rm ch}$) is investigated on the basis of the HIJING model of nucleus–nucleus interactions. It is shown that, for the interaction of lead nuclei at $\sqrt{s} = 5$ TeV per nucleon, the shadowing effect results in a considerable reduction of the cross section for (mini)jet production (approximately by a factor of 4); this in turn reduces the total transverse energy and the charged-particle multiplicity by a factor of 2.7. Upon taking into account the QCD evolution of nuclear structure functions in Q^2, the shadowing effect becomes less pronounced (by a factor of 1.9 for PbPb interactions). It is shown that global observables can be used to test models of parton shadowing.

1. INTRODUCTION

Among experimental features used to characterize interaction processes in ultrarelativistic nuclear physics, much attention is given to global observables by which one usually means the (pseudo)rapidity distributions of the total transverse energy E_T and the charged-particle multiplicity $n_{\rm ch}$. The physics of global observables is an important line of investigations into the interaction of ultrarelativistic nuclei in the research programs for the RHIC and LHC colliders [1], which are now under construction. It was shown (see, for example, [2]) that the total transverse energy and the multiplicity are determined primarily by the production of so-called (mini)jets—that is, jets of $p_T \sim 2$ GeV. Detailed knowledge of the cross sections for (mini)jet production and of the transverse energy carried by product (mini)jets is of importance for obtaining deeper insights into the dynamics of interactions at early stages and into the subsequent evolution of the parton system formed.

By the early stage, we mean here the time interval $\tau \sim 1/p_T \simeq 0.1$ fm/c, which corresponds to the state of nuclear matter upon the completion of all hard interactions, but which precedes the commencement of the thermalization of the system via secondary interactions.

Knowing the initial properties of such a system, one can assess, among other things, the time of its thermalization and to investigate the possibility of formation of a fully equilibrated thermalized partonic medium—that is, a quark–gluon plasma [3].

It should be noted that, in all probability, only an event-by-event analysis of the fluxes of the transverse energy and multiplicity can provide an answer to the question of whether an equilibrium state has been reached in a specific nuclear collision [4]. Effects associated with the collective behavior of dense strongly interacting nuclear matter are smeared in integrated distributions. Owing to a high statistical significance, the pseudorapidity distributions of the total transverse energy and multiplicity are nevertheless highly sensitive to some other specific nuclear effects that distort the original physical pattern of nucleus–nucleus collisions.

By specific nuclear effects, one usually means the reaction of a nuclear medium. For relevant calculations to be more convenient, this reaction is partitioned into independent effects, such as the effect of jet quenching (energy loss) in a dense nuclear medium [5] and the shadowing of structure functions. It should be borne in mind, however, that this partition is merely an ad hoc trick because, in fact, the above effects are not independent and can in principle be described on the basis of a unified mechanism [6].

Investigation of the deep-inelastic scattering of electrons and muons on nuclei revealed the suppression of the ratio of the nuclear structure functions $F_2^A(x, Q^2)$ to the free-nucleon structure functions $F_2^N(x, Q^2)$. Later on, a detailed analysis of this phenomenon over wide ranges of the Bjorken variable $x = Q^2/2M, 10^{-5} \le x \le 0.8$, and of the 4-momentum transfer squared Q^2, $0.05 \le Q^2 \le$

*e-mail: shmatov@lhe.jinr.ru

150 GeV^2, was performed on the basis of experimental data from CERN [7] and FNAL [8]. It was established that the ratio of a parton distribution within an intranuclear nucleon (referred to in the following as a nuclear structure function) to the corresponding parton structure function within a free nucleon (referred to in the following as a parton structure function), $R_A = F_{i/A}/F_{i/N}$, depends strongly on the variable x. For x values in the interval between 0.3 and 0.7, the distributions of quarks and gluons are suppressed [European Muon Collaboration (EMC) effect], while, in the interval $0.1 \leq x \leq 0.3$, the parton structure functions $F_{i/A}$ are in excess of $F_{i/N}$. Finally, $R_A(x)$ is again suppressed in the region $x \leq 0.1$.

Various phenomenological models [9] were used to explain this behavior of nuclear structure functions; however, no adequate description has been found so far. For events characterized simultaneously by small values of the Bjorken variable x, about 10^{-4}, and relatively high values of the 4-momentum transfer squared Q^2, about 1000 GeV^2, there do not exist experimental data either.

Presently, it is expected that, at LHC energies, a considerable fraction of the total transverse energy (up to 30%) will be determined by processes where x and Q^2 take values on precisely these orders of magnitude. Therefore, it is necessary to perform a more thorough experimental investigation of the behavior of nuclear structure functions in the above regions of x and Q^2.

Shadowing effects modify the pseudorapidity distributions of global observables, and these modifications can also be used to study jet quenching by a dense nuclear medium [10].

The main objective of the present study is to find out how the distributions of global observables are affected by changes in parton structure functions due to nuclear-matter shadowing.

That there are ambiguities in parton distributions because of nuclear-medium effects leads to ambiguities in determining multiplicities and transverse energies in nucleus–nucleus collisions and in assessing the background for jet-reconstruction algorithms. It will be demonstrated below how the distributions of multiplicities and transverse energies can be used to test various parton-shadowing models.

In our calculations performed for the case where lead nuclei interact at the LHC energy ($\sqrt{S} = 5$ TeV per nucleon), we used the parametrization of nuclear parton distributions that is adopted in the HIJING model of nucleus–nucleus interactions [11]. The Q^2 evolution of the shadowing effect was taken into account on the basis of the EKS98 model [12], which allows for the scale dependence of nuclear-medium effects. For this, the Q^2 evolution of the ratio $R_A(x, Q^2)$ from the initial scale $R_A(x, Q_0^2)$, where $Q_0^2 \sim 4$ GeV^2, was considered by using the modified Dokshitzer–Gribov–Lipatov–Altarelli–Parisi evolution equations for structure functions [13].

Within these models, we have also analyzed the effect of various sets of parton structure functions on the predictions of the shadowing models used.

2. MULTIPARTICLE-PRODUCTION PROCESSES IN NUCLEUS–NUCLEUS INTERACTIONS

Multiparticle-production processes in nucleus–nucleus interactions are considered as a combination of hard or semihard ($p_T \geq p_0$) and soft particle-production processes. By soft processes, we mean those that cannot be computed within renormalizable QCD. The cutoff parameter p_0 depends on the set of parametrizations used for the quark and gluon structure functions. As a rule, it is about 1 to 2 GeV. Under the assumption of independent binary parton–parton interactions, the production of minijets (that is, jets of $p_T \sim p_0$), whose detection in experiments is impossible, is the main source of multiplicity and transverse energy fluxes. In the leading order of QCD at the level of nucleon–nucleon interactions, the cross section for (mini)jet production is given by

$$\frac{d\sigma^{\rm jet}}{dy}(\sqrt{s_{NN}}, p_0) = \frac{1}{2}\int\limits_{p_0^2}^{s/4} dp_T^2 dy_2 \frac{d\sigma^{\rm jet}}{dp_T^2 dy_1 dy_2}, \quad (1)$$

$$\frac{d\sigma^{\rm jet}}{dp_T^2 dy_1 dy_2} = K\sum_{i,j,k,l} x_1 f_i(x_1, p_T^2) x_2 f_j(x_2, p_T^2)$$
$$\times \left[\frac{d\hat{\sigma}^{ij\to kl}}{d\hat{t}}(\hat{s}, \hat{t}, \hat{u}) + \frac{d\hat{\sigma}^{ij\to kl}}{d\hat{t}}(\hat{s}, \hat{u}, \hat{t})\right]\frac{1}{1+\delta_{kl}},$$

where p_0 is the cutoff parameter, $x_1 = x_T(e^{y_1} + e^{y_2})/2$ and $x_2 = x_T(e^{-y_1} + e^{-y_2})/2$ are the momentum fractions carried by the primary partons i and j, $x_T = 2p_T/\sqrt{s}$, and y_1 and y_2 are the rapidities of the product partons. Summation is performed over all flavors, and the factor of $K \approx 2$ was introduced to take into account higher QCD orders.

The rapidity distribution of the number of (mini)jets produced in a nucleus–nucleus collision at a fixed impact parameter is obtained from expression (1) by multiplying it by the nuclear overlap function; that is,

$$\frac{dN_{AA}}{dy}(\sqrt{s_{NN}}, p_0, b) = 2T_{AA}(b)\frac{\sigma^{\rm jet}}{dy}(\sqrt{s_{NN}}, p_0),$$
$$T_{AA}(|\mathbf{b}|) = \int d^2\mathbf{r} T_A(\mathbf{r}) T_A(\mathbf{b}-\mathbf{r}), \quad (2)$$

where $\mathbf{r}$ is the two-dimensional vector determining the interaction vertex, $\mathbf{b}$ is the impact-parameter vertex, and $T_A(\mathbf{r})$ is the nuclear thickness computed under the assumption of the Woods–Saxon distribution for the nuclear density $\rho_A(\mathbf{r})$. The mean number of charged hadrons per (pseudo)rapidity unit, $dn_{\rm ch}/dy$, can be obtained from (2) by substituting, into (1), the fragmentation function $D_{h/i}(z,Q^2)/\pi z$ [14] for the transition of quarks and gluons into final observable particles.

The flux of the total transverse energy per rapidity unit due to (mini)jet production in an AA interaction is given by

$$\frac{dE_T^{jet}}{dy}(\sqrt{s_{NN}},p_0,b) = T_{AA}(b)K \tag{3}$$
$$\times \int dp_T^2 dy_2 \sum_{i,j,k,l} x_1 f_i(x_1,p_T^2) x_2 f_j(x_2,p_T^2)$$
$$\times \left[\frac{d\hat{\sigma}^{ij\to kl}}{d\hat{t}}(\hat{s},\hat{t},\hat{u}) + \frac{d\hat{\sigma}^{ij\to kl}}{d\hat{t}}(\hat{s},\hat{u},\hat{t})\right]\frac{p_T}{1+\delta_{kl}}.$$

As was indicated above, the total cross section for AA interactions is represented as the sum of the cross sections for soft and hard particle-production processes ($\sigma^{\rm soft}$ and $\sigma^{\rm jet}$, respectively): $\sigma^{\rm tot} = \sigma^{\rm jet} + \sigma^{\rm soft}$. Accordingly, the expressions for calculating the charged-particle multiplicity and the transverse energy are written as

$$\frac{dn_{\rm ch}^{\rm tot}}{dy} = \frac{dn_{\rm ch}^{\rm jet}}{dy} + \frac{dn_{\rm ch}^{\rm soft}}{dy}, \frac{dE_T^{\rm tot}}{dy} = \frac{dE_T^{\rm jet}}{dy} + \frac{dE_T^{\rm soft}}{dy},$$

where $n_{\rm ch}$ is the number of hadrons produced in (semi)hard interactions, while $dn_{\rm ch}^{\rm soft}/dy$ and $dE_T^{\rm soft}/dy$ are the terms representing the contributions of soft processes to, respectively, the integrated flux of the multiplicity and the integrated flux of transverse energy. In order to take these processes into account, use is usually made of phenomenological models of nuclear–nuclear collisions like the dual parton model and FRITIOF [15].

3. NUCLEAR SHADOWING WITHIN THE PARTON MODEL

At sufficiently high energies, nuclei can be treated as objects consisting of a set of valence quarks surrounded by a cloud of sea quarks and gluons. The shadowing of the color charge leads to a reduction of the parton-interaction probability and, hence, to a reduction of the total cross section for particle production in nucleus–nucleus interactions. In order to take into account the shadowing effect, a coefficient that characterizes the degree of shadowing of two interacting partons at given values of x, p_T^2, and A is introduced in the integrand on the right-hand side of (1).

Our calculations are based on the HIJING model of nucleus–nucleus interactions [11], where the x and A evolution of the shadowing effect is realized as a global parametization [16] of EMC, NMC, and E665 data [7, 8] for various sets of nuclei in the form

$$R_A(x) \equiv \frac{f_{i/A}(x)}{Af_{i/N}(x)} \tag{4}$$
$$= 1 + 1.19\ln^{1/6}A[x^3 - 1.5(x_0+x_L)x^2 + 3x_0x_Lx]$$
$$- \left[\alpha_A - \frac{1.08(A^{1/3}-1)}{\ln(A+1)}\sqrt{x}\right]e^{-x^2/x_0^2},$$

where $\alpha_A = 0.1(A^{1/3}-1)$, $x_0 = 0.1$, $x_L = 0.7$, and A is the atomic number of the nucleus involved.

The shadowing of partons is taken into account by replacing, in (1), the parton distributions within the free nucleon, $f_{i/N}(x)$, by the parton distributions within an intranuclear nucleon, $f_{i/A}(x) = R_A(x)Af_{i/N}(x)$.

It is assumed that the degree of nuclear shadowing is identical for valence and for sea quarks, as well as for gluons. Within the model used, we do not consider shadowing for unrenormalizable processes—that is, the shadowing of the structure functions for $Q^2 < 4$ GeV^2 processes and the Q^2 evolution of the effect. In order to take into account the dependence of the effect on the impact parameter of a nuclear collision, a dependence on the distance r from the center of the nucleus to the interaction vertex is introduced in the parameter α_A in the form

$$\alpha_A = 0.1(A^{1/3}-1)\frac{4}{3}\sqrt{1-r^2/R_A^2}, \tag{5}$$

where R_A is the radius of the nucleus.

On the basis of the above assumptions, we have investigated the behavior of global variables for the sample of 10000 events of collisions between lead nuclei at a c.m. energy of $\sqrt{s} = 5$ TeV per nucleon and impact-parameter values varying between 0 and $3R_A$. The pseudorapidity distributions of the total transverse energy are displayed in Fig. 1*a* for various scenarios of nucleus–nucleus interactions. The distribution represented by curve *1* was obtained under the assumption that there is no parton shadowing, but final-state parton interaction—that is, the jet-quenching effect [17]—was included. This effect leads to the emergence of a broad maximum in the central pseudorapidity region of the distribution $dE_T/d\eta$ [18]. Curve *2* corresponds to the case where we disregarded both the shadowing and the jet-quenching effect. The third and the fourth distribution were computed by using the quark and gluon structure

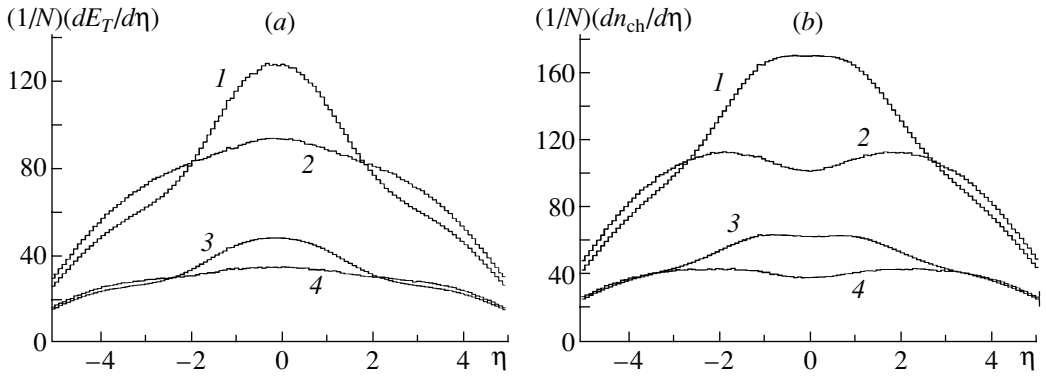

Fig. 1. Pseudorapidity (η) distributions of (*a*) the total transverse energy dE_T (in GeV) and (*b*) the charged-particle multiplicity $dn_{\rm ch}$ for 10000 events of PbPb interactions at $\sqrt{s} = 5$ TeV per projectile nucleon. The curves were computed for the cases where (*1*) there is no shadowing, but the jet-quenching effect is taken into account; (*2*) medium effects are completely ignored; (*3*) both the shadowing and the jet-quenching effect are taken into account; and (*4*) the shadowing effect is taken into account, but no losses in the nuclear medium are assumed.

functions modified within the nucleus (*3*) with and (*4*) without allowance for the jet-quenching effect.

As can be seen from the figure, shadowing does not distort the shape of the distributions, but it reduces the absolute height of the distribution by a factor of 2.7.

From the form of Eqs. (1) and (4), it follows that the charged-particle multiplicity, which is directly related to the jet-production cross section (2), must be proportional to the square of the degree of shadowing, $dn_{ch}/d\eta \sim R_A^2(x)$. In central collisions of lead nuclei at a c.m. energy of 5 TeV per nucleon, (mini)jet-production processes are characterized by mean values of x about 7×10^{-4} at $Q_0^2 = 4$ GeV^2; at such x values, $R_A = 0.5$ and the multiplicity is expected to decrease by a factor of about 4.

At the same time, it can be seen from Fig. 1*b* that the shadowing effect also leads to the reduction of the density of the charged-particle multiplicity, $dn_{\rm ch}/d\eta$, at $\eta = 0$ by a factor of 2.7 both when the jet-quenching effect is taken into account and when the final-state interaction of partons is disregarded.

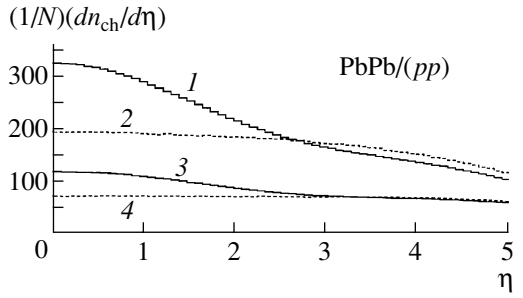

Fig. 2. As in Fig. 1*b*, but the distributions here are normalized to the analogous distributions for the case of proton–proton interactions at the same energy.

This deviation from the expected decrease is associated with the reduction of the shadowing effect with increasing distance between the center of the nucleus and the vertex of nucleon–nucleon interaction; it can also be due to fragmentation effects and to unrenormalizable contributions to the cross section—that is, to soft processes, whose shadowing is not considered in the present study. It should be noted that the influence of strong processes must be especially pronounced when the jet-quenching mechanism is introduced in the process of nucleus–nucleus interactions, because this effect leads to a redistribution of the multiplicity, shifting it toward lower p_T values [11]. From the distributions presented above, this cannot be seen, however, since the Q^2 evolution of nuclear structure functions is not considered in the shadowing model used.

It is interesting to note that, for $\eta \geq 2.5$, the distributions obtained with and without allowance for the jet-quenching effect differ insignificantly; that is, the high-η region is insensitive to this effect. This can clearly be seen if we examine the charged-particle multiplicity for PbPb collisions that is normalized to the analogous distribution for proton–proton interactions (see Fig. 2). At the same time, the region $\eta \geq 2.5$ is very sensitive to the shadowing effect and can be used, in studying nuclear structure functions in the small-x region, to obtain experimental information not distorted by final-state interactions.

4. SCALE EVOLUTION OF THE PARTON-SHADOWING EFFECT

As was indicated above, the parametrization in Eq. (4) was obtained under the assumption that the

Cross section for (mini)jet production at the NN level for various sets of parton structure functions

	Cross section σ_{jet}, mb		
	D01	CTEQ2L	GRV 92LO
Without shadowing	130.7	289.3	764.2
With allowance for shadowing:			
Ca	46.3	100.4	259.8
Nb	40.5	83.9	236.9
Pb	32.7	71.5	192.6

shadowing effect undergoes no scale evolution; that is, there is no QCD evolution of the quark and gluon structure functions F_q^A, $F_{\bar{q}}^A$, and F_g^A in Q^2. However, experimental data suggest that the ratio R_A depends strongly on the scale of the 4-momentum transfer squared Q^2 [7, 8]. In the Q^2 range between 4 and 100 GeV^2, the ratio $R_{F_2}^A$ increases from 0.54 to 0.66 at $x = 0.001$. The theoretical calculations from [13, 19], which are based on solving modified evolution equations within the Dokshitzer–Gribov–Lipatov–Altarelli–Parisi formalism, revealed that, with increasing 4-momentum transfer squared, the shadowing of gluons in a nucleus becomes less important than the shadowing of quarks. Later on, some phenomenological models (see, for example, [12]) that make it possible to take into account the shadowing-effect-induced corrections to nuclear structure functions were developed on the basis of the results obtained. It turned out that, for (mini)jet-production cross sections and, hence, for the total transverse energy and the charged-particle multiplicity, these models yield strongly different estimates. By way of example, the results of the calculations for the pseudorapidity distribution of the number of (mini)jets are displayed in Fig. 3 for two phenomenological models of shadowing. There, $N_{\text{jet}}(\text{shadowing})/N_{\text{jet}}$ is the ratio of the number of (mini)jets that are formed in collisions of lead nuclei at an energy of 5 TeV per nucleon and which are calculated with allowance for shadowing to the number of (mini)jets obtained by using structure functions without shadowing.

The inclusion of Q^2 evolution substantially reduces the influence of shadowing: the distribution obtained with the parametrization in Eq. (4) (solid line) is nearly twice as high as the distribution computed on the basis of the EKS98 model [12] (dash-dotted line). In our calculations, we also considered that the present-day accuracy in determining nuclear structure functions is rather poor ($\delta xg(x) \sim 30\%$ at $x = 0.0001$ and $Q^2 = 5$ GeV^2 [20]). However, the predictions of the two models used differ so strongly that, despite large uncertainties in the calculations, we can conclude that the global observables being considered are highly sensitive to various aspects of the dynamics of nucleus–nucleus interactions and can be used to test experimentally parton-shadowing models, especially at high luminosities of future hadron colliders (RHIC, LHC).

We note that the (mini)jet-production cross sections computed by formula (1) depend strongly on the set of structure functions used.

We have performed a comparative analysis of the cross sections for (mini)jet production in AA interactions, σ_{jet}, for three sets of parton structure functions. The results of the calculations for the relevant cross sections are quoted in the table both for the case where shadowing is disregarded and for the case where the scale evolution of shadowing in various nuclei is taken into account. It can be seen that, although the cross-section values change sizably upon going over from one set of structure functions to another, the ratio of the cross section where shadowing is taken into account to the cross section where this effect is disregarded remains unchanged for the same nucleus. Thus, the EKS98 model of shadowing is not sensitive to the choice of set of structure functions (at least within their class considered here).

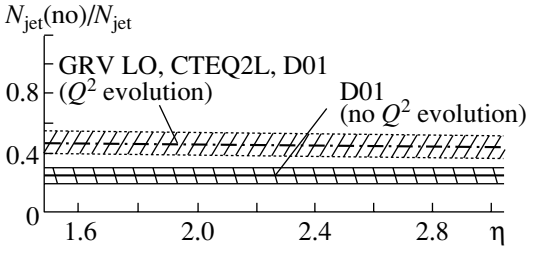

Fig. 3. Ratio of the number of (mini)jets that is calculated with allowance for shadowing to the number of (mini)jets that is obtained under the assumption that there is no shadowing for PbPb interactions at $\sqrt{s} = 5$ TeV per nucleon. The calculations were performed (dash-dotted line) with and (solid line) without allowance for scale evolution.

5. CONCLUSION

We have studied the effect of parton shadowing on the distributions of global observables. Specifically, we have considered the distributions $dE_T/d\eta$ and $dn_{\mathrm{ch}}/d\eta$.

We have used two models of parton shadowing: (i) that which allows for scale evolution and (ii) that which disregards it. The calculations based on the second model have revealed that, for PbPb interactions at an energy of 5 TeV per nucleon, the inclusion of shadowing in the structure functions leads to a reduction of the transverse-energy density and the charged-particle multiplicity by a factor of 2.7.

Upon taking into account the scale evolution of nuclear structure functions [model (i)], this effect is reduced by a factor of about 1.9. Thus, the distributions of global observables have proved to be highly sensitive to the choice of parton-shadowing model. This circumstance can be used to test the proposed scenario of shadowing.

It has also been established that, within the existing models of shadowing, the use of different sets of parton structure functions has no effect on the behavior of the distributions of global observables.

ACKNOWLEDGMENTS

We are grateful to I.A. Golutvin and A.I. Malakhov (Joint Institute for Nuclear Research) for interest in this study and support and to A.V. Leonidov (Lebedev Institute of Physics, Russian Academy of Sciences) and V.T. Kim (Petersburg Nuclear Physics Institute, Russian Academy of Sciences) for critical comments.

REFERENCES

1. K. Geiger, Phys. Rep. **258**, 237 (1995); M. V. Savina *et al.*, Yad. Fiz. **62**, 2263 (1999) [Phys. At. Nucl. **62**, 2084 (1999)]; S. A. Bass *et al.*, Nucl. Phys. A **661**, 205 (1999); S. Scherer *et al.*, hep-ph/9903392; M. J. Bleicher *et al.*, Phys. Rev. C **62**, 024904 (2000).
2. K. Kajantie, P. Landshoff, and J. Lindfors, Phys. Rev. Lett. **59**, 2527 (1987); K. J. Eskola, K. Kajantie, and J. Lindfors, Nucl. Phys. B **323**, 37 (1989); Phys. Lett. B **214**, 613 (1988).
3. K. J. Eskola, K. Kajantie, and P. Ruuskanen, Eur. Phys. J. C **1**, 627 (1998); Phys. Lett. B **332**, 191 (1994); K. J. Eskola and K. Kajantie, Z. Phys. C **75**, 515 (1997); K. J. Eskola, Prog. Theor. Phys. Suppl. **129**, 1 (1997).
4. M. Gazdzicki, A. Leonidov, and G. Roland, Eur. Phys. J. C **6**, 365 (1999); Feng Liu *et al.*, Eur. Phys. J. C **8**, 649 (1999).
5. M. Gyulassy and X. N. Wang, Nucl. Phys. B **420**, 583 (1994); M. Gyulassy, X. N. Wang, and M. Plumer, Phys. Rev. D **51**, 3436 (1995); R. Baier, Yu. L. Dokshitzer, S. Peigne, and D. Schiff, Phys. Lett. B **345**, 277 (1995).
6. M. Gyulassy and L. McLerran, Phys. Rev. C **56**, 2219 (1997).
7. M. Arneodo *et al.*, Nucl. Phys. B **483**, 3 (1997); Nucl. Phys. B **441**, 12 (1995); **333**, 1 (1990); P. Amaudruz *et al.*, Z. Phys. C **51**, 387 (1991).
8. M. R. Adams *et al.*, Phys. Rev. Lett. **68**, 3266 (1992); Phys. Lett. B **287**, 375 (1992).
9. V. Barone *et al.*, Z. Phys. C **58**, 541 (1993); L. Frankfurt and M. Strikman, Phys. Rep. **160**, 235 (1988); A. De Roeck and E. A. De Wolf, Phys. Lett. B **388**, 843 (1996); **367**, 392 (1994); R. J. M. Covolan and E. Predazzi, *Hadronic Physics with Multi-GeV Electrons* (Les Houches, 1990).
10. M. V. Savina *et al.*, JINR Rapid Commun., No. 87, 45 (1998).
11. M. Gyulassy and X. N. Wang, Phys. Rev. D **44**, 3501 (1991).
12. K. J. Eskola, V. J. Kolhinen, and P. Ruuskanen, Nucl. Phys. B **535**, 351 (1998); K. J. Eskola, V. J. Kolhinen, and C. A. Salgado, Eur. Phys. J. C **9**, 61 (1999).
13. A. H. Mueller and J. Qiu, Nucl. Phys. B **268**, 427 (1986).
14. B. Andersson, G. Gustafson, and B. Söderberg, Z. Phys. C **20**, 317 (1983).
15. B. Andersson *et al.*, Nucl. Phys. B **281**, 289 (1987); B. Nilson-Almqvist and E. Stenlund, Comput. Phys. Commun. **43**, 387 (1987).
16. A. H. Mueller, Nucl. Phys. B **335**, 115 (1990); F. E. Close, J. Qiu, and R. G. Roberts, Phys. Rev. D **40**, 2820 (1989).
17. X. N. Wang, Phys. Rep. **280**, 287 (1997).
18. M. V. Savina *et al.*, JINR Rapid Commun., No. 91, 65 (1998).
19. L. V. Gribov, E. M. Levin, and M. G. Ryskin, Phys. Rep. **100**, 1 (1983); K. J. Eskola, Nucl. Phys. B **400**, 240 (1993); S. Kumano, Phys. Rev. C **48**, 2016 (1993).
20. A. M. Cooper, R. C. E. Devenish, and A. De Roeck, Preprint No. 97-226, DESY (Hamburg, 1997); J. Huston *et al.*, FERMILAB-Pub-98/046-T (Batavia, 1998).

Translated by A. Isaakyan

Physics of Atomic Nuclei, Vol. 64, No. 11, 2001, pp. 2043–2050. Translated from Yadernaya Fizika, Vol. 64, No. 11, 2001, pp. 2130–2137.

ELEMENTARY PARTICLES AND FIELDS
Theory

Collisions of Domain Walls in a Supersymmetric Model

V. A. Gani* **and A. E. Kudryavtsev****

Institute of Theoretical and Experimental Physics, Bol'shaya Cheremushkinskaya ul. 25, Moscow, 117259 Russia

Received October 18, 2000; in final form, January 23, 2001

Abstract—A collision of two parallel domain walls in a supersymmetric model is analyzed by using both the effective-Lagrangian approximation and a numerical solution to the equations of motion for the scalar components of the superfields involved. Two cases—that where a configuration belonging to the type of two parallel walls is saturated in the sense of Bogomol'nyi, Prasad, and Sommerfeld (BPS) and that where such a configuration is not BPS-saturated—are considered individually. For the first case, it is shown that, at low initial velocities, a collision of the walls is virtually an elastic reflection somewhat delayed in time. It is also demonstrated that, in this case, it is possible to introduce a collective variable that has the meaning of an internal parameter of the configuration and which can be treated as a dynamical (time-dependent) variable and to describe the dynamics of the system in terms of an effective Lagrangian. For the second case, it is found that, for collisions, there is a critical value of $v_{\rm cr} \approx 0.9120$ for the initial velocity v_i. For $v_i < v_{\rm cr}$, the reflection of the walls occurs, the vacuum between the walls remaining unchanged. For $v_i > v_{\rm cr}$, the collision process is accompanied by a change in the vacuum state between the walls.

1. INTRODUCTION

The presence of domain walls in supersymmetric models involving scalar superfields is associated with the existence of degenerate vacua. If there are a few isolated degenerate vacua, there can exist domain walls between each pair of such vacua. The question of intersection of two or more domain walls has been intensively studied in recent years. In this connection, it is worth noting the studies of Shifman and Voloshin [1–3]. Within the Wess–Zumino model involving two chiral superfields, it was shown in [1] that, for a domain wall saturated in the sense of Bogomol'nyi, Prasad, and Sommerfeld (BPS), there exist not only zero modes associated with a shift of such a wall as a discrete unit but also zero modes associated with a change in the internal parameter of the relevant configuration. In [2], Voloshin investigated stability of some domain-wall-type configurations and considered the possibility of formation of their intersections. Some questions concerning BPS-saturated intersections of domain walls were also discussed in the studies reported in [4, 5], which appeared somewhat later. A one-parameter family of domain walls in a generalized Wess–Zumino model that involves two scalar superfields was presented in [3]. A configuration that corresponds to the intersection of two domain walls at a small angle was considered in [6] for the case where a static solution in the form of two parallel walls is known analytically. For a collision of two walls, the time evolution of the process is investigated here in Section 3 by using a similar method. The study of Smilga and Veselov [7], who considered the effective Lagrangian of $SU(2)$ supersymmetric QCD and solved numerically the equations of motion, is also worthy of note. In this way, they found domain-wall-type solutions, which include both BPS-saturated and BPS-unsaturated solutions.

2. DESRIPTION OF THE MODEL

Following [1–3, 6], we consider a supersymmetric model that involves two chiral superfields Φ and Ξ and the superpotential

$$W(\Phi,\Xi) = \frac{m^2}{\lambda}\Phi - \frac{1}{3}\lambda\Phi^3 - \alpha\Phi\Xi^2,$$

where m is a mass parameter and λ and α are coupling constants. We assume that all parameters are real-valued and positive and denote by ϕ and χ the scalar components of the superfields Φ and Ξ, respectively. Their dynamics is described by the Lagrangian

$$\mathcal{L} = (\partial\phi)^2 + (\partial\chi)^2 - \left(\frac{m^2}{\lambda} - \lambda\phi^2 - \alpha\chi^2\right)^2 - 4\alpha^2\phi^2\chi^2\,. \quad (1)$$

In the following, we everywhere consider configurations of the type of domain walls orthogonal to the x

*e-mail: gani@heron.itep.ru
**e-mail: kudryavt@heron.itep.ru

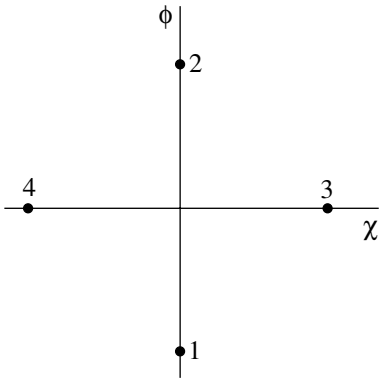

Fig. 1. Positions of the vacua in the model being considered.

axis. We assume that the fields ϕ and χ are independent of other coordinates. The surface density of the wall energy is given by

$$E = \int_{-\infty}^{+\infty} \left[\left(\frac{\partial\phi}{\partial t}\right)^2 + \left(\frac{\partial\phi}{\partial x}\right)^2 + \left(\frac{\partial\chi}{\partial t}\right)^2 \right. \quad (2)$$
$$\left. + \left(\frac{\partial\chi}{\partial x}\right)^2 + \left(\frac{m^2}{\lambda} - \lambda\phi^2 - \alpha\chi^2\right)^2 + 4\alpha^2\phi^2\chi^2 \right] dx.$$

From (2), we can easily obtain first-order differential equations of the type of the BPS equations [8]. Indeed, we consider time-independent configurations $\phi(x)$ and $\chi(x)$. We transform (2) as follows:

$$E = \int_{-\infty}^{+\infty} \left[\frac{\partial\phi}{\partial x} - \left(\frac{m^2}{\lambda} - \lambda\phi^2 - \alpha\chi^2\right)\right]^2 dx \quad (3)$$
$$+ \int_{-\infty}^{+\infty} \left[\frac{\partial\chi}{\partial x} + 2\alpha\phi\chi\right]^2 dx$$
$$+ \int_{-\infty}^{+\infty} \left[2\frac{\partial\phi}{\partial x}\left(\frac{m^2}{\lambda} - \lambda\phi^2 - \alpha\chi^2\right) - 4\alpha\phi\chi\frac{\partial\chi}{\partial x}\right] dx.$$

It can easily be seen that the third integral is an integral of a total derivative; that is,

$$\int_{-\infty}^{+\infty} \frac{dF}{dx} dx = F|_{x=+\infty} - F|_{x=-\infty} = Q,$$

where

$$F[\phi(x), \chi(x)] = 2\phi\left(\frac{m^2}{\lambda} - \frac{\lambda}{3}\phi^2 - \alpha\chi^2\right).$$

The quantity Q, which can be referred to as a topological charge of the configuration, depends only on the boundary conditions for the functions $\phi(x)$ and $\chi(x)$, but it is independent of their behavior at finite x.

The first and the second integral in (3) are integrals of nonnegative functions. It follows that, if we seek configurations satisfying given boundary conditions and having a minimal energy, it is necessary to require that the integrands there vanish; that is,

$$\frac{d\phi}{dx} = \frac{m^2}{\lambda} - \lambda\phi^2 - \alpha\chi^2, \quad (4)$$
$$\frac{d\chi}{dx} = -2\alpha\phi\chi.$$

Configurations that satisfy preset boundary conditions and the set of first-order differential Eqs. (4) are referred to as BPS-saturated configurations. The energy of a BPS-saturated configuration is obviously equal to Q. If $Q = 0$, boundary conditions forbid the existence of nontrivial BPS-saturated configurations (by a trivial configuration, we mean a solution that coincides with the same vacuum over the entire space).

The potential in the Lagrangian given by Eq. (1) has four degenerate minima occurring at the points $(\pm m/\lambda, 0)$ and $\left(0, \pm m/\sqrt{\lambda\alpha}\right)$ in the $(\phi,\ \chi)$ plane. We number them as is illustrated in Fig. 1. In all, there are four vacuum states, whence it follows that six types of domain walls between the different vacua are possible in the model being considered. All of these, with the exception of the wall between vacua 3 and 4, are BPS-saturated. That BPS configurations of the wall type cannot exist between vacua 3 and 4 follows from the vanishing of the topological charge $Q_{34} = Q_{43}$ when boundary conditions of the type being considered are imposed on the fields ϕ and χ. For the remaining types of walls, we can easily obtain $Q_{12} = -Q_{21} = (8/3)Q_0$ and $Q_{13} = -Q_{31} = Q_{14} = -Q_{41} = Q_{42} = -Q_{24} = Q_{32} = -Q_{23} = (4/3)Q_0$, where $Q_0 \equiv m^3/\lambda^2$.

For the sake of convenience, we will henceforth use the dimensionless variables f and h that are related to ϕ and χ by the equations

$$\phi = \frac{m}{\lambda} f\ ,\ \chi = \frac{m}{\sqrt{\lambda\alpha}} h\ .$$

In terms of the new variables (f, h), the vacuum states of the model being considered are represented by the points $(\pm 1, 0)$ and $(0, \pm 1)$. We also introduce the notation $\lambda/\alpha = \rho$ and set $m = 1$. The BPS Eqs. (4) then take the form

$$\frac{df}{dx} = 1 - f^2 - h^2, \quad (5)$$
$$\frac{dh}{dx} = -\frac{2}{\rho} fh.$$

Dividing the first equation in (5) by the second one, we obtain

$$\frac{df}{dh} = -\frac{\rho}{2}\frac{1 - f^2 - h^2}{fh}.$$

This is an ordinary differential equation (a linear one if f^2 is treated as a function of h), whose general solution can be represented in the form

$$f^2 = 1 - \frac{\rho h^2}{\rho - 2} - Ch^\rho, \tag{6}$$

where C is a constant of integration (it is assumed that $\rho \neq 2$). The constant C changes within the interval $C^* \leq C < +\infty$, where $C^* = 2/(2-\rho)$. In [3], Shifman and Voloshin discussed the properties of the solution given by (6) and obtained explicit expressions for $f(x)$ and $h(x)$ at $\rho = 4$ for arbitrary C. The trajectories in the (f, h) plane that are specified by Eq. (6) are shown in Fig. 2 for some values of the constant C. It is worthy of note that, from the second equation in (5), we immediately obtain

$$x = -\frac{\rho}{2}\int \frac{dh}{hf(h)}. \tag{7}$$

The integral on the right-hand side of Eq. (7) is expressed in terms of elementary functions at $\rho = 1$ and $\rho = 4$. At $\rho = 1$, the model being considered reduces to the trivial case of two noninteracting scalar fields $\tilde{\phi} = (\phi + \chi)/\sqrt{2}$ and $\tilde{\chi} = (\chi - \phi)/\sqrt{2}$. In the following, we everywhere assume that $\rho = 4$.

At $C = C^* = -1$, we find from (6) that

$$f = \pm(1 - h^2). \tag{8}$$

Choosing the minus sign in (8), substituting this expression into (7), and performing integration there, we obtain

$$f_{13}(x - x_0) = f_{14}(x - x_0) = \frac{1}{2}\left(\tanh\frac{x - x_0}{2} - 1\right), \tag{9}$$

$$h^2_{13}(x - x_0) = h^2_{14}(x - x_0) = \frac{1}{2}\left(1 + \tanh\frac{x - x_0}{2}\right),$$

where x_0 is a constant of integration. The solution in (9) corresponds to a wall between vacua 1 and 3 or 1 and 4, depending on the choice of sign in taking the square root of h^2. The position of the wall is determined by the constant x_0. If the plus sign is chosen in Eq. (8), we arrive at expressions for the $3 \to 2$ and $4 \to 2$ walls; that is,

$$f_{32}(x - x_0) = f_{42}(x - x_0) = \frac{1}{2}\left(1 + \tanh\frac{x - x_0}{2}\right), \tag{10}$$

$$h^2_{32}(x - x_0) = h^2_{42}(x - x_0) = \frac{1}{2}\left(1 - \tanh\frac{x - x_0}{2}\right).$$

The energies of the configurations (9) and (10) are equal to $4/3$ [$(4/3)m^3/\lambda^2$ in dimensional units]. At arbitrary values of C from (6) and (7), we obtain a family of solutions for walls between vacua 1 and 2 [3]:

$$f_{12}(x - x_0) = \frac{e^{2(x-x_0)} - C - 1}{(e^{x-x_0} + 1)^2 + C}, \tag{11}$$

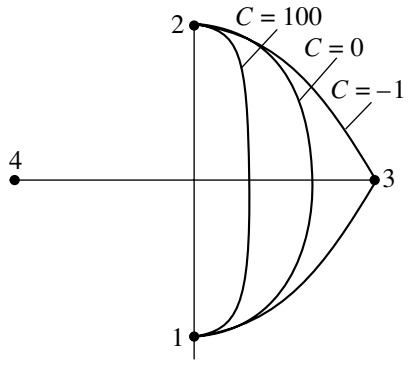

Fig. 2. Trajectories in the (f, h) plane that are specified by Eq. (6) at $\rho = 4$ and some values of the constant C. Shown in the figure are branches that were computed for positive values of h. The numbering of the vacuum states corresponds to that in Fig. 1.

$$h^2_{12}(x - x_0) = \frac{2e^{x-x_0}}{(e^{x-x_0} + 1)^2 + C}.$$

At $\rho = 4$, the constant C changes in the interval $-1 \leq C < +\infty$. We note that the energy of the configurations in (11) is independent of the parameter C and is equal to $8/3$, the quantity x_0 determining the shift of the wall along the x axis; it is obvious that this shift does not affect the energy either. We choose x_0 in such a way as to ensure fulfillment of the equality $f(0) = 0$ in (11):

$$x_0 = -\frac{1}{2}\ln(C + 1).$$

The solution given by (11) can then be recast into the form [6]

$$f_{12}(x) = \frac{a(e^{2x} - 1)}{a + 2e^x + ae^{2x}}, \tag{12}$$

$$h^2_{12}(x) = \frac{2e^x}{a + 2e^x + ae^{2x}},$$

where $a = \sqrt{1 + C}$, $0 \leq a < +\infty$. Introducing the parameter s via the relation

$$\cosh s = 1/a, \tag{13}$$

we obtain

$$f_{12}(x) = \frac{1}{2}\left(\tanh\frac{x + s}{2} + \tanh\frac{x - s}{2}\right), \tag{14}$$

$$h^2_{12}(x) = \frac{1}{2}\left(1 - \tanh\frac{x + s}{2}\tanh\frac{x - s}{2}\right).$$

We note that $f_{12}(x)$ is merely the sum $f_{13}(x + s) + f_{32}(x - s)$. This statement is valid for any value of s. At large $s \gg 1$, we also have, to an exponential accuracy, the relation

$$h_{12}(x) \approx h_{13}(x + s) + h_{32}(x - s).$$

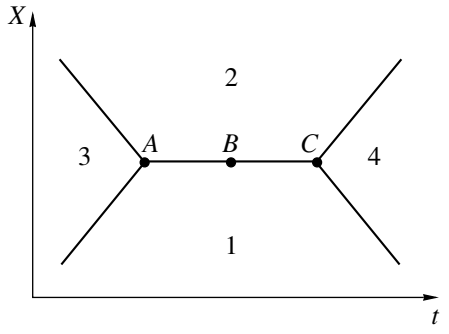

Fig. 3. Schematic representation of a collision between $1 \to 3$ and $3 \to 2$ domain walls. Numbers denote vacuum states in accordance with their arrangement in Fig. 1.

[In taking the square root of $h_{12}^2(x)$, we choose a plus sign.] Thus, we see that, for $s \gg 1$, the configuration specified by Eq. (14) has the form of two walls situated at the points $x = \pm s$. A transition between vacua 1 and 3 and a transition between vacua 3 and 2 occur at $x = -s$ and $x = +s$, respectively. It should be emphasized that Eq. (13) determines real-valued s only for $0 \le a \le 1$—in the region $1 < a < +\infty$, the parameter s is pure imaginary.

3. TIME DEPENDENCE FOR BPS-SATURATED CONFIGURATIONS

The problem of intersection of two domain walls within the supersymmetric model being discussed was investigated in [6]. Instead of solving the exact equations of motion for the fields involved, the authors of [6] made use of the following trick. It has already been mentioned above that, at $s \gg 1$, a configuration of the type in (14) represents two parallel $1 \to 3$ and $3 \to 2$ domain walls separated by the distance $2s$. If we now assume that s is not a constant but a quantity (weakly) dependent on the coordinate along the wall (for example, y), which is orthogonal to the x axis, we will obtain a configuration formed by two (slightly) nonparallel domain walls, which therefore intersect at a small angle.

On the basis of a similar argument, we consider here the time evolution of a collision between the $1 \to 3$ and $3 \to 2$ walls. We substitute expressions (14), which describe a configuration belonging to the type of $1 \to 3$ and $3 \to 2$ walls at the points $x = -s$ and $x = +s$ into the expression that is obtained for energy from (2) with allowance for the definition of the fields f and h in terms of the fields ϕ and χ. Assuming that the parameter s is not a constant but a quantity dependent on the time t [this procedure is approximate in that the functions in (14) at $s = s(t)$ must not be solutions to the equations of motion for the fields f and h; at this point, it is not assumed that the dependence $s(t)$ is weak], we obtain

$$E = 2E_0 + \mathcal{H}_{\text{eff}}, \tag{15}$$

where $E_0 = 4/3$ is the energy of the $1 \to 3$ or the $3 \to 2$ wall and

$$\mathcal{H}_{\text{eff}} = \frac{1}{2} m(s) \dot{s}^2. \tag{16}$$

Here, we have introduced the notation

$$m(s) = 4 \left[s \tanh s + \frac{5}{3} - \frac{2s}{\tanh s} + \frac{1}{\tanh^2 s} \left(\frac{s}{\tanh s} - 1 \right) \right]. \tag{17}$$

For the function $s(t)$, the effective Hamiltonian (16) yields the differential equation

$$m(s)\ddot{s} + \frac{1}{2} m'(s) \dot{s}^2 = 0\,. \tag{18}$$

In order to investigate the process of wall collision, it is necessary to take the initial configuration (14) at some $s(0) \gg 1$ and $\dot{s}(0) < 0$. Since the parameter s in (14) has the meaning of half the distance between the walls, such an initial configuration corresponds to the $1 \to 3$ and $3 \to 2$ walls approaching each other along the x axis, their initial velocities being $|\dot{s}(0)|$. By numerically solving Eq. (18) with the aforementioned initial conditions, it can be shown that $s(t)$ decreases to zero. In the region of small s, the equation can be solved analytically. The result is

$$m(s) \approx \frac{32}{15} s^2, \tag{19}$$
$$s(t) = \sqrt{2s(t_*)\dot{s}(t_*)(t - t_*) + s^2(t_*)},$$

where t_* is the time instant at which the numerical solution to Eq. (18) is matched with the analytic expression (19). It can be seen that the function $s(t)$ behaves as $\sqrt{t - t_0}$, where t_0 possesses the following property: the closer the matching instant t_* to the time instant at which the numerical solution for $s(t)$ vanishes, the closer t_0 to t_*. For the case of two interacting Skyrmions in the $(2 + 1)$-dimensional σ model, an equation that is similar to (18), but which involves a function $m(s)$ of a different form, was discussed in [9]. A square-root (singular) behavior of the variational function $s(t)$ [$s(t) \sim \sqrt{t - t_0}$], which determines the distance between the Skyrmions, was also found in that study.

When s changes from $+\infty$ to 0, the parameter a takes values from 0 to 1. At $s = 0$ (the point A in Fig. 3), we find for the fields in Eq. (14) that

$$f(x) = \tanh \frac{x}{2}, \quad h(x) = \frac{1}{\sqrt{2} \cosh \dfrac{x}{2}}. \tag{20}$$

In the region $1 < a < +\infty$, the parameter s defined according to (13) becomes a pure imaginary quantity;

therefore, it is convenient to introduce the variable $\tilde{s}$ specified by the relation

$$\cos\tilde{s} = 1/a. \tag{21}$$

The effective Hamiltonian for $\tilde{s}$ is analogous to that in (16); that is,

$$\mathcal{H}_{\text{eff}} = \frac{1}{2}\tilde{m}(\tilde{s})\dot{\tilde{s}}^2, \tag{22}$$

where

$$\tilde{m}(\tilde{s}) = 4\left[\tilde{s}\tan\tilde{s} - \frac{5}{3} + \frac{2\tilde{s}}{\tan\tilde{s}} + \frac{1}{\tan^2\tilde{s}}\left(\frac{\tilde{s}}{\tan\tilde{s}} - 1\right)\right]. \tag{23}$$

When $a = 1$ (or $s = 0$), we go over from the variable s to the variable $\tilde{s}$, which increases from 0 to $\pi/2$. At $\tilde{s} = \pi/2$ (the point B in Fig. 3), the profiles of the fields f and h are given by

$$f(x) = \tanh x, h(x) \equiv 0. \tag{24}$$

After that, $\tilde{s}$ decreases to zero and becomes pure imaginary. When this variable reaches the value of $\tilde{s} = 0$ (the point C in Fig. 3), we return to the variable s, which begins to increase from 0 to $+\infty$. We note that, for $\tilde{s} \ll 1$ and $|\tilde{s} - \pi/2| \ll 1$, we have also used approximate analytic solutions to the equation of motion. The variables s and $\tilde{s}$ versus time are displayed in Fig. 4 for two values of the initial wall velocity ($|\dot{s}(0)| = 0.05$ and $|\dot{s}(0)| = 0.1$). In order to test the applicability of the above approximation, where we have treated s as a dynamical variable, we solved numerically the Cauchy problem, taking the same initial conditions for the set of field equations

$$\frac{\partial^2 f}{\partial t^2} - \frac{\partial^2 f}{\partial x^2} - 2f(1 - f^2 - h^2) + \frac{4}{\rho}fh^2 = 0, \tag{25}$$
$$\frac{\partial^2 h}{\partial t^2} - \frac{\partial^2 h}{\partial x^2} - \frac{2}{\rho}h(1 - f^2 - h^2) + \frac{4}{\rho^2}hf^2 = 0,$$

which follow from the Lagrangian specified by Eq. (1). A comparison of these results reveals that, at low values of the initial wall velocities ($|\dot{s}(0)| \ll 1$), numerical solutions to the set of Eqs. (25) (the equations of motion) comply well with the approximate solutions that are obtained from the effective Lagrangian. This good agreement means that, at identical boundary conditions—that is, at identical values of $\dot{s}(0)$—one cannot visually observe a sizable distinction between the evolution of the initial conditions according to the set of Eqs. (25) and the configurations that are specified by (14) and which correspond to values of the parameter s at the same values of t. This confirms that the dynamical-variable approximation used is reasonable in studying the interaction of domain walls. With increasing initial wall velocity $|\dot{s}(0)|$, the numerical solutions to the field problem specified by Eqs. (25) begin to deviate significantly from solutions

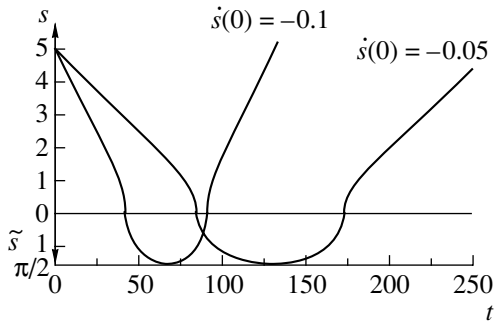

Fig. 4. Unified dynamical variable s, $\tilde{s}$ for two different values of the initial wall velocity $|\dot{s}(0)|$.

to Eq. (18), which follows from the effective Hamiltonian featuring one dynamical variable s, whence we conclude that different degrees of freedom play an important role in fast collisions.

4. TIME DEPENDENCE FOR NON-BPS CONFIGURATIONS

Let us now consider a collision of $3 \to 2$ and $2 \to 4$ walls (and $3 \to 1$ and $1 \to 4$ walls as well). In contrast to the preceding case, there does not exist here an exact solution yielding a configuration belonging to the type of two $3 \to 2$ and $2 \to 4$ walls situated consecutively by analogy with the $1 \to 2$ solution (14). For this reason, we have to construct a trial solution of the $3 \to 2 \to 4$ type. This can be done, for example, by taking a superposition of two elementary walls $3 \to 2$ and $2 \to 4$ situated at the points $x = -x_0$ and $x = +x_0$, respectively; that is,

$$f_{324}(x, x_0) = f_{32}(x + x_0) + f_{24}(x - x_0) - 1, \tag{26}$$
$$h_{324}(x, x_0) = h_{32}(x + x_0) + h_{24}(x - x_0),$$

where

$$f_{32}(x) = \frac{1}{2}\left(1 + \tanh\frac{x}{2}\right), \tag{27}$$
$$h_{32}(x) = \sqrt{\frac{1}{2}\left(1 - \tanh\frac{x}{2}\right)},$$
$$f_{24}(x) = \frac{1}{2}\left(1 - \tanh\frac{x}{2}\right), \tag{28}$$
$$h_{24}(x) = -\sqrt{\frac{1}{2}\left(1 + \tanh\frac{x}{2}\right)}.$$

We note that, upon the substitution of $f = 0$ into the set of Eqs. (25), one can easily obtain the exact diagonal solution $3 \to 4$:

$$f_{34}(x) \equiv 0, \quad h_{34}(x) = -\tanh\frac{x}{2}. \tag{29}$$

The energy of this configuration is $E_{34} = 16/3$. In order to obtain the energy of the configuration in (26)

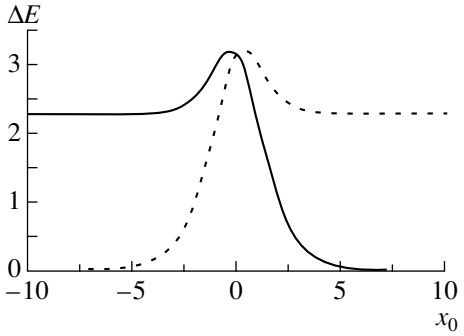

Fig. 5. Potential ΔE_{324} as a function of x_0 (solid curve) and potential ΔE_{314} as a function of $-x_0$ (dashed curve).

as a function of x_0, we must substitute (26) into the Hamiltonian. As a result, we obtain

$$E_{324}(x_0) = 2E_0 + \Delta E_{324}(x_0), \tag{30}$$

where

$$\Delta E_{324} = \int\limits_{-\infty}^{+\infty} dx \left[2\frac{df_{32}}{dx}\frac{df_{24}}{dx} + 2\rho\frac{dh_{32}}{dx}\frac{dh_{24}}{dx} \right. \tag{31}$$
$$+ (1 - f_{324}^2 - h_{324}^2)^2 + \frac{4}{\rho}f_{324}^2 h_{324}^2$$
$$- (1 - f_{32}^2 - h_{32}^2)^2 - \frac{4}{\rho}f_{32}^2 h_{32}^2$$
$$\left. -(1 - f_{24}^2 - h_{24}^2)^2 - \frac{4}{\rho}f_{24}^2 h_{24}^2 \right].$$

For the sake of brevity, we have introduced here the following notation: $f_{32} \equiv f_{32}(x + x_0)$, $h_{32} \equiv h_{32}(x + x_0)$, $f_{24} \equiv f_{24}(x - x_0)$, and $h_{24} \equiv h_{24}(x - x_0)$. We have obtained ΔE_{324} as a function of x_0 numerically (Fig. 5, solid curve). In the limit of large x_0, the configuration in (26) reduces to two isolated walls $3 \to 2$ and $2 \to 4$. Therefore, their total energy is $2E_0$, and we have $\Delta E_{324} \approx 0$. It can be seen from Fig. 5 that the energy ΔE_{324} increases with decreasing x_0. At $x_0 = 0$, we have $\Delta E_{324}(0) \approx 3.119$. This corresponds to $E_{324}(0) \approx 5.786$. It should be noted that $E_{324}(0)$ is greater than $E_{34} = 16/3 \approx 5.333$. The energy of the $3 \to 2 \to 4$ configuration (26) has a maximum at $x_0 \approx -0.37$ with $(\Delta E_{324})_{\max} \approx 3.202$. At negative x_0 of large magnitude, $\Delta E_{324}(x_0)$ approaches the asymptotic value of 2.274. It should be noted, however, that, at negative x_0, the trial configuration (26) has, in fact, a form of the $3 \to 1 \to 4$ type (see Fig. 6) rather than a form of the $3 \to 2 \to 4$ type. It is obvious that, by analogy with (26), we can construct a $3 \to 1 \to 4$ ansatz of the form

$$f_{314}(x, x_0) = f_{31}(x + x_0) + f_{14}(x - x_0) + 1, \tag{32}$$
$$h_{314}(x, x_0) = h_{31}(x + x_0) + h_{14}(x - x_0),$$

where

$$f_{31}(x) = -\frac{1}{2}\left(1 + \tanh\frac{x}{2}\right), \tag{33}$$
$$h_{31}(x) = \sqrt{\frac{1}{2}\left(1 - \tanh\frac{x}{2}\right)};$$
$$f_{14}(x) = -\frac{1}{2}\left(1 - \tanh\frac{x}{2}\right), \tag{34}$$
$$h_{14}(x) = -\sqrt{\frac{1}{2}\left(1 + \tanh\frac{x}{2}\right)}.$$

The energy of the $3 \to 1$ and $1 \to 4$ walls is identical to the energy of the $3 \to 2$ and $2 \to 4$ walls. Therefore, the energy of the configuration in (32) as a function of x_0 is given by

$$E_{314}(x_0) = 2E_0 + \Delta E_{314}(x_0), \tag{35}$$

where the "potential" $\Delta E_{314}(x_0)$ is analogous to $\Delta E_{324}(x_0)$ in (31). The profile of the function $\Delta E_{314}(x_0)$ is identical to that of $\Delta E_{324}(x_0)$. It was mentioned above that, at $x_0 < 0$, the ansatz in (26) has a form of the $3 \to 1 \to 4$ type (Fig. 6*b*). As to the configuration in (32), it has a form of the $3 \to 2 \to 4$ type at negative values of x_0 (Fig. 6*d*). It should be noted that $h_{324}(x, -x_0) \neq h_{314}(x, x_0)$; that is, the configurations in Figs. 6*a* and 6*d* are not identical. The same is true for the configurations in Figs. 6*b* and 6*c* as well. In order to compare the energies of the configurations in (26) and (32), which belong to the same type, it is necessary to plot the graphs of $\Delta E_{324}(x_0)$ and $\Delta E_{314}(-x_0)$ [or of $\Delta E_{314}(x_0)$ and $\Delta E_{324}(-x_0)$] in the same coordinate axes. This is precisely what was done in Fig. 5, from which we can see that, for the chosen type, a configuration characterized by positive values of x_0 has a minimum energy.

We solved numerically the set of field Eqs. (25) with the initial conditions (26), where the $3 \to 2$ and $2 \to 4$ walls are situated at a distance $2x_0 \gg 1$ and approach each other with initial velocities v_i. Depending on the initial velocities, various types of evolution were observed. As long as v_i was less than a critical value $v_{\rm cr}^{\rm num}$, the $3 \to 2$ and $2 \to 4$ walls collided and then moved apart to infinity. As a result, we again obtained a $3 \to 2 \to 4$ configuration after a collision. For initial velocities satisfying the condition $v_i > v_{\rm cr}^{\rm num}$, the collision process proceeded in a somewhat different way. The difference was that, after a collision event, we observed a $3 \to 1 \to 4$ configuration. For the critical velocity, we obtained the value of $v_{\rm cr}^{\rm num} \approx 0.9120$. The presence of different collision regimes is a consequence of the fact that the energy of the $3 \to 2 \to 4$ configuration is not degenerate in the parameter x_0; that is, there is a potential interaction between the $3 \to 2$ and $2 \to 4$ domain walls. It should be noted that there is no potential interaction in the case of BPS-saturated walls.

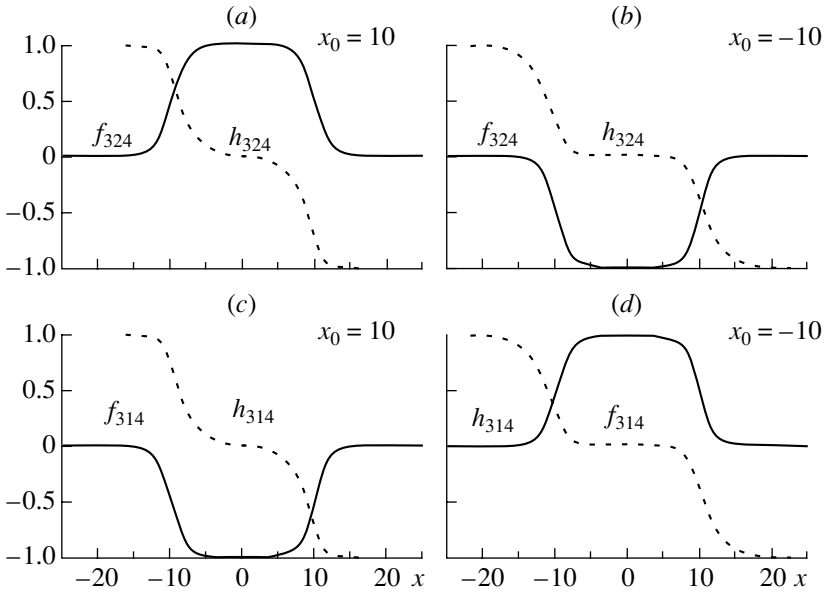

Fig. 6. Profiles of the fields (solid curves) $f(x)$ and (dashed curves) $h(x)$ for the $3 \to 2 \to 4$ (26) and $3 \to 1 \to 4$ configurations (32) at $x_0 = \pm 10$.

Within the potential approach, it is also possible to explain the existence of the critical velocity. From Fig. 5, it can be seen that (inelastic) reflection can be expected if the kinetic energy of the $3 \to 2$ and $2 \to 4$ walls is less than $\Delta E^* \approx 3.119$ (this is the energy that corresponds to the intersection of the graphs). The critical-velocity value of $v_{cr}^* \approx 0.8874$, which is close to the "experimental" value of $v_{\rm cr}^{\rm num}$, corresponds to the energy ΔE^*. If the kinetic energy of the walls exceeds ΔE^*, it is natural to expect that a collision process results in the formation of a configuration that belongs to the type in (26) and which is characterized by negative x_0. But the configuration in (26) at negative x_0 is of the $3 \to 1 \to 4$ type (see Fig. 6), and it can be seen from Fig. 5 that, in this sector, configurations of the type in (32) have a lower energy. Therefore, the configuration in (26) for $x_0 < 0$ will decay into (32), whereupon the $3 \to 1$ and the $1 \to 4$ wall formed move apart at infinity.

It should also be noted that the initial configuration (26) at $x_0 = 0$ with $v_i = 0$ can be interpreted as an excitation of the static solution (29), whence it follows that, upon radiating part of the energy, such an initial configuration leads to the formation of the kink that has the form (29) and which features an excited discrete (shape) mode. At nonzero values of x_0 or v_i, we were unable to obtain such an excited kink in numerical calculations—we observed a pair of walls moving apart, either $3 \to 1$ and $1 \to 4$ or $3 \to 2$ and $2 \to 4$.

5. CONCLUSION

To summarize, we note once again that collisions of $1 \to 3$ and $3 \to 2$ (or $1 \to 4$ and $4 \to 2$) walls differ substantially from collisions of $3 \to 1$ and $1 \to 4$ (or $3 \to 2$ and $2 \to 4$) walls. In the first case, there is an exact static solution that is BPS-saturated and which corresponds to two parallel walls. Here, the energy of the configuration is independent of the parameter specifying the distance between the walls. Therefore, there is no "potential" interaction between them, and their collision at any (arbitrarily small) initial velocities is accompanied by a change in the vacuum between the walls (see Fig. 3). For a configuration formed by two parallel walls $3 \to 1$ and $1 \to 4$, there does not exist an exact solution. For this reason, we have constructed initial conditions from two separate solutions $3 \to 1$ and $1 \to 4$ and found that the energy depends on the degree of their overlap—that is, on the distance between the walls. Hence, a "potential" interaction arises between them. This leads to the emergence of two collision modes: at initial velocities less than the critical value, colliding walls are reflected without a change in the vacuum between the walls, while, at initial velocities greater than the critical value, the reflection of the colliding walls is accompanied by a change in the vacuum between the walls.

ACKNOWLEDGMENTS

We are grateful to M. B. Voloshin, A. V. Smilga, and A. I. Veselov for stimulating discussions.

This work was supported by the Russian Foundation for Basic Research (project nos. 98-02-17316 and 00-15-96562).

REFERENCES

1. M. A. Shifman, Phys. Rev. D **57**, 1258 (1998).
2. M. B. Voloshin, Phys. Rev. D **57**, 1266 (1998).
3. M. A. Shifman and M. B. Voloshin, Phys. Rev. D **57**, 2590 (1998).
4. M. Shifman and T. ter Veldhuis, Phys. Rev. D **62**, 065004 (2000).
5. D. Binosi, M. Shifman, and T. ter Veldhuis, TPI-MINN-00/27-T; hep-th/0006026.
6. S. V. Troitsky and M. B. Voloshin, Phys. Lett. B **449**, 17 (1999).
7. A. V. Smilga and A. I. Veselov, Nucl. Phys. B **515**, 163 (1998).
8. E. Bogomol'nyi, Yad. Fiz. **24**, 861 (1976) [Sov. J. Nucl. Phys. **24**, 449 (1976)]; M. K. Prasad and C. H. Sommerfeld, Phys. Rev. Lett. **35**, 760 (1975).
9. A. Kudryavtsev, B. Piette, and W. Zakrzewski, Phys. Lett. A **180**, 119 (1993).

Translated by A. Isaakyan

Physics of Atomic Nuclei, Vol. 64, No. 11, 2001, pp. 2051–2057. Translated from Yadernaya Fizika, Vol. 64, No. 11, 2001, pp. 2138–2144.

ELEMENTARY PARTICLES AND FIELDS
Theory

Phase Structure of the Nambu–Jona-Lasinio Model in a Constant Electromagnetic Field in d-Dimensional Curved Spacetime

Yu. I. Shil'nov* **and V. V. Chitov****

Kharkov State University, ul. Svobody 4, Kharkov, 61077 Ukraine

Received July 28, 2000; in final form, January 26, 2001

Abstract—Dynamical symmetry breaking in the Nambu–Jona-Lasinio model in a constant external electromagnetic field is studied in curved spacetime of arbitrary dimension. The effective potential of composite bifermion fields is calculated in the proper-time formalism to terms linear in curvature. Curvature- and electromagnetic-field-induced phase transitions are analyzed. © *2001 MAIK "Nauka/Interperiodica".*

1. INTRODUCTION

Models of four-fermion interaction, such as the Nambu–Jona-Lasinio (NJL) model [1] or the Gross–Neveu (GN) model [2], are usually considered as effective low-energy theories describing strong-interaction physics [3]. Such models possess nontrivial properties, including a dynamical symmetry breaking and dynamical mass generation, that are of particular importance in quantum field theory [4].

The mechanism of dynamical symmetry breaking depends substantially on temperature, density, chemical potential, external fields, curvature, and topology of spacetime, whose presence renders the phase structure of the NJL and GN models more complicated. It was revealed that a magnetic field always breaks chiral symmetry, whereas an electric field tends to restore it [5–11].

The effect of a gravitational field on dynamical symmetry breaking was also considered. In particular, it was found that the curvature of spacetime may induce phase transitions [12–16], which must be taken into account in constructing realistic scenarios of the evolution of the early Universe.

In the present study, we examine dynamical symmetry breaking within the NJL model in curved spacetime of d dimensions in an external electromagnetic field. We use dimensional regularization because, in the case under consideration, it is the most convenient regularization scheme [17]. The contribution of a constant electromagnetic field such that $\mathbf{E}\cdot\mathbf{H}=0$ is calculated exactly in the proper-time formalism [18], whereas the dependence on curvature is taken into account as a linear contribution to the effective potential of composite bifermion fields. The results of our numerical analysis suggest the existence of additional phase transitions induced both by the electromagnetic field and by the curvature of space.

2. EFFECTIVE POTENTIAL OF THE MODEL

The NJL model in curved spacetime of arbitrary dimension is described by the action functional [1]

$$S=\int d^dx\sqrt{-g}\left\{i\bar\psi\gamma^\mu(x)D_\mu\psi + \frac{\lambda}{2N}\left[(\bar\psi\psi)^2+(\bar\psi i\gamma_5\psi)^2\right]\right\}, \quad (1)$$

where g is the determinant of the metric tensor; λ is the coupling constant; and the covariant derivative D_μ is given by

$$D_\mu=\partial_\mu-ieA_\mu-\frac{i}{4}\omega^{ab}{}_\mu\,\sigma_{ab}, \quad (2)$$

where A_μ is the vector potential of the electromagnetic field and $\omega^{ab}{}_\mu$ is the usual spin connection.

The local Dirac matrices $\gamma_\mu(x)$ are expressed in terms of the conventional matrices γ_a in flat space and the vierbein e^a_μ as

$$\gamma^\mu(x)=\gamma^a e^\mu_a(x),\quad \sigma_{ab}=\frac{i}{2}[\gamma_a,\gamma_b]. \quad (3)$$

By N, we denote the number of the bispinor fields ψ_a. The dimension of the spinor representation is assumed to be equal to four. Greek and Latin indices correspond to curved tangent space and flat tangent space, respectively.

Introducing the auxiliary fields

$$\sigma=-\frac{\lambda}{N}(\bar\psi\psi),\quad \pi=-\frac{\lambda}{N}\bar\psi i\gamma_5\psi, \quad (4)$$

*e-mail: shilnov@mail.ru
**e-mail: Vladislav.V.Chitov@univer.kharkov.ua

1063-7788/01/6411-2051$21.00

we can recast the action functional (1) into the form

$$S = \int d^d x\sqrt{-g}\left\{ i\bar{\psi}\gamma^\mu D_\mu \psi - \frac{N}{2\lambda}\left(\sigma^2+\pi^2\right) - \bar{\psi}(\sigma + i\pi\gamma_5)\psi \right\}. \quad (5)$$

In the leading order of $1/N$ expansion, the standard expression for the effective action is then given by

$$\frac{1}{N}\Gamma_{\text{eff}}(\sigma,\pi) = -\int d^d x\sqrt{-g}\,\frac{\sigma^2+\pi^2}{2\lambda} - i\ln\det\left[i\gamma^\mu(x)D_\mu - (\sigma + i\gamma_5\pi)\right]. \quad (6)$$

Since the final expression depends only on $\sigma^2+\pi^2$, we set $\pi = 0$. This means that we actually go over to the GN model [2]. Defining the effective potential for constant σ and π as

$$V_{\text{eff}} = -\frac{\Gamma_{\text{eff}}}{N\int d^d x\sqrt{-g}},$$

we obtain

$$V_{\text{eff}} = \frac{\sigma^2}{2\lambda} + i\,\text{tr}\,\ln\langle x|\left[i\gamma^\mu(x)D_\mu - \sigma\right]|x\rangle. \quad (7)$$

Using the Green's function satisfying the equation

$$(i\gamma^\mu D_\mu - \sigma)_x\, G(x,x',\sigma) = \delta(x-x'), \quad (8)$$

we derive the formula

$$V'_{\text{eff}}(\sigma) = \frac{\sigma}{\lambda} - i\,\text{tr}\,G(x,x,\sigma). \quad (9)$$

For the effective potential, the linear correction in curvature is readily calculated by employing the local-momentum representation [19, 20]. Using the special Riemann coordinates [19, 21], we arrive at

$$g_{\mu\nu}(x) = \eta_{\mu\nu} - \frac{1}{3}R_{\mu\rho\sigma\nu}\,y^\rho y^\sigma, \quad (10)$$

$$e^\mu{}_a(x) = \delta^\mu_a + \frac{1}{6}R^\mu{}_{\rho\sigma a}\,y^\rho y^\sigma, \quad (11)$$

$$\omega^{ab}{}_\mu\sigma_{ab} = \frac{1}{2}R^{ab}{}_{\mu\lambda}\,y^\lambda\sigma_{ab}, \quad (12)$$

$$y = x - x'. \quad (13)$$

The vector potential of the electromagnetic field is given by

$$A_\mu(x) = -\frac{1}{2}F_{\mu\nu}x^\nu, \quad (14)$$

where $F_{\mu\nu}$ is the strength tensor of the electromagnetic field. Substituting Eqs. (10)–(12) into Eq. (8), we find that the Green's function satisfies the equation

$$\left[i\gamma^a\left(\delta^\mu_a + \frac{1}{6}R^\mu{}_{\rho\sigma a}\,y^\rho y^\sigma\right) \times\left(\partial_\mu - \frac{i}{8}R_{bc\mu\lambda}\,y^\lambda\sigma^{bc} - ieA_\mu\right) - \sigma\right] \times G(x,x',\sigma) = \delta(x-x'). \quad (15)$$

We then expand the Green's function in powers of the curvature of spacetime; that is,

$$G = G_0 + G_1 + \ldots, \quad (16)$$

where G_0 is the Green's function in a flat space, $G_1 \sim R$, etc. After straightforward but tedious computations, we arrive at

$$\tilde{G}_1(x-x',\sigma) = \int dx''\,G_{00}(x-x'',\sigma) \times\left[-\frac{i}{6}\,\gamma^a R^\mu{}_{\rho\sigma a}\,(x''-x')^\rho(x''-x')^\sigma\,\partial^{x''}_\mu \times\tilde{G}_0(x''-x',\sigma) - \frac{1}{8}\,\gamma^a\sigma^{bc}R_{bca\lambda}\,(x''-x')^\lambda \times\tilde{G}_0(x''-x',\sigma)\right], \quad (17)$$

where the function $\tilde{G}$ is related to G by the equation

$$G(x,x') = \exp\left[ie\int\limits_x^{x'} A_\mu dx^\mu\right]\tilde{G}(x-x') \quad (18)$$

and G_{00} is the Green's function for free fermions in a flat spacetime. In what follows, we do not discriminate between Greek and Latin indices because this is beyond the approximation linear in curvature.

In order to derive the effective potential on the basis of expression (9), we need only the values of all relevant quantities in the limit $x \to x'$. We can also simplify formula (17) by considering a space of constant curvature R, where

$$R_{\mu\sigma\kappa\lambda} = \frac{R}{d(d-1)}\left(\eta_{\mu\kappa}\eta_{\sigma\lambda} - \eta_{\mu\lambda}\eta_{\kappa\sigma}\right). \quad (19)$$

Thus, the expression for the Green's function $\tilde{G}_1$ in the space of arbitrary dimension d takes the form

$$\tilde{G}_1(0,\sigma) = -\frac{iR}{12d(d-1)} \times\int dz G_{00}(-z,\sigma)\left[2\gamma^\nu z_\nu z^\mu\,\partial_\mu\,\tilde{G}_0(z,\sigma) - 2z^2\gamma^\mu\,\partial_\mu\,\tilde{G}_0(z,\sigma) + 3(d-1)\gamma^\mu z_\mu\,\tilde{G}_0(z,\sigma)\right]. \quad (20)$$

We consider the electromagnetic-field configuration

$$\mathcal{G} = -\frac{1}{8}F_{\mu\nu}F_{\rho\sigma}\epsilon^{\mu\nu\rho\sigma} = \mathbf{E}\cdot\mathbf{H} = 0,$$
$$\mathcal{F} = \frac{1}{4}F_{\mu\nu}F^{\mu\nu} = \frac{1}{2}(H^2 - E^2) \neq 0. \quad (21)$$

The proper-time representation for the Green's functions in a flat space has the form [18]

$$\tilde{G}_0(z,\sigma) = e^{-i\frac{\pi d}{4}} \int_0^\infty \frac{ds}{(4\pi s)^{d/2}} e^{-is\sigma^2} \times \exp\left(-\frac{i}{4s} z_\mu C^{\mu\nu} z_\nu\right) \left(\sigma + \frac{1}{2s}\gamma^\mu C_{\mu\nu} z^\nu - \frac{e}{2}\gamma^\mu F_{\mu\nu} z^\nu\right) \left[(e\xi s)\coth(e\xi s) - \frac{es}{2}\gamma^\mu\gamma^\nu F_{\mu\nu}\right], \quad (22)$$

$$\tilde{G}_{00}(-z,\sigma) = e^{-i\frac{\pi d}{4}} \int_0^\infty \frac{dt}{(4\pi t)^{d/2}} \times \exp\left[-i\left(\sigma^2 t + \frac{z^2}{4t}\right)\right] \left(\sigma + \frac{1}{2t}\gamma^\mu z_\mu\right), \quad (23)$$

where

$$C_{\mu\nu} = \eta_{\mu\nu} + F_\mu{}^\lambda F_{\lambda\nu} \frac{(e\xi s)\coth(e\xi s) - 1}{\xi^2} \quad (24)$$

and $\xi^2 = E^2 - H^2$ is an invariant of the electromagnetic field.

There are two qualitatively different cases. If $E > H$, in which case the magnetic field can be reduced to zero by a Lorentz transformation, ξ is real. Upon the Wick rotation $is \to s, it \to t$, which is necessary for evaluating the relevant integral in Euclidean space, the function $\cot(e\xi s)$ in the integrand tends to infinity at regularly spaced points. The existence of an infinite number of poles on the contour of integration means that we must take into account the contribution of the respective residues, whereupon the effective potential develops an imaginary part, which indicates that the ground state is unstable, with the result that it can decay, producing particles. However, a solution to this problem is beyond the scope of the present article. We only mention that such an instability stems from the absence of asymptotically free fermion states in a constant external electric field. In order to study a dynamical breakdown of symmetry, we chose the simplest possibility of relatively small ξ values at which particle production rate is exponentially suppressed. In this case, the real part of the effective potential still determines the ground state of the system being considered to the required accuracy. As a consequence, the mechanism of a dynamical symmetry breaking is governed by the real part of the effective potential exclusively; technically, this means that we need only the principal values of all integrals. In what follows, we everywhere discard the imaginary part of the effective potential.

If $E < H$, in which case we can obtain a purely magnetic field, ξ is pure imaginary, with the result that, upon a Wick rotation, the function $\cot(e\xi s)$ has no poles on the real axis other than that at the origin.

Substituting the expression for the Green's function in a flat space into formula (20) and performing a Wick rotation and some transformations, we obtain the effective potential in the form

$$V_{\text{eff}}(\sigma) = \frac{\sigma^2}{2\lambda} + \frac{2}{(4\pi)^{d/2}} \text{p.v.} \int_0^\infty \frac{ds}{s^{d/2+1}} e^{-s\sigma^2} (e\xi s) \times \cot(e\xi s) - \frac{R}{3d(4\pi)^{d/2}} \times \text{p.v.} \int_0^\infty \int_0^\infty \frac{ds\,dt\,e^{-(s+t)\sigma^2}}{(s+t)^{d/2+1}(1+(e\xi t)\cot(e\xi s))^2} \times \Big[-(e\xi t)\left((e\xi t) + (e\xi s)\right) + \left(\left(4 - \frac{d}{2}\right)(e\xi t) + \frac{3d}{2}(e\xi s)\right)\cot(e\xi s) + (e\xi t)\left(\left(\frac{3d}{2} - 4\right)(e\xi s) - \frac{d}{2}(e\xi t)\right)\cot^2(e\xi s)\Big]. \quad (25)$$

The integrals appearing in this expression diverge at the lower limit; therefore, we must regularize them. The simplest regularization scheme involves introducing a cutoff parameter Λ; moreover, this scheme is necessary for comparing our result with the results for $d = 3, 4$ in the limit $\xi \to 0$ [15]:

$$V_{\text{eff}}^{(d=3)}(\sigma) = \frac{\sigma^2}{2\lambda} + \frac{\Lambda^3}{6\pi^{3/2}} \left\{\left(1 - 2\frac{\sigma^2}{\Lambda^2}\right) \times \exp\left(-\frac{\sigma^2}{\Lambda^2}\right) + 2\sqrt{\pi}\sigma^3 \,\text{erfc}\left(\frac{\sigma}{\Lambda}\right) - \frac{R}{4\Lambda^2}\left[\exp\left(-\frac{\sigma^2}{\Lambda^2}\right) - \sqrt{\pi}\,\sigma\,\text{erfc}\left(\frac{\sigma}{\Lambda}\right)\right]\right\}, \quad (26)$$

$$V_{\text{eff}}^{(d=4)}(\sigma) = \frac{\sigma^2}{2\lambda} + \frac{1}{(4\pi)^2}\left\{\left(\Lambda^4 - \Lambda^2\sigma^2\right) \times \exp\left(-\frac{\sigma^2}{\Lambda^2}\right) + \sigma^4 \,\text{Ei}\left(\frac{\sigma^2}{\Lambda^2}\right) - \frac{R}{6}\left[\exp\left(-\frac{\sigma^2}{\Lambda^2}\right) - \sigma^2\,\text{Ei}\left(\frac{\sigma^2}{\Lambda^2}\right)\right]\right\} \quad (27)$$

with

$$\text{erfc}(x) = \frac{2}{\sqrt{\pi}} \int_x^\infty e^{-t^2} dx, \quad (28)$$

$$\text{Ei}(x) = \int_x^\infty \frac{\exp(-s)}{s}\, ds. \quad (29)$$

Expanding (26) and (27) and retaining only those terms that do not vanish in the limit $\Lambda \to 0$, we arrive at

$$V_{\rm eff}^{(d=3)}(\sigma) = \frac{\sigma^2}{2\lambda_R} + \frac{\sigma^3}{3\pi} + \frac{R\sigma}{24\pi}, \tag{30}$$

$$\frac{1}{\lambda_R} = \frac{1}{\lambda} - \frac{\Lambda}{\pi^{3/2}}, \tag{31}$$

$$V_{\rm eff}^{(d=4)}(\sigma) = \frac{\sigma^2}{2\lambda} \tag{32}$$
$$- \frac{1}{(4\pi)^2}\left\{2\,\Lambda^2\sigma^2 + \sigma^4\left(\ln\frac{\sigma^2}{\Lambda^2} + \gamma - \frac{3}{2}\right)\right.$$
$$\left. + \frac{R\,\sigma^2}{6}\left(\ln\frac{\sigma^2}{\Lambda^2} + \gamma - 1\right)\right\} + \mathcal{O}\left(\frac{\sigma^2}{\Lambda^2}\right),$$

where γ is the Euler constant.

A regularization in terms of a ζ function is the most convenient for our purposes because it can be used in the case of arbitrary space dimensions. Performing the first integration by means of the formula

$$\int_0^\infty dx x^{s-1} e^{-ax}\coth(cx)$$
$$= \Gamma(s)\left[2^{1-s}c^{-s}\zeta\left(s, \frac{a}{2c}\right) - a^{-s}\right],$$

we obtain

$$\frac{2}{(4\pi)^{d/2}}\text{p.v.}\int_0^\infty \frac{ds}{s^{d/2-1}} e^{-s\sigma^2}(e\xi s)\coth(e\xi s) \tag{33}$$
$$= \text{Re}\left\{\left(\frac{ie\xi}{2\pi}\right)^{d/2}\Gamma\left(1-\frac{d}{2}\right)\right.$$
$$\left.\times\left[2\zeta\left(1-\frac{d}{2}, \frac{\sigma^2}{2ie\xi}\right) - \left(\frac{\sigma^2}{2ie\xi}\right)^{d/2-1}\right]\right\}.$$

Although the integral diverges at the lower limit, the expression with the ζ function is finite because the functions $\Gamma(z)$ and $\zeta(z,x)$ can be analytically continued to all points of the domain $\text{Re}(z) < 0$, with the exception of the poles of $\Gamma(z)$ at $z = 0,\ -1,\ -2, \ldots$.

In the limit of a weak electromagnetic field ($e\xi \ll \sigma^2$), the curvature-dependent term in the effective potential is simplified. Since the curvature R is assumed to be small in the linear approximation, we obtain

$$V_R = -\frac{R}{6(4\pi)^{d/2}}\int_0^\infty dx e^{-x\sigma^2} x^{-d/2} \tag{34}$$
$$= -\frac{R\sigma}{6(4\pi)^{d/2}}\Gamma\left(1-\frac{d}{2}\right).$$

This expression is also finite for $2 < d < 4$. Thus, we can rewrite the effective potential in such a way that it becomes finite and free from the cutoff parameter Λ:

$$\text{Re}\, V_{\rm eff}(\sigma) = \frac{\sigma^2}{2\lambda} - \frac{R\,\sigma^{d-2}}{6(4\pi)^{d/2}}\Gamma\left(1-\frac{d}{2}\right) \tag{35}$$
$$+ \text{Re}\left\{\left(\frac{ie\xi}{2\pi}\right)^{d/2}\Gamma\left(1-\frac{d}{2}\right)\right.$$
$$\left.\times\left[2\,\zeta\left(1-\frac{d}{2}, \frac{\sigma^2}{2ie\xi}\right) - \left(\frac{\sigma^2}{2ie\xi}\right)^{\frac{d}{2}-1}\right]\right\}.$$

3. PHASE STRUCTURE OF THE MODEL

In order to find the ground state of the system, it is necessary to determine the σ value at which the effective potential has the global minimum. The conditions of the global minimum are as follows: the vanishing of the first derivative (stationarity condition),

$$\left.\frac{\partial\,\text{Re}\, V_{\rm eff}(\sigma)}{\partial\sigma}\right|_{\sigma_{\min}} = 0; \tag{36}$$

the positiveness of the second derivative (stability of the extremum),

$$\left.\frac{\partial^2\,\text{Re}\, V_{\rm eff}(\sigma)}{\partial\sigma^2}\right|_{\sigma_{\min}} \geq 0; \tag{37}$$

and the condition that the effective potential at this minimum is smaller than its values at other local minima,

$$\text{Re}\, V_{\rm eff}(\sigma_{\min}) \leq \text{Re}\, V_{\rm eff}(0). \tag{38}$$

If $H > E$, the parameter ξ is pure imaginary, in which case it is convenient to use the parameter ρ defined as $\rho = \sqrt{H^2 - E^2} = i\xi$. The effective potential then takes the form

$$V_{\rm eff}(\sigma) = \frac{\sigma^2}{2\lambda} - \frac{R\,\sigma^{d-2}}{6(4\pi)^{d/2}}\Gamma\left(1-\frac{d}{2}\right) \tag{39}$$
$$+ \left(\frac{e\rho}{2\pi}\right)^{d/2}\Gamma\left(1-\frac{d}{2}\right)$$
$$\times\left[2\,\zeta\left(1-\frac{d}{2}, \frac{\sigma^2}{2e\rho}\right) - \left(\frac{\sigma^2}{2e\rho}\right)^{\frac{d}{2}-1}\right].$$

From the condition of the vanishing of the first derivative, it follows that

$$\frac{1}{\lambda} - \frac{(d-2)R\,\sigma^{d-4}}{6(4\pi)^{d/2}}\Gamma\left(1-\frac{d}{2}\right) \tag{40}$$
$$- \frac{1}{2\pi}\left(\frac{e\rho}{2\pi}\right)^{\frac{d}{2}-1}\Gamma\left(2-\frac{d}{2}\right)$$
$$\times\left[2\,\zeta\left(2-\frac{d}{2}, \frac{\sigma^2}{2e\rho}\right) - \left(\frac{\sigma^2}{2e\rho}\right)^{\frac{d}{2}-2}\right] = 0.$$

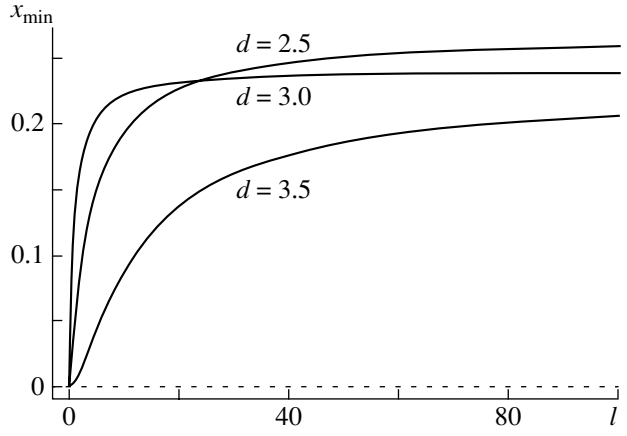

Fig. 1. Dependence of $x_{\min}$ on l in a magnetic field at $r = 1$.

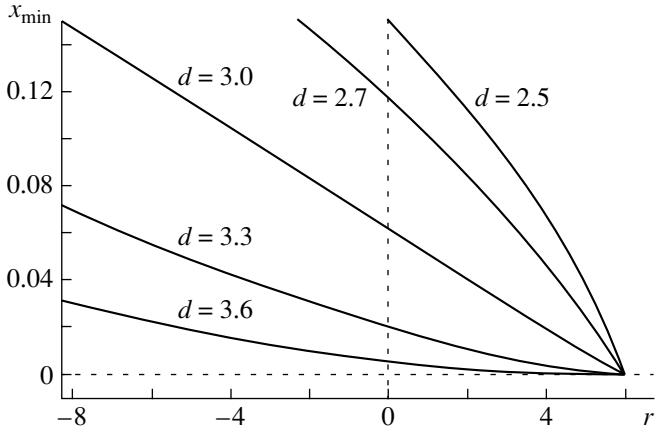

Fig. 2. Dependence of $x_{\min}$ on r in a magnetic field at $l = 1$.

To minimize the number of the parameters, we introduce dimensionless parameters in the stationarity condition; that is,

$$\frac{1}{l} + \frac{(r+6)x^{d-4}}{3(4\pi)^{d/2}}\,\Gamma\left(2-\frac{d}{2}\right) \qquad (41)$$
$$-\frac{4}{(4\pi)^{d/2}}\,\Gamma\left(2-\frac{d}{2}\right)\zeta\left(2-\frac{d}{2},x^2\right) = 0,$$

where

$$l = \lambda\,(2e\rho)^{\frac{d}{2}-1},\quad r = \frac{R}{2e\rho},\quad \frac{\sigma^2}{2e\rho} = x^2. \qquad (42)$$

Any nontrivial solution $x_{\min}$ satisfying the conditions in (36)–(38) corresponds to a minimum of the effective potential, $\sigma_{\min} = x_{\min}\sqrt{2e\rho} \neq 0$. The results of our numerical analysis are presented in Figs. 1 and 2.

Figure 1 shows $x_{\min}$ as a function of l at various values of d and the fixed value of $r = 1$, which is less than the critical value r_c. It can be seen that a nontrivial solution exists for any positive value of the coupling constant and that, for $l \to \infty$, it tends to $x_{\rm as}$. This solution has the form

$$\frac{(r+6)\,x_{\rm as}^{d-4}}{12} - \zeta\left(2-\frac{d}{2},x_{\rm as}^2\right) = 0. \qquad (43)$$

Note that $x_{\rm as}$ tends to zero when $r \to r_c$. Hence, the critical value r_c is given by

$$r_c = 6 + 12x^{4-d}\zeta\left(2-\frac{d}{2},1+x^2\right)\Big|_{x\to 0}, \qquad (44)$$

whence we obtain $r_c^{d<4} = 6$ for $d < 4$ and $r_c^{d=4} = 0$ for $d = 4$.

Figure 2 illustrates the second-order phase transition induced by the curvature $R = 2er\rho$ for various d. The symmetry is dynamically broken at $r < r_c$, and the ground state corresponds to a nontrivial solution $x_{\min}$. The symmetric phase corresponds to $r > r_c$. Since $r = \dfrac{R}{2e\rho}$, we conclude that a magnetic field breaks the symmetry, whereas a curvature tends to restore it. It should be borne in mind that the value of $r_c = 6$ is consistent with the condition that the curvature is small. The point is that, in the weak-field limit, $\sigma^2 \gg 2e\rho$, whereas the expansion in the curvature is valid for $R \ll \sigma^2$; therefore, the parameter $r = \dfrac{R}{2e\rho} = \dfrac{R}{\sigma^2}\dfrac{\sigma^2}{2e\rho}$ can be substantially greater than other parameters of the model.

In the case of $E > H$, the parameter ξ is real. In dimensionless units, the effective potential and the stationarity condition are given by

$$\mathrm{Re}\,v_{\rm eff}(x) = \frac{x^2}{2\,l} - \frac{r\,x^{d-2}}{6(4\pi)^{d/2}}\Gamma\left(1-\frac{d}{2}\right) \qquad (45)$$
$$+\frac{2}{(4\pi)^{d/2}}\Gamma\left(1-\frac{d}{2}\right)\mathrm{Re}\left[i^{d/2}\zeta\left(1-\frac{d}{2},-ix^2\right)\right],$$

$$\frac{1}{l} + \frac{r\,x^{d-4}}{3(4\pi)^{d/2}}\Gamma\left(2-\frac{d}{2}\right) - \frac{4}{(4\pi)^{d/2}}\Gamma\left(2-\frac{d}{2}\right) \qquad (46)$$
$$\times\mathrm{Re}\left[i^{d/2-1}\zeta\left(2-\frac{d}{2},-ix^2\right)\right] = 0,$$

where

$$v(x) = V(\sigma)(2e\xi)^{-d/2},\quad l = \lambda(2e\xi)^{\frac{d}{2}-1}, \qquad (47)$$
$$r = \frac{R}{2e\xi},\quad x^2 = \frac{\sigma^2}{2e\xi}.$$

The dependence of $x_{\min} = \sigma_{\min}/\sqrt{2e\xi}$ on the parameters l and r for various values of d was obtained numerically. This dependence at constant r and d

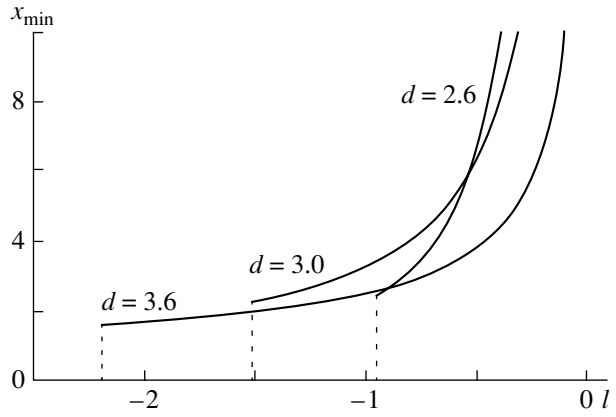

Fig. 3. Dependence of $x_{\min}$ on l in an electric field at $r = 3$.

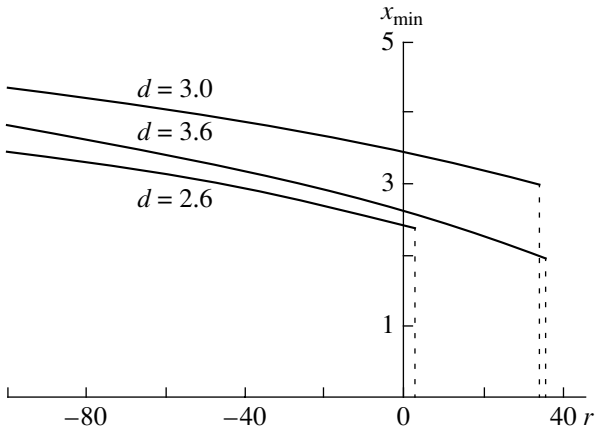

Fig. 4. Dependence of $x_{\min}$ on r in an electric field at $l = -0.9$.

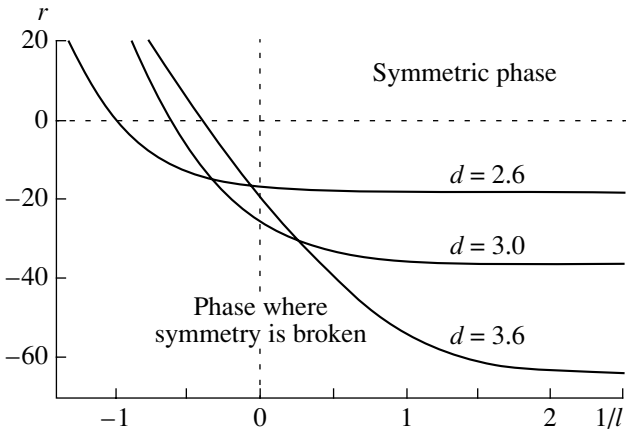

Fig. 5. Phase diagram $(r, 1/l)$ in an electric field.

$(r < r_c)$ is shown in Fig. 3; it is typical of first-order phase transitions. It can be concluded that this phase transition is induced by the electric field (at constant λ) or by a change in the coupling constant λ (at constant ξ).

Thus, an increase in the electric field restores symmetry, whereas an increase in the coupling constant breaks it.

The first-order phase transition (for $l > l_c$) induced by the curvature r is shown in Fig. 4. The curvature also restores symmetry. In both cases (Fig. 3 and Fig. 4), the critical point of the phase transition is determined by Eq. (38). It can be seen from the phase diagram in Fig. 5 that, in contrast to what occurs in flat spacetime, where symmetry is broken only at negative values of the coupling constant λ, nonsymmetric phase in curved spacetime can exist at positive values of the coupling constant as well.

4. CONCLUSION

We have studied the effect of external gravitational and electromagnetic fields on the phase structure of the four-fermion model in spacetime of arbitrary dimension.

In the case of a magnetic field, it has been shown that chiral symmetry is restored at $r = R/2e\rho = 6$ for all $d < 4$. The approximation used is applicable at these values of the parameter r, because the relevant simplifications in our formulas stem from the assumption that $e\rho/\sigma^2 \ll 1$, whereas the local-momentum representation is valid at small R/σ^2. For this reason, $R/2e\rho$ can be considerably greater than other parameters of the system.

In the case of an electric field, a first-order phase transition occurs not only at negative values of the coupling constant (as in flat space) but also at positive values. Both the curvature and the electric field tend to restore broken symmetry.

It turns out that the pattern of the phase transition undergoes no qualitative changes for values of d in the range $2 < d < 4$.

ACKNOWLEDGMENTS

The work of V.V. Chitov was supported in part by the International Science Education Program (ISEP) (grant no. PSU 082120).

REFERENCES

1. Y. Nambu and G. Jona-Lasinio, Phys. Rev. **122**, 345 (1961).
2. D. Gross and A. Neveu, Phys. Rev. D **10**, 3235 (1974).
3. T. Muta, *Foundation of Quantum Chromodynamics: An Introduction to Perturbative Methods in Gauge Theories* (World Sci., Singapore, 1987); M. Bando, T. Kugo, and K. Yamawaki, Phys. Rep. **164**, 217 (1988); B. Rosenstein, B. J. Warr, and S. H. Park, Phys. Rep. **205**, 59 (1991); T. Hatsuda and T. Kinuhiro, Phys. Rep. **247**, 221 (1994); J. Bijnens, Phys. Rep. **265**, 369 (1996).

4. *Dynamical Symmetry Breaking,* Ed. by E. Fahri and R. Jackiw (World Sci., Singapore, 1981); *Proceedings of the Workshop on Dynamical Symmetry Breaking, Nagoya, 1990,* Ed. by T. Muta and K. Yamawaki; *Proceedings of the International Workshop on Electroweak Symmetry Breaking,* Ed. by W. A. Bardeen, J. Kodaira, and T. Muta (World Sci., Singapore, 1991); V. A. Miransky, *Dynamical Symmetry Breaking in Quantum Field Theories* (World Sci., Singapore, 1993).
5. B. J. Harrington, S. Y. Park, and A. Yildiz, Phys. Rev. D **11**, 1472 (1975); M. Stone, Phys. Rev. D **14**, 3568 (1976); S. Kawati, G. Konisi, and H. Miyata, Phys. Rev. D **28**, 1537 (1983).
6. S. P. Klevansky and R. H. Lemmer, Phys. Rev. D **39**, 3478 (1989); S. P. Klevansky, Rev. Mod. Phys. **64**, 649 (1992); Lect. Notes Phys. **516**, 113 (1999).
7. K. G. Klimenko, Theor. Math. Phys. **89**, 211 (1991); **89**, 388 (1991); Z. Phys. C **54**, 323 (1992); I. Krive and S. Naftulin, Phys. Rev. D **46**, 2737 (1992); D. K. Kim and K. G. Klimenko, J. Phys. A **31**, 5565 (1998); K. Klimenko, A. S. Vshivtsev, and B. V. Magnitsky, Nuovo Cimento A **107**, 439 (1994); Pis'ma Zh. Éksp. Teor. Fiz. **61**, 847 (1995) [JETP Lett. **61**, 871 (1995)].
8. H. Suganuma and T. Tatsumi, Ann. Phys. (N. Y.) **208**, 470 (1991); Prog. Theor. Phys. **90**, 379 (1993).
9. V. Gusynin, V. Miransky, and I. Shovkovoy, Phys. Rev. D **52**, 4718 (1995); Phys. Lett. B **349**, 477 (1995); Nucl. Phys. B **462**, 249 (1996).
10. D. Cangemi, G. Dunne, and E. D'Hoker, Phys. Rev. D **51**, R2513 (1995); **52**, R3163 (1995); C. N. Leung, Y. J. Ng, and A. W. Ackly, Phys. Rev. D **54**, 4181 (1996); D. S. Lee, C. N. Leung, and Y. J. Ng, Phys. Rev. D **55**, 6504 (1997); V. A. Miransky, hep-th/9805159; E. J. Ferrer and V. Incera, SUNY-FRE-98-11, hep-ph/9810473; D. S. Lee, P. N. McGraw, Y. J. Ng, and I. A. Shovkovy, Phys. Rev. D **59**, 085008 (1999).
11. M. Ishi-i, T. Kashiwa, and N. Tanemura, Prog. Theor. Phys. **100**, 353 (1998); S. Kanemura, H.-T. Sato, and H. Tochimura, Nucl. Phys. B **517**, 567 (1998).
12. T. Muta and S. D. Odintsov, Mod. Phys. Lett. A **6**, 3641 (1991); C. T. Hill and D. S. Salopek, Ann. Phys. (N.Y.) **213**, 21 (1992); T. Inagaki, T. Muta, and S. D. Odintsov, Mod. Phys. Lett. A **8**, 2117 (1993); E. Elizalde, S. D. Odintsov, and Yu. I. Shil'nov, Mod. Phys. Lett. A **9**, 913 (1994); T. Inagaki, S. Mukaigawa, and T. Muta, Phys. Rev. D **52**, R4267 (1995); E. Elizalde, S. Leseduarte, S. D. Odintsov, and Yu. I. Shil'nov, Phys. Rev. D **53**, 1917 (1996); S. Kanemura and H.-T. Sato, Mod. Phys. Lett. A **24**, 1777 (1995); G. Miele and P. Vitale, Nucl. Phys. B **494**, 365 (1997); P. Vitale, Nucl. Phys. B **551**, 490 (1999); J. Hashida, S. Mukaigawa, T. Muta, *et al.,* Phys. Rev. D **59**, 101302 (1999); HUPD-9909, gr-qc/9907014.
13. E. V. Gorbar, Phys. Rev. D **61**, 024013 (2000).
14. I. L. Buchbinder, S. D. Odintsov, and I. L. Shapiro, *Effective Action in Quantum Gravity* (Inst. of Physics Publ., Bristol, 1992).
15. T. Inagaki, T. Muta, and S. D. Odintsov, Prog. Theor. Phys. Suppl. **127**, 93 (1997).
16. D. M. Gitman, S. D. Odintsov, and Yu. I. Shil'nov, Phys. Rev. D **54**, 2968 (1996); B. Geyer, L. N. Granda, and S. D. Odintsov, Mod. Phys. Lett. A **11**, 2053 (1996); E. Elizalde, S. D. Odintsov, and A. Romeo, Phys. Rev. D **54**, 4152 (1996); T. Inagaki, S. D. Odintsov, and Yu. I. Shil'nov, Int. J. Mod. Phys. A **14**, 481 (1999); E. Elizalde, Yu. I. Shil'nov, and V. V. Chitov, Class. Quantum Grav. **15**, 735 (1998).
17. G. 't Hooft and M. Veltman, Nucl. Phys. B **44**, 189 (1972).
18. J. Schwinger, Phys. Rev. **82**, 664 (1951).
19. T. S. Bunch and L. Parker, Phys. Rev. D **20**, 2499 (1979).
20. L. Parker and D. Toms, Phys. Rev. D **29**, 1584 (1984).
21. A. Z. Petrov, *Einstein Spaces* (Fizmatgiz, Moscow, 1961; Pergamon, Oxford, 1969).

Translated by R. Rogalyov